FAR-INFRARED STUDIES OF SUPERCONDUCTING THIN FILMS AND FABRY-PEROT RESONATORS MADE OF SUCH FILMS

By

VLADIMIR BOYCHEV

A DISSERTATION PRESENTED TO THE GRADUATE SCHOOL
OF THE UNIVERSITY OF FLORIDA IN PARTIAL FULFILLMENT
OF THE REQUIREMENTS FOR THE DEGREE OF
DOCTOR OF PHILOSOPHY

UNIVERSITY OF FLORIDA

2001

ACKNOWLEDGMENTS

I chose carefully one of the several best dissertation advisers that UF's Department of Physics could offer to me. Throughout my graduate study I have had a number of occasions which have confirmed that Professor David B. Tanner is the right choice for me. I was as careful in choosing my committee members as well. I express my sincere thanks to the chairman of my committee, Dr. **David Tanner**, **current** and past committee members in alphabetical order, Drs. John Graybeal, **Arthur Hebard**, **Selman Hershfield**, Peter Hirschfeld, **Charles Hooper**, Joseph Simmons and **Zhuomin Zhang**, for their patience, encouragement, and advice throughout my doctoral research, as well as for agreeing to compensate my slow writing with fast reading of this relatively thick dissertation.

Invaluable was the assistance from my collaborator A. Ravi Kumar. I also thank Leila Vale and David Rudman for producing the samples that we have been studying.

Very important for me has been the atmosphere of mutual help and shared experiences created by my friends, past and present colleagues from (or collaborators with) Dr. Tanner's infrared group: Manuel Quijada, Axel Zibold, Jungseek Hwang, Lev Gasparov, Sean Moore, Charles Porter, Dorothy John, Nacira Tache, Hsiang-Lin Liu, Eric Fons, Andrew Wint, Jason DeRoche, Young-Duck Yoon, Sunkwang Hong, Akito Ugawa, and several undergraduate students that have joined our group during summers; as well as from other groups: Steven Patamia, Kingshuk Majumdar, Youli Kanev, Valeri Kotov Fadi Zeini, Gareth Granroth, Anatoly Efimov, Mark Moores, Tat-Sang Choy, Mark Gunderson, Richard Pietri-Santiago, and many others.

I am grateful for the friendly teaching, administrative or technical support by the professors whose courses I chose to attend, the members of the machine shop, electronics shop, cryogenics lab, computer team, teaching advisers, and some other students, faculty, and staff members of the Physics Department, as well as other offices of the University of Florida. I appreciate the curiosity and efforts of most of the students whom I had the pleasure to teach. The LaTeXtemplate by Youli Kanev and Mike Jones is greatly appreciated. Thanks to go the UF editorial office with whose help I managed to get the right count of dots and commas in this thesis (O.K., dissertation;). But none of the above would have been possible if it were not for the International Students and Scholars Services to help me deal with INS and to make sure that I am always insured even if I do not want to be. I must mention especially John Graybeal, Peter Hirschfeld, Sergei Obukhov, Dwight Adams, Larry Phelps, Larry Frederick, Greg Labbe, Edward Storch, Robert DeSerio, Ray Thomas, Cindy Bright, Susan Rizzo, Chandra Chegireddy, Dan Rosigno, Brent Nelson, Alan Dorsey, and John Yelton.

I am very thankful to Dr. Zhuomin Zhang for financial and moral support especially during spring 2001, to Dr. Hendrik Monkhorst for helping me establish a credit history in this country by co-signing the loan I needed to bring my family here, to Dr. Gary Ihas for offering me a part-time internship during my first summer at the University of Florida, and to Dr. Richard Woodard for smoothing all red-tape support interruptions with zero-interest loans—that is better than the credit union!

Special thanks go to all those who also should have been named and acknowledged herein, but are not.

I thank the department administrators for allowing me to finish my dissertation, a process they should not have interrupted, in the first place.

My parents, family, relatives, and friends have supported me throughout most of my studies, career, and life.

Finally, I am happy to acknowledge the support of our research by the National Science Foundation, grants numbers CTS-9812027 and CTS-0082969.

TABLE OF CONTENTS

ACKNOWLEDGMENTS ii

ABSTRACT x

CHAPTERS

1 INTRODUCTION 1

2 ELECTROMAGNETISM 7

- 2.1 Electromagnetic Field 7
  - 2.1.1 Introduction 7
  - 2.1.2 Maxwell's Equations 9
  - 2.1.3 Material Equations 10
  - 2.1.4 Boundary Conditions 15
  - 2.1.5 Electromagnetic Energy, Momentum, Angular Momentum and Their Conservation 17
    - 2.1.5.1 General case 17
    - 2.1.5.2 Harmonic fields in linear, isotropic, homogeneous media 19
- 2.2 Electromagnetic Radiation 20
  - 2.2.1 Radio-Frequency Transmission Line 20
  - 2.2.2 Wave Equation 22
  - 2.2.3 Electromagnetic Waves 25
  - 2.2.4 Electromagnetic Waves within Insulating Media. Polarization of the Waves. 27
  - 2.2.5 Electromagnetic Waves within Conducting Media 30
    - 2.2.5.1 Waves within low-conductivity media 36
    - 2.2.5.2 Waves within high-conductivity media 37
    - 2.2.5.3 Metal or dielectric? 37
  - 2.2.6 Products of Harmonic Electromagnetic Fields in Complex Notation 39
  - 2.2.7 Energy and Momentum of Harmonic Electromagnetic Fields 40
  - 2.2.8 Electromagnetic Spectrum 42
  - 2.2.9 Quantization of the Electromagnetic Field 48

3 INTERACTION OF OPTICAL WAVES WITH MATTER 52

- 3.1 Optical Properties of Matter 52

3.1.1 Optical Characteristics . . . 52
3.1.2 Wave Impedance . . . 54
3.1.3 Kramers–Kronig Relations . . . 58
3.1.4 Dispersion . . . 60
3.1.5 Classical Models for the Optical Properties of Matter . . . 60
3.1.5.1 Drude model for free charge carriers . . . 60
3.1.5.2 Lorentz model for bound charge carriers . . . 66
3.1.6 Sum Rules . . . 74
3.1.7 Dispersion in Insulators. Group Velocity . . . 75
3.1.8 Perfect Conductors . . . 77
3.1.9 Superconductors . . . 78
3.2 Reflection and Transmission . . . 81
3.3 General Remarks about Reflection and Transmission . . . 81
3.3.1 Reflection and Refraction at the Interface between Two Dielectrics . . . 86
3.3.1.1 TE waves (s-polarization) . . . 87
3.3.1.2 TM waves (p-polarization) . . . 89
3.3.1.3 Brewster effect . . . 91
3.3.1.4 Total reflection . . . 91
3.3.1.5 Reflectance and transmittance . . . 92
3.3.1.6 Principle of reversibility . . . 93
3.3.2 Reflection from and Transmission through a Conducting Surface . . . 95
3.3.2.1 Normal incidence on a conducting surface . . . 96
3.3.3 Reflectance and Phase Dispersion Relations . . . 97
3.3.4 Determination of Optical Characteristics by the Dispersion Relations . . . 98
3.4 Optics of Thin Films and Multi-Layered Structures . . . 100
3.4.1 Reflection from and Transmission through a Single Layer . . . 101
3.4.1.1 Reflection and transmission coefficients . . . 103
3.4.1.2 Reflectance, transmittance and absorptance . . . 105
3.4.1.3 Fabry-Perot resonance . . . 108
3.4.1.4 Single absorbing layer, normal incidence. . . . 109
3.4.2 Reflection and Transmission by Two Layers . . . 111
3.4.3 Reflection and Transmission by Many Layers . . . 113
3.4.4 Reflection and Transmission Using Matrix Method . . . 114
3.5 Theoretical Background of Flat FP Resonators . . . 118

4 SUPERCONDUCTIVITY OF THE CUPRATES . . . 122

4.1 Review of Early Studies on the Cuprates . . . 122
4.1.1 Mid-Infrared Absorption . . . 123

4.1.1.1 Ceramic samples 123
4.1.1.2 Crystal samples and thin films 127
4.2 Review of More Recent Studies on the Cuprates 129
4.2.1 A Second Look at Mid-Infrared Absorption 130
4.2.1.1 $La_{2-x}Sr_xCuO_4$ 130
4.2.1.2 Bi cuprates 133
4.2.1.3 Y cuprates 138

5 INFRARED SPECTROSCOPY 140

5.1 Introduction 140
5.1.1 Spectrum Variables and Units 144
5.1.2 Optical Conductance 146
5.1.3 Spectrometers 149
5.1.3.1 Monochromators 149
5.1.3.2 Interferometers 150
5.1.3.3 Comparison of monochromators and interferometers 151
5.2 Fourier Transform Spectroscopy 152
5.2.1 Generic Michelson Interferometer 152
5.2.2 Details of FT-IRS 162
5.3 Equipment 163
5.3.1 Bruker FT-IR Interferometer. Reflection Stage. 163
5.3.2 Bolometer 164
5.4 Samples 166

6 TRANSMITTANCE AND REFLECTANCE 175

6.1 Introduction 175
6.2 Measurements of Silicon Substrates 180
6.2.1 Naked Silicon Substrates 180
6.2.2 Bufferless Silicon Substrates (Sample NIST 02) 191
6.2.2.1 Transmittance through Sample NIST 02 191
6.2.2.2 Front-side reflectance from Sample NIST 02 194
6.2.2.3 Back-side reflectance from Sample NIST 02 194
6.2.2.4 Results for Sample NIST 02 and discussion 194
6.2.3 Buffered Silicon Substrates (Sample NIST 39) 204
6.2.3.1 Transmittance through Sample NIST 39 204
6.2.3.2 Front-side reflectance from Sample NIST 39 207
6.2.3.3 Back-side reflectance from Sample NIST 39 210
6.2.3.4 Results for Sample NIST 39 and discussion 210
6.3 YBCO Films on Buffered Si Substrates 215
6.3.1 Sample NIST 255 215
6.3.1.1 Transmittance through Sample NIST 255 215

6.3.1.2 Results for NIST 255 and discussion 219
6.3.1.3 Front-side reflectance from Sample NIST 255 . . . 223
6.3.1.4 Back-side reflectance from Sample NIST 255 225
6.3.2 Sample NIST 256 232
6.3.2.1 Transmittance through Sample NIST 256 232
6.3.2.2 Results for Sample NIST 256 and discussion 235
6.3.2.3 Front-side reflectance from Sample NIST 256 . . . 236
6.3.2.4 Back-side reflectance from Sample NIST 256 236
6.3.3 Sample NIST 73 241
6.3.3.1 Transmittance through Sample NIST 73 242
6.3.3.2 Results for Sample NIST 73 and discussion 242
6.3.3.3 Front-side reflectance from Sample NIST 73 248
6.3.3.4 Back-side reflectance from Sample NIST 73 255
6.3.4 Sample NIST 74 257
6.3.4.1 Transmittance through Sample NIST 74 257
6.3.4.2 Results for Sample NIST 74 and discussion 261
6.3.4.3 Front-side reflectance from Sample NIST 74 265
6.3.4.4 Back-side reflectance from Sample NIST 74 269
6.4 Analysis of the Transmittance and Reflectance 272
6.4.1 Fitting Procedure 272
6.4.2 Transmittance 276
6.4.3 Optical Characteristics of the $YBa_2Cu_3O_{7-\delta}$ Films 280
6.4.3.1 Samples NIST 255 and NIST 256 281
6.4.3.2 Samples NIST 73 and NIST 74 289
6.4.4 Reflectance 300
6.5 Discussion 308
6.5.1 Antireflection Effect 308
6.5.2 The Effect of Optical Resonance 313
6.5.3 Fitting Parameters 314

7 ABSORPTANCE OF $YBa_2Cu_3O_{7-\delta}$ THIN FILMS 317

7.1 Introduction 317
7.2 Sample NIST 255 319
7.2.1 Absorptance in the Normal State 319
7.2.1.1 Front-side absorptance of Sample NIST 255 319
7.2.1.2 Back-side absorptance of Sample NIST 255 319
7.2.1.3 Fringe-averaged absorptance of Sample NIST 255 . 322
7.2.1.4 Effect of the film thickness 323
7.2.2 Absorptance in the Superconducting State 338
7.3 Sample NIST 256 342
7.3.1 Absorptance in the Normal State 342
7.3.1.1 Front-side absorptance of Sample NIST 256 342
7.3.1.2 Back-side absorptance of Sample NIST 256 342

7.3.2 Absorptance in the Superconducting State 345
7.4 Sample NIST 73 345
7.4.1 Absorptance in the Normal State 349
7.4.1.1 Front-side absorptance of Sample NIST 73 349
7.4.1.2 Back-side absorptance of Sample NIST 73 349
7.4.2 Absorptance in the Superconducting State 352
7.5 Sample NIST 74 355
7.5.1 Absorptance in the Normal State 355
7.5.1.1 Front-side absorptance of Sample NIST 74 355
7.5.1.2 Back-side absorptance of Sample NIST 74 355
7.5.2 Absorptance in the Superconducting State 355

8 FABRY-PEROT RESONATORS 361

8.1 Introduction 361
8.2 Theory of Superconducting FP Resonators 365
8.3 Review of Previous Studies 369
8.4 Measured Fabry-Perot Transmittance 371
8.4.1 Fabry-Perot resonator 2 372
8.4.2 Fabry-Perot resonator 1 378
8.4.3 Fabry-Perot resonator 3 381
8.5 Calculated Transmittance Compared to Experiment 383
8.6 Discussion 387
8.6.1 Coupling of Simple Resonators into a Compound One 387
8.6.2 Partial Fabry-Perot Resonators 389
8.6.3 Optimization of the Resonant Transmittance 394
8.6.4 The Effect of the Vacuum-Gap Thickness 394
8.6.5 The Effect of the $YBa_2Cu_3O_{7-\delta}$ Film Thickness 405

9 CONCLUSION 408

REFERENCES 414

BIOGRAPHICAL SKETCH 425

Abstract of Dissertation Presented to the Graduate School
of the University of Florida in Partial Fulfillment of the
Requirements for the Degree of Doctor of Philosophy

FAR-INFRARED STUDIES OF SUPERCONDUCTING THIN FILMS AND FABRY-PEROT RESONATORS MADE OF SUCH FILMS

By

Vladimir Boychev

December 2001

Chairman: David B. Tanner
Major Department: Physics

Using Fourier transform interferometers, we studied high-temperature superconducting $YBa_2Cu_3O_{7-\delta}$ (YBCO) thin films on silicon substrates in the far-infrared spectral range. We measured front-side reflectance, back-side reflectance (first measurement of this kind, with the incident ray coming from the substrate side), and transmittance at several temperatures in both the normal and superconducting state. Two select samples with closest matching characteristics were mounted facing each other in order to form Fabry-Perot resonators. The resonator gap was changed by spacers of various thickness. The resonator transmission was measured.

Initially, several samples were measured within the spectral range 10–100 cm^{-1} (wave number) or 1000–100 μm (wavelength). We could fit the results using the Drude model for the normal state, and the two-fluid model for the superconducting state of the YBCO film, a constant permittivity for the Si substrate, and ignoring the two thin buffer layers of YSZ and CeO_2.

Interference, optical resonance, and antireflection on the infrared properties of high-temperature superconducting (HTSC) films were observed and quantitatively

analyzed. At certain frequencies the back-side reflectance can be deeply modulated by oscillating the temperature above and below a critical value—enabling the use of the film as a far-infrared intensity modulator. Analysis of the absorptance, calculated from the measured reflectance and transmittance, showed that the absorptance from the back (substrate) side is higher. This fact demonstrates potential for designing radiation detectors based on superconducting thin films.

The complex refractive index of the films was determined. The effect of partial coherence on the Fabry-Perot resonator transmittance was studied. A complex interplay among the cavity length, substrate thickness, and phase shift upon reflection, affecting the magnitude of the resonant transmittance and finesse, was studied thoroughly to deduce an optimization method.

Recently, new samples were measured over the range 17–600 cm^{-1}. This wider spectral region allows a greater fit accuracy. We included phonons within the SiO_2 layer on the substrate back surface, and phonons of the YSZ buffer layer and the YBCO film, in order to fit the measured results. Spectral beating caused by close-in-frequency phonon oscillators in opposite layers was observed. Two strong and wide oscillators indicate that the SiO_2 and YSZ layers are amorphous.

CHAPTER 1
INTRODUCTION

In this introduction a number of terms (some of which may be unfamiliar to all readers) will be used. Most of these are properly introduced and explained later in this dissertation, or at least the reader will be referred to an appropriate source of information.

Superconductivity is a macroscopic manifestation of an essentially quantum-mechanical phenomenon. At some critical temperature T_c, every superconductor undergoes a phase transition; below T_c, the superconductor is characterized by zero electrical resistance and perfect diamagnetism,[1] provided the electrical current density and the magnetic field are less than their respective critical values. Ever since 1911 when the phenomenon of superconductivity was discovered by the group of Heike Kamerlingh Onnes, the interest in experiments, theory, and applications of superconductors has grown continuously. Many metals, alloys, and intermetallic compounds have been found to be superconductors. An extremely powerful boost in the field of superconductivity occurred in 1986 when Bednorz and Müller discovered the first high-temperature superconductor—lanthanum cuprate perovskite ($La_{2-x}Ca_xCuO_4$, $x = 0.15$, $T_c = 30$ K) and later ($Ba_xLa_{5-x}Cu_5O_y$, $T_c = 35$ K). This was the start of the cuprates era. The fast-paced research that followed quickly led to further record-breaking cuprates:[2] $YBa_2Cu_3O_{7-\delta}$ ($\delta \simeq 0.10$, $T_c = 93$ K, 1987), $Bi_2Sr_2Ca_2Cu_3O_{10}$ ($T_c = 110$ K, 1988), $Tl_2Ba_2Ca_2Cu_3O_{10}$

---

[1] That is, any magnetic field is expelled out of a material in the superconducting state.

[2] Here the optimally-doped compositions are listed. Naturally, one can expect that they were not the first to be produced and studied.

(T_c = 125 K, 1988), and $Hg_2Sr_2CaCu_2O_{8+\delta}$ (T_c = 133 K, 1993) [1, p. 22]. Most importantly, since 1987 the superconducting state can be maintained by using the much more abundant and cheaper coolant: liquid nitrogen. This fact has widened the potential applications of superconductors significantly.

Very recently a superconducting transition was discovered in MgB_2 (magnesium diboride). This has become the source of renewed excitement in the superconducting community which culminated in a very busy postdeadline session at the March 2001 Meeting of the American Physical Society in Seattle that lasted till about midnight. Even though the critical temperature of MgB_2 is modest (39 K), this new-type superconductor is important for two reasons: first, by detailed studies of the isotope effect and various substitutions it may be possible to raise the critical temperature significantly,[3] an approach that was proven to be quite successful in the cuprate case; and second, the new superconductor presents another instance of a high-temperature superconductor that offers an opportunity to get another "projection" of the superconductivity phenomenon which could facilitate the understanding of the mechanism of high-temperature superconductivity. Our current studies, however, do not cover this new superconductor.

Unlike the low-temperature superconductors, the cuprates are characterized by the following:[4]

- very high critical temperature;
- complex unit cell containing a large number of atoms; most cuprates have orthorhombic structure (but close to tetragonal) like the 123 compounds (e.g., $YBa_2Cu_3O_{7-\delta}$ because of the quasi-one-dimensional Cu–O chains which cause anisotropy in the a–b plane), yet some are tetragonal;

---

[3] Unfortunately the initial attempts to do so have not been successful to date.

[4] Some of these peculiarities will be introduced and covered in more detail later.

- layered structure which results in highly anisotropic physical properties;
- superconducting properties due to the quasi-two dimensional CuO_2 planes;
- quasi-one-dimensional Cu–O chains in 123 compounds, or Bi–O layers in other cuprates, acting as reservoirs for charge carriers;
- p-type carriers (most cases);
- low charge-carrier concentrations leading to large penetration depths ($\lambda \sim 0.2\ \mu$m for currents in the a–b plane, and even larger for currents along the c–axis);
- very short coherence lengths ($\xi \sim 2.5$ nm in the a–b plane, and ~ 0.3 nm along the c-axis); these small values of ξ make superconducting fluctuations, grain boundaries and defects very important;
- "clean" limit (coherence length $\xi \ll$ free path ℓ of charge carriers);
- normal skin effect ($\ell \ll \lambda$);
- strong coupling ($3.5k_BT_c < 2\Delta \in [4,7]k_BT_c$);
- linear DC resistivity in the normal state;
- Hall coefficient with a strong temperature dependence;
- type II superconductor with large Ginsburg-Landau ratio ($\kappa \sim 100$);
- very high critical magnetic fields;
- high sensitivity to doping levels, and complex phase diagram;
- spin gap or pseudogap;

- d-wave (or in some cases possibly p-wave) pairing, or a superposition of one of these wave functions with an s-wave;
- Possible Fermi-liquid behaviour in the normal state for strongly overdoped materials;
- undoped parent compounds which are spin 1/2 antiferromagnetic insulators;
- isotope effect that depends strongly on the hole concentration.

The complicated structure and properties of the new superconductors have presented some major difficulties. Physicists had to include the entire array of experimental methods and tools[5] that had evolved during the 20^{th} century and which had been used successfully to study numerous solids with diverse properties; moreover, they had to employ all existing theoretical models and to propose a number of new ones in an attempt to explain the various anomalies observed in the cuprates.[6] As time goes by physicists are learning more and more about the cuprates. Some significant progress has already been made, but a thorough understanding of how high-temperature superconductors "tick" has yet to be achieved. There are still hopes that sooner or later room-temperature superconductivity could be achieved. But even if this turns out to be far in the future, the better superconductors are studied, the more successfully they can be engineered and utilized into practice.

---

[5] Such as isotope effect studies, heat-capacity measurements, high-pressure studies, studies of the transport properties (electrical and thermal conductivity, Hall effect, thermopower) in the $\boldsymbol{a}$–$\boldsymbol{b}$ plane and later in the $\boldsymbol{c}$ direction, flux quantization measurements using Superconducting QUantum Interference Devices (SQUIDs), Angle-Resolved PhotoEmission Spectroscopy (ARPES) measurements, Fourier Transform Infra-Red (FTIR) spectroscopy, Raman spectroscopy, microwave magnetic penetration depth measurements, Nuclear Magnetic Resonance (NMR), Josephson Tunneling, magnetic fluxoid lattice and glass studies (melting, pinning, etc.).

[6] Bardeen–Cooper–Schrieffer theory, Ginsburg-Landau theory, Lawrence-Doniach model, polaron-bipolaron model, Fermi liquid, marginal Fermi liquid, simple Hubbard model, three-band Hubbard model, t–J model, resonance valence bond (RVB) model, etc.

Infrared spectroscopy is an important and powerful experimental method to study superconductors. In contrast to tunneling and photoemission measurements, the infrared light penetrates deeply (0.2–1.0 μm) into superconductors, and therefore infrared spectroscopy is less sensitive to surface defects and especially to insulating surface layers. Infrared spectroscopy can be used to study free carriers, low-energy excitations, infrared-active phonons and other peculiarities of the electronic structure. Before the high-temperature superconductors were discovered, infrared spectroscopy had produced some essential results such as the temperature dependence of the gap in low-temperature superconductors, and after that it has been used to study the cuprates as well, though in the latter case the results could not be interpreted as quickly and easily. Some meaningful data about the gap and pseudogap of the cuprates have already been obtained and relatively successfully interpreted. The earlier studies were often done on low-quality microtwinned or single-crystal bulk samples, as well as on thick films. Later, better-quality crystalline samples and thin films have been studied. Thin-film studies are especially important for a number of practical applications such as microwave and infrared detectors or sensors, filters, modulators, delay lines, antennae, resonators, transmission lines, and magnetometers employing field-dependent microwave absorption.

Material scientists, physicists, and chemists have done elaborate studies aimed at selecting better substrate–buffer-layer combinations compatible with the superconducting film, as well as perfecting the buffer-layer and film deposition techniques. Thin cuprate films are characterized by far-infrared spectra that differ significantly from those of the bulk of thick-film samples.

This dissertation is a modest contribution to the far-infrared studies of superconducting thin films. The current introductory chapter precedes the following material:

Chapter 2 presents the basic theory of electromagnetism and electromagnetic waves within various media. A number of useful quantities are introduced and explained.

Chapter 3 introduces more optical characteristics, and presents the classical models of dispersion due to both "free" and bound charge carriers. Reflection from and transmission through a single interface are considered, followed by various methods for calculating the optical properties of thin films and multi-layered structures.

Chapter 4 provides some general background for the superconductivity of the cuprates and reviews previous infrared studies of the cuprates.

Chapter 5 explains the basics of infrared spectroscopy and describes the equipment as well as the samples that have been used in our studies.

Chapter 6 presents the measured far-infrared transmittance, front-side and back-side reflectance, the fits to these data, and their analysis.

Chapter 7 combines the measured transmittance and reflectance from the appropriate side in order to get the front-side and back-side absorptance. The effect of film thickness on the absorptance has been studied. The results are discussed and can be utilized in the design and optimization of infrared detectors.

Chapter 8 presents our measurements of transmittance through Fabry-Perot resonators made of a couple of samples facing each other and separated by a suitable spacer. The fits to the data, as well as discussion of the results, are given. Ways to optimize such structures are shown.

Finally, chapter 9 summarizes our conclusions and future research plans.

CHAPTER 2
ELECTROMAGNETISM

2.1 Electromagnetic Field

2.1.1 Introduction

Most of this section is based on some well-known books by famous authors [2–6], listed in the order their first edition appeared (even if it were not translated immediately into English). Here I must add a book by Griffiths [7], a very good undergraduate textbook, but still (or maybe because of that) it is very informative on many topics.

For the purpose of clarity complex quantities within this text will be denoted with a tilde above the symbol,[1] e.g., a complex quantity A will appear as $\widetilde{A}$. Real parts of complex quantities will be denoted with prime ($'$), and imaginary parts will be denoted with double prime ($''$) superscripts, i.e., $\widetilde{A} = A' + \mathrm{i}\,A''$ where $\mathrm{i}^2 = -1$. The asterisk (*) means complex conjugate as usual: $\widetilde{A}^* = (A' + \mathrm{i}\,A'')^* = A' - \mathrm{i}\,A''$.

The measurable physical quantities themselves are always real. Complex quantities are introduced in the equations for convenience in two cases:

- For the case of harmonic fields[2] and sources of the fields, complex notation in exponential form leads to convenient math simplification;[3]

---

[1] The presence of a tilde above a symbol does not preclude it to be real in special cases.

[2] This is not restrictive: Using the Fourier theorem [8], a very broad class of (practically any realistic) fields can be reduced to a superposition of harmonic fields.

[3] Differentiation ($\boldsymbol{\nabla}$) or integration ($\int \mathrm{d}x \int \mathrm{d}y \int \mathrm{d}z$) of the real quantities with respect to space, is replaced simply by multiplication or division of their complex forms by $\mathrm{i}\,\omega\boldsymbol{k}$, and similarly, differentiation ($\partial/\partial t$) or integration ($\int \mathrm{d}t$) of the real quantities with respect to time, is replaced simply by multiplication or division of their complex forms by $-\mathrm{i}\,\omega t$. Explanation for the minus

- For the case of absorbing media with Joule losses either the conductivity or the permittivity "become" complex. Additionally, at frequencies low enough, so that the magnetic losses become important, the permeability "becomes" complex, too. Introducing of such complex media "coefficients" preserves the equations in the same form as they have for non-absorbing media. The complex constants take into account the phase lag of the medium response with respect to the driving "force"

The final result for any field can be obtained by taking the real part at the end of any calculation including only linear operations (addition, subtraction, integration, and differentiation) applied on the complex fields[4] and/or their sources.[5] Should nonlinear operations (such as products, exponentiation and more complicated functions) be done on the fields and/or their source, one has to take the real parts of all fields first, and then do the prescribed operations. There is one exception when time-averaged products are considered which will be given in subsection 2.2.6. Another exception is the division operation which has been considered at the end of subsection 3.3 with respect to the Fresnel coefficients.

---

sign is given in subsection 2.2.3

[4] Electric field $\widetilde{\boldsymbol{E}}$, electric displacement $\widetilde{\boldsymbol{D}}$, magnetic field $\widetilde{\boldsymbol{H}}$, and magnetic induction (magnetic-flux density) $\widetilde{\boldsymbol{B}}$.

[5] Surface density $\widetilde{\boldsymbol{J}}$ of the electric current and volume density $\widetilde{\varrho}$ of free electric charges.

2.1.2 Maxwell's Equations

Classical electromagnetic fields are described by the macroscopic Maxwell's equations which have the following differential form (SI units):[6]

Ampère's law
$$\boldsymbol{\nabla} \times \widetilde{\boldsymbol{H}} = \frac{\partial \widetilde{\boldsymbol{D}}}{\partial t} + \widetilde{\boldsymbol{J}}, \tag{2.1}$$

Faraday's law
$$\boldsymbol{\nabla} \times \widetilde{\boldsymbol{E}} = -\frac{\partial \widetilde{\boldsymbol{B}}}{\partial t}, \tag{2.2}$$

Gauss' and Coulomb's law
$$\boldsymbol{\nabla} \cdot \widetilde{\boldsymbol{D}} = \widetilde{\varrho}, \tag{2.3}$$

No magnetic monopoles
$$\boldsymbol{\nabla} \cdot \widetilde{\boldsymbol{B}} = 0, \tag{2.4}$$

Continuity equation
$$\boldsymbol{\nabla} \cdot \widetilde{\boldsymbol{J}} = -\frac{\partial \widetilde{\varrho}}{\partial t}, \tag{2.5}$$

where the real parts of the complex quantities from the equations are the electric field $\boldsymbol{E}'$, the magnetic induction $\boldsymbol{B}'$, the electric displacement $\boldsymbol{D}'$, the magnetic field $\boldsymbol{H}'$, the net current density $\boldsymbol{J}'$ due to the movement of free electric charges, and the net volume density ϱ' of free electric charges.

Actually, the continuity equation 2.5 is not independent; it can be derived by taking the divergence of equation 2.1 and then substituting equation 2.3.

For the special case of static fields all the tildes disappear, and the time-derivative terms vanish from Maxwell's equations.

For the purpose of brevity only the differential form of the equations will be given in most cases herein. The integral form of Maxwell's equations can be found in the books by Stratton [3], Born and Wolf [5], Jackson [6], and in many other sources on electromagnetic theory.

---

[6] By the way, Coulomb is pronounced "Koul′onn"! //

2.1.3 Material Equations

The properties of the medium are characterized by the additional set of material (constitutive) equations. Let us begin with the special quasi-static (non-relativistic) case of harmonic-in-time, relatively weak fields within a physically isotropic, homogeneous, linear (i.e., non-absorbing or weakly-absorbing) medium for which the material equations have a simple linear form with scalar coefficients.

For DC-insulators, e.g., dielectrics, which are characterized by zero DC conductivity,[7] and whose absorption (if any) is due to bound charge carriers, it would be convenient to use material equations of the form:

$$\widetilde{\boldsymbol{D}} = \widetilde{\varepsilon}\,\varepsilon_o \widetilde{\boldsymbol{E}}; \qquad \widetilde{\boldsymbol{B}} = \widetilde{\mu}\,\mu_o \widetilde{\boldsymbol{H}}, \tag{2.6}$$

where $\widetilde{\varepsilon} = \varepsilon' + \mathrm{i}\,\varepsilon''$ is the complex relative dielectric permittivity and ε_o the permittivity of vacuum, $\widetilde{\mu} = \mu' + \mathrm{i}\,\mu''$ the complex relative magnetic permeability and μ_o is the permeability of vacuum. Strictly speaking only the real parts deserve the name relative, but for the lack of better terminology, when the SI system of units is used, "relative" is preserved even for the generalized complex quantities. The imaginary parts of the coefficients (ε'', μ'') describe the phase lag of the medium response $(\widetilde{\boldsymbol{D}}, \widetilde{\boldsymbol{B}})$ with respect to the "driving force" $(\widetilde{\boldsymbol{E}}, \widetilde{\boldsymbol{H}})$.

For DC-conductors, e.g., metals, in which the displacement current[8] $\partial\widetilde{\boldsymbol{D}}/\partial t \ll \widetilde{\boldsymbol{J}}$, and whose absorption is predominantly due to free charge carriers, it would be convenient to use material equations of the form:

---

[7] This is the reason why Ohm's law is not important for DC-insulators.

[8] This inequality is the reason why the left equation 2.6 is not important for DC-conductors.

$$\widetilde{\boldsymbol{J}} = \widetilde{\sigma}\,\widetilde{\boldsymbol{E}} = \widetilde{\boldsymbol{E}}\,/\,\widetilde{\rho}; \qquad \widetilde{\boldsymbol{B}} = \widetilde{\mu}\,\mu_o\,\widetilde{\boldsymbol{H}}, \tag{2.7}$$

where the left equation is the differential form of Ohm's law, $\widetilde{\sigma} = \sigma' + \sigma''$ is the complex specific conductivity and its inverse $\widetilde{\rho} = \rho' + \rho''$ is the specific resistivity. Similarly to the previous case, the imaginary part of the coefficient (the conductivity σ'') describes the phase lag of the medium response (the current density $\widetilde{\boldsymbol{J}}$) with respect to the "driving force" (the electric field $\widetilde{\boldsymbol{E}}$).

When one is interested to study the interaction of electromagnetic fields with matter in a more detailed manner, often another version of the first two constitutive relations is used:

$$\widetilde{\boldsymbol{D}} = \widetilde{\boldsymbol{P}} + \varepsilon_o\,\widetilde{\boldsymbol{E}}; \qquad \widetilde{\boldsymbol{B}} = \mu_o\,(\widetilde{\boldsymbol{M}} + \widetilde{\boldsymbol{H}}), \tag{2.8}$$

where the real parts of the complex quantities are called polarization $\boldsymbol{P}'$, and magnetization $\boldsymbol{M}'$, respectively.

For isotropic linear media the polarization is proportional to the electric field, and the magnetization is proportional to the magnetic field:

$$\widetilde{\boldsymbol{P}} = \widetilde{\chi}_e\,\varepsilon_o\,\widetilde{\boldsymbol{E}}; \qquad \widetilde{\boldsymbol{M}} = \widetilde{\chi}_m\,\widetilde{\boldsymbol{H}}, \tag{2.9}$$

where $\widetilde{\chi}_e$ and $\widetilde{\chi}_m$ are the complex electric and magnetic susceptibility, which characterize the medium contribution to $\widetilde{\varepsilon}$ and $\widetilde{\mu}$, respectively. The latter statement can be proven easily if we use the left ones of equations 2.15, 2.8, 2.9 on the one hand, and the right ones on the other, whereupon we get:

$$\text{complex} \qquad \widetilde{\varepsilon} = 1 + \widetilde{\chi}_e; \qquad \widetilde{\mu} = 1 + \widetilde{\chi}_m, \tag{2.10}$$

$$\text{real parts} \qquad \varepsilon' = 1 + \chi'_e; \qquad \mu' = 1 + \chi'_m, \tag{2.11}$$

$$\text{imaginary parts} \qquad \varepsilon'' = \chi''_e; \qquad \mu'' = \chi''_m. \tag{2.12}$$

In equations 2.10 and 2.11, the unity stands for the contribution of vacuum. Here I must mention that vacuum has neither magnetic nor dielectric properties, which is reflected clearly in the Gaussian system of units. However in SI, in order to preserve the historically accepted units,[9] vacuum is given artificially dielectric properties through ε_o and magnetic properties through μ_o.

The coefficients[10] in the material equations characterize the medium, and in general are complex.

In the simplest idealized case (non-existent in nature) these quantities are constant; that is, they are independent of time, frequency, position, field strength and direction, temperature, as well as on the history of any of these variables. Initially we shall consider the simple non-absorbing case with real coefficients, and later some simple absorbing cases for which either a complex permittivity $\widetilde{\varepsilon}$ or a complex conductivity $\widetilde{\sigma}$ must be used. It turns out that it is most convenient to use only the real parts of both, as explained at the end of this subsection.

For optical frequencies the magnetic properties of the medium can be ignored, so we shall consider that μ is real and unity ($\widetilde{\chi}_m = 0$). In this case the second of equations 2.15 is reduced to its form for vacuum

---

[9] Such as ampére, coulomb, farad, henry, ohm, tesla, volt, weber.

[10] Namely, conductivity $\widetilde{\sigma}$, dielectric permittivity $\widetilde{\varepsilon}$, or susceptibility $\widetilde{\chi}_e$, and magnetic permeability $\widetilde{\mu}$, or susceptibility $\widetilde{\chi}_m$.

$$\widetilde{\boldsymbol{B}} = \mu_o \widetilde{\boldsymbol{H}}. \tag{2.13}$$

Nevertheless, in order to preserve the general form of the equations, which is applicable for lower-than-optical frequencies as well, a real permeability will be kept as a place-holder/reminder.

The constitutive equations can be generalized for more complicated cases:

- For an anisotropic medium (e.g., non-cubic crystals) the coefficients are second-rank tensors;
- For an absorbing medium at least one of the coefficients is complex. Such complex coefficients depend on the frequency and the tildes above the coefficients make our equations ready for this case;
- When the fields are strong enough (e.g., focused laser beam), non-linear terms in the material equations cannot be neglected;
- For fast moving bodies relativistic relations must be used;
- In some cases (such as dielectric or magnetic hysteresis, as well as current in a gas of free ions) [5], the coefficients depend on the fields and their history;
- In certain cases the dependence on temperature or time (aging of the medium, chemical reactions, or phase transitions) must be considered;
- Finally, for complex inhomogeneous media one has to solve numerically formidable boundary value and/or scattering problems;
- In the intermediate case of planar layered media (a special case of inhomogeneous media) each layer is characterized by its own coefficients and the

problem is reduced to successive application of the boundary conditions for each interface. Such cases are considered later in chapter 3, starting from the simplest case of one interface (section 3.2) and continuing with multi-layered structures (section 3.4).

Various types of media can be characterized by the values or dependencies of the material coefficients: Very simplistically, substances with $\sigma' \approx 0$ at angular frequency $\omega = 0$ are insulators (dielectrics or vacuum); conductors (e.g., metals) have relatively high σ', while semiconductors have intermediate values of σ'. More accurately, the temperature dependence of σ' is decreasing for metals, but increasing for semiconductors. Most substances are non-magnetic ($\mu' = 1$ and $\chi'_m = 0$ at least approximately). For diamagnets $\mu' < 1$ and $\chi'_m < 0$, whereas for paramagnets $\mu' > 1$ and $\chi'_m > 0$. Finally, ferromagnetics are characterized by $\mu' \gg 1$ and $\chi'_m \gg 0$. Also, their magnetic permeability and susceptibility depend on the magnetic field and show hysteresis. In such a case their differential varieties, giving the slope of the respective dependence, can be used:

$$\widetilde{\mu}_d = \partial\widetilde{\boldsymbol{B}} \,/\, \partial\widetilde{\boldsymbol{H}}; \qquad \widetilde{\chi}_{md} = \partial\widetilde{\boldsymbol{M}} \,/\, \partial\widetilde{\boldsymbol{H}}. \tag{2.14}$$

Note, that for a non-absorbing medium either $\sigma' \rightarrow 0$ (ideal electric insulator, i.e., perfectly transparent medium), or $\sigma' \rightarrow \infty$ (ideal electric conductor, i.e., perfectly reflecting medium). For these two simple cases Ohm's law 2.16 becomes unimportant, as within such non-absorbing media either $\widetilde{\boldsymbol{J}} = 0$, or $\widetilde{\boldsymbol{E}} = 0$, respectively.

Most difficult to describe and most interesting is the intermediate case of bad conductors, i.e., leaky insulators. Similar is the case of good conductors or insulators at very high (optical) frequencies: both the bound and the free charge carriers contribute to the conducting and dielectric properties. In most practical cases it is not easy to separate the contributions by these two types of charge carriers. Therefore, it is convenient to accept the following convention: currents that are in phase with the electric field will be described as conducting currents by σ' regardless of what fractions of these currents are due to free or bound charge carriers; similarly, currents that are $\pi/2$ rad out-of-phase from the electric field will be described as polarizing currents by ε' regardless of what parts of these currents are due to bound or free charge carriers. This seems to be the most widespread convention among researchers of optical properties of matter, and is the choice for this dissertation, too. Therefore, from this point on, the following form of the material equations will be mostly used

$$\widetilde{\boldsymbol{D}} = \varepsilon' \varepsilon_o \widetilde{\boldsymbol{E}}; \qquad \widetilde{\boldsymbol{B}} = \widetilde{\mu} \mu_o \widetilde{\boldsymbol{H}}, \tag{2.15}$$

Ohm's law

$$\widetilde{\boldsymbol{J}} = \sigma' \widetilde{\boldsymbol{E}}, \tag{2.16}$$

In some equations (e.g., in subsection 2.2.2) tildes are kept over both $\widetilde{\sigma}$ and $\widetilde{\varepsilon}$ as a reminder, but such equations must be adapted according to the applicable convention: removing the tilde from either one, or replacing both with their real parts, respectively.

In order to present the equations in a form that is ready for more general cases, I was forced to "expose" the tip of the "iceberg" about absorbing media at this early stage. More details and a more systematic presentation are given in subsection 2.2.5, as well as in section 3.1.

2.1.4 Boundary Conditions

Let us consider two semi-infinite media filling all of space. On the surface forming the interface between them, the following boundary conditions apply (derivation can be found in many books [3,6,5]):

$$\hat{\mathbf{n}}_{1,2} \cdot (\boldsymbol{D}^{(2)} - \boldsymbol{D}^{(1)}) = \varrho_s; \qquad \hat{\mathbf{n}}_{1,2} \cdot (\boldsymbol{B}^{(2)} - \boldsymbol{B}^{(1)}) = 0, \tag{2.17}$$

$$\hat{\mathbf{n}}_{1,2} \times (\boldsymbol{E}^{(2)} - \boldsymbol{E}^{(1)}) = 0; \qquad \hat{\mathbf{n}}_{1,2} \times (\boldsymbol{H}^{(2)} - \boldsymbol{H}^{(1)}) = \boldsymbol{J}_s, \tag{2.18}$$

where ϱ_s is the surface density of electric charges located at the interface, $\boldsymbol{J}_s$ the surface density of electric current flowing along the interface. The subscripts denote the medium and $\hat{\mathbf{n}}_{12}$ is a unit vector that is normal to the interface and its direction is from medium (1) to medium (2).

The boundary conditions, equations 2.17 and 2.18, can be projected on the normal (subscript n) and a tangential (subscript τ) axis along the surface current:

$$D_n^{(2)} - D_n^{(1)} = \varrho_s; \qquad B_n^{(2)} - B_n^{(1)} = 0, \tag{2.19}$$

$$E_\tau^{(2)} - E_\tau^{(1)} = 0; \qquad H_\tau^{(2)} - H_\tau^{(1)} = J_s. \tag{2.20}$$

The latter form makes it transparent that the normal components of $\boldsymbol{B}$ and the tangential components of $\boldsymbol{E}$ are continuous; in contrast the normal components of $\boldsymbol{D}$ and the tangential components of $\boldsymbol{H}$ can experience a jump at the interface whenever surface electric charges and/or surface electric currents are present there. This jump results from a spatial discontinuity of the medium. Similarly, one can consider a jump due to a time discontinuity of the field sources (switching on or off) [5].

The boundary conditions given above hold true even for an imaginary surface within any uniform medium, but this is a trivial case.

2.1.5 Electromagnetic Energy, Momentum, Angular Momentum and Their Conservation

2.1.5.1 General case

For convenience, only the basic equations are listed here. Derivations can be found in a number of sources [2,5–7]. Here all fields are real because the equations are quadratic with respect to the fields and/or their sources, and so the generalization to complex notation is not straightforward. Therefore, it will be done later.

1. The energy density for the magnetic and the electric field, respectively, is

$$u_m = \int_0^{\boldsymbol{B}} \boldsymbol{H} \cdot \mathrm{d}\boldsymbol{\mathcal{B}}; \qquad u_e = \int_0^{\boldsymbol{E}} \boldsymbol{D} \cdot \mathrm{d}\boldsymbol{\mathcal{E}}. \tag{2.21}$$

   where $\boldsymbol{\mathcal{B}}$ and $\boldsymbol{\mathcal{E}}$ are dummy variables for the magnetic-field-flux density and the electric field, respectively. The integrals can be taken when the material equations are linear and isotropic

$$u_m = \boldsymbol{H} \cdot \boldsymbol{B} \,/\, 2; \qquad u_e = \boldsymbol{D} \cdot \boldsymbol{E} \,/\, 2, \tag{2.22}$$

   and combining these two terms we get the total energy density of the electromagnetic field

$$u_{em} = u_m + u_e = (\boldsymbol{B} \cdot \boldsymbol{H} + \boldsymbol{E} \cdot \boldsymbol{D}) \,/\, 2. \tag{2.23}$$

2. The Poynting vector (i.e., the electromagnetic-energy-flux density) is

$$\boldsymbol{S} = \boldsymbol{E} \times \boldsymbol{H}. \tag{2.24}$$

3. The volume density of the electromagnetic-field momentum is

$$\boldsymbol{g}_{em} = \boldsymbol{S}/\,v^2 = \boldsymbol{S}/\,(n\,c)^2. \tag{2.25}$$

4. The volume density of the electromagnetic-field angular momentum is

$$\boldsymbol{L}_{em} = \boldsymbol{r} \times \boldsymbol{g}_{em} = \boldsymbol{r} \times \boldsymbol{S}\,/\,c^2. \tag{2.26}$$

5. The continuity equation in this case is simply the energy-conservation law

$$\boldsymbol{\nabla} \cdot \boldsymbol{S} + \frac{\partial u_{em}}{\partial t} + \boldsymbol{J} \cdot \boldsymbol{E} = 0, \tag{2.27}$$

   where the third term represents the power per unit volume related to the conversion of electromagnetic energy into mechanical energy.

6. Momentum conservation can be expressed by

$$\boldsymbol{\nabla} \cdot (-\mathcal{T}) + \frac{\partial}{\partial t}(\boldsymbol{p}_{mech} + \boldsymbol{g}_{em}) = 0, \tag{2.28}$$

   where $\boldsymbol{p}_{mech}$ is the volume density of mechanical momentum, and $-\mathcal{T}$ is the momentum-flux volume density. Here $\mathcal{T}$ is the symmetric, second-rank, stress tensor. In general it can include an elastic, electric, and magnetic terms. For the special case of vacuum the elastic term is zero and what is left is Maxwell's electromagnetic stress tensor with components

$$\mathcal{T}_{ij} = \varepsilon_o\,(E_i\,E_j - \delta_{ij}\,E^2/\,2) + (B_i\,B_j - \delta_{ij}\,B^2/\,2)/\,\mu_o, \tag{2.29}$$

   where the portion before the plus sign gives the stress within dielectric materials, whereas the portion after the plus sign gives the stress within magnetic materials. The electromagnetic stress tensor for more complicated cases can be found in more advanced books [3,4].

7. Angular momentum conservation is expressed by

$$\begin{aligned} 0 &= \boldsymbol{r} \times \boldsymbol{\nabla} \cdot (-\mathcal{T}) + \frac{\partial}{\partial t} \boldsymbol{r} \times (\boldsymbol{p}_{mech} + \boldsymbol{g}_{em}) \\ &= \boldsymbol{r} \times \boldsymbol{\nabla} \cdot (-\mathcal{T}) + \frac{\partial}{\partial t} (\boldsymbol{L}_{mech} + \boldsymbol{L}_{em}), \end{aligned} \tag{2.30}$$

where $\boldsymbol{L}_{mech} = \boldsymbol{r} \times \boldsymbol{p}_{mech}$ is the volume density of the mechanical angular momentum, and $\boldsymbol{r} \times \boldsymbol{\nabla} \cdot (-\mathcal{T})$ is the torque volume density.

8. The differential form of Joule-Lenz's law

$$\frac{\partial P}{\partial V} = \boldsymbol{J} \cdot \boldsymbol{E} = \rho \boldsymbol{J}^2 = \sigma \boldsymbol{E}^2, \tag{2.31}$$

gives the power per unit volume that is converted into heat.

The equations in this subsection up to this point are general and hold true for any real fields, even static ones.

2.1.5.2 Harmonic fields in linear, isotropic, homogeneous media

A few additional points follow for this special case.

1. The energy densities of the magnetic and electric parts of the wave are

$$u_m = H\,B/2 = B^2/(2\,\mu\,\mu_o) = E^2/(2\,v^2\mu\,\mu_o) = \varepsilon\,\varepsilon_o\,E^2/2, \tag{2.32}$$

$$u_e = D\,E/2 = \varepsilon\,\varepsilon_o\,E^2/2 = u_m, \tag{2.33}$$

and so the total energy density of the electromagnetic wave is

$$u_{em} \;=\; u_m \;+\; u_e \;=\; 2\,u_m \;=\; 2\,u_e \;=\; \varepsilon\,\varepsilon_o\,E^2. \tag{2.34}$$

2. The magnitude of the Poynting vector for the case of a transverse monochromatic wave with mutually orthogonal electric and magnetic fields is

$$\begin{aligned} S \;&=\; |\boldsymbol{S}| \;=\; |\boldsymbol{E} \times \boldsymbol{H}| \;=\; E\,H \;=\; E\,B\,/\,(\mu\,\mu_o) \;=\; E^2/\,(v\,\mu\,\mu_o) \\ &=\; v\,\varepsilon\,\varepsilon_o\,E^2 \;=\; v\,u_{em} \;=\; n\,c\,\varepsilon\,\varepsilon_o\,E^2. \end{aligned} \tag{2.35}$$

3. The time-average of S is the intensity of the wave:

$$I \;=\; \langle S \rangle \;=\; n\,c\,\varepsilon\,\varepsilon_o\,\left\langle E^2 \right\rangle \;=\; n\,c\,\varepsilon\,\varepsilon_o\,E_o^2/\,2. \tag{2.36}$$

4. The pressure exerted by an electromagnetic wave is

$$p \;=\; v\,g_{em} \;=\; S\,/\,v \;=\; S\,/\,(n\,c) \;=\; \varepsilon\,\varepsilon_o\,E^2. \tag{2.37}$$

2.2 Electromagnetic Radiation

2.2.1 Radio-Frequency Transmission Line

Let us consider the transmission line with distributed parameters shown in Figure 2.1. The distributed parameters are characterized by the following linear densities: series resistance R, series inductance L, parallel conductance G, and parallel capacity C [3, pp. 549–550]. The series impedance per unit length and the

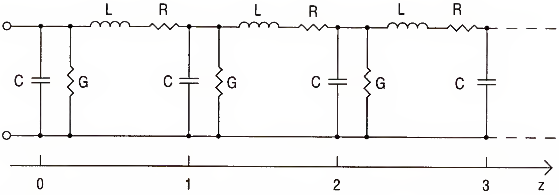

Figure 2.1: Schematic model of a transmission line with distributed parameters.

parallel admittance per unit length are

$$\widetilde{Z}_s \;=\; R \,-\, \mathrm{i}\,\omega\, L; \qquad\qquad \widetilde{Y}_p \;=\; G \,-\, \mathrm{i}\,\omega\, C. \tag{2.38}$$

The voltage and current distributions along the line must satisfy the following first-order coupled differential equations:

$$\frac{\partial \widetilde{V}}{\partial z} \;=\; -L\,\frac{\partial \widetilde{I}}{\partial t} \,-\, R\,\widetilde{I} \;=\; -(R \,-\, \mathrm{i}\,\omega\, L)\,\widetilde{I} \;=\; -\widetilde{Z}_s\,\widetilde{I}, \tag{2.39}$$

$$\frac{\partial \widetilde{I}}{\partial z} \;=\; -C\,\frac{\partial \widetilde{V}}{\partial t} \,-\, G\,\widetilde{V} \;=\; -(G \,-\, \mathrm{i}\,\omega\, C)\,\widetilde{V} \;=\; -\widetilde{Y}_p\,\widetilde{V}, \tag{2.40}$$

which can be decoupled at the expense of increasing the order by one to get the second-order telegraphic equations

$$\frac{\partial^2 \widetilde{U}}{\partial z^2} \;=\; L\,C\,\frac{\partial^2 \widetilde{U}}{\partial t^2} \,+\, (L\,G \,+\, R\,C)\,\frac{\partial \widetilde{U}}{\partial t} \,+\, R\,G\,\widetilde{U}, \tag{2.41}$$

where $\widetilde{U}$ can be either the voltage $\widetilde{V}$, or the current $\widetilde{I}$, in complex notation. Replacing the time partial derivative by[11] $-\mathrm{i}\,\omega$ we can eliminate the time dependence, and thus get the Helmholtz equation[12] (which can also be obtained directly by using the right most terms of equations 2.39 and 2.40)

---

[11] Explanation for the minus sign is given in subsection 2.2.3

$$\frac{\partial^2 \widetilde{U}}{\partial z^2} = (-\mathrm{i}\omega L)(-\mathrm{i}\omega C)\widetilde{U} - \mathrm{i}\omega(LG + RC)\widetilde{U} + RG\widetilde{U}$$

$$= (R - \mathrm{i}\omega L)(G - \mathrm{i}\omega C)\widetilde{U} = \widetilde{Z}_s \widetilde{Y}_p \widetilde{U}. \qquad (2.42)$$

The solution of equations 2.41 is a current-voltage wave traveling to the right (top signs), or to the left (bottom signs)

$$\widetilde{I} = \widetilde{I}_o\, \mathrm{e}^{\pm \mathrm{i}\widetilde{k}z - \mathrm{i}\omega t}; \qquad \widetilde{V} = \pm \widetilde{Z}\,\widetilde{I}, \qquad (2.43)$$

where $\widetilde{Z}$ is the characteristic impedance of the transmission line. The same solution applies also for equations 2.42, except for the fact that now the time dependence is optional.

Substituting the solution 2.43 into equations 2.39 and 2.40 we get two equations. By multiplying or dividing these equations we get the propagation constant $\widetilde{k}$ and the characteristic impedance $\widetilde{Z}$ of the transmission line

$$\widetilde{k} = \mathrm{i}\sqrt{\widetilde{Z}_s \widetilde{Y}_p}; \qquad \widetilde{Z} = \sqrt{\widetilde{Z}_s \,/\, \widetilde{Y}_p}. \qquad (2.44)$$

2.2.2 Wave Equation

Let us consider a medium that is isotropic, but possibly inhomogeneous. Taking the curl of Ampère's law 2.1 and Faraday's law 2.2, and using two of the material equations 2.15, we get two coupled equations [9]:

---

[12] Compare with equation 2.62

$$\boldsymbol{\nabla}\times(\boldsymbol{\nabla}\times\widetilde{\boldsymbol{H}}) = +\boldsymbol{\nabla}\times\left(\tilde{\varepsilon}\,\varepsilon_o\,\frac{\partial\widetilde{\boldsymbol{E}}}{\partial t}\right) + \boldsymbol{\nabla}\times\widetilde{\boldsymbol{J}}, \tag{2.45}$$

$$\boldsymbol{\nabla}\times(\boldsymbol{\nabla}\times\widetilde{\boldsymbol{E}}) = -\boldsymbol{\nabla}\times\left(\tilde{\mu}\,\mu_o\,\frac{\partial\widetilde{\boldsymbol{B}}}{\partial t}\right). \tag{2.46}$$

Applying the vector equalities (which hold true even for complex quantities)

$$\boldsymbol{\nabla}\times(\boldsymbol{\nabla}\times\widetilde{\boldsymbol{A}}) = \boldsymbol{\nabla}(\boldsymbol{\nabla}\cdot\widetilde{\boldsymbol{A}}) - \boldsymbol{\nabla}^2\widetilde{\boldsymbol{A}}, \tag{2.47}$$

$$\boldsymbol{\nabla}\times(\tilde{\alpha}\,\widetilde{\boldsymbol{A}}) = (\boldsymbol{\nabla}\tilde{\alpha})\times\widetilde{\boldsymbol{A}} + \tilde{\alpha}\,\boldsymbol{\nabla}\times\widetilde{\boldsymbol{A}}, \tag{2.48}$$

$$\boldsymbol{\nabla}\cdot(\tilde{\alpha}\,\widetilde{\boldsymbol{A}}) = (\boldsymbol{\nabla}\tilde{\alpha})\cdot\widetilde{\boldsymbol{A}} + \tilde{\alpha}\,\boldsymbol{\nabla}\cdot\widetilde{\boldsymbol{A}}, \tag{2.49}$$

and substituting Maxwell's equations 2.1–2.4, and the constitutive relations 2.15 where necessary, one can decouple the wave equations for the electromagnetic field:

$$\widetilde{\Box}\widetilde{\boldsymbol{H}} + \boldsymbol{\nabla}\left(\frac{\boldsymbol{\nabla}\tilde{\mu}}{\tilde{\mu}}\cdot\widetilde{\boldsymbol{H}}\right) + \frac{\boldsymbol{\nabla}\tilde{\varepsilon}}{\tilde{\varepsilon}}\times(\boldsymbol{\nabla}\times\widetilde{\boldsymbol{H}}) = \frac{\boldsymbol{\nabla}\tilde{\varepsilon}}{\tilde{\varepsilon}}\times\widetilde{\boldsymbol{J}} - \boldsymbol{\nabla}\times\widetilde{\boldsymbol{J}}, \tag{2.50}$$

$$\widetilde{\Box}\widetilde{\boldsymbol{E}} + \boldsymbol{\nabla}\left(\frac{\boldsymbol{\nabla}\tilde{\varepsilon}}{\tilde{\varepsilon}}\cdot\widetilde{\boldsymbol{E}}\right) - \frac{\boldsymbol{\nabla}\tilde{\mu}}{\tilde{\mu}}\times(\boldsymbol{\nabla}\times\widetilde{\boldsymbol{E}}) = \tilde{\mu}\,\mu_o\,\sigma\,\frac{\partial\widetilde{\boldsymbol{E}}}{\partial t} - \varepsilon_o\,\boldsymbol{\nabla}\frac{\tilde{\varrho}}{\tilde{\varepsilon}}. \tag{2.51}$$

Above $\widetilde{\Box}$ is the complex d'Alembertian operator

$$\widetilde{\Box} = \boldsymbol{\nabla}^2 - \tilde{\mu}\,\mu_o\,\tilde{\varepsilon}\,\varepsilon_o\,\frac{\partial^2}{\partial t^2} = \boldsymbol{\nabla}^2 - \frac{\tilde{\mu}\,\tilde{\varepsilon}}{c^2}\,\frac{\partial^2}{\partial t^2}. \tag{2.52}$$

In the special case of vacuum ($\tilde{\mu} = 1 = \tilde{\varepsilon}$) it is reduced to the usual d'Alembertian

$$\Box = \boldsymbol{\nabla}^2 - \mu_o\,\varepsilon_o\,\frac{\partial^2}{\partial t^2} = \boldsymbol{\nabla}^2 - \frac{1}{c^2}\frac{\partial^2}{\partial t^2}. \tag{2.53}$$

Even if we created some electric charge distribution, e.g., with the time dependence of an electromagnetic wave, within a conductor, such an oscillating charge distribution would fall off exponentially [5, p. 736]:

$$\tilde{\varrho} = \tilde{\varrho}_o \exp\left(-\mathrm{i}\,\omega\,t - t\,/\,\tilde{\tau}\right), \tag{2.54}$$

where $\tilde{\tau} = \tilde{\varepsilon}\,\varepsilon_o\,/\,\sigma$ is the complex relaxation time. When the conductivity σ is appreciable, $\omega\,\tau' \ll 1$, and it is clear that any charge oscillation within a good conductor, caused by an electromagnetic wave, would be damped long before a full cycle has been completed. Hence, for good conductors $\tilde{\varrho} = 0$ for all practical purposes.[13] Therefore, for conducting media with $\boldsymbol{\nabla}\tilde{\mu} = 0$, but with possibly inhomogeneous dielectric function, the wave equations are:

$$\tilde{\Box}\widetilde{\boldsymbol{H}} + \frac{\boldsymbol{\nabla}\tilde{\varepsilon}}{\tilde{\varepsilon}} \times (\boldsymbol{\nabla} \times \widetilde{\boldsymbol{H}}) = \frac{\boldsymbol{\nabla}\tilde{\varepsilon}}{\tilde{\varepsilon}} \times \tilde{\boldsymbol{J}} - \boldsymbol{\nabla} \times \tilde{\boldsymbol{J}}, \tag{2.55}$$

$$\tilde{\Box}\widetilde{\boldsymbol{E}} + \boldsymbol{\nabla}\left(\frac{\boldsymbol{\nabla}\tilde{\varepsilon}}{\tilde{\varepsilon}} \cdot \widetilde{\boldsymbol{E}}\right) = \tilde{\mu}\,\mu_o\,\sigma\,\frac{\partial \widetilde{\boldsymbol{E}}}{\partial t}. \tag{2.56}$$

where $\tilde{\boldsymbol{J}}$ is given by Ohm's law 2.16. Provided the conductivity is uniform, i.e., $\boldsymbol{\nabla}\sigma = 0$, by using Faraday's law 2.2, we transform the last term in equation 2.55 into another form

$$\boldsymbol{\nabla} \times \tilde{\boldsymbol{J}} = \sigma\,\boldsymbol{\nabla} \times \widetilde{\boldsymbol{E}} = -\sigma\,\frac{\partial \widetilde{\boldsymbol{B}}}{\partial t} = -\sigma\,\tilde{\mu}\,\mu_o\,\frac{\partial \widetilde{\boldsymbol{H}}}{\partial t}. \tag{2.57}$$

---

[13] The only term with $\tilde{\varrho}$ in the wave equations 2.50 and 2.51 would vanish even for a bad conductor, provided we were dealing with a homogeneous "leaky" dielectric.

The presence of first derivatives of the fields with respect to time in the wave equations is an immediate indication that only damped electromagnetic waves are possible within conducting media.

For homogeneous conducting media the wave equations 2.55 and 2.56 are further reduced to

$$\tilde{\Box}\widetilde{\boldsymbol{H}} = \tilde{\mu}\,\mu_o\,\sigma\,\frac{\partial\widetilde{\boldsymbol{H}}}{\partial t}; \qquad \tilde{\Box}\tilde{\boldsymbol{E}} = \tilde{\mu}\,\mu_o\,\sigma\,\frac{\partial\tilde{\boldsymbol{E}}}{\partial t}, \tag{2.58}$$

where equation 2.57 has been used.

Finally, for the simplest case of an uniform, non-absorbing medium (e.g., transparent dielectric), in equations 2.58 we can substitute $\sigma = 0$; furthermore the material coefficients become real, and we get the regular d'Alembert equations

$$\Box\widetilde{\boldsymbol{H}} = 0; \qquad \Box\tilde{\boldsymbol{E}} = 0. \tag{2.59}$$

All of the equations, from the beginning of the chapter to this point, can be reduced to their form for vacuum by first substituting $\tilde{\varepsilon} = 1 = \tilde{\mu}$, $\tilde{\varrho} = 0 = \tilde{\sigma}$ (and $\tilde{\boldsymbol{J}} = 0$) and then substituting $\widetilde{\boldsymbol{H}}$ and $\tilde{\boldsymbol{D}}$ using the reduced material equation 2.13 and its analog obtained by reducing the left equation 2.15.

2.2.3 Electromagnetic Waves

The wave equations listed above imply the existence of electromagnetic waves. These equations have various solutions depending on the boundary and initial conditions. The waves can be either monochromatic or with complicated wave forms. According to Fourier's theorem [8], any general field can be represented as a superposition (an integral for the continuous case or a sum for the discrete one) of an infinite (or for special cases—finite) number of components with various frequencies. Therefore, one can simply consider a monochromatic solution. By solving the wave equation in different coordinate systems one can get solutions with different form of the wave fronts. E.g., in spherical coordinates one would get spherical waves, in elliptical coordinates elliptical waves, in cylindrical coordinates cylindrical waves. Herein, for simplicity and brevity, only the solution in Cartesian coordinates will be considered—plane waves. Thus, a possible dynamic solution of equations 2.59 is a plane, running, electromagnetic wave

$$\widetilde{\boldsymbol{H}} = \widetilde{\boldsymbol{H}}_o \, \mathrm{e}^{\mp \mathrm{i}\,(\omega t - \boldsymbol{k}\cdot\boldsymbol{r})}; \qquad \widetilde{\boldsymbol{E}} = \widetilde{\boldsymbol{E}}_o \, \mathrm{e}^{\mp \mathrm{i}\,(\omega t - \boldsymbol{k}\cdot\boldsymbol{r})}, \tag{2.60}$$

where ω is the angular frequency, $\boldsymbol{k}$ is the wave vector pointing in the direction of propagation (its magnitude is the wave number k), and $\boldsymbol{r}$ is the distance from a reference planar wave front containing the coordinate origin. The quantities with subscript "o" are the complex amplitudes [5–7].

At this moment we are free to choose either the top or the bottom signs in the exponents above. However, once the choice has been made, one has to be consistent as some further definitions depend on it. Namely, the complex refractive index is defined as $\widetilde{n} = n \pm \mathrm{i}\,\kappa$, the complex dielectric permittivity as $\widetilde{\varepsilon} = \varepsilon' \pm \mathrm{i}\,\varepsilon''$, and the complex conductivity as $\widetilde{\sigma} = \sigma' \pm \mathrm{i}\,\sigma''$. Because of the latter three definitions, the top signs tend to be chosen most often by physicists, and will be used from now on in this dissertation. Engineers seem to prefer the bottom signs, though.

In general, for any waves we have

$$\omega = 2\,\pi\,\nu, \tag{2.61}$$

where ν is the frequency, and its inverse $1/\nu$ is the period.[14] An important fact is that the frequency and the angular frequency do not depend on the medium characteristics. In other words, when a monochromatic electromagnetic wave crosses the interface between two media, its ν and ω remain the same.

If one does not care about the temporal properties of electromagnetic waves, but is only interested in their spatial characteristics, by substituting the ansatz solution 2.60 into 2.59 one can get the Helmholtz equation

$$[\boldsymbol{\nabla}^2 + (\omega\,/\,c)^2]\,\widetilde{\boldsymbol{H}}_o(\boldsymbol{r}) = 0; \qquad [\boldsymbol{\nabla}^2 + (\omega\,/\,c)^2]\,\widetilde{\boldsymbol{E}}_o(\boldsymbol{r}) = 0. \tag{2.62}$$

2.2.4 Electromagnetic Waves within Insulating Media. Polarization of the Waves.

Let us consider an insulating, transparent medium characterized by relative permittivity ε, relative permeability μ, as well as by DC conductivity $\sigma_{DC} = 0$ ($\boldsymbol{J} = 0$ at $\omega = 0$). In such a medium, the plane, running, electromagnetic wave described by equations 2.60, propagates with phase velocity equal to the velocity of light within that medium [5–7]

$$v = 1\,/\,\sqrt{\mu\,\mu_o\,\varepsilon_1\,\varepsilon_o} = c\,/\,\sqrt{\mu\,\varepsilon}. \tag{2.63}$$

where c is the speed of light

$$c = 1\,/\,\sqrt{\mu_o\,\varepsilon_o}. \tag{2.64}$$

The fact that in vacuum electromagnetic waves propagate with phase velocity equal to the speed of light has been the initial clue that light is actually a certain type of electromagnetic waves.

---

[14] Usually the period is denoted with T, but reserving the latter symbol for the absolute temperature, I prefer to use $1/\nu$.

The ratio of equations 2.64 and 2.63 is in fact the refractive index of the transparent material:

$$n = c / v = \sqrt{\mu \varepsilon}. \tag{2.65}$$

We have the usual relations in a convenient, though very redundant form:

$$\begin{aligned} v &= \lambda \nu = \lambda \omega / (2 \pi) = \omega / k, && (2.66) \\ \omega &= 2 \pi v / \lambda = k v, && (2.67) \\ k &= 2 \pi / \lambda = 2 \pi \nu / v = \omega / v. && (2.68) \end{aligned}$$

where λ is the wavelength within the insulating medium.

Combining equations 2.65 and 2.68 we get:

$$k = n \omega / c. \tag{2.69}$$

Let us now substitute the wave solution 2.60 into the wave equation 2.59, and into Maxwell's equations 2.1–2.4 (with $\widetilde{\boldsymbol{J}} = 0$), using also the material equations 2.15. This is equivalent to replacing the operators $\boldsymbol{\nabla}$ and $\partial / \partial t$ with $\mathrm{i}\, \boldsymbol{k}_1$ and $-\mathrm{i}\, \omega$, respectively; and so we get

$$\boldsymbol{k}^2 = \omega^2 / v^2, \tag{2.70}$$

$$\boldsymbol{k} \cdot \boldsymbol{B} = 0; \qquad \boldsymbol{k} \cdot \boldsymbol{D} = 0, \tag{2.71}$$

$$\begin{aligned} \boldsymbol{k} \times \boldsymbol{H} &= -\omega \boldsymbol{D} = -\varepsilon \varepsilon_o \omega \boldsymbol{E}, && (2.72) \\ \boldsymbol{k} \times \boldsymbol{E} &= \omega \boldsymbol{B} = \mu \mu_o \omega \boldsymbol{H}. && (2.73) \end{aligned}$$

Equation 2.70 leads to equations 2.68 and 2.69. Any of the other three lines shows that in a non-conducting, linear, isotropic, homogeneous medium the three vectors $\boldsymbol{k}$, $\boldsymbol{E}$ (or $\boldsymbol{D}$), and $\boldsymbol{B}$ (or $\boldsymbol{H}$), are mutually perpendicular to each other, i.e., the electromagnetic waves are of the transverse type (TEM). Moreover, from the last two equations above one can see that the electric and magnetic field are in phase with each other. Indeed, if we take their magnitudes, we get the relations

$$kH = \omega D; \qquad H = vD \tag{2.74}$$

$$kE = \omega B; \qquad E = vB \tag{2.75}$$

The two equations on the right side were obtained from those on the left side using equation 2.67.

All equations for non-conducting media can be applied for the special case of vacuum, provided we set $\mu = 1 = \varepsilon$. Hence, in vacuum the electromagnetic waves are transverse, and $\boldsymbol{E}$ and $\boldsymbol{H}$ are in phase between each other, as well.

If the electric field vector is always parallel to some constant vector the wave is linearly polarized. There are two independent states of linear polarization as there are two directions perpendicular to the wave vector. E.g., if $\boldsymbol{k}$ is horizontal, $\boldsymbol{E}$ is always normal to it, but can be either horizontal or vertical.

Any other linear polarization can be obtained as a superposition of the above two added in phase.

When the two independent waves, linearly polarized in two orthogonal directions, have the same amplitude, but differ in phase by 90^o or -90^o, one gets left or right circular polarization. If one looks in the direction of $\boldsymbol{k}$, for left (right) circular polarization, $\boldsymbol{E}$ is turning clockwise (counterclockwise) with time at any given position $\boldsymbol{r}$. If, furthermore, the two perpendicular components have different amplitudes, then the resultant polarization is elliptic rather than circular. The elliptically polarizeed light can also be represented as a sum of a circularly polarizeed wave and a linearly polarizeed wave. Clearly, the circular polarization is a special case of the elliptic polarization.

When circularly polarizeed light is incident on some transparent, anisotropic crystals the two polarizations can be transmitted to a different degree and thus the transmitted light becomes elliptically polarized.

2.2.5 Electromagnetic Waves within Conducting Media

The electric field of an electromagnetic wave incident upon a conducting medium will induce Foucault vortex currents within the medium. When the frequency is high enough not all of the currents can follow the electric field instantaneously. In all cases, a current, that is out of phase with the electric field, can be represented as a sum of two components: active and reactive. The active component is perfectly in phase with the electric field and leads to Joule's losses (given by equation 2.31), whereas the reactive component is out-of-phase by $\pi/2$ rad with the electric field of the waveand leads to a lossless oscillation of electromagnetic energy forth and back. Faced with losses due to active induced currents, we can expect that the permittivity $\widetilde{\varepsilon}$ and conductivity $\widetilde{\sigma}$ of a conducting medium should become complex.[15] The active currents are related to the real part σ' of the conductivity, or to the imaginary part ε'' of the permittivity, whereas the reactive currents are related to the imaginary part σ'' of the conductivity or the real part ε' of the permittivity, respectively.

The electromagnetic properties of some medium can be characterized by any of the following four couples of quantities: (σ', σ''), (ε', ε''), (σ'', ε''), and (σ', ε'). In this dissertation the latter choice has been adopted.[16] Therefore, in Ohm's law (the left equation 2.7 only the real part σ' of the conductivity will be considered, as shown in equations 2.16 and 2.77; the imaginary part σ'' will be hidden in the displacement vector $\boldsymbol{D}$:

---

[15] In the general case, there could be magnetic losses, too. However, at optical frequencies these losses, as well as the magnetic properties of the medium are negligible, so we can consider $\widetilde{\mu}$ to be a real constant $\mu \approx 1$.

[16] But to make this presentation thorough, all of the above quantities will be introduced and the relationships among them will be given.

$$\widetilde{\boldsymbol{D}} = \varepsilon' \varepsilon_o \widetilde{\boldsymbol{E}}; \qquad \widetilde{\boldsymbol{B}} = \mu \mu_o \widetilde{\boldsymbol{H}}, \tag{2.76}$$

$$\widetilde{\boldsymbol{J}} = \sigma' \widetilde{\boldsymbol{E}}. \tag{2.77}$$

From Maxwell's equations only Ampère's law 2.1 is affected by the non-zero conductivity σ'. Substitution of Ohm's law 2.77 and the harmonic wave solution leads us to the following equation [10]

$$\widetilde{\boldsymbol{k}} \times \widetilde{\boldsymbol{H}} = -\omega \widetilde{\boldsymbol{D}} - \mathrm{i}\sigma' \widetilde{\boldsymbol{E}} = -\omega \varepsilon_o \left[\varepsilon' + \mathrm{i}\sigma' / (\varepsilon_o \omega)\right] \widetilde{\boldsymbol{E}}. \tag{2.78}$$

The first term here is related to the dielectric properties of the medium, and the second one – to its conductivity. Even if we were to assume that the electric field was real and avoided using complex representation, equation 2.78 makes it immediately clear that the wave vector and the magnetic field in conducting media should be complex. Physically, the complex magnetic field describes its phase lag from the electric field, whereas the imaginary part of the complex wave vector implies that the electromagnetic wave within the absorbing medium are damped. Moreover, comparison between equations 2.78 and 2.72 shows that we could preserve the appearance of the equations for the insulating case, provided for the conducting case we introduced a complex dielectric permittivity

$$\widetilde{\varepsilon} = \varepsilon' + \mathrm{i}\varepsilon'' = \varepsilon' + \mathrm{i}\sigma'/(\varepsilon_o \omega). \tag{2.79}$$

whereupon equation 2.78 is reduced to

$$\widetilde{\boldsymbol{k}} \times \widetilde{\boldsymbol{H}} = -\omega \boldsymbol{D} - \mathrm{i}\sigma' \boldsymbol{E} = -\omega \varepsilon_o \widetilde{\varepsilon} \boldsymbol{E}. \tag{2.80}$$

This is equivalent to representing the conducting properties of the medium as a "dielectric" properties and including them as the imaginary part of the complex dielectric permittivity. The appearance of such complex functions is due to the fact that as frequency is increased the response of the medium (e.g., $\boldsymbol{D}$) begins to lag behind the "driving force" ($\boldsymbol{E}$ in the considered example). Thus the fraction of the response that is in-phase with the fields is represented by the real part of the complex response function (ε'), the one that lags $\pi/2$ rad behind is given by the imaginary part of the complex response function (ε''), and the ratio of these two components determines the actual phase lag [11, pp. 452–454].

Next substituting the wave solution into the wave equation 2.58 we get

$$\widetilde{\boldsymbol{k}}^2 = \omega^2 / v^2 + \mathrm{i}\, \omega\, \mu\, \mu_o\, \sigma' = \omega^2\, \widetilde{\varepsilon}\, \varepsilon_o\, \mu\, \mu_o. \tag{2.81}$$

On the other hand squaring

$$\widetilde{\boldsymbol{k}} = \widetilde{k}\, \hat{\mathbf{k}} = \boldsymbol{k}' + \mathrm{i}\, \boldsymbol{k}''; \qquad \hat{\mathbf{k}}^2 = 1 \tag{2.82}$$

we get

$$\widetilde{\boldsymbol{k}}^2 = \boldsymbol{k}'^2 - \boldsymbol{k}''^2 + 2\,\mathrm{i}\, \boldsymbol{k}' \cdot \boldsymbol{k}''. \tag{2.83}$$

For the isotropic case, or cubic crystals,[17] the real and imaginary parts of the wave vector are collinear and $\boldsymbol{k}' \cdot \boldsymbol{k}'' = k'\, k''$. In this case, separating the real and imaginary parts from equations 2.81 and 2.83 gives

$$k'^2 - k''^2 = \omega^2\, \varepsilon'\, \varepsilon_o\, \mu\, \mu_o; \qquad 2\, k'\, k'' = \omega\, \mu\, \mu_o\, \sigma'. \tag{2.84}$$

---

[17] Normal incidence upon the crystal surface is assumed.

The solution of these simultaneous equations, taking the real branch, is

$$k'^2 = \frac{\omega^2 \varepsilon' \varepsilon_o \mu \mu_o}{2} \left[\sqrt{1 + \sigma'^2 / (\varepsilon' \varepsilon_o \omega)^2} + 1 \right], \tag{2.85}$$

$$k''^2 = \frac{\omega^2 \varepsilon' \varepsilon_o \mu \mu_o}{2} \left[\sqrt{1 + \sigma'^2 / (\varepsilon' \varepsilon_o \omega)^2} - 1 \right]. \tag{2.86}$$

These equations can be abbreviated by trigonometric or hyperbolic substitutions [12]. The trigonometric substitution is

$$\tan\theta = \sigma' / (\omega \varepsilon' \varepsilon_o), \tag{2.87}$$

$$k'^2 = \omega^2 \varepsilon' \varepsilon_o \mu \mu_o \sec\theta \cos^2(\theta/2), \tag{2.88}$$

$$k''^2 = \omega^2 \varepsilon' \varepsilon_o \mu \mu_o \sec\theta \sin^2(\theta/2). \tag{2.89}$$

And the hyperbolic one is

$$\sinh\vartheta = \sigma'/(\omega \varepsilon' \varepsilon_o), \tag{2.90}$$

$$k'^2 = \omega^2 \varepsilon' \varepsilon_o \mu \mu_o \cosh^2(\vartheta/2), \tag{2.91}$$

$$k''^2 = \omega^2 \varepsilon' \varepsilon_o \mu \mu_o \sinh^2(\vartheta/2). \tag{2.92}$$

Now, let us consider what happens with the wave solution when the wave vector is complex:

$$\widetilde{\boldsymbol{H}} = \widetilde{\boldsymbol{H}}_o \, \mathrm{e}^{-\boldsymbol{k}''\cdot\boldsymbol{r}} \mathrm{e}^{\pm \mathrm{i}(\omega t - \boldsymbol{k}'\cdot\boldsymbol{r})}; \qquad \widetilde{\boldsymbol{E}} = \widetilde{\boldsymbol{H}}_o \, \mathrm{e}^{-\boldsymbol{k}''\cdot\boldsymbol{r}} \mathrm{e}^{\pm \mathrm{i}(\omega t - \boldsymbol{k}'\cdot\boldsymbol{r})} \tag{2.93}$$

Evidently, the result is a spatially damped wave with a penetration depth (skin depth)

$$\begin{aligned}\delta &= \frac{1}{k''} = \sqrt{\frac{2}{\omega^2\,\varepsilon'\,\varepsilon_o\,\mu\,\mu_o\left[\sqrt{1 + \sigma'^2/(\varepsilon'\,\varepsilon_o\,\omega)^2} - 1\right]}} \\ &= \sqrt{\frac{2\,\varepsilon'\,\varepsilon_o}{\mu\,\mu_o\,\sigma'^2}}\,\sqrt{\sqrt{1 + \sigma'^2/(\varepsilon'\,\varepsilon_o\,\omega)^2} + 1}. \qquad (2.94)\end{aligned}$$

The damping is caused by conversion of electromagnetic-wave energy into Joule heat due to inducing Foucault vortex currents within the medium.

Furthermore, from equation 2.93 it is clear that the planes of constant phase are perpendicular to $\boldsymbol{k}'$, whereas the planes of constant amplitude are perpendicular to $\boldsymbol{k}''$. In the general case of oblique incidence of an electromagnetic wave onto a conducting surface these two parts of the wave vector are not collinear, and hence the two sets of planes are not parallel to each other. Even worse: because of the effects from the damping, the surfaces of equal electric-field magnitude $\left|\widetilde{\boldsymbol{E}}\right|$ are not plane at all. Such waves are inhomogeneous [3–5] and can be called "plane" only conditionally.

The phase velocity and the wavelength within a conducting medium are reduced in comparison with the respective quantities for a non-conducting medium with all other characteristics being identical

$$v = \frac{\omega}{k'} = \sqrt{\frac{2\,/\,(\varepsilon'\,\varepsilon_o\,\mu\,\mu_o)}{\sqrt{1 + \sigma'^2\,/\,(\varepsilon'\,\varepsilon_o\,\omega)^2} + 1}}, \qquad (2.95)$$

$$\lambda = \frac{2\,\pi\,v}{\omega} = \frac{2\,\pi}{\omega}\sqrt{\frac{2\,/\,(\varepsilon'\,\varepsilon_o\,\mu\,\mu_o)}{\sqrt{1 + \sigma'^2/\,(\varepsilon'\,\varepsilon_o\,\omega)^2} + 1}}. \qquad (2.96)$$

For the next step it is convenient to represent the complex wave vector in phasor form

$$\widetilde{\boldsymbol{k}} \;=\; \hat{\mathrm{k}}\left|\widetilde{k}\right|\mathrm{e}^{\mathrm{i}\varphi}; \qquad \hat{\mathrm{k}}^2 \;=\; 1 \qquad \text{where} \tag{2.97}$$

$$\left|\widetilde{k}\right| \;=\; \sqrt{k'^2 \,+\, k''^2} \;=\; \sqrt{\omega^2\,\varepsilon'\,\varepsilon_o\,\mu\,\mu_o\,\sqrt{1 \,+\, \sigma'^2/\,(\varepsilon'\,\varepsilon_o\,\omega)^2}} \tag{2.98}$$

$$\tan\varphi \;=\; \frac{k''}{k'} \;=\; \sqrt{\frac{\sqrt{1 \,+\, \sigma'^2/\,(\varepsilon'\,\varepsilon_o\,\omega)^2} \;-\; 1}{\sqrt{1 \,+\, \sigma'^2/\,(\varepsilon'\,\varepsilon_o\,\omega)^2} \;+\; 1}}. \tag{2.99}$$

Let us now consider equation 2.73 with a complex wave vector

$$\omega\,\widetilde{\boldsymbol{B}} \;=\; \mu\,\mu_o\,\omega\,\widetilde{\boldsymbol{H}}_1 \;=\; \widetilde{\boldsymbol{k}}\times\widetilde{\boldsymbol{E}} \;=\; \left|\widetilde{k}\right|\,\mathrm{e}^{\mathrm{i}\varphi}\,\hat{\mathrm{k}}\times\boldsymbol{E}. \tag{2.100}$$

From this equation it is clear that the phase of the complex wave vector happens to be also the phase difference between the electric and magnetic components of the wave. With the chosen sign conventions the phase is positive, i.e., the magnetic wave lags behind the electric one. For the special case $\sigma' \approx \sigma_{DC} \;=\; 0$ at $\omega \approx 0$, we return to the case of the insulating medium and the phase is zero. Conversely, for a perfectly conducting medium with $\sigma' \approx \sigma_{DC} \rightarrow \infty$ at $\omega \approx 0$, the phase is $\pi/4$ rad.

Taking the modulus of equation 2.100 we get the ratio of the magnetic and electric amplitudes within the conducting medium

$$|\boldsymbol{B}|\;/\;|\boldsymbol{E}| \;=\; \left|\widetilde{k}\right|\;/\,\omega. \tag{2.101}$$

where $\left|\widetilde{k}\right|$ is given by equation 2.98.

Approximations can be made for the limiting cases of low or high conductivity by expanding all radicals in series with respect to the small parameter and keeping only the lowest-order non-vanishing terms.

2.2.5.1 Waves within low-conductivity media

For the case of low conductivity ($\sigma' \ll \omega\varepsilon'\varepsilon_o$) the results are

$$k' = \omega\sqrt{\varepsilon'\,\varepsilon_o\,\mu\,\mu_o}\left[1 + \frac{1}{8}\left(\frac{\sigma'}{\varepsilon'\,\varepsilon_o\,\omega}\right)^2\right], \tag{2.102}$$

$$k'' = \frac{\sigma'}{2}\sqrt{\frac{\mu\,\mu_o}{\varepsilon'\,\varepsilon_o}}, \tag{2.103}$$

$$\frac{\left|\tilde{k}\right|}{\omega} = \frac{|\boldsymbol{B}|}{|\boldsymbol{E}|} = \sqrt{\varepsilon'\,\varepsilon_o\,\mu\,\mu_o}\left[1 + \left(\frac{\sigma'}{2\varepsilon'\,\varepsilon_o\,\omega}\right)^2\right], \tag{2.104}$$

$$\tan\varphi = \frac{\sigma'}{2\,\varepsilon'\,\varepsilon_o\,\omega}, \tag{2.105}$$

$$v = \frac{\omega}{2\pi}\lambda = \sqrt{\varepsilon'\,\varepsilon_o\,\mu\,\mu_o}\left[1 - \frac{1}{2}\left(\frac{\sigma'}{2\,\varepsilon'\,\varepsilon_o\,\omega}\right)^2\right]. \tag{2.106}$$

If $\sigma' = 0$ is substituted into equations 2.102–2.106, we recover the respective relations for an insulator.

2.2.5.2 Waves within high-conductivity media

For the case of high conductivity ($\sigma' \gg \omega\varepsilon'\varepsilon_o$) the results are

$$k' = \sqrt{\frac{\omega\,\sigma'\,\mu\,\mu_o}{2}}\left(1 + \frac{\varepsilon'\,\varepsilon_o\,\omega}{2\,\sigma'}\right), \tag{2.107}$$

$$k'' = \sqrt{\frac{\omega\,\sigma'\,\mu\,\mu_o}{2}}\left(1 - \frac{\varepsilon'\,\varepsilon_o\,\omega}{2\,\sigma'}\right), \tag{2.108}$$

$$\left|\widetilde{k}\right| / \omega = |\boldsymbol{B}| \,/\, |\boldsymbol{E}| = \sqrt{\mu\,\mu_o\,\sigma' / \omega}, \tag{2.109}$$

$$\tan\varphi = 1 - \frac{\varepsilon'\,\varepsilon_o\,\omega}{\sigma'}, \tag{2.110}$$

$$v = \frac{\omega}{2\,\pi}\lambda = \sqrt{\frac{2\,\omega}{\sigma'\,\mu\,\mu_o}}\left(1 - \frac{\varepsilon'\,\varepsilon_o\,\omega}{2\,\sigma'}\right). \tag{2.111}$$

If we let $\sigma' \to \infty$ in equations 2.107–2.111, we recover the respective relations for a perfect conductor.

2.2.5.3 Metal or dielectric?

Rather than representing the conducting properties of the medium as "dielectric" ones, and including them as the imaginary part of the complex dielectric permittivity, as we did in equation 2.79, we can do exactly the opposite: represent the dielectric properties of the medium[18] as "conducting" ones, and include them as the imaginary part of the complex conductivity

$$\widetilde{\sigma} = \sigma' + \mathrm{i}\,\sigma'' = \sigma' + \mathrm{i}\,\varepsilon_o\,(1 - \varepsilon')\,\omega, \tag{2.112}$$

---

[18] It is customary to leave the "contribution" of vacuum to the dielectric properties as it is.

whereupon we get

$$\widetilde{\boldsymbol{k}} \times \widetilde{\boldsymbol{H}} = -\omega\, \widetilde{\boldsymbol{D}} - \mathrm{i}\,\sigma'\, \widetilde{\boldsymbol{E}} = -\omega\, \varepsilon_o\, \widetilde{\boldsymbol{E}} - \mathrm{i}\,\widetilde{\sigma}\, \widetilde{\boldsymbol{E}}. \tag{2.113}$$

This duality of the possible approaches is the result of an inherent ambiguity of the dielectric AC response and conducting AC response of the medium. The two can be distinguished unambiguously only at DC fields ($\omega = 0$), which cause the free charges to move, and the bound charges to be displaced. At low frequencies the difference is partially preserved in the sense that the free charges are characterized by mostly real conductivity, and the bound charges are characterized by mostly real dielectric function. However, at optical frequencies even this difference is already entirely blurred, as both free and bound charges oscillate in a very similar manner, with a certain phase delay with respect to the field [13, pp. 776–777].

Another way, to understand this is given by J. D. Jackson [6]. The dispersion of both metals and dielectrics is governed by a number of resonances.[19] The only essential difference between metals and dielectrics is that the former have the Drude resonance centered at zero frequency, whereas the latter do not have a zero-frequency resonance. Thus, as the frequency is increased the importance of the Drude peak diminishes until the difference with dielectrics is lost.

In conclusion, it can be summarized that:

- good conductors at low frequencies are described sufficiently by σ' which dominates ε';
- good insulators at low frequencies are described sufficiently by ε' which dominates σ';

---

[19] This is covered in some detail in subsection 3.1.5.

- bad conductors or leaky insulators at low and intermediate frequencies require the use of both σ' and ε';
- "good" conductors and "good" insulators at optical frequencies are not that good anymore and also require the use of both σ' and ε';
- at sufficiently high frequencies the optical differences between metals and insulators disappear completely.

2.2.6 Products of Harmonic Electromagnetic Fields in Complex Notation

In this and the next subsections all fields are considered to be harmonic waves propagating within a non-absorbing medium, that is, they are given by equations 2.60, or similar ones.

If one needs the products of fields (e.g., $\boldsymbol{H} \cdot \boldsymbol{B}$), one has to take the real parts first:

$$\begin{aligned}
\boldsymbol{H} \cdot \boldsymbol{B} &= \mathrm{Re}\left\{\widetilde{\boldsymbol{H}}\right\} \cdot \mathrm{Re}\left\{\widetilde{\boldsymbol{B}}\right\} = (\widetilde{\boldsymbol{H}}^* + \widetilde{\boldsymbol{H}}) \cdot (\widetilde{\boldsymbol{B}}^* + \widetilde{\boldsymbol{B}}) / 4 \\
&= (\widetilde{\boldsymbol{H}}^* \cdot \widetilde{\boldsymbol{B}}^* + \widetilde{\boldsymbol{H}} \cdot \widetilde{\boldsymbol{B}} + \widetilde{\boldsymbol{H}}^* \cdot \widetilde{\boldsymbol{B}} + \widetilde{\boldsymbol{H}} \cdot \widetilde{\boldsymbol{B}}^*) / 4 \\
&= (\widetilde{\boldsymbol{H}}_o^* \cdot \widetilde{\boldsymbol{B}}_o^* \mathrm{e}^{2\mathrm{i}(\omega t - \boldsymbol{k} \cdot \boldsymbol{r})} + \widetilde{\boldsymbol{H}}_o \cdot \widetilde{\boldsymbol{B}}_o \mathrm{e}^{-2\mathrm{i}(\omega t - \boldsymbol{k} \cdot \boldsymbol{r})} \\
&\quad + \widetilde{\boldsymbol{H}}_o^* \cdot \widetilde{\boldsymbol{B}}_o + \widetilde{\boldsymbol{H}}_o \cdot \widetilde{\boldsymbol{B}}_o^*) / 4. \qquad (2.114)
\end{aligned}$$

However, in optics the fields are quickly oscillating with time whereas most detectors give us only the time-averaged values. Thus, upon time-averaging equation 2.114, the oscillating exponential terms vanish and we are left with [2]

$$\begin{aligned}\langle \boldsymbol{H}\cdot\boldsymbol{B}\rangle &= \frac{1}{4}\left\langle \widetilde{\boldsymbol{H}}_o^{*}\cdot\widetilde{\boldsymbol{B}}_o + \widetilde{\boldsymbol{H}}_o\cdot\widetilde{\boldsymbol{B}}_o^{*}\right\rangle = \frac{1}{4}\left((\widetilde{\boldsymbol{H}}_o\cdot\widetilde{\boldsymbol{B}}_o)^{*} + \widetilde{\boldsymbol{H}}_o\cdot\widetilde{\boldsymbol{B}}_o^{*}\right)\\ &= \frac{1}{2}\,\mathrm{Re}\left\{\widetilde{\boldsymbol{H}}_o\cdot\widetilde{\boldsymbol{B}}_o^{*}\right\} = \frac{1}{2}\,\mathrm{Re}\left\{\widetilde{\boldsymbol{H}}\cdot\widetilde{\boldsymbol{B}}^{*}\right\} = \frac{1}{2}\,\mathrm{Re}\left\{\widetilde{\boldsymbol{H}}^{*}\cdot\widetilde{\boldsymbol{B}}\right\}. \qquad (2.115)\end{aligned}$$

A similar derivation can be made for both tensor product (which will not be used herein) and cross product:

$$\begin{aligned}\langle \boldsymbol{E}\times\boldsymbol{H}\rangle &= \frac{1}{4}\left\langle \widetilde{\boldsymbol{E}}_o^{*}\times\widetilde{\boldsymbol{H}}_o + \widetilde{\boldsymbol{E}}_o\times\widetilde{\boldsymbol{H}}_o^{*}\right\rangle\\ &= \frac{1}{4}\left((\widetilde{\boldsymbol{E}}_o\times\widetilde{\boldsymbol{H}}_o)^{*} + \widetilde{\boldsymbol{E}}_o\times\widetilde{\boldsymbol{H}}_o^{*}\right) = \frac{1}{2}\,\mathrm{Re}\left\{\widetilde{\boldsymbol{E}}_o\times\widetilde{\boldsymbol{H}}_o^{*}\right\}\\ &= \frac{1}{2}\,\mathrm{Re}\left\{\widetilde{\boldsymbol{E}}\times\widetilde{\boldsymbol{H}}^{*}\right\} = \frac{1}{2}\,\mathrm{Re}\left\{\widetilde{\boldsymbol{E}}^{*}\times\widetilde{\boldsymbol{H}}\right\}. \qquad (2.116)\end{aligned}$$

Above, the time-averaging symbols for the case of harmonic functions mean the following

$$\langle \boldsymbol{B}\rangle = \nu\int_0^{1/\nu}\boldsymbol{B}\,\mathrm{d}t. \qquad (2.117)$$

2.2.7 Energy and Momentum of Harmonic Electromagnetic Fields

Below, the basic equations are only listed for convenience. Derivations can be found in advanced courses [2,6].

The complex, time-averaged energy densities for the magnetic and the electric field are respectively

$$\langle \widetilde{u}_m \rangle \;=\; \widetilde{\boldsymbol{H}} \cdot \widetilde{\boldsymbol{B}}^* / \, 4; \qquad\qquad \langle \widetilde{u}_e \rangle \;=\; \widetilde{\boldsymbol{D}} \cdot \widetilde{\boldsymbol{E}}^* / \, 4. \tag{2.118}$$

The complex, time-averaged Poynting vector is

$$\left\langle \widetilde{\boldsymbol{S}} \right\rangle \;=\; \widetilde{\boldsymbol{E}} \times \widetilde{\boldsymbol{H}}^* / \, 2. \tag{2.119}$$

The magnitude of the real part of this complex, time-averaged Poynting vector is the intensity of the electromagnetic wave

$$I \;=\; \left| \mathrm{Re} \left\{ \langle \widetilde{\boldsymbol{S}} \rangle \right\} \right| . \tag{2.120}$$

The intensity of an electromagnetic wave within an uniform absorbing medium is given by

$$I \;=\; \frac{c\,\varepsilon_o \, |\widetilde{\varepsilon}\,\widetilde{n}|}{2} \, \left| \widetilde{E}_o \right|^2 . \tag{2.121}$$

If the medium is not absorbing $|\widetilde{\varepsilon}\widetilde{n}|$ in the latter expression will simply be replaced by εn. More details about absorbing media were given in subsection 2.2.5.

The complex continuity equation for the case of harmonic fields is

$$\boldsymbol{\nabla} \cdot \widetilde{\boldsymbol{S}} \;+\; \frac{\partial(\widetilde{u}_e \;-\; \widetilde{u}_m)}{\partial t} \;+\; \widetilde{\boldsymbol{J}} \;\cdot\; \widetilde{\boldsymbol{E}}^* \;=\; 0. \tag{2.122}$$

The real part of this equation is the energy conservation law for the case of harmonic fields, while its imaginary part is related to the reactive energy and its alternating conversion between electric and magnetic form.

2.2.8 Electromagnetic Spectrum

The electromagnetic spectrum is a continuum covering the total range of frequencies or wavelengths of the electromagnetic waves. Very simplistically it extends in frequency from zero to infinity, or in wavelength from infinity to zero. Actually, it is bound on both sides in a narrower range that comprises the current state of the art in the technology for generation and/or detection of electromagnetic waves.

Currently there are no theoretical indications that the lower theoretical bound for energy or frequency should exceed zero. But it is very hard to generate and detect waves with frequency very close to zero as their wavelength would tend to be infinite and the needed antennae must be really huge. The lowest frequency (about 8 Hz) that has been observed is for the standing waves between the ionosphere and the Earth [10]. Greater success might be accomplished within an AC circuit or transmission line if no radiation into free space is required. But even in this case, when the frequency gets very low it is hard to distinguish the oscillations from plain DC. Besides, these are no waves in free space anymore. On the other extreme, we depend on our ability to measure cosmic gamma rays with very high energy (frequency). Also, at very high energies one reaches unprobed secrets of nature like: What happened in a tiny period of time after the big bang? What was there before the big bang? Problems which have stumbled modern physics for now. Anyway, from the quantum theory of electromagnetic waves it is immediately clear that infinite frequencies are impossible as the corresponding photons would have infinite energy.

A rough division of the spectrum is: ionizing rays, optical waves, radio waves, AC electrical waves. A finer division for each of these is presented in Tables[20] 2.1–

---

[20] The information presented in these tables has been collected from numerous internet sites.

2.5. The limits of the various regions are often not very specific and vary in the literature sources. Besides, often some of the regions overlap—because of historical reasons the differentiation between them is made based on the method of generation rather than on some essential physical characteristics. Of course, the waves from the overlapping regions are physically indistinguishable. Close to the upper limit of the spectrum (high-energy cosmic gamma rays) we still cannot generate, but we can only detect very rare events reaching us from space.

Table 2.1: Ionizing Electromagnetic Waves.

Spectral Range	E, eV	ν, THz	λ, nm
γ-Ray Bursts	$1.00(10^{15}\text{–}10^{21})$	$2.42\times(10^{17}\text{–}10^{23})$	$1.24\times(10^{-9}\text{–}10^{-15})$
Cosmic and Accelerator γ Rays	$1.00(5\times10^{6}\text{–}10^{15})$	$1.21(10^{9}\text{–}2\times10^{17})$	$1.24(2\times10^{-4}\text{–}10^{-9})$
Nuclear-Decay γ Rays	$1.00(10^{2}\text{–}5\times10^{6})$	$1.21(2\times10^{4}\text{–}10^{9})$	$1.24(10^{1}\text{–}2\times10^{-4})$
Hard X-Rays	$1.24\times(10^{2}\text{–}10^{8})$	$3.00\times(10^{4}\text{–}10^{10})$	$1.00\times(10^{1}\text{–}10^{-5})$
Soft X-Rays	$1.24\times(10^{1}\text{–}10^{2})$	$3.00\times(10^{3}\text{–}10^{4})$	$1.00\times(10^{2}\text{–}10^{1})$

Table 2.1 presents the ionizing electromagnetic waves. The energy is by far the most frequently used variable for these rays, even though in x-ray analysis the wavelength is also very convenient.

Tables 2.2–2.4 cover the optical region of the spectrum. Table 2.2 lists the ultraviolet (UV) sub-ranges. Strictly speaking, the extreme (vacuum) ultraviolet (VUV) also belongs to the ionizing rays and should be at the bottom of Table 2.1, but for simplicity, this sub-range of the UV region is listed together with the rest of the UV sub-ranges. In medicine the soft UV rays are subdivided by their effect on human skin into UV A, B, and C. Both the energy and the wavelength are in common use, the former being preferred for the VUV, and the latter for the softer UV ranges.

Table 2.2: Ultraviolet Electromagnetic Waves.

Spectral Range	$\breve{\nu}$, $10^2\mathrm{cm}^{-1}$	E, eV	ν, THz	λ, nm
VUV	500–14300	6.20–177.	$(15.0\text{–}42.8)\times10^3$	200–7.0
UV C	333–500	4.13–6.20	$(1.00\text{–}1.50)\times10^3$	300–200
UV B	286–333	3.54–4.13	857–1000	350–300
UV A	263–286	3.26–3.54	790–857	380–350

Table 2.3 is a detailed enumeration of the pure colors in the visible range of the electromagnetic spectrum. The wavelength in nanometers seems to be the most popular spectroscopic variable in the visible, but physicists like the energy in electronvolts, too. The colors are subjective to a certain extent. Furthermore, the bounds of the visible part of the spectrum are also somewhat subjective—not all persons can see the lowest and highest visible wavelengths. The maximum sensitivity of the human eye is at wavelengths about $\lambda_{max} = 555$ nm. For any particular pure color a sub-range that is closer to λ_{max} appears lighter, whereas a sub-range that is farther from λ_{max} appears darker (deeper).

Table 2.4, even though the shortest, is most related to the current dissertation — it presents the infrared (IR) range. Here the spectroscopic wave number in reciprocal centimeters is the unit of choice, but the wavelength in micrometers and the photon energy in milli-electronvolts are also very popular.

Table 2.5 includes the radio and electric electromagnetic waves, characterized by either the frequency or the wavelength. It starts with the microwaves:

- decimillimetric wavelengths,

Table 2.3: Visible Electromagnetic Waves.

Color	$\breve{\nu}$, 10^3cm^{-1}	E, eV	ν, THz	λ, nm
violet	26.3–23.8	3.26–2.95	789–714	380–420
indigo	23.8–22.0	2.95–2.72	714–659	420–455
dark blue	22.0–21.3	2.72–2.64	659–638	455–470
blue	21.3–20.6	2.64–2.55	638–618	470–485
light blue	20.6–20.0	2.55–2.48	618–600	485–500
cyan	20.0–19.2	2.48–2.38	600–577	500–520
dark green	19.2–18.9	2.38–2.34	577–566	520–530
green	18.9–18.5	2.34–2.30	566–555	530–540
light green	18.5–18.2	2.30–2.25	555–545	540–550
yellow-green	18.2–17.4	2.25–2.16	545–521	550–575
light yellow	17.4–17.3	2.16–2.15	521–519	575–578
yellow	17.3–17.2	2.15–2.13	519–515	578–582
dark yellow	17.2–17.1	2.13–2.12	515–512	582–585
light orange	17.1–16.8	2.12–2.08	512–504	585–595
orange	16.8–16.4	2.08–2.03	504–491	595–610
dark orange	16.4–16.1	2.03–1.99	491–481	610–622
light red	16.1–15.2	1.99–1.88	481–454	622–660
red	15.2–13.9	1.88–1.72	454–416	660–720
dark red	13.9–12.8	1.72–1.59	416–384	720–780

Table 2.4: Infrared Electromagnetic Waves.

Spectral Range	$\breve{\nu}$, cm^{-1}	E, meV	ν, THz	λ, μm
near IR	4000–13500	496–1670	120–405	2.5–0.74
mid IR	200–4000	24.8–496	6.0–120	50–2.5
far IR	5–400	0.62–49.6	0.15–12	2000–25

- millimetric wavelengths or EHF (Extremely High Frequencies) – used for military and space communications and satellite TV, and
- centimetric wavelengths or SHF (Super High Frequencies) – used for wireless communications.

Next come the radio waves:

- USW (Ultra Short – decimetric – Wavelengths) or UHF (Ultra High Frequencies) – used for TV broadcasting,
- USW (Ultra Short – metric – Wavelengths) or VHF (Very High Frequencies) used for TV and FM broadcasting,
- SW (Short – decametric – Wavelengths) or HF (High Frequencies),
- MW (Middle – hectometric – Wavelengths) or MF (Middle Frequencies) – used for AM broadcasting,
- LW (Long – kilometric – Wavelengths) or LF (Low Frequencies),
- VLW (Very Long – decakilometric – wavelengths) or SLF (Super Low Frequencies).

Finally, the electric waves are listed:

- voice (hectokilometric – wavelengths) or ULF (Ultra Low Frequencies),
- megametric – wavelengths or ELF (Extremely Low Frequencies),
- decamegametric – wavelengths or SELF (Sub? Extremely Low Frequencies),
- hectomegametric – wavelengths or SELF (Sub? Extremely Low Frequencies).

The acronym SELF for the latter two regions was found at `http://www.rso.utah.edu/teacher/radfund/fslide5.html` and I assume it stands for "Sub Extremely Low Frequencies". The electric waves have been considered hard[21] to be radiated and detected in free space since incredibly huge antennae, comparable to their wavelengths, would be necessary. Instead, they can propagate along transmission lines and electrical networks. An example is the AC power network.

Table 2.5: Radio and Electric Electromagnetic Waves.

Spectral Range	E, μeV	ν, Hz	λ, m
decimillimetric	$1.24(1\text{–}10)10^{3}$	$(3\text{–}30)10^{11}$	$(10\text{–}1)10^{-4}$
EHF (millimetric)	$1.24(1\text{–}10)10^{2}$	$(3\text{–}30)10^{10}$	$(10\text{–}1)10^{-3}$
SHF (centimetric)	$1.24(1\text{–}10)10^{1}$	$(3\text{–}30)10^{9}$	$(10\text{–}1)10^{-2}$
UHF (USW, decimetric)	$1.24(1\text{–}10)10^{0}$	$(3\text{–}30)10^{8}$	$(10\text{–}1)10^{-1}$
VHF (USW, metric)	$1.24(1\text{–}10)10^{-1}$	$(3\text{–}30)10^{7}$	$(10\text{–}1)10^{0}$
HF (SW, decametric)	$1.24(1\text{–}10)10^{-2}$	$(3\text{–}30)10^{6}$	$(10\text{–}1)10^{1}$
MF (MW, hectametric)	$1.24(1\text{–}10)10^{-3}$	$(3\text{–}30)10^{5}$	$(10\text{–}1)10^{2}$
LF (LW, kilometric)	$1.24(1\text{–}10)10^{-4}$	$(3\text{–}30)10^{4}$	$(10\text{–}1)10^{3}$
VLW (SLF, decakilometric)	$1.24(1\text{–}10)10^{-5}$	$(3\text{–}30)10^{3}$	$(10\text{–}1)10^{4}$
ULF (voice, hectokilometric)	$1.24(1\text{–}10)10^{-6}$	$(3\text{–}30)10^{2}$	$(10\text{–}1)10^{5}$
ELF (megametric)	$1.24(1\text{–}10)10^{-7}$	$(3\text{–}30)10^{1}$	$(10\text{–}1)10^{6}$
SELF (decamegametric)	$1.24(1\text{–}10)10^{-8}$	$(3\text{–}30)10^{0}$	$(10\text{–}1)10^{7}$
SELF (hectomegametric)	$1.24(1\text{–}10)10^{-9}$	$(3\text{–}30)10^{-1}$	$(10\text{–}1)10^{8}$

Humans have evolved with the ability to see a very narrow part of the electromagnetic spectrum, the visible region. For the rest of the spectrum one cannot rely on one's perceptions, and hence one needs special detectors sensitive for a particular region of the spectrum. Some detectors for the infrared region will be covered in the chapter on Experimental Methods.

---

[21] Some hobbyists have disproven this belief by studying waves down to the lowest frequencies generated by very powerful natural sources—lightnings—using sub-wavelength antennae.

This subsection is based on information found in various sources [14–16,7], as well as obtained from searches on the internet, too numerous to list here.

2.2.9 Quantization of the Electromagnetic Field

Maxwell's theory describes the wave properties of electromagnetic radiation. In the beginning of the XX century it gradually became clear that simultaneously it has corpuscular properties as well.

Any body emits thermal radiation, and absorbs incident radiation. A body that is both a perfect emitter and absorber of radiation is called ideal black body. Its radiation depends only on temperature and some spectral variable. The blackbody spectral radiance (radiant flux emitted from a unit of blackbody area into a unity of solid angle) is given by the Planck formula (in three different spectral variables):

$$\begin{aligned} L(\omega,T) &= \frac{c\,u_{em}(\omega,T)}{4} = \frac{\hbar\,\omega^3}{4\,\pi^2\,c^2}\left[\mathrm{e}^{\hbar\omega/(k_B T)} - 1\right]^{-1}, && (2.123)\\ L(\nu,T) &= \frac{c\,u_{em}(\nu,T)}{4} = \frac{2\,\pi\,h\,\nu^3}{c^2}\left[\mathrm{e}^{h\,\nu/(k_B T)} - 1\right]^{-1}, && (2.124)\\ L(\lambda,T) &= \frac{c\,u_{em}(\lambda,T)}{4} = \frac{2\,\pi\,c^2\,h}{\lambda^5}\left[\mathrm{e}^{h\,c/(\lambda\,k_B T)} - 1\right]^{-1}, && (2.125) \end{aligned}$$

where k_B is the Boltzmann constant, T the absolute temperature, h the Planck constant, and u_{em} the equilibrium spectral energy density of the blackbody radiation, e.g., within a cavity of the black body [10]. The three spectral radiances given above have different dimensions, such that the three products

$$L(\omega,T)\,\mathrm{d}\omega = L(\nu,T)\,\mathrm{d}\nu = L(\lambda,T)\,\mathrm{d}\lambda \qquad (2.126)$$

have the dimension of energy flux [W/m^2].

At low frequencies ($\hbar\omega \ll k_B T$) equation 2.123 reduces to the classical Rayleigh–Jeans formula

$$L(\omega, T) \;=\; \frac{c\, u_{em}(\omega, T)}{4} \;=\; \frac{k_B\, T\, \omega^2}{4\, \pi^2\, c^2}. \tag{2.127}$$

and at high frequencies ($\hbar\omega \gg k_B T$) equation 2.123 is reduced to the classical Wien's formula in contemporary notation (that is, with the Planck constant, which had not been introduced yet at the time Wien wrote his formula)

$$L(\omega, T) \;=\; \frac{c\, u_{em}(\omega, T)}{4} \;=\; \frac{\hbar\, \omega^3}{4\, \pi^2\, c^2} \exp - \frac{\hbar\, \omega}{k_B\, T}, \tag{2.128}$$

In order to obtain the blackbody spectral radiance Planck had to reach beyond classical physics; he considered the statistics of quantum oscillators representing the atoms in the walls of the black body. Thus he reached the conclusion that electromagnetic energy is emitted and absorbed by small bites he called quanta, characterized by energy $h\nu$.

By introducing

$$\xi \;=\; \frac{h\, c}{\lambda\, k_B\, T}, \tag{2.129}$$

equation 2.125 can be simplified to

$$L(\xi, T) \;=\; \frac{2\, (k_B\, T)^5}{c^3\, h^4} \left[e^{\xi} \,-\, 1 \right]^{-1}, \tag{2.130}$$

Equating the derivative with respect to ξ to zero we get the transcedent equation

$$5 \left[e^{\xi} \,-\, 1 \right] \;=\; \xi\, e^{\xi}, \tag{2.131}$$

whose numerical solution is $\xi_{max} = 4.965$. Thus we obtain Wien's displacement law. It describes how the wavelength corresponding to the maximum of a blackbody spectrum varies with T:

$$\lambda_{max}[\mathrm{mm}] \;=\; \frac{h\,c}{\xi_{max}\,k_B\,T} \;=\; \frac{2.9}{T[\mathrm{K}]}. \tag{2.132}$$

Integrating equation 2.123 over ω with

$$\zeta \;=\; \frac{\hbar\omega}{k_B T}, \tag{2.133}$$

we get the Stefan–Boltzmann law

$$\begin{aligned} L(T) \;&=\; \frac{c}{4}\int_0^\infty u_{em}(\omega, T)\,\mathrm{d}\omega \;=\; \frac{c\,(k_B\,T)^4}{4\,\pi^2\,(\hbar\,c)^3}\int_0^\infty \frac{\zeta^3\,\mathrm{d}\zeta}{\mathrm{e}^\zeta\,-\,1} \\ &=\; \frac{c\,(k_B\,T)^4}{4\,\pi^2\,(\hbar\,c)^3}\,\frac{\pi^4}{15} \;=\; \frac{\pi^2(k_B\,T)^4}{60\,c^2\,\hbar^3} \;=\; \sigma_{SB}\,T^4. \end{aligned} \tag{2.134}$$

where $\sigma_{SB} = 5.67032 \times 10^{-8}\ \mathrm{W}\cdot\mathrm{m}^{-2}\cdot\mathrm{K}^{-4}$ is the Stefan–Boltzmann constant.

Einstein developed further the ideas of Planck by introducing the notion of electromagnetic quanta. In the optical region of the spectrum he called these quanta photons. Einstein suggested that any electromagnetic wave of frequency ν, actually comprises a collection of quanta, each of which is characterized by energy $\mathfrak{E}$ and momentum with magnitude $\mathfrak{p}$:

$$\mathfrak{E} \;=\; h\,\nu \;=\; \hbar\omega \qquad\qquad \mathfrak{p} \;=\; h\,\nu\,/\,c. \tag{2.135}$$

The energy of a photon relates it to frequency which is a wave characteristic; the momentum of a photon on the other hand is a particle characteristic. Thus photons were the first micro-objects that, contrary to what one expects based on macro-world experience, were found to behave in a Janus-like manner, both as waves and particles. They were called wave-particles, or even wavicles (by Arthur Edington).

The wave properties of light had been known for quite a while. They are demonstrated in a most clear way by the phenomena of diffraction and interference. Experiments in the beginning of XX century and their interpretation disclosed the particle side of photons. Armed with the new concept of photons, in 1905 Einstein was able to explain the photoelectric effect which brought him the Nobel prize. In 1922 the corpuscular properties of photons were demonstrated even more convincingly by the Compton effect [16].

The probability to find a photon is proportional to the intensity of the electromagnetic wave, that is to the square of the electric field.

Photons and electromagnetic quanta in general, being micro-objects are subject to Heisenberg's uncertainty relations.

CHAPTER 3
INTERACTION OF OPTICAL WAVES WITH MATTER

3.1 Optical Properties of Matter

The optical properties of matter can be described by various optical characteristics. Some of them have already been introduced in the preceding chapter, especially in subsection 2.2.5.

3.1.1 Optical Characteristics

In this subsection, more optical characteristics are described and the relationships between them are given. The treatment is still for conducting media, which is most general: indeed, the relations for dielectric media and vacuum can be obtained as special cases.

Combining equations 2.79 and 2.112 we get that the two different approaches to describing the phase lag of the response of the medium are related by

$$\widetilde{\varepsilon} = 1 + \mathrm{i}\,\widetilde{\sigma}/(\varepsilon_o \omega), \tag{3.1}$$

or, respectively, for the real and imaginary parts

$$\varepsilon' = 1 - \sigma''/(\varepsilon_o \omega); \qquad \varepsilon'' = \sigma'/(\varepsilon_o \omega). \tag{3.2}$$

Another optical characteristic is the complex refractive index,[1] in various representations [11, pp. 456–457]:

$$\widetilde{n} = c/\widetilde{v} = \sqrt{\widetilde{\varepsilon}\,\mu} = \widetilde{k}\,c/\omega = n' + \mathrm{i}\,n''. \tag{3.3}$$

Its real part determines the phase velocity, and its imaginary part is related to the spatial decay of the wave.

By squaring equation 3.3 we get the dispersion relation

$$\widetilde{n}^2 = (c/\widetilde{v})^2 = \widetilde{\varepsilon}\,\mu = (k' + \mathrm{i}\,k'')^2(c/\omega)^2 = (n' + \mathrm{i}\,n'')^2. \tag{3.4}$$

The real and imaginary parts of the middle and right (third and fifth) terms are

$$\mu\,\varepsilon' = n'^2 - n''^2; \qquad \mu\,\sigma'/(\varepsilon_o\,\omega) = \mu\,\varepsilon'' = 2\,n'\,n''. \tag{3.5}$$

which can be solved for n'^2 and n''^2

$$n'^2 = \frac{\mu}{2}\left(\varepsilon' + \sqrt{\varepsilon'^2 + \varepsilon''^2}\right); \quad n''^2 = \frac{\mu}{2}\left(\varepsilon' + \sqrt{\varepsilon'^2 + \varepsilon''^2}\right). \tag{3.6}$$

If a plane wave is propagating in the $\hat{\boldsymbol{\zeta}}$-direction its intensity loss is determined by the attenuation (absorption) coefficient

$$\alpha = -\mathrm{d}\ln I/\,\mathrm{d}\zeta, \tag{3.7}$$

---

[1] Traditionally written as $N = n + \mathrm{i}\,\kappa$, or $\widetilde{n} = n + \mathrm{i}\,\kappa$.

which is just another way to write the well-known dependence of the intensity as a function of the traveled distance ζ within some medium

$$I(\zeta) \;=\; I_o\,\mathrm{e}^{-\alpha\zeta}. \tag{3.8}$$

Here I_o is the intensity at the origin of the ζ-axis. Usually the origin is chosen at the interface and then I_o is the intensity of the incident beam. Since the intensity is proportional to the squared electric field (see equation 2.121)

$$\alpha \;=\; 2\,k'' \;=\; 2\,\omega\,n''\,/\,c, \tag{3.9}$$

and using the right-side equation 3.5, we get another relation

$$\mu\,\sigma' \;=\; c\,\varepsilon_o\,n'\,\alpha. \tag{3.10}$$

3.1.2 Wave Impedance

For the plane wave considered here $\boldsymbol{E}(\boldsymbol{r},t) \;=\boldsymbol{E}(\zeta,t)$ and $\boldsymbol{H}(\boldsymbol{r},t) \;=\boldsymbol{H}(\zeta,t)$, and therefore the differential operator nabla can be simplified

$$\boldsymbol{\nabla} \;=\; \hat{\boldsymbol{\zeta}}\frac{\partial}{\partial\zeta}; \qquad \text{where} \qquad \hat{\boldsymbol{\zeta}}^2 \;=\; 1. \tag{3.11}$$

Substituting this operator and the material equations 2.15 into Ampère's law 2.1 and Faraday's law 2.2, applying $\hat{\boldsymbol{\zeta}}\times$ to the latter equation and expanding the double cross product, we get (assuming a plane harmonic wave within a linear medium with complex characteristics)

$$\frac{\partial \widetilde{\boldsymbol{E}}}{\partial \zeta} = \mathrm{i}\,\omega\,\widetilde{\mu}\,\mu_o\,(\widetilde{\boldsymbol{H}} \times \hat{\zeta}), \tag{3.12}$$

$$\frac{\partial (\widetilde{\boldsymbol{H}} \times \hat{\zeta})}{\partial \zeta} = (\mathrm{i}\,\omega\,\widetilde{\varepsilon}\,\varepsilon_o - \widetilde{\sigma})\,\widetilde{\boldsymbol{E}}. \tag{3.13}$$

Comparison of these relations with equations 2.39 and 2.40 shows that the two sets of equations are in perfect correspondence; each component of $\widetilde{\boldsymbol{E}}$ and $\widetilde{\boldsymbol{H}} \times \hat{\zeta}$ corresponds to $\widetilde{V}$ and $\widetilde{I}$, respectively. This analogy allows us, following Schelkunoff, to write the series impedance and parallel admittance per unit length of the medium [3, pp. 283–284]:

$$\widetilde{Z}_s = -\mathrm{i}\,\omega\,\widetilde{\mu}\,\mu_o; \qquad \widetilde{Y}_p = \widetilde{\sigma} - \mathrm{i}\,\omega\,\widetilde{\varepsilon}\,\varepsilon_o. \tag{3.14}$$

Armed with these relations, by analogy with equations 2.44, we get directly the complex propagation constant and the characteristic wave impedance of the medium

$$\widetilde{k} = \mathrm{i}\sqrt{\widetilde{Z}_s\,\widetilde{Y}_p} = \sqrt{\omega^2\,\widetilde{\varepsilon}\,\varepsilon_o\,\widetilde{\mu}\,\mu_o + \mathrm{i}\,\omega\,\widetilde{\mu}\,\mu_o\,\widetilde{\sigma}}, \tag{3.15}$$

$$\widetilde{Z} = \sqrt{\widetilde{Z}_s/\,\widetilde{Y}_p} = \sqrt{\frac{\omega\,\widetilde{\mu}\,\mu_o}{\omega\,\widetilde{\varepsilon}\,\varepsilon_o + \mathrm{i}\,\widetilde{\sigma}}} = \frac{\omega\,\widetilde{\mu}\,\mu_o}{\sqrt{\widetilde{\varepsilon}\,\varepsilon_o\,\widetilde{\mu}\,\mu_o\,\omega^2 + \mathrm{i}\,\omega\,\widetilde{\mu}\,\mu_o\,\widetilde{\sigma}}}. \tag{3.16}$$

In vacuum the latter equations are reduced to

$$k_o = \pm\omega\,/\,c; \qquad Z_o = \sqrt{\mu_o\,/\,\varepsilon_o} = 376.6\Omega. \tag{3.17}$$

Using equations 2.64 and 3.17, the relations 3.15 and 3.16 can be represented as

$$\widetilde{k} \;=\; k_o\sqrt{\widetilde{\mu}\,\widetilde{\varepsilon} \,+\, \mathrm{i}\,\widetilde{\sigma}\,/\,(\varepsilon_o\,\omega)} \;=\; k_o\sqrt{\widetilde{\mu}\,\varepsilon' \,+\, \mathrm{i}\,\sigma'/\,(\varepsilon_o\,\omega)}, \qquad (3.18)$$

$$\widetilde{Z} \;=\; Z_o\sqrt{\frac{\widetilde{\mu}}{\widetilde{\varepsilon} \,+\, \mathrm{i}\,Z_o\,\widetilde{\sigma}\,/\,\omega}} \;=\; Z_o\sqrt{\frac{\widetilde{\mu}}{\varepsilon' \,+\, \mathrm{i}\,Z_o\,\sigma'/\,\omega}}, \qquad (3.19)$$

where the right-side terms were written in compliance with the convention chosen in subsection 2.2.5.

Squaring equation 3.15 we get

$$\widetilde{\boldsymbol{k}}^2 \;=\; \widetilde{\varepsilon}\,\varepsilon_o\,\widetilde{\mu}\,\mu_o\,\omega^2 \,+\, \mathrm{i}\,\omega\,\widetilde{\mu}\,\mu_o\,\widetilde{\sigma}, \qquad (3.20)$$

where $\widetilde{\boldsymbol{k}} \,=\, \widetilde{k}\,\hat{\mathbf{k}}$ is the complex wave vector[2]

$$\widetilde{\boldsymbol{k}} \,=\, \boldsymbol{k}' \,+\, \mathrm{i}\,\boldsymbol{k}'' \,=\, \hat{\mathbf{k}}\left|\widetilde{\boldsymbol{k}}\right|\mathrm{e}^{\mathrm{i}\varphi}; \qquad \hat{\mathbf{k}}^2 \,=\, 1; \qquad (3.21)$$

$$\left|\widetilde{\boldsymbol{k}}\right| \,=\, \sqrt{\boldsymbol{k}'^2 \,+\, \boldsymbol{k}''^2}; \qquad \tan\varphi \,=\, \boldsymbol{k}''/\boldsymbol{k}'. \qquad (3.22)$$

Invoking the analogy again, similarly to the right-side equation 2.43, we can write the left-side equation

$$\widetilde{\boldsymbol{E}} \,=\, \widetilde{Z}\,(\widetilde{\boldsymbol{H}} \times \hat{\boldsymbol{\zeta}}); \qquad \hat{\boldsymbol{\zeta}} \times \widetilde{\boldsymbol{E}} \,=\, \widetilde{Z}\,\widetilde{\boldsymbol{H}}. \qquad (3.23)$$

The right-side equation is obtained by applying the cross product $\hat{\boldsymbol{\zeta}}\times$ to the left-side equation 3.23. Equations 3.23 show that even in conducting media, as long as the media are linear, $\widetilde{\boldsymbol{E}}$, $\widetilde{\boldsymbol{H}}$, and $\hat{\boldsymbol{\zeta}}$ are orthogonal to each other. Writing equation 3.23 in scalar form produces

---

[2] Note that since the real and imaginary parts of $\widetilde{\boldsymbol{k}}$ are collinear vectors (isotropic or cubic medium), their ratio is a scalar, as one should expect for the phase equation to make sense.

$$\widetilde{Z} = \widetilde{E}_a/\widetilde{H}_a, \tag{3.24}$$

where $\widetilde{E}_a$ and $\widetilde{H}_a$ are the complex amplitudes of the electric and magnetic field, taken at the same point[3] ζ, and divided by their respective unit vectors.

The wave impedance is also related to the complex, time-averaged Poynting vector

$$\left\langle \widetilde{\boldsymbol{S}} \right\rangle = \frac{\widetilde{\boldsymbol{E}} \times \widetilde{\boldsymbol{H}}^*}{2} = \widetilde{\boldsymbol{E}} \times \frac{\hat{\zeta} \times \widetilde{\boldsymbol{E}}^*}{2\,\widetilde{Z}^*} = \frac{(\widetilde{\boldsymbol{E}} \cdot \widetilde{\boldsymbol{E}}^*)\,\hat{\zeta}}{2\,\widetilde{Z}^*}, \tag{3.25}$$

$$\left\langle \widetilde{S} \right\rangle = \frac{\widetilde{E}^2}{2\,\widetilde{Z}^*}. \tag{3.26}$$

The complex, time-averaged “magnitude’ $\left\langle \widetilde{S} \right\rangle$ (equation 3.26) of $\left\langle \widetilde{\boldsymbol{S}} \right\rangle$ (equation 3.25) can be obtained by dividing equation 3.25 by the unit vector $\hat{\boldsymbol{S}}$.

From equation 3.16 using equations 3.21 and 3.22 we get yet another expression for the characteristic wave impedance of the medium

$$\widetilde{Z} = \frac{\omega\,\widetilde{\mu}\,\mu_o}{\widetilde{k}} = \frac{\omega\,\widetilde{\mu}\,\mu_o}{\sqrt{k'^2 + k''^2}}\,\mathrm{e}^{-\mathrm{i}\varphi}. \tag{3.27}$$

Squaring the latter equation gives

$$\widetilde{Z}^2 = \frac{\omega^2\,\widetilde{\mu}^2\,\mu_o^2}{\widetilde{k}^2} = \frac{\omega^2\,\widetilde{\mu}^2\,\mu_o}{c^2\,\varepsilon_o\,\widetilde{k}^2} = \frac{\omega^2\,\widetilde{\mu}^2\,Z_o^2}{c^2\,\widetilde{k}^2} = \frac{\widetilde{\mu}^2\,Z_o^2}{\widetilde{n}^2}, \tag{3.28}$$

which relates the impedance with the complex refractive index. Equations 2.64, 3.17, and 3.3 have been used for the chain of transformations in equation3.28.

---

[3] Both fields must be taken in the same point in order to ensure that any damping effect causing variation with the coordinate ζ is removed. It is convenient to measure both field amplitudes at the surface, especially when we are dealing with a conducting medium.

Finally, it must be pointed out that electromagnetic waves are damped within good conductors at a distance of the order of the penetration (skin) depth 2.94. The result of this fact is that the Foucault currents are localized within a surface sheet of thickness δ. For such a case, all equations for the wave impedance listed in this subsection actually give the surface (sheet) impedance of the conductor in $\Omega/\square$.

3.1.3 Kramers–Kronig Relations

Many complex optical characteristics, describing the response of an optical structure to excitation by electromagnetic waves, were introduced in the previous two subsections. If one of these optical characteristics (e.g., $\tilde{\varepsilon}$) is the coefficient in a linear relationship between an external variable—stimulus (e.g., $\tilde{\boldsymbol{E}}$ of an electromagnetic wave)—and an internal variable—response (e.g., $\tilde{\boldsymbol{D}}$)—of the optical structure, then that relationship is non-local in time due to the frequency dependence of the coefficient. This can be seen using the convolution theorem from Fourier analysis. In most cases the spatial dispersion is small and can be neglected. Thus, we can assume the relationship is local in space. Treating the coefficient as an analytical function of the complex frequency $\tilde{\mathit{\Omega}}$ and using Cauchy's theorem for contour integration in the upper half-plane, one can derive a relation between the real and imaginary parts of that coefficient—the Kramers–Kronig relation, e.g., for the complex permittivity [17,6,18]:

$$\tilde{\varepsilon}(\omega) - 1 = -\frac{\mathrm{i}}{\pi}\mathcal{P}\int_{-\infty}^{\infty} \frac{\tilde{\varepsilon}(\mathit{\Omega}) - 1}{\mathit{\Omega} - \omega}\,\mathrm{d}\mathit{\Omega}, \tag{3.29}$$

where $\mathcal{P}$ preceding the integral denotes principal-part integration, and $\mathit{\Omega}$ is a dummy integration variable for the angular frequency. The latter is already real since the contribution from the upper semicircle of infinite radius vanishes and only the integration along the real-frequency axis remains.

The requirement to get a real response from a real stimulus leads to

$$\widetilde{\varepsilon}^{*}(\omega) = \widetilde{\varepsilon}(-\omega), \tag{3.30}$$

or

$$\varepsilon'(\omega) = \varepsilon'(-\omega); \qquad \varepsilon''(\omega) = -\varepsilon''(-\omega), \tag{3.31}$$

and so the real (imaginary) part of the permittivity is even (odd) function of the frequency.

Using these relations, and separating the real and imaginary parts of equation 3.29, we get the Kramers–Kronig relations.

$$\varepsilon'(\omega) - 1 = \frac{2}{\pi}\mathcal{P}\int_0^\infty \frac{\Omega\varepsilon''(\Omega)}{\Omega^2 - \omega^2}\,\mathrm{d}\Omega, \tag{3.32}$$

$$\varepsilon''(\omega) = -\frac{2\omega}{\pi}\mathcal{P}\int_0^\infty \frac{\varepsilon'(\Omega) - 1}{\Omega^2 - \omega^2}\,\mathrm{d}\Omega. \tag{3.33}$$

Thus, if one knows either the real or the imaginary part of the complex permittivity at all frequencies, then one can calculate the other one at all frequencies.

The latter equation can be generalized for conducting media

$$\varepsilon''(\omega) = \frac{\sigma_{DC}}{\varepsilon_o\omega} - \frac{2\omega}{\pi}\mathcal{P}\int_0^\infty \frac{\varepsilon'(\Omega) - 1}{\Omega^2 - \omega^2}\,\mathrm{d}\Omega, \tag{3.34}$$

where σ_{DC} is the DC conductivity of the medium.

3.1.4 Dispersion

A number of optical characteristics were introduced in subsections 2.2.5 and 3.1.1. Some of them are macroscopic and can be measured, others can be modeled microscopically. Comparison between the measured and theoretically calculated quantities is exactly the very fact that is behind the progress of sciences by studying the optical properties of matter.

We are dealing with a case of dispersion if any of the material equations is non-local either in space (spatial or wave-vector dispersion), or in time (time or frequency dispersion). In most cases the effect of spatial dispersion is negligible compared to that of frequency dispersion. Because of that fact, herein I will be concerned only with the latter type of dispersion, and will drop the adjective.

Dispersion is manifested in the fact that, within various media (other than vacuum), the phase speed of electromagnetic waves depends on frequency. Naturally, dispersion can be observed for all other characteristics that are related to that speed. Monochromatic waves are not suitable to observe dispersion: at least two different frequencies are needed, or better yet—scanning a continuous spectrum.

Within spectral regions where the refractive index is an increasing (decreasing) function we are dealing with normal (anomalous) dispersion.

3.1.5 Classical Models for the Optical Properties of Matter

Here some simple classical models describing optical properties and dispersion will be presented, following Drude and Lorentz.

3.1.5.1 Drude model for free charge carriers

At the turn of the 20th century P. Drude applied the kinetic theory of gases to the valence electrons within a metal [19,20,13,11]. The periodic potential within the metal is approximated by a rectangular box, and while the electrons are in the bulk they are "free", similarly to the molecules of a gas.

Assumptions of the model:

- even though the concentration of valence electrons within a metal is about a thousand times higher than the concentration of molecules in a regular gas under normal conditions, and the pressure of the electron "gas" is enormous (ca. 3400 atm), the kinetic theory of gases is applicable to the electron "gas";
- the valence electrons move chaotically with high thermal velocities. Due to this thermal chaos the vector-average of the thermal velocity vanishes. Therefore the thermal velocity can be characterized by its root-mean-square value v_m;
- the valence electrons are scattered by collisions with the ion cores, whereas the collisions between electrons are unimportant;
- between collisions with the ion cores the valence electrons within a metal are totally free and move along a straight line in compliance with Newton's first law;
- collisions with the ion cores are instantaneous and cause abrupt reflection of the valence electrons in a random direction;
- the mean free time τ between two successive collisions is called relaxation time, and its inverse is the scattering rate $1/\tau$;
- the electrons get thermalized to the environment only through said collisions.
- in an external electric field an additional velocity is added to the thermal velocity. Upon averaging of the net velocity only the average of the additional velocity due to the electric field is left and is known as the drift velocity $\boldsymbol{v}_d$;

- taking into account the fact that $v_d \ll v_m$, it follows that the mean free path is $l = v_m \tau$.

If an external electric field[4] $\boldsymbol{E}$ is applied, the equation of motion for the electrons is the equationof a driven frictionless oscillator with zero resonance frequency

$$m \frac{\mathrm{d}^2 \boldsymbol{r}}{\mathrm{d}t^2} = -e\,\boldsymbol{E}, \tag{3.35}$$

where $-e$ is the charge, and m is the mass of an electron. The magnetic part of the Lorentz force does not accelerate the electron tangentially, but just changes the direction of its velocity. Furthermore, in most cases the magnetic-force effects are small and so they have been neglected in equation 3.35. Solving this equation, the additional velocity of an electron, after a time t has elapsed from its last collision, is

$$\boldsymbol{v}_d = -e\,t\,\boldsymbol{E}/m. \tag{3.36}$$

Thus, according to the Drude model, the drift velocity is the average velocity between two successive collisions:

$$\boldsymbol{v}_d = -e\,\tau\,\boldsymbol{E}/m, \tag{3.37}$$

Let us consider Ohm's law 2.16 first in the case of a DC electric field $\boldsymbol{E}$. Microscopically the current density can be represented by

$$\boldsymbol{J} = -n_e\,e\,\boldsymbol{v}_d, \tag{3.38}$$

---

[4] One might think that here one should use the local microscopic field at the instantaneous position of an electron. However, the electrons are moving with a high thermal velocity which has an averaging effect—the mean field a conduction electron "feels" is equal to the applied external electric field.

where the concentration $n_e = N/V$ (number per unit volume) of conduction electrons within the metal, N is their number, and V is the volume of the metal.[5]

Combining equations 3.38 and 3.37 we get the microscopic representation of Ohm's law

$$\boldsymbol{J} \;=\; [n_e\, e^2\, \tau /\, m]\, \boldsymbol{E}, \tag{3.39}$$

and the Drude result for the DC conductivity

$$\sigma_o \;=\; n_e\, e^2\, \tau /\, m, \tag{3.40}$$

Taking the scattering into account is equivalent to adding a damping term due to viscous "friction", i.e., the equation of electron motion 3.35 is replaced with the equation of a driven damped oscillator with zero resonance frequency

$$m\,\frac{\mathrm{d}\boldsymbol{v}_d}{\mathrm{d}t} \;+\; \frac{m}{\tau}\,\boldsymbol{v}_d \;=\; -e\,\boldsymbol{E}. \tag{3.41}$$

The derivation of this equation can be found in Ashcroft and Mermin [13, p. 11]. Generalization of the latter equation for the case of AC fields is trivial:

$$m\,\frac{\mathrm{d}\widetilde{\boldsymbol{v}}_d}{\mathrm{d}t} \;+\; \frac{m}{\tau}\,\widetilde{\boldsymbol{v}}_d \;=\; -e\,\widetilde{\boldsymbol{E}}. \tag{3.42}$$

Substitution of the oscillating electric field and drift velocity

$$\widetilde{\boldsymbol{E}}(t) \;=\; \boldsymbol{E}(\omega)\,\mathrm{e}^{-\mathrm{i}\omega t}; \qquad\qquad \widetilde{\boldsymbol{v}}_d(t) \;=\; \boldsymbol{v}_d(\omega)\,\mathrm{e}^{-\mathrm{i}\omega t} \tag{3.43}$$

leads to

$$-\mathrm{i}\,m\,\boldsymbol{v}_d(\omega) \;+\; (m/\,\tau)\,\boldsymbol{v}_d(\omega) \;=\; -e\,\boldsymbol{E}(\omega). \tag{3.44}$$

---

[5] The concentration here cannot be denoted simply by n as usual, because the latter is reserved for the refractive index.

Solving for the drift velocity and substitution into Ohm's law results in the Fourier image of Ohm's law

$$\boldsymbol{J}(\omega) \;=\; \widetilde{\sigma}(\omega)\; \boldsymbol{E}(\omega), \tag{3.45}$$

where

$$\widetilde{\sigma}(\omega) \;=\; \sigma_{DC}/(1 \;-\; \mathrm{i}\,\omega\,\tau), \tag{3.46}$$

is the Drude AC conductivity. As expected, for $\omega = 0$ this expression is reduced to the Drude DC conductivity σ_{DC}. In the limit of low frequencies ($\omega\tau \ll 1$) the Drude AC conductivity can still be approximated by the Drude DC conductivity σ_{DC}.

Separating the real and imaginary parts of the Drude AC conductivity we get

$$\widetilde{\sigma}(\omega) \;=\; \frac{\sigma_{DC}}{1 \,+\, (\omega\,\tau)^2} \;+\; \mathrm{i}\,\frac{\sigma_{DC}\,\omega\,\tau}{1 \,+\, (\omega\,\tau)^2} \tag{3.47}$$

From this equation it can be seen that

- at low frequencies ($\omega \ll 1/\tau$) $\sigma' \simeq \sigma_{DC}$ and $\sigma'' \simeq 0$, i.e., all the current is in phase with the electric field and leads to Joule dissipation;

- at high frequencies ($\omega \gg 1/\tau$) both σ' and σ'' are very small, but $\sigma' \ll \sigma''$ i.e., all the current is $\pi/2$ rad out of phase with the electric field as the frequency is too high for the electrons to be able to follow the field—the inductive response dominates the resistive one;

- at the switch-over frequency ($\omega = 1/\tau$) both σ' and σ'' are equal to half the DC value $\sigma' = \sigma_{DC}/2 = \sigma''$. This value is the maximum one for the inductive response, and half of the maximum value σ_{DC} for the resistive response. The electrons are moving in resonance with the electric field, oscillating with a maximum amplitude.

Substitution of the Drude conductivity 3.46 into equation 3.1 results in the Drude permittivity

$$\widetilde{\varepsilon} = 1 + \frac{\mathrm{i}\,\sigma_{DC}}{\varepsilon_o\,\omega\,(1 - \mathrm{i}\,\omega\,\tau)}, \tag{3.48}$$

which is complex, but its high frequency ($\omega \gg 1/\tau$) limit is real:

$$\varepsilon = 1 - \omega_p^2\,/\,\omega^2. \tag{3.49}$$

Here the plasma frequency is defined by

$$\omega_p = \sqrt{n_e\,e^2\,/\,(m\,\varepsilon_o)}. \tag{3.50}$$

When $\omega < \omega_p$ the Drude permittivity is negative and so below the plasma edge electromagnetic waves decay exponentially upon entering the metal. But above the plasma frequency $\omega > \omega_p$ the Drude permittivity is positive and therefore electromagnetic waves above the plasma edge can propagate through the metal—at high frequencies the metal becomes transparent. At frequency $\omega = \omega_p$ the plasma edge of metals is observed: the transmittance is significant (very low) just above (below) the plasma edge at ω_p.

Using the DC conductivity (equation 3.40) and the plasma frequency (equation 3.50), equation 3.46 can be transformed into

$$\widetilde{\sigma}(\omega) = \varepsilon_o\,\tau\,\omega_p^2\,/\,(1 - \mathrm{i}\,\omega\,\tau). \tag{3.51}$$

Setting $\omega = 0$ in the latter equation gives another expression for the DC conductivity:

$$\sigma_{DC} = \widetilde{\sigma}(0) = \varepsilon_o\,\tau\,\omega_p^2. \tag{3.52}$$

The Drude model is a simple one, but gives a very good first approximation for the conductivity of "free" charge carriers. Still, this model has its limitations: it gives wrong classical estimates for the thermal velocity of the valence electrons, it cannot account for the temperature dependence of the conductivity, and it has problems with the heat capacity and paramagnetic susceptibility of the electron gas.

3.1.5.2 Lorentz model for bound charge carriers

The bound electrons can be described well by another simple model due to Lorentz: the atom of a medium is represented by a Lorentz oscillator: an electron with electric charge $-e$ and effective[6] mass m^*, positioned at $\boldsymbol{r}$, bound to the ion core by a harmonic restoring force. The natural resonant angular frequency of the oscillator is ω_o. To allow for losses due to anharmonic coupling to various other excitations, we can include proportional-to-velocity damping force with a damping constant $\mathit{\Gamma}$. The behavior of the oscillator in a harmonic driving electric field is described by the following equation of motion [11,10,6]:

$$m^* \frac{\mathrm{d}^2\widetilde{\boldsymbol{r}}}{\mathrm{d}t^2} + m^* \mathit{\Gamma} \frac{\mathrm{d}\widetilde{\boldsymbol{r}}}{\mathrm{d}t} + m^* \omega_o^2 \widetilde{\boldsymbol{r}} = -e \widetilde{\boldsymbol{E}}_l, \tag{3.53}$$

where $\widetilde{\boldsymbol{E}}_l$ is the local harmonic electric field in complex notation. It can be approximated by the externally applied electric field $\widetilde{\boldsymbol{E}}$ only for low-density media, e.g., rare gases.

Comparing equations 3.53 and 3.35, one can see that the Drude model can formally be obtained as a special case of the Lorentz model with $\omega_o = 0$.

---

[6] Lorentz used the free-electron mass m and this is certainly correct for an electron in an isolated atom, but when the electron is within a solid the effect of the crystal lattice must be taken into account by using the effective mass m^*.

The solution of equation 3.53 is

$$\widetilde{\boldsymbol{r}} = \frac{-e\,\widetilde{\boldsymbol{E}}_l\,/\,m^*}{\omega_o^2 - \omega^2 - \mathrm{i}\,\Gamma\omega}. \tag{3.54}$$

This equation can be interpreted in the following way: the electromagnetic wave sets the electron into a driven oscillation. The energy of the wave absorbed by the oscillator is proportional to the square of the amplitude of the oscillations $\widetilde{\boldsymbol{r}}_o \cdot \widetilde{\boldsymbol{r}}_o^* = \widetilde{\boldsymbol{r}} \cdot \widetilde{\boldsymbol{r}}^*$. The oscillating electron moves with acceleration and radiates back the absorbed energy. However, only a fraction of the emitted photons re-join the electromagnetic wave—the rest are absorbed and dissipated by other non-radiative processes and excitations, such as phonons.

If there are N such oscillators within a small volume V, the polarization is

$$\widetilde{\boldsymbol{P}} = -e\,\widetilde{\boldsymbol{r}}\,N\,/\,V = \frac{(e^2\,N\,/\,m^*\,V)\,\widetilde{\boldsymbol{E}}_l}{\omega_o^2 - \omega^2 - \mathrm{i}\,\Gamma\omega} = \varepsilon_o\,\widetilde{\chi}_e\,\widetilde{\boldsymbol{E}}. \tag{3.55}$$

Therefore, if we assume that $\widetilde{\boldsymbol{E}}_l \approx \widetilde{\boldsymbol{E}}$

$$\widetilde{\varepsilon} = 1 + \widetilde{\chi}_e = 1 + \frac{(e^2\,n_e/\varepsilon_o\,m^*)}{\omega_o^2 - \omega^2 - \mathrm{i}\,\Gamma\omega}, \tag{3.56}$$

where $n_e = N/V$ is the volume concentration of Lorentz oscillators. Equation 3.56 shows that the dielectric function $\widetilde{\varepsilon}$, the susceptibility $\widetilde{\chi}_e$, as well as quantities related to them, such as the refractive index $\widetilde{n}$ and the phase speed $\widetilde{v}$, all of which are generally complex, must depend on frequency. Hence, this simple classical model can explain the dispersive phenomena. This is only an approximate model: above we have assumed that the local microscopic field is the same as the applied macroscopic field which is only true for low-density media. For greater accuracy, in the case of denser media, one must use the Clausius–Mossotti relation which takes into account the difference between the local and the macroscopic electric fields [6,21].

Furthermore, the equations above apply for the simplistic case of just one type of oscillator. If there are several types of oscillators a summation over all of them is needed:

$$\widetilde{\varepsilon} = 1 + \widetilde{\chi}_e = 1 + \frac{1}{\varepsilon_o} \sum_j \frac{q_j^2 \, n_j \, / \, m_j^*}{\omega_j^2 - \omega^2 - \mathrm{i} \, \Gamma_j \, \omega}, \tag{3.57}$$

where ω_j is the resonant angular frequency for the Lorentz oscillators of the j^{th} type, characterized by effective mass m_j^*, electrical charge q_j, damping constant Γ_j, and volume concentration n_j.

The resonant angular frequencies of many resonances are far above the particular spectral range that is being studied. Their contribution to the permittivity can be approximated by a real constant $(\varepsilon_\infty - 1)$:

$$\widetilde{\varepsilon} = 1 + \widetilde{\chi}_e = \varepsilon_\infty + \frac{1}{\varepsilon_o} \sum_{j=1}^{\mathcal{N}} \frac{q_j^2 \, n_j \, / \, m_j^*}{\omega_j^2 - \omega^2 - \mathrm{i} \, \Gamma_j \, \omega}, \tag{3.58}$$

where the sum includes the complex contribution of the $\mathcal{N}$ lowest resonances which are close to the studied spectral range, whereas

$$\varepsilon_\infty - 1 = \frac{1}{\varepsilon_o} \sum_{j \geq \mathcal{N}} \frac{q_j^2 \, n_j \, / \, m_j^*}{\omega_j^2 - \omega^2 - \mathrm{i} \, \Gamma_j \, \omega} \approx \frac{1}{\varepsilon_o} \sum_{j \geq \mathcal{N}} \frac{q_j^2 \, n_j \, / \, m_j^*}{\omega_j^2}, \tag{3.59}$$

is the contribution of the resonances that are far above the studied spectral range. It is approximately real because $\omega \ll \omega_j$ when $j = \mathcal{N}, \quad \mathcal{N} + 1, \ \ldots$.

Except for the effective mass, equation 3.58 is a purely classical result. The more accurate quantum-mechanical treatment leads to a similar result. The quantum-mechanical effects can be accounted for in several different ways: semi-classically by introducing an effective electric charge q^*, or quantum-mechanically by introducing either of two "flavors" of oscillator strength (f_j or S_j) [17,22,11,23].

After all generalizations listed above, the final results are

$$\widetilde{\varepsilon} - \varepsilon_\infty = +\frac{1}{\varepsilon_o} \sum_{\substack{j=1 \\ \omega_j \neq 0}}^{\mathcal{N}} \frac{q_j^{*2}\, n_j \,/\, m_j^*}{\omega_j^2 - \omega^2 - \mathrm{i}\,\Gamma_j\,\omega} = \sum_{\substack{j=1 \\ \omega_j \neq 0}}^{\mathcal{N}} \frac{\omega_{pj}^2}{\omega_j^2 - \omega^2 - \mathrm{i}\,\Gamma_j\,\omega} \tag{3.60}$$

$$= \frac{n_e\, e^2}{\varepsilon_o\, m} \sum_{\substack{j=1 \\ \omega_j \neq 0}}^{\mathcal{N}} \frac{f_j}{\omega_j^2 - \omega^2 - \mathrm{i}\,\Gamma_j\,\omega} = \omega_p^2 \sum_{\substack{j=1 \\ \omega_j \neq 0}}^{\mathcal{N}} \frac{f_j}{\omega_j^2 - \omega^2 - \mathrm{i}\,\Gamma_j\,\omega} \tag{3.61}$$

$$= \sum_{\substack{j=1 \\ \omega_j \neq 0}}^{\mathcal{N}} \frac{S_j \omega_j^2}{\omega_j^2 - \omega^2 - \mathrm{i}\,\Gamma_j\,\omega}, \tag{3.62}$$

where the Lorentz oscillators of the j^{th} type are characterized by effective electrical charge q_j^*, or by either flavor of oscillator strength (f_j or S_j), as well as by plasma frequency

$$\omega_{pj} = \sqrt{q_j^{*2}\, n_j \,/\, (\varepsilon_o\, m_j^*)}, \tag{3.63}$$

which is the analog of the plasma frequency ω_p introduced for free electrons with equation 3.50

By setting $\omega = 0$ into equations 3.60–3.62 one can see that the quantity

$$S_j = \omega_{pj}^2 \,/\, \omega_j^2 = f_j \omega_p^2 \,/\, \omega_j^2, \tag{3.64}$$

is the contribution of the j^{th} oscillator to the static dielectric constant. Note that the expression with S_j cannot be used for free carriers (Drude oscillator), because S_j would diverge when $\omega_j = 0$!

Though the quantum-mechanical results are similar by appearance to the classical ones, still, the quantities have different meanings: ω_j is the angular frequency corresponding to a transition between two quantum states, and Γ_j is its uncertainty due to broadening of the states. Notably, the oscillator strength f_j is a purely quantum factor[7] which cannot be derived within the limits of any classical model [17], [10, p. 115]. Still, Jackson [6, pp. 309–310] has given the following intuitive interpretation (slightly modified in order to fit to my notation): N_j molecules or atoms of type j within a small volume V (concentration $n_j = N_j/V$) with f_j electrons per molecule or atom, respectively, . . .

When the angular frequency exceeds significantly the range we are dealing with, then the dielectric function becomes real and almost constant, approximately equal to ε_∞.

If one were to cover the whole electromagnetic spectrum up to the highest known frequencies of cosmic γ-rays, then one would find that $\varepsilon_\infty = 1$. However, that is not practical. Thus, for optical spectroscopy within the ultraviolet range, ε_∞ accounts for oscillators (transitions) within the x-ray (photons knocking off inner-shell electrons) and γ range (photons knocking hadrons off the nuclei); for spectroscopy within the visible range, the effects of the UV-region (high energy interband transitions) are added to ε_∞; and for the case of infrared spectroscopy, ε_∞ also includes the contribution of oscillators within the visible range (medium-energy interband transitions). Naturally, the high-energy processes become "frozen" when the photon energy is lower by orders of magnitude, that is, one cannot expect to knock off hadrons from the atomic nuclei with infrared light.

For oscillating bound electrons the natural frequencies turn out to be within the visible or UV range of the spectrum, whereas for oscillating ions (phonons) the absorption frequencies are within the infrared range.

In equations 3.60–3.62, the hiding of some details in ω_{pj}^2, or $\omega_p^2 f_j$, or S_j, respectively, is not just a trivial trick: it allows one to apply the Lorentz model even for e.g., magnon absorption without the need to specify what quantities corresponds to the charge, effective mass, etc.

---

[7] The quantum-mechanical oscillator strength customarily has two subscripts denoting the initial and final state. Here for simplicity both of them are combined into j, and we consider that the ground state is the initial one.

It is easy to separate the real and imaginary parts:

$$\begin{aligned}\varepsilon' - \varepsilon_\infty &= \sum_{\substack{j=1\\ \omega_j \neq 0}}^{\mathcal{N}} \frac{\omega_{pj}^2\,(\omega_j^2 - \omega^2)}{(\omega_j^2 - \omega^2)^2 - (\Gamma_j \omega)^2} \\ &= \sum_{\substack{j=1\\ \omega_j \neq 0}}^{\mathcal{N}} \frac{f_j\,\omega_p^2\,(\omega_j^2 - \omega^2)}{(\omega_j^2 - \omega^2)^2 - (\Gamma_j\,\omega)^2} = \sum_{\substack{j=1\\ \omega_j \neq 0}}^{\mathcal{N}} \frac{S_j(\omega_j^2 - \omega^2)}{(\omega_j^2 - \omega^2)^2 - (\Gamma_j\,\omega)^2},\end{aligned} \tag{3.65}$$

$$\begin{aligned}\varepsilon'' &= \sum_{\substack{j=1\\ \omega_j \neq 0}}^{\mathcal{N}} \frac{\omega_{pj}^2 \Gamma_j\,\omega}{(\omega_j^2 - \omega^2)^2 - (\Gamma_j\,\omega)^2} \\ &= \sum_{\substack{j=1\\ \omega_j \neq 0}}^{\mathcal{N}} \frac{f_j\,\omega_j^2\,\Gamma_j\,\omega}{(\omega_j^2 - \omega^2)^2 - (\Gamma_j\,\omega)^2} = \sum_{\substack{j=1\\ \omega_j \neq 0}}^{\mathcal{N}} \frac{S_j\,\Gamma_j\,\omega}{(\omega_j^2 - \omega^2)^2 - (\Gamma_j\,\omega)^2}.\end{aligned} \tag{3.66}$$

Plots and detailed discussion of the two equations above can be found in Wooten [17], Burns [11], and Ziman [21]. From the real and imaginary parts of the dielectric function, one can calculate the refractive index n' and the extinction coefficient n''. The Lorentz model confirms that in most spectral regions we are dealing with normal dispersion. Only in very narrow regions centered around each resonant frequency the dispersion is anomalous.

When both free and bound carriers of electric charge are present, the dielectric function can be approximated by a Drude–Lorentz model which is a sum of a Drude part describing the free carriers, and a Lorentz part describing the bound carriers, whereupon we get

$$\widetilde{\varepsilon}_{DL} = \varepsilon_\infty + \widetilde{\varepsilon}_D + \widetilde{\varepsilon}_L. \tag{3.67}$$

The Lorentz term is

$$\begin{aligned}\widetilde{\varepsilon}_L &= \sum_{\substack{j=1\\ \omega_j\neq 0}}^{\mathcal{N}} \frac{\omega_{pj}^2}{\omega_j^2 - \omega^2 - \mathrm{i}\,\Gamma_j\,\omega} \\ &= \sum_{\substack{j=1\\ \omega_j\neq 0}}^{\mathcal{N}} \frac{f_j\,\omega_p^2}{\omega_j^2 - \omega^2 - \mathrm{i}\,\Gamma_j\,\omega} = \sum_{\substack{j=1\\ \omega_j\neq 0}}^{\mathcal{N}} \frac{S_j\,\omega_j^2}{\omega_j^2 - \omega^2 - \mathrm{i}\,\Gamma_j\,\omega}, \qquad (3.68)\end{aligned}$$

It can describe bound charge-carriers (including those localized on impurity or defect states), interband transitions of charge carriers, lattice vibrations (phonons), magnons, etc.

The Drude term can be obtained formally from the first term of the sum in equation 3.60, for which $\omega_1 = 0$ and $\Gamma_1 = 1/\tau_1$, and the subscript can be dropped

$$\widetilde{\varepsilon}_D = -\frac{\omega_p^2}{\omega(\omega + \mathrm{i}/\tau)} = -\frac{\omega_p^2}{\omega(\omega + \mathrm{i}\,\Gamma)}, \qquad (3.69)$$

where Γ is the scattering rate and τ is the relaxation time for the "free" charge carriers. It describes the "free" carriers in metals, the normal charge carriers in superconductors, and conduction electrons and holes within semiconductors. A separate Drude term must be used for each type of "free" carriers.

Strictly speaking, when dealing with solids one has to account for the local internal field. As a first approximation, it can be done by using the Lorentz–Lorenz model which leads to the Clausius–Mossotti relation. Therefore, for dielectric materials one should divide $\widetilde{\varepsilon} - 1$ in all equations above by $(\widetilde{\varepsilon + 2})/3$. However, in conductors where "free" charge careers are present, the Drude term describing them dominates $\widetilde{\varepsilon}$ at low frequencies. And since the wave function of a free carrier has a wide spatial distribution, it feels the average electric field rather than the local field—no use of the Clausius–Mossotti relation is needed for conductors [17].

Still, the Lorentz term is needed to describe the oscillations or transitions of the core electrons which are bound.

From equation 3.69 we get the real and imaginary parts of the Drude permittivity

$$\varepsilon'_D = -\frac{\omega_p^2}{\omega^2 + 1/\tau^2}; \qquad \varepsilon''_D = \frac{\omega_p^2/\tau}{\omega(\omega^2 + 1/\tau^2)}. \tag{3.70}$$

If $1/\tau \ll \omega_p$ the absolute value of the real part is significantly larger than the imaginary one: $\varepsilon''_D \ll |\varepsilon'_D|$. Additionally, the real Drude permittivity, with the ε_∞ included, is negative below the plasma edge, i.e., for $\omega < \omega_p/\sqrt{\varepsilon_\infty}$ [23]. Under these conditions, $n' \ll n''$ according to equation 3.5. This explains the high reflectance of metals below their plasma edge. Indeed, from equation 3.126 the reflectance is

$$R = \frac{(n' - 1)^2 + n''^2}{(n' + 1)^2 + n''^2} = 1 - \frac{4n'}{(n' + 1)^2 + n''^2} \lesssim 1. \tag{3.71}$$

At very low frequencies $\omega \ll 1/\tau$ the refractive index and the extinction are very large and approximately equal $1 \ll n' \approx n''$ and then we get the Hagen–Rubens formula [24], [5, p. 746]:

$$\begin{aligned} \mathcal{R} &= \frac{(n' - 1)^2 + n''^2}{(n' + 1)^2 + n''^2} = 1 - \frac{4n'}{(n' + 1)^2 + n''^2} \approx 1 - \frac{2}{n'} \\ &= 1 - 2\sqrt{2/\varepsilon''} = 1 - 2\sqrt{\frac{2\omega(\omega^2 + 1/\tau^2)}{\omega_p^2/\tau}} \approx 1 - \frac{2}{\omega_p}\sqrt{\frac{2\omega}{\tau}}. \end{aligned} \tag{3.72}$$

From the Drude permittivity, equation 3.69, using relation 3.1, we get the Drude conductivity

$$\tilde{\sigma}_D = \mathrm{i}\,\varepsilon_o \frac{\omega_p^2}{\omega(\omega + \mathrm{i}/\tau)}, \tag{3.73}$$

Separating the real and imaginary parts of the Drude term 3.69, we get

$$\varepsilon'_D = -\frac{(\tau\omega_p)^2}{1 + (\tau\omega)^2}; \qquad \varepsilon''_D = \frac{\tau\omega_p^2/\omega}{1 + (\tau\omega)^2} \tag{3.74}$$

Therefore, using equation 3.2 we derive the Drude conductivity

$$\sigma'_D = \varepsilon_o \frac{\tau\omega_p^2}{1 + (\tau\omega)^2} = \frac{\sigma_{DC}}{1 + (\tau\omega)^2}, \tag{3.75}$$

where

$$\sigma_{DC} = \varepsilon_o \tau \omega_p^2 \tag{3.76}$$

is the DC conductivity of the “free” carriers according to the Drude model.

3.1.6 Sum Rules

Various sum rules exist which can be of help in the analysis of experimental data [17]. The oscillator strengths (the squares of the matrix elements of the electric dipole moment) introduced in the previous subsection satisfy the f-sum rule (oscillator-strength sum rule). The f-sum rule for a free atom with Z electrons is

$$\sum_j f_j = Z, \tag{3.77}$$

whereas for a solid it becomes

$$\int_0^\infty \omega\, \varepsilon''(\omega)\, \mathrm{d}\omega = \frac{1}{2}\pi\, \omega_p^2 = \frac{1}{\varepsilon_o} \int_0^\infty \sigma'(\omega)\, \mathrm{d}\omega, \tag{3.78}$$

where the integral on the left side characterizes the absorption of energy at all frequencies (see Wooten [17, p. 77]), and it is related to the integral on the right side through equation 2.79.

Another sum rule exists for the electronic loss function $-1/\widetilde{\varepsilon}$

$$-\int_0^{\infty} \omega \, \mathrm{Im}\,\{1/\widetilde{\varepsilon}(\omega)\}\; \mathrm{d}\omega \;=\; \frac{1}{2}\,\pi\,\omega_p^2. \tag{3.79}$$

The sum rules 3.78 and 3.79 can be derived using the Kramers–Kronig relations [17].

Frequently, partial sum rules can be applied to get the effective number $N_{eff}(\omega_c)$ of carriers per atom (for pure metals) or per formula unit (for compounds), that contribute to the optical properties in some finite spectral range from 0 to ω_c. E.g., applying equation 3.78 in the superconductor from 0 to ω_c, and using the plasma frequency definition 3.50, we get the partial f-sum rule [17,25]:

$$\varepsilon_o \int_0^{\omega_c} \omega\, \varepsilon''(\omega)\, \mathrm{d}\omega \;=\; \frac{\pi\, N_{eff}(\omega_c)\, e^2}{2\, m^*\, V_u} \;=\; \int_0^{\omega_c} \sigma'(\omega)\, \mathrm{d}\omega, \tag{3.80}$$

where m^* is the effective mass of the effective carriers with charge $\pm e$ (holes or electrons), and V_u is the volume per atom or per formula unit, and ω_c is the cut-off angular frequency.

3.1.7 Dispersion in Insulators. Group Velocity

Dispersion for the general case of conducting media is given by the frequency dependence the optical properties covered in subsection 3.1.1. The classical model for dispersion is presented in subsection 3.1.5.

All results can also be applied for dispersion in insulators. At low frequency $\omega \ll 1/\tau$ we must substitute everywhere $\varepsilon'' \propto \sigma' \approx \sigma_{CD} = 0$.

Naturally, in vacuum there is no dispersion. The same is true for very rarified gases.

For simplicity here we shall consider a wave propagating along one of the Cartesian axes, e.g., in direction $\hat{\mathbf{z}}$. For a general direction of propagation see Born and Wolf [5].

The phase velocity is the speed with which a given phase value moves in space. Differentiating the constant phase of an electromagnetic wave leads to the following result for the phase speed [5, pp. 16–19]:

$$v \;=\; \mathrm{d}z/\mathrm{d}t \;=\; \omega/k; \qquad\qquad \widetilde{v} \;=\; \mathrm{d}\widetilde{z}/\mathrm{d}t \;=\; \omega/\widetilde{k}, \tag{3.81}$$

where the left equation is for dielectrics, whereas the right equation is for conductors. Note that for conductors $\widetilde{z}$ is complex because so is the wave number $\widetilde{k}$. This reflects the fact that penetration into conductors beyond the skin depth is not possible. For vacuum the phase velocity is simply the velocity of light c.

Let us consider a group of waves within a narrow frequency range $\Delta\omega$, centered around an average angular frequency $\langle\omega\rangle$, and within a narrow wave number range Δk ($\Delta\widetilde{k}$), centered around an average wave number $\langle k\rangle$ ($\langle\widetilde{k}\rangle$), is propagating in a dielectric (conducting) medium. Then the peak—and any other constant amplitude—travels in space with a group velocity [5, pp. 21–23] given by equation 3.82 (3.83), respectively

$$v^{(g)} \;=\; z/t \;=\; (\mathrm{d}\omega/\mathrm{d}k)_{\langle k\rangle} \;=\; (\mathrm{d}k/\mathrm{d}\omega)^{-1}_{\langle\omega\rangle}\,, \tag{3.82}$$

$$\widetilde{v}^{(g)} \;=\; \widetilde{z}/t \;=\; \left(\mathrm{d}\omega/\mathrm{d}\widetilde{k}\right)_{\langle\widetilde{k}\rangle} \;=\; \left(\mathrm{d}\widetilde{k}/\mathrm{d}\omega\right)^{-1}_{\langle\omega\rangle}. \tag{3.83}$$

3.1.8 Perfect Conductors

Perfect conductors do not exist, but considering of such extreme cases is a good illustration. Perfect conductors are idealized monocrystals with perfect translational symmetry, i.e., no defects of any type. According to Bloch's theorem [26,13], within perfect crystals there is no scattering of the charge carriers. Therefore, perfect conductors can be described by the results for regular conductors if one takes the limit $\tau \rightarrow \infty$. Taking that limit in equation 3.73, we get the conductivity of a perfect conductor

$$\widetilde{\sigma}_D = \mathrm{i}\,\varepsilon_o \lim_{\tau\to\infty} \frac{\omega_p^2}{\omega + \mathrm{i}/\tau} = \varepsilon_o \omega_p^2 \lim_{\tau\to\infty} \frac{\mathrm{i}\,(\omega - \mathrm{i}/\tau)}{\omega^2 + 1/\tau^2} \tag{3.84}$$

$$= \varepsilon_o \omega_p^2 \lim_{\tau\to\infty} \left[\frac{1/\tau}{\omega^2 + 1/\tau^2} + \mathrm{i}\,\frac{\omega}{\omega^2 + 1/\tau^2}\right] = \pi\varepsilon_o \omega_p^2 \left[\delta(\omega) + \frac{\mathrm{i}}{\pi\omega}\right].$$

The latter transformation was performed by using the improper limit of the Lorentzian δ-sequence function [27, eq. 1.173].

Or the real and imaginary parts of the conductivity for a perfect conductor are

$$\sigma'_D = \pi\varepsilon_o\omega_p^2\delta(\omega); \qquad \sigma''_D = \varepsilon_o\omega_p^2/\omega. \tag{3.85}$$

The real part of the conductivity satisfies the sum rule 3.78 if we note that $\delta(\omega)$ is an even function and therefore integrated from 0 to ∞ it gives $1/2$.

From equation 3.85 it is clear that the DC conductivity of a perfect conductor is infinite (both the real and imaginary parts are infinite). At all other frequencies the real part is zero and the imaginary part, which represent the inductive response, dominates.

From equations 3.2 and 3.85, for the permittivity of a perfect conductor we get

$$\varepsilon'_D = \mathrm{i}\,\pi\omega_p^2\delta(\omega)/\omega = 0; \qquad \varepsilon''_D = \mathrm{i}\,(\omega_p/\omega)^2, \tag{3.86}$$

where at DC the L'Hospital's rule has been used for the real part.

Finally, including ε_∞, the refractive index of a perfect conductor is

$$\widetilde{n} = \sqrt{\widetilde{\varepsilon}} = \begin{cases} \mathrm{i}\sqrt{(\omega_p/\omega)^2 - \varepsilon_\infty}, & (0 \le \omega < \omega_p/\sqrt{\varepsilon_\infty}) \\ \\ \sqrt{\varepsilon_\infty - (\omega_p/\omega)^2}, & (\omega > \omega_p/\sqrt{\varepsilon_\infty}). \end{cases} \tag{3.87}$$

At frequencies below $\omega_p/\sqrt{\varepsilon_\infty}$, $n' = 0$ and there is a stepwise impedance[8] mismatch with vacuum (n = 1), which would make any perfect conductor also a perfect reflector. Indeed substituting $n' = 0$ into the left-middle term of equation 3.71 will produce 1 immediately.

3.1.9 Superconductors

The optical properties of superconductors resemble those of perfect conductors. The main difference is that the superconductors are characterized by an energy gap of 2Δ. For low-temperature superconductors, the theory of Bardeen–Cooper–Schrieffer gave the absolute-zero gap [28]

$$\mathcal{E}_g(0) = 2\Delta(0) = 3.528 k_B T_c. \tag{3.88}$$

Furthermore, at temperatures within the range from $T_c/2 to T_c$, in the limit of weak coupling of the Cooper pairs, the theory leads to the following expression for the temperature dependence of the gap energy [28,29]

---

[8] According to equation 3.28 the wave impedance is inversely proportional to the refractive index.

$$\mathcal{E}_g(T) \;=\; 2\Delta(T) \approx 3.48\sqrt{1\;-\;T/T_c}. \tag{3.89}$$

Various experiments on high-temperature superconductors give significantly higher values for the absolute-zero gap, within the range from $4k_BT_c$ to $7k_BT_c$, which is a strong proof that the coupling in high-temperature superconductors must be quite strong [28]. In the past there has been some discussion whether the cuprates have an s- or d-wave symmetry of the energy gap. The experiments were difficult and initially ambiguous, but as time went by and more experimental evidence was gathered, it became increasingly clear that the d-wave theory is the winner. Therefore for a thin $YBa_2Cu_3O_{7-\delta}$ film with $T_c \approx 82\ K$, one expects the gap to be in the range from 229 to 400 cm^{-1} rather than the 200 cm^{-1} predicted by the theory of Bardeen–Cooper–Schrieffer. Moreover, infrared studies show that we are dealing with a pseudo gap which, instead of decreasing as the temperature grows towards T_c, just becomes less pronounced. This is due to the fact that the temperature is not as low as for the classical superconductors. So, even though the Cooper pairs cannot absorb within the energy gap, there are other excitations in the crystal, or some normal electrons, that can absorb within the gap.

Due to the superconducting fraction of the conducting electrons, high-temperature superconductors at very low temperatures $T \gtrsim 0$ are almost as perfect reflectors as perfect conductors, for frequencies within the pseudo-gap.

The field of an incident electromagnetic wave penetrates into any superconductor, but is damped exponentially on a length-scale determined by the London penetration depth [1]

$$\lambda_L \;=\; \sqrt{m^*/(\mu_o n_s^* e^{*2})} \;=\; \sqrt{m/(\mu_o n_s e^2)}, \tag{3.90}$$

where $m^* = 2m$ and $e^* = 2m$ are the effective mass and electric charge of a Cooper pair, respectively, and $n_s^* = n_s/2$ is the effective concentration of such pairs; all of these quantities were expressed by the respective ones for single superconducting electrons.

If all conducting electrons were to condense into Cooper pairs, then the London penetration depth would be $\lambda_L = c/\omega_p$.

For simplicity normal incidence and $T = 0\ K$ are assumed below. The electric field transmitted through the surface of the superconductor for frequencies within the gap can be found approximately if we substitute expression 3.87 for the refractive index into the amplitude transmission coefficient

$$E_t/E_i = t = 2/(1 + \tilde{n}) \approx -2\mathrm{i}\,\omega/\omega_p. \tag{3.91}$$

The purely imaginary transmission coefficient means that the electric field E_t transmitted through the surface of the superconductor is out of phase with the incident electric field E_i by $-\pi/2$ rad. Also $E_t \ll E_i$ since $\omega < 2\Delta/\hbar \ll \omega_p$. Furthermore, the purely imaginary refractive index of the superconductor means that no power is absorbed at the interface. On the average, no power[9] is transmitted further than $3\lambda_L$ from the interface into the superconductor, i.e., if the superconducting layer is thicker than $3\lambda_L$, then $\mathcal{T} = n' \left|t\right|^2 = 0$. The purely imaginary conductivity for $\omega > 0$ indicates that the electric current induced within the superconductor is out of phase with E_i by $-\pi/2$ rad. Therefore it is inductive in character, which confirms again that no energy is dissipated.

---

[9] Due to the inductive response of the superconductor, energy oscillates forth and back, but averaged for any integer number of cycles, the Poynting vector decays with the characteristic length equal to the London penetration depth λ_L.

The transmitted magnetic field on the superconducting side of the interface is

$$H_t \;=\; \tilde{n}\sqrt{\varepsilon_o/\mu_o}E_t \approx \mathrm{i}\,(\omega_p/\omega)E_t \;=\; 2\sqrt{\varepsilon_o/\mu_o}E_i \;=\; 2H_i, \qquad (3.92)$$

where the relationship 2.101 between the electric and magnetic field of an electromagnetic wave, equation 3.87 for the complex refractive index of a perfect metal and the transmitted electric field 3.91 have been used.

The results for the transmitted fields are easy to interpret: with a normally incident wave the fields $\boldsymbol{E}_i$ and $\boldsymbol{H}_i$ are tangential to the interface; conservation of tangential components, with the reflected fields being $\boldsymbol{E}_r \simeq -\boldsymbol{E}_i$ and $\boldsymbol{H}_r \simeq \boldsymbol{H}_i$, is satisfied by the transmitted fields $\boldsymbol{E}_t \simeq 0$ and $\boldsymbol{H}_t \simeq 2\boldsymbol{H}_i$.

At any temperature $T < T_c$, for frequencies $\omega > \Delta/\hbar$ above the energy gap the photons have enough energy to disassociate Cooper pairs, driving electrons up to unoccupied normal levels. As a result the superconductor starts to behave similarly to a normal metal. Likewise, at any frequency $\omega > \Delta/\hbar$ when the temperature is sufficiently high $T > \Delta/k_B$, the phonons have enough energy to disassociate Cooper pairs, driving electrons up to unoccupied normal levels. Finally, when both $\omega > \Delta/\hbar$ and $T > \Delta/k_B$, these two effects can be present simultaneously. This is one of the factors complicating the analysis of data for high-temperature superconductors.

3.2 Reflection and Transmission

3.3 General Remarks about Reflection and Transmission

From this point on the media in multi-layered structures will be denoted with consecutive numbers used as subscripts. To avoid confusion with vacuum, the numbering of the media will start from 1, even when medium 1 is vacuum.

In any uniform medium a plane wave propagates (until it is completely damped if the medium is conducting) in a constant direction. When such a wave meets an interface between two uniform media various interesting phenomena can happen which are the subject of this section. These phenomena include reflection, refraction, total internal reflection, perfect reflection, etc. In many cases the term "refraction" has been replaced by "transmission" and the transcript t is used occasionally for the respective quantities, since r is reserved for the quantities describing the reflected wave. All results summarized below can be obtained by application of the boundary conditions 2.19 and 2.20. From this point on, the subscripts of the angles will denote the medium, and interfaces will be denoted with double subscripts including the numbers of the two adjacent layers. For the sake of brevity often only the results are summarized. Derivations and more details can be found in a number of sources [10,3,18,5,6,30].

Let the plane interface between two uniform media be a sharp, step-wise discontinuity with an infinite area. Some convenient definitions and facts following from the boundary conditions come next:

- The reflected and refracted waves have the same frequency as the incident wave;
- The incident (backward) normal $\hat{\mathbf{n}}_{2,1}$ is the perpendicular to the interface at the point of incidence, directed from medium 2 to medium 1;
- The incident (backward) normal $\hat{\mathbf{n}}_{2,1}$ is used as a reference for the angles of incidence and reflection, whereas the oppositely-directed (forward) normal $\hat{\mathbf{n}}_{1,2}$ is used as a reference for the angle of refraction;
- For the case of oblique incidence, the incident ray and the incident normal define the plane of incidence. Clearly, for normal incidence the plane of incidence is not defined;

- When the incidence is oblique, all rays can be projected on the forward normal $\hat{\mathbf{n}}_{1,2}$. Rays with positive projections on the forward normal (e.g., incident, primary transmitted, etc.) will be called forward-propagating and quantities related to them will be denoted with a $^{(+)}$ superscripts. Conversely, rays with negative projections on the forward normal (e.g., primary reflected, secondary reflected, etc.) will be called backward-propagating, and quantities related to them will be denoted with a $^{(-)}$ superscripts.

- Both the equi-phase and equi-amplitude sets of parallel planes are orthogonal to the plane of incidence. In most cases these two sets of planes coincide. Only when a non-normal incidence onto an absorbing medium is present the two sets of parallel planes are at an angle (the angle of refraction) with respect to each other;

- The point of incidence is taken as the origin of a Cartesian coordinate system. One axis (z) is opposite to the incident normal, another (y) is along the intersection of the interface surface and the plane of incidence, and the third axis (x) lies in the interface and is normal to the plane of incidence;

- The incident, reflected, and refracted rays (i.e., wave vectors $\boldsymbol{k}$) lie in the plane of incidence;

- The refracted ray satisfies Snell's law

$$\sin\widetilde{\theta}_t/\sin\widetilde{\theta}_i \;=\; \widetilde{v}_2/\widetilde{v}_1 \;=\; \widetilde{n}_1/\widetilde{n}_2 \;=\; \widetilde{n}_{2,1} \tag{3.93}$$

  where $\widetilde{\theta}_i$ and $\widetilde{\theta}_t$ are the complex angles of incidence and refraction (transmission), $\widetilde{n}$ and $\widetilde{v}$ are the complex refractive index and phase velocity in the medium denoted by the respective subscript;[10]

---

[10] Complex quantities have been used to describe the fairly general case with a flat interface between two conducting media. For any non-absorbing dielectric medium the respective quanti-

- In the case of a multi-layered structure, after the first interface on whose second side there is an absorbing medium all angles become complex—indeed, chain application of Snell's law proves that from the first absorbing layer on all angles are complex;
- The angle of reflection $\widetilde{\theta}_r$ is equal to the angle of incidence $\widetilde{\theta}_i$. In the special case when the ray incident on a multi-layered structure has not crossed any absorbing layer, these two angles are real;
- When we are dealing with two dielectric media, and the second one has lower optical density ($n_2 < n_1$), if the angle of incidence θ_i exceeds the critical value $\theta_{cr} = \arcsin n_2/n_1$, the phenomenon of total internal reflection occurs, and the angle of refraction $\widetilde{\theta}_t$ becomes complex;
- The incident ray ($\boldsymbol{E}_i$, $\boldsymbol{H}_i$) can be decomposed into two independent linear polarizations: s-polarization ($\boldsymbol{E}_{i\perp}$, $\boldsymbol{H}_{i\parallel}$), and p-polarization ($\boldsymbol{E}_{i\parallel}$, $\boldsymbol{H}_{i\perp}$), where the subscript shows which field is perpendicular ($\perp$), and parallel ($\parallel$) to the plane of incidence. The equations for these two polarizations are completely separate. The energy flux density of the incident wave is equal to the sum of the respective contributions from the two polarizations. Indeed, $\boldsymbol{E}_i^2 = \boldsymbol{E}_{i\perp}^2 + \boldsymbol{E}_{i\parallel}^2$.

All quantities that belong to a particular medium will have as a subscript the number of the medium, whereas quantities characterizing an interface will have a double subscript, including the numbers of the two adjacent layers. In most cases the first and/or the last medium is vacuum or air, but in the most general case either one of these two media may be an absorbing medium with complex characteristics. The incident ray is assumed to be coming from the medium with the

---

ties become real.

lowest number, and the ray transmitted through the whole multi-layered structure propagates into the medium with the highest number. A superscript plus "+" (minus "−") will mark quantities pertaining to waves propagating within the cone of directions leading to a medium with a higher (lower) number. The plus superscript may be dropped, but the minus one will always be explicit.

It is convenient to use the wave vector and the wave impedance of the j^{th} medium which according to equations 3.18 and 3.19 is

$$\widetilde{k}_j \;=\; k_o\sqrt{\widetilde{\mu}_j[\varepsilon'_j \,+\, \mathrm{i}\,\sigma'_j/(\varepsilon_o\omega)]}, \tag{3.94}$$

$$\widetilde{Z} \;=\; Z_o\sqrt{\frac{\widetilde{\mu}_j}{\varepsilon'_j \,+\, \mathrm{i}\,Z_o\sigma'_j/\omega}}. \tag{3.95}$$

For absorbing media, with either dielectric or conducting absorption[11] these quantities are complex, but for non-absorbing media they are reduced to real quantities.

In the latter two equations, $k_o = \pm\omega/c$ is the wave number in vacuum, and $Z_o = \sqrt{\mu_o/\varepsilon_o}$ is the wave impedance of vacuum, both from equations 3.17.

By definition, the Fresnel coefficients are the ratios of the reflected or transmitted electric field to the incident electric field.

$$\widetilde{r}_{j,j+1} \;=\; \widetilde{E}_j^-/\widetilde{E}_j^+; \qquad\qquad \widetilde{t}_{j,j+1} \;=\; \widetilde{E}_{j+1}^+/\widetilde{E}_j^+, \tag{3.96}$$

where $\widetilde{r}_{j,j+1}$ and $\widetilde{t}_{j,j+1}$ are, respectively, the Fresnel reflection and transmission coefficient for the interface between media j and $j+1$; the electric fields are: $\widetilde{E}_j^+$ of the forward-propagating (incident) wave within medium j, $\widetilde{E}_j^-$ of the backward-propagating (reflected) wave within medium j, $\widetilde{E}_{j+1}^+$ of the forward-propagating (refracted) wave within medium $j+1$. Applying equations 3.96 for the case of backside incidence we get:

---

[11] Or at low, below optical, frequencies possibly magnetic absorption.

$$\widetilde{r}_{j+1,j} = \widetilde{E}^{+}_{j+1}/\widetilde{E}^{-}_{j+1}; \qquad \widetilde{t}_{j+1,j} = \widetilde{E}^{-}_{j}/\widetilde{E}^{-}_{j+1}, \tag{3.97}$$

where the Fresnel reflection and transmission coefficients are for the interface between media $j+1$ and j; the electric fields are: $\widetilde{E}^{-}_{j+1}$ of the backward-propagating (incident from the back) wave within medium $j+1$, $\widetilde{E}^{+}_{j+1}$ of the forward-propagating (reflected) wave within medium $j+1$, $\widetilde{E}^{-}_{j}$ of the backward-propagating (refracted) wave within medium j.

In general case of at least one absorbing medium, the Fresnel coefficients are complex, but when the media on both sides of the interface $(j, j+1)$ are non-absorbing, the Fresnel coefficients become real quantities, provided no total reflection is involved.

Division is a non-linear operation, and one might expect that in the definitions of the Fresnel coefficients one of the fields should be complex conjugate. However, the Fresnel coefficients are an exception from the general rule mentioned in subsections 2.1.1 and 2.2.6. Indeed, division cancels the oscillating factors, and only the constant ratio of the amplitudes remains, which is desirable. Conversely, if we were to complex conjugate either the numerator or the denominator, not only the oscillating factors would not cancel, but the ratio would oscillate with the doubled frequency which is not physical.

3.3.1 Reflection and Refraction at the Interface between Two Dielectrics

Here the case involving a single interface is considered. Though it is the simplest one, it is important as it is the fundamentum for treating of the more complicated ones, involving multi-layered optical structures.

Application of the boundary conditions leads to the Fresnel's formulae given below separately for the two possible polarizations. For simplicity non-absorbing media are assumed and therefore all refractive indices are real. The angles will also be real if either $n_1 < n_2$, or $\theta_i < \theta_{cr}$ when $n_1 > n_2$. When these conditions are met, the Fresnel coefficients also become real. An illustration is given in Fig. 3.1

3.3.1.1 TE waves (s-polarization)

TE wave means transverse-electric—the electric field $\boldsymbol{E}$ is orthogonal to the plane of incidence, and the magnetic field $\boldsymbol{H}$ lies in that plane. Often this linear polarization is denoted as s-polarization, and below the respective quantities are marked by a superscript "$^{(s)}$". For this case the Fresnel coefficients have the form

$$r_{1,2}^{(s)} = \frac{Z_2 \cos\theta_1 - Z_1 \cos\theta_2}{Z_2 \cos\theta_1 + Z_1 \cos\theta_2} = \frac{\cos\theta_1 - \mu_{2,1}\sqrt{n_{1,2}^2 - \sin^2\theta_1}}{\cos\theta_1 + \mu_{2,1}\sqrt{n_{1,2}^2 - \sin^2\theta_1}}, \tag{3.98}$$

$$t_{1,2}^{(s)} = \frac{2Z_2 \cos\theta_1}{Z_2 \cos\theta_1 - Z_1 \cos\theta_2} = \frac{2\cos\theta_1}{\cos\theta_1 + \mu_{2,1}\sqrt{n_{1,2}^2 - \sin^2\theta_1}}, \tag{3.99}$$

where[12]

$$n_{1,2} = n_2/n_1; \qquad \mu_{2,1} = \mu_1/\mu_2 \tag{3.100}$$

are, respectively, the ratios of the refractive indexes and magnetic permeabilities at the interface (1,2) between medium 1 and 2. Using

$$Z_1/Z_2 = \mu_{2,1} \sin\theta_1/\sin\theta_2 = \mu_1 \sin\theta_1/(\mu_2 \sin\theta_2), \tag{3.101}$$

---

[12] The forward normal $\hat{\mathbf{n}}_{j,j+1}$ to the interface between media j and $j+1$, can be distinguished unambiguously from the ratio $n_{j,j+1}$ of the refractive indexes at the same interface, if one notices that the former symbol is bold and has a hat, unlike the latter one. In this section we are dealing with the special case $j = 1$.

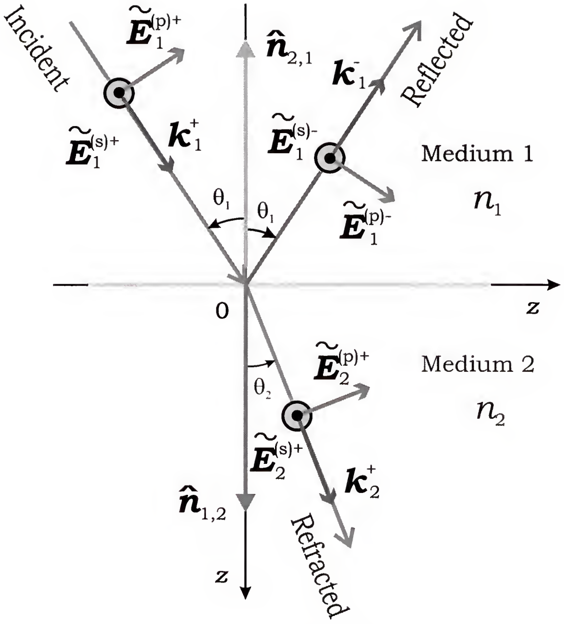
Incident
$\tilde{\boldsymbol{E}}_1^{(p)+}$
$\hat{\boldsymbol{n}}_{2,1}$
$\boldsymbol{k}_1^-$
Reflected
$\tilde{\boldsymbol{E}}_1^{(s)+}$
$\boldsymbol{k}_1^+$
$\tilde{\boldsymbol{E}}_1^{(s)-}$
Medium 1
θ_1
θ_1
n_1
$\tilde{\boldsymbol{E}}_1^{(p)-}$
0
z
$\tilde{\boldsymbol{E}}_2^{(p)+}$
Medium 2
θ_2
n_2
$\tilde{\boldsymbol{E}}_2^{(s)+}$
$\boldsymbol{k}_2^+$
$\hat{\boldsymbol{n}}_{1,2}$
z
Refracted

Figure 3.1: Reflection and refraction of the s-polarization and p-polarizations at the interface between medium 1 and 2.

the Fresnel's formulae 3.98 and 3.99 can be converted to

$$r_{1,2}^{(s)} = \frac{\mu_2 \tan\theta_2 - \mu_1 \tan\theta_1}{\mu_2 \tan\theta_2 + \mu_1 \tan\theta_1}; \qquad t_{1,2}^{(s)} = \frac{2\mu_2 \tan\theta_2}{\mu_2 \tan\theta_2 + \mu_1 \tan\theta_1}. \tag{3.102}$$

The latter two Fresnel equations, when $\mu_2 = \mu_1$, are reduced to

$$r_{1,2}^{(s)} = \frac{-\sin(\theta_1 - \theta_2)}{\sin(\theta_1 + \theta_2)}; \qquad t_{1,2}^{(s)} = \frac{n_{2,1} \sin(2\theta_1)}{\sin(\theta_1 + \theta_2)}. \tag{3.103}$$

The negative sign of $r_{1,2}^{(s)}$ is in agreement with the fact that when $n_1 < n_2$ there is a phase change of π rad upon reflection. Conversely, when $n_1 > n_2$, there is no such phase change as $\sin(\theta_1 - \theta_2) < 0$ and therefore $r_{1,2}^{(s)} > 0$.

For normal incidence equations 3.98 and 3.99 or their equivalent 3.102 are simplified to

$$r_{1,2}^{(s)} = \frac{\mu_2 n_1 - \mu_1 n_2}{\mu_2 n_1 + \mu_1 n_2}; \qquad t_{1,2}^{(s)} = \frac{2\mu_2 n_1}{\mu_2 n_1 + \mu_1 n_2}. \tag{3.104}$$

Finally, when the two media have identical magnetic properties ($\mu_{2,1} = \mu_1/\mu_2 = 1$), all μ factors in the various expressions of the Fresnel coefficients get cancelled.

3.3.1.2 TM waves (p-polarization)

TM wave means transverse-magnetic—the magnetic field $\boldsymbol{H}$ is orthogonal to the plane of incidence, and the electric field $\boldsymbol{E}$ lies in that plane. Often this linear polarization is denoted as p-polarization, and below the respective quantities are marked by a superscript "$^{(p)}$". From this moment on, when a polarization superscript is absent, it will imply that the respective equation holds for both polarizations.

$$r_{1,2}^{(p)} = \frac{Z_2 \cos\theta_2 - Z_1 \cos\theta_1}{Z_1 \cos\theta_1 + Z_2 \cos\theta_2} = \frac{\sqrt{n_{1,2}^2 - \sin^2\theta_1} - \mu_{2,1} n_{1,2}^2 \cos\theta_1}{\mu_{2,1} n_{1,2}^2 \cos\theta_1 + \sqrt{n_{1,2}^2 - \sin^2\theta_1}} \tag{3.105}$$

$$t_{1,2}^{(p)} = \frac{2 Z_2 \cos\theta_1}{Z_1 \cos\theta_1 + Z_2 \cos\theta_2} = \frac{2 n_{1,2} \cos\theta_1}{\mu_{2,1} n_{1,2}^2 \cos\theta_1 + \sqrt{n_{1,2}^2 - \sin^2\theta_1}} \tag{3.106}$$

Using equation 3.101, the Fresnel's formulae 3.105 and 3.106 can be converted to

$$r_{1,2}^{(p)} = \frac{\mu_2 \sin(2\theta_2) - \mu_1 \sin(2\theta_1)}{\mu_1 \sin(2\theta_1) + \mu_2 \sin(2\theta_2)}; \quad t_{1,2}^{(p)} = \frac{4 \mu_2 \sin\theta_2 \cos\theta_1}{\mu_1 \sin(2\theta_1) + \mu_2 \sin(2\theta_2)}. \tag{3.107}$$

The latter two Fresnel equations, when $\mu_{2,1} \equiv \mu_1/\mu_2 = 1$, are reduced to

$$r_{1,2}^{(p)} = \frac{\tan(\theta_2 - \theta_1)}{\tan(\theta_1 + \theta_2)}; \qquad t_{1,2}^{(p)} = \frac{2 \cos\theta_1 \sin\theta_2}{\sin(\theta_1 + \theta_2) \cos(\theta_1 - \theta_2)}. \tag{3.108}$$

For normal incidence equations 3.107 are simplified to

$$r_{1,2}^{(p)} = \frac{\mu_2 n_1 - \mu_1 n_2}{\mu_1 n_2 + \mu_2 n_1}; \qquad t_{1,2}^{(p)} = \frac{2 \mu_2 n_1}{\mu_1 n_2 + \mu_2 n_1}. \tag{3.109}$$

Finally, when the two media have identical magnetic properties ($\mu_1 = \mu_2$), all μ factors get cancelled.

Here it should be noted that the sign of $r_{1,2}^{(p)}$ depends on the convention for referencing the fields. Herein the picture (see Fig. 3.1) given by Heavens [30, Fig. 4.1], Yeh [18, Fig. 3.3], and Knittl [31, Fig. 2-2] is followed, which is the opposite of that of Jackson [6, Fig. 7.6] and Matveev [10, Fig. 65]. The chosen convention ensures a better symmetry of the Fresnel coefficients.

3.3.1.3 Brewster effect

The angle of incidence for which $r_{0,2}^{(p)} = 0$ is called Brewster angle θ_B. From equation 3.108 we have $\tan(\theta_1 + \theta_2) = \infty \rightarrow \theta_1 + \theta_2 = \pi/2$ rad, and using Snell's law we get the Brewster law $\theta_B = \arctan n_2/n_1$.

Since upon reflection at the Brewster angle θ_B, only the s-polarization is reflected, the Brewster effect can be used for linear polarization.

In actual materials, at $\theta_1 = \theta_B$, $r_{1,2}^{(p)}$ does not vanish completely, but has a minimum value. Therefore, the linear polarization obtained by applying the Brewster effect on unpolarized light is not complete—in reality the reflected waves are elliptically polarizeed. This deviation from the Fresnel results is due to the fact that physical interfaces are never as abrupt as it was assumed.

The Brewster effect is a result of the transverse character of electromagnetic waves [10].

3.3.1.4 Total reflection

When $n_1 > n_2$ and $\theta_1 > \theta_{cr}$ the phenomenon of total reflection can be observed. Snell's law is still applicable, but the angle of refraction θ_2 is complex even though all other quantities may be real. Naturally, such a complex angle of refraction does not have a geometrical representation anymore.

In this case, before the total reflection occurs, the wave penetrates the second medium to a penetration depth [10]

$$\delta = \frac{\lambda_2/(2\pi)}{\sqrt{n_{2,1}^2 \sin^2\theta_2 - 1}}, \tag{3.110}$$

which is of the order of λ_2. The refracted wave takes the form of an evanescent wave. Such a wave is present only within a surface layer of the second medium which is behind the illuminated portion of the interface and whose thickness is equal to the penetration depth. The evanescent wave is not a plane one because it is damped exponentially within the second medium, which is characterized by the penetration depth. Its phase velocity depends on the refractive index of the first medium and on the angle of incidence

$$v_e = \frac{c}{n_1 \sin\theta_1} = \frac{\sin\theta_{cr}}{\sin\theta_1} v_2 < v_2, \tag{3.111}$$

and is always smaller than the phase velocity within the second medium.

In this case the Fresnel reflection coefficient is reduced to

$$\widetilde{r} = \exp(2\mathrm{i}\,\varphi_{1,2}), \tag{3.112}$$

$$\varphi_{1,2}^{(s)} = -\arctan\frac{\lambda_2 Z_1}{2\pi\delta Z_2 \cos\theta_1}; \qquad \varphi_{1,2}^{(p)} = -\arctan\frac{\lambda_2 Z_2}{2\pi\delta Z_1 \cos\theta_1} \tag{3.113}$$

The amplitudes do not change and therefore all of the incident energy is reflected, hence the name “total reflection”. But the phases change, and the change is different for the two polarizations.

The partial penetration within the second medium results in a slight lateral shift of the reflected ray — Goos–Hänchen effect [6]. This effect cannot be observed at normal incidence.

3.3.1.5 Reflectance and transmittance

The coefficient of reflection (transmission) of energy or intensity is called reflectance (transmittance). Using the Poynting vector and the definition of intensity 2.121 we get

$$\mathcal{R}^{(s)}_{1,2} = \left| \frac{\hat{\mathbf{n}}_{2,1} \cdot \widetilde{\boldsymbol{S}}^{(s)-}_1}{\hat{\mathbf{n}}_{2,1} \cdot \widetilde{\boldsymbol{S}}^{(s)+}_1} \right| = \left| \widetilde{r}^{(s)}_{1,2} \right|^2 = \widetilde{r}^{(s)}_{1,2}\, \widetilde{r}^{(s)*}_{1,2}, \tag{3.114}$$

$$\mathcal{R}^{(p)}_{1,2} = \left| \frac{\hat{\mathbf{n}}_{2,1} \cdot \widetilde{\boldsymbol{S}}^{(p)-}_1}{\hat{\mathbf{n}}_{2,1} \cdot \widetilde{\boldsymbol{S}}^{(p)+}_1} \right| = \left| \widetilde{r}^{(p)}_{1,2} \right|^2 = \widetilde{r}^{(p)}_{1,2}\, \widetilde{r}^{(p)*}_{1,2}, \tag{3.115}$$

$$\begin{aligned} \mathcal{T}^{(s)}_{1,2} = \left| \frac{\hat{\mathbf{n}}_{2,1} \cdot \widetilde{\boldsymbol{S}}^{(s)+}_2}{\hat{\mathbf{n}}_{2,1} \cdot \widetilde{\boldsymbol{S}}^{(s)+}_1} \right| &= \left| \frac{\widetilde{n}_2 \cos \widetilde{\theta}_2}{\widetilde{n}_1 \cos \widetilde{\theta}_1} \right| \left| \widetilde{t}^{(s)}_{1,2} \right|^2 \\ &= \sqrt{\frac{\widetilde{n}_2 \cos \widetilde{\theta}_2\, \widetilde{n}^*_2 \cos \widetilde{\theta}^*_2}{\widetilde{n}_1 \cos \widetilde{\theta}_1\, \widetilde{n}^*_1 \cos \widetilde{\theta}^*_1}}\; \widetilde{t}^{(s)}_{1,2}\, \widetilde{t}^{(s)*}_{1,2}, \end{aligned} \tag{3.116}$$

$$\begin{aligned} \mathcal{T}^{(p)}_{1,2} = \left| \frac{\hat{\mathbf{n}}_{2,1} \cdot \widetilde{\boldsymbol{S}}^{(s)+}_2}{\hat{\mathbf{n}}_{2,1} \cdot \widetilde{\boldsymbol{S}}^{(s)+}_1} \right| &= \left| \frac{\widetilde{n}_2 \cos \widetilde{\theta}_2}{\widetilde{n}_1 \cos \widetilde{\theta}_1} \right| \left| \widetilde{t}^{(p)}_{1,2} \right|^2 \\ &= \sqrt{\frac{\widetilde{n}_2 \cos \widetilde{\theta}_2\, \widetilde{n}^*_2 \cos \widetilde{\theta}^*_2}{\widetilde{n}_1 \cos \widetilde{\theta}_1\, \widetilde{n}^*_1 \cos \widetilde{\theta}^*_1}}\; \widetilde{t}^{(p)}_{1,2}\, \widetilde{t}^{(p)*}_{1,2}. \end{aligned} \tag{3.117}$$

Naturally, when the media are non-absorbing the complex characteristics in the equations above will be replaced by real ones.

3.3.1.6 Principle of reversibility

Note that for generality both media are assumed to be absorbing. Also, the equations within this subsection hold true for both s and p polarizations. When the fields are real, reversing the rays is equivalent to time reversal[13] [18]. If complex notation is being used for harmonic fields, then reversing the rays is equivalent to time reversal plus complex conjugation. The complex conjugation ensures that we stay with the chosen sign in the time-exponents. Because of the fact that Fresnel's coefficients are defined so that they do not depend on time (the time factors of the numerator and denominator cancel), there is no need to show explicitly the time reversal in the equations below. Therefore, only the complex conjugation and the switched subscripts remind us that a time-reversal operation has been performed on some quantities.

---

[13] This is similar to the principle of reversibility from classical mechanics: a time reversal causes all particles to reverse their velocity vectors.

Thus, if the rays are reversed, so that the incident ray is coming from medium 2, and the transmitted ray is propagating into medium 1, using the definitions of the Fresnel coefficients 3.96 and 3.97, we can prove that

$$\widetilde{r}^{*}_{2,1} \;=\; -\widetilde{r}_{1,2}; \qquad\qquad \widetilde{t}_{2,1}\,\widetilde{n}_1\;\cos\theta_1 \;=\; \widetilde{t}_{1,2}\,\widetilde{n}_2\;\cos\theta_2. \tag{3.118}$$

We owe equations 3.118 to Stokes who used them to explain the dark central spot in Newton's rings [18]. The minus sign in the left equation 3.118 is present, because upon reflection from an optically denser (with higher refractive index) medium there is a phase change of $\pi/2$ rad. Note that one term of the left equation for which either the numerator or the denominator is a backward-propagating wave, is complex conjugate.

Moreover, if the interface between the two media does not absorb or scatter, again using the definitions of the Fresnel coefficients, we can get that

$$1 \;=\; \widetilde{t}^{*}_{2,1}\,\widetilde{t}_{1,2} \;-\; \widetilde{r}^{*}_{2,1}\,\widetilde{r}_{1,2} \;=\; \left|\frac{\widetilde{n}_2\cos\widetilde{\theta}_2}{\widetilde{n}_1\cos\widetilde{\theta}_1}\right| \left|\widetilde{t}_{1,2}\right|^2 \;+\; \left|\widetilde{r}_{1,2}\right|^2 \;=\; \mathcal{T}_{1,2} \;+\; \mathcal{R}_{1,2}, \tag{3.119}$$

which is simply an expression for the conservation of energy. Note that either the factors with switched subscripts, that is, the first subscriptis greater than the second one, or those with non-switched subscripts, must be complex conjugate.

Finally, substituting equations 3.118 into the definitions of reflectance and transmittance 3.114-3.117, we get that the latter two are symmetric[14] with respect to ray reversal:

$$\mathcal{R}_{2,1} = \mathcal{R}_{1,2}; \qquad \mathcal{T}_{2,1} = \mathcal{T}_{1,2}. \tag{3.120}$$

3.3.2 Reflection from and Transmission through a Conducting Surface

As Snell's law and the Fresnel's formulae are linear relations with respect to the refractive indices (wave impedances), they remain true for the case of absorbing media, provided that the appropriate characteristics are replaced by complex quantities.

The more general case of oblique incidence is quite complicated and has been treated in detail by Stratton [3]. The complication arises from the fact that the surfaces of constant amplitude are parallel to the interface, whereas those of constant real phase are perpendicular to the refracted rays. Therefore, except for the special case of normal incidence, these two sets of planes are not parallel to each other, and so the wave within the conducting medium is inhomogeneous [5].

The law of Snellius becomes

$$n_1 \sin\theta_1 = \widetilde{n}_2 \sin\widetilde{\theta}_2 = (n_2' + \mathrm{i}\, n_2'') \sin\widetilde{\theta}_2. \tag{3.121}$$

Here the angle of refraction $\widetilde{\theta}_2$ is complex and cannot be interpreted geometrically as the angle of refraction.

---

[14] This is only true for the case of a single interface! When more interfaces are present it can be true only for multi-layered structures that are completely symmetric with respect to their central plane.

3.3.2.1 Normal incidence on a conducting surface

As an example for the application of the complex relationships, only the simple case of normal incidence onto a conducting surface will be covered herein. The media will be considered non-magnetic, i.e., $\mu \approx 1$ is a real constant.

The Fresnel coefficients for normal incidence on a conducting surface become

$$\widetilde{r}^{(s)}_{1,2} = \frac{\mu_2 n_1 - \mu_1 \widetilde{n}_2}{\mu_2 n_1 + \mu_1 \widetilde{n}_2} = \frac{\mu_2 n_1 - \mu_1 (n'_2 + \mathrm{i}\, n''_2)}{\mu_2 n_1 + \mu_1 (n'_2 + \mathrm{i}\, n''_2)} = \widetilde{r}^{(p)}_{1,2}; \tag{3.122}$$

$$\widetilde{t}^{(s)}_{1,2} = \frac{2\mu_2 n_1}{\mu_2 n_1 + \mu_1 \widetilde{n}_2} = \frac{2\mu_2 n_1}{\mu_2 n_1 + \mu_1 (n'_2 + \mathrm{i}\, n''_2)} = \widetilde{t}^{(p)}_{1,2}, \tag{3.123}$$

or if $\mu_1 = \mu_2$

$$\widetilde{r}^{(s)}_{1,2} = \frac{n_1 - \widetilde{n}_2}{n_1 + \widetilde{n}_2} = \frac{n_1 - n'_2 - \mathrm{i}\, n''_2}{n_1 + n'_2 + \mathrm{i}\, n''_2} = \widetilde{r}^{(p)}_{1,2}; \tag{3.124}$$

$$\widetilde{t}^{(s)}_{1,2} = \frac{2n_1}{n_1 + \widetilde{n}_2} = \frac{2n_1}{n_1 + n'_2 + \mathrm{i}\, n''_2} = \widetilde{t}^{(p)}_{1,2} \tag{3.125}$$

It should be noted, that when an absorbing medium is present, all amplitude and power quantities for the refracted wave refer to a point just after and infinitely close to the respective interface. As the wave propagates further into the medium its amplitude (intensity) are decreased further due to absorption which depends on the traveled distance.

Finally, substituting the latter relations into equations 3.114–3.117 we get the reflectance from and transmittance through the interface surface of a conducting medium

$$\mathcal{R}^{(s)}_{1,2} = \left|\frac{n_1 - \widetilde{n}_2}{n_1 + \widetilde{n}_2}\right|^2 = \frac{(n_1 - n_2')^2 + n_2''^2}{(n_1 + n_2')^2 + n_2''^2} = \mathcal{R}^{(p)}_{1,2}, \tag{3.126}$$

$$\mathcal{T}^{(s)}_{1,2} = \frac{|\widetilde{n}_2|}{n_1}\left|\frac{2n_1}{n_1 + \widetilde{n}_2}\right|^2 = \frac{2n_1\sqrt{n_2'^2 + n_2''^2}}{(n_1 + n_2'^2)^2 + n_2''^2} = \mathcal{T}^{(p)}_{1,2} \tag{3.127}$$

3.3.3 Reflectance and Phase Dispersion Relations

The Fresnel reflection coefficient can be represented as

$$\widetilde{r}(\omega) = |\widetilde{r}(\omega)| \exp\left[\mathrm{i}\,\varphi_r(\omega)\right] = \sqrt{\mathcal{R}(\omega)} \exp\left[\mathrm{i}\,\varphi_r(\omega)\right], \tag{3.128}$$

or

$$\ln \widetilde{r}(\omega) = \ln|\widetilde{r}(\omega)| + \mathrm{i}\,\varphi_r(\omega) = \ln\sqrt{\mathcal{R}(\omega)} + \mathrm{i}\,\varphi_r(\omega). \tag{3.129}$$

Replacing $\varepsilon'(\omega) - 1$ and $\varepsilon''(\omega)$ in the Kramers–Kronig relations 3.32 and 3.33 with $\frac{1}{2}\ln\mathcal{R}(\omega)$ and $\varphi_r(\omega)$, respectively, gives the dispersion relations

$$\ln\mathcal{R}(\omega) = \frac{4}{\pi}\mathcal{P}\int_0^\infty \frac{\Omega\varphi_r(\Omega)}{\Omega^2 - \omega^2}\mathrm{d}\Omega, \tag{3.130}$$

$$\varphi_r(\omega) = -\frac{\omega}{\pi}\mathcal{P}\int_0^\infty \frac{\ln\mathcal{R}(\Omega)}{\Omega^2 - \omega^2}\mathrm{d}\Omega. \tag{3.131}$$

Detailed proof of these relations can be found in Wooten's book [17, Appendix G]. The latter equation is especially useful as it relates the unknown phase with the reflectance—a quantity that can be measured. As written the expression has a singularity at $\Omega = \omega$. It can be removed by adding

$$\frac{\omega}{\pi}\mathcal{P}\int_0^\infty \frac{\ln\mathcal{R}(\omega)}{\Omega^2 - \omega^2}\mathrm{d}\Omega = 0. \tag{3.132}$$

in order to get

$$\varphi_r(\omega) \;=\; \frac{\omega}{\pi}\int_0^\infty \frac{\ln\left[\mathcal{R}(\Omega)/\mathcal{R}(\omega)\right]}{\omega^2 \;-\; \Omega^2}\mathrm{d}\Omega. \tag{3.133}$$

After the singularity has been removed in this manner, the sign for principal-part integration is no longer needed. The absence of a singularity in the latter equation can be checked by using L'Hospital's rule. It is noteworthy that a systematic error in the measurement of the reflectance would not affect the phase. Furthermore, any spectral regions in which the reflectance happens to be equal to $\mathcal{R}(\omega)$ do not contribute to the phase as $\ln 1 = 0$.

Finally, comparison of equations 3.114 and 3.115 with 3.117 and 3.117, shows that the formal substitutions

$$\widetilde{r} \rightarrow \widetilde{t}, \qquad\qquad \varphi_r \rightarrow \varphi_t, \qquad\qquad \mathcal{R} \rightarrow \left|\frac{\widetilde{n}_1\cos\widetilde{\theta}_1}{\widetilde{n}_2\cos\widetilde{\theta}_2}\right|\widetilde{\mathcal{T}} \tag{3.134}$$

everywhere in this subsection will produce similar dispersion relations for the transmittance and its phase change.

3.3.4 Determination of Optical Characteristics by the Dispersion Relations

The practical application of the phase-reflectance dispersion relation 3.133 involves a reliable measurement of the reflectance in as wide spectral range from ω_{min} to ω_{max} as possible, and using reasonable extrapolations in the low-frequency from 0 to ω_{min} and high-frequency from ω_{max} to ∞ regions.

A widely used high-frequency extrapolation is

$$\mathcal{R}(\Omega) \;=\; \mathcal{R}(\omega_{max})\left(\omega_{max}/\Omega\right)^s. \tag{3.135}$$

In the spectral range from 37,000 to 100,000 cm^{-1} the reflectance is due to interband transitions and $0 \leq s \leq 4$. Above ca. 100000 cm^{-1} the reflectance is due to "free" electrons and $s = 4$.

For a dielectric the low-frequency extrapolation is constant reflectance, whereas for conductors the Hagen-Rubens approximation is used:

$$\mathcal{R}(\Omega) = 1 - A\sqrt{\Omega}. \tag{3.136}$$

If suitable values of the free electron frequency, the interband exponent s, and the constant A are chosen, the results will not be affected significantly.

Once the phase has been calculated, and the Fresnel reflection coefficient found, if the reflectance was measured under normal incidence, one can determine the complex refractive index. Using equation3.128 we can represent relation 3.122 in the form

$$\sqrt{\mathcal{R}}(\cos\varphi_r + \mathrm{i}\sin\varphi_r) = \tilde{r}_{1,2} = \frac{n_1 - n_2' + \mathrm{i}\,n_2''}{n_1 + n_2' + \mathrm{i}\,n_2''}. \tag{3.137}$$

Separating the real and imaginary part of this equation and solving the two simultaneous equations for n' and n'' leads to

$$n'(\omega) = \frac{n_1[1 - \mathcal{R}(\omega)]}{1 + \mathcal{R}(\omega) - 2\sqrt{\mathcal{R}(\omega)}\cos\varphi_r(\omega)}, \tag{3.138}$$

$$n''(\omega) = \frac{2n_1\sqrt{\mathcal{R}(\omega)}\sin\varphi_r(\omega)}{1 + \mathcal{R}(\omega) - 2\sqrt{\mathcal{R}(\omega)}\cos\varphi_r(\omega)}. \tag{3.139}$$

Finally, using the appropriate relationships, the complex permittivity and conductivity, as well as the penetration depth and absorption coefficient can be obtained.

3.4 Optics of Thin Films and

Multi-Layered Structures

This section presents some general methods for calculating the reflectance and transmittance of multi-layered, homogeneousand isotropic within the limits of each layer structures. All interfaces are presumed to be flat and parallel to each other. The simplest such structure is considered in subsection 3.4.1.

For a single layer, using the Fresnel coefficients for each interface, it is straightforward to perform an Airy summation of all partial contributions, due to the multiple reflections within the layer, to the reflected and transmitted waves. A similar treatment is still possible for two layers [32]. But as the number of layers increases this method becomes too complicated and inconvenient.

The general method for solving such problems is to assume there are forward- and backward-propagating waves within each layer except for the last medium in which only a forward-propagating wave exist. Then the boundary conditions for the tangential components of $\boldsymbol{E}$ and $\boldsymbol{H}$ are applied for each interface, $\boldsymbol{H}$ is expressed through $\boldsymbol{E}$, and by solving the simultaneous equations all amplitude coefficients can be determined in terms of the incident amplitude. These results allow one to calculate the reflection and transmission coefficients for the multi-layered structure. Actually, this is exactly how expressions for the Fresnel coefficients for a single interface are obtained. For the case of a single layer this method is presented by Heavens [30, pp. 59–62]. Abelès has shown how to express the amplitudes in successive media by the respective Fresnel coefficients [33], [30, p. 61].

Most interesting are the three recursive methods that are suitable for computerization:

- Method of Pierre Rouard [34,30]: the bottom-most (right-most) two layers are replaced by one effective one, and its effective characteristics are calculated; the same procedure is repeated recursively until a single layer remains.

- Method of Antonín Vašíček [35,30], similar to the previous one, but the order is reversed: the top-most (left-most) two layers are replaced by one effective one, and its effective characteristics are calculated; the same procedure is repeated recursively until a single layer remains.

- Matrix method [18]: every interface is represented by a transmission matrix, and every layer by a propagation matrix; then a multi-layered structure is represented by a product of such matrices. The matrix elements of the resultant matrix are related to the Fresnel coefficients for the entire multi-layered structure.

Some of these methods for solving of multi-layered optical structures will be covered in this section.

3.4.1 Reflection from and Transmission through a Single Layer

Now we are dealing with a single layer (medium 2), surrounded by two flat and parallel to each other interfaces, immersed into two (in general different) semi-infinite media 1 and 3. This is illustrated by Fig. 3.2. The three media are assumed to be isotropic and uniform. Suppose a parallel beam is incident upon such a structure from the bottom left corner of Figure 3.2. A single ray of unit amplitude represents that beam on the figure. For easy tracing of the rays an oblique incidence is assumed. Similar phenomena occur for normal incidence, too, but the rays are retracing each other and their graphical representations is more difficult.

Each time a ray hits an interface it is split into reflected and transmitted fractions. The transmitted one reaches the next interface and in its turn undergoes splitting, etc. Thus, a certain portion of the electromagnetic wave shuttles

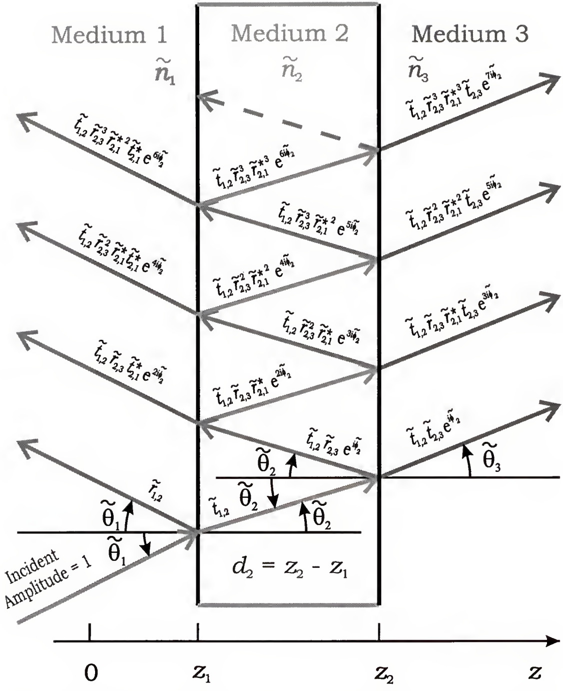
Medium 1
Medium 2
Medium 3
$\tilde{n}_1$
$\tilde{n}_2$
$\tilde{n}_3$
$\tilde{t}_{1,2}\tilde{r}^3_{2,3}\tilde{r}^{*2}_{2,1}\tilde{t}^*_{2,1}e^{6i\tilde{\phi}_2}$
$\tilde{t}_{1,2}\tilde{r}^3_{2,3}\tilde{r}^{*3}_{2,1}e^{6i\tilde{\phi}_2}$
$\tilde{t}_{1,2}\tilde{r}^3_{2,3}\tilde{r}^{*3}_{2,1}\tilde{t}_{2,3}e^{7i\tilde{\phi}_2}$
$\tilde{t}_{1,2}\tilde{r}^3_{2,3}\tilde{r}^{*2}_{2,1}e^{5i\tilde{\phi}_2}$
$\tilde{t}_{1,2}\tilde{r}^2_{2,3}\tilde{r}^{*2}_{2,1}\tilde{t}_{2,3}e^{5i\tilde{\phi}_2}$
$\tilde{t}_{1,2}\tilde{r}^2_{2,3}\tilde{r}^*_{2,1}\tilde{t}^*_{2,1}e^{4i\tilde{\phi}_2}$
$\tilde{t}_{1,2}\tilde{r}^2_{2,3}\tilde{r}^{*2}_{2,1}e^{4i\tilde{\phi}_2}$
$\tilde{t}_{1,2}\tilde{r}^2_{2,3}\tilde{r}^*_{2,1}e^{3i\tilde{\phi}_2}$
$\tilde{t}_{1,2}\tilde{r}_{2,3}\tilde{r}^*_{2,1}\tilde{t}_{2,3}e^{3i\tilde{\phi}_2}$
$\tilde{t}_{1,2}\tilde{r}_{2,3}\tilde{t}^*_{2,1}e^{2i\tilde{\phi}_2}$
$\tilde{t}_{1,2}\tilde{r}_{2,3}\tilde{r}^*_{2,1}e^{2i\tilde{\phi}_2}$
$\tilde{t}_{1,2}\tilde{r}_{2,3}e^{i\tilde{\phi}_2}$
$\tilde{t}_{1,2}\tilde{t}_{2,3}e^{i\tilde{\phi}_2}$
$\tilde{\theta}_2$
$\tilde{\theta}_3$
$\tilde{r}_{1,2}$
$\tilde{\theta}_1$
$\tilde{t}_{1,2}$
$\tilde{\theta}_2$
$\tilde{\theta}_2$
$\tilde{\theta}_1$
Incident Amplitude = 1
$d_2 = z_2 - z_1$
0
z_1
z_2
z

Figure 3.2: Multiple reflections from and transmissions through a single layer.

forth and back within the layer. Upon each consecutive reflection the intensity of the shuttling wave decreases, approaching asymptotically zero as the order of the reflection grows to infinity. The "lost" intensity is actually transmitted into the respective adjacent medium. If layer 2 is absorbing, then the intensity decreases even faster with increasing the order of reflections or transmissions, because the phase change $\widetilde{\varphi}_2$ while the wave propagates through medium 2 would then be complex.

The phases shown in Fig. 3.2 are correct just as the ray is leaving the interface after the last reflection or transmission.

3.4.1.1 Reflection and transmission coefficients

Summing the initially reflected light with the contribution of all subsequent transmissions into medium 1, Airy obtained the total reflection coefficient for layer 2, sandwiched between media 1 and 3 [18,30]:

$$\begin{aligned}\widetilde{r}_{1-3} &= \widetilde{r}_{1,2} + \widetilde{t}_{1,2}\,\widetilde{t}^{*}_{2,1}\,\widetilde{r}_{2,3}\,\mathrm{e}^{2\mathrm{i}\widetilde{\varphi}_2}[1 + \widetilde{r}^{*}_{2,1}\,\widetilde{r}_{2,3}\,\mathrm{e}^{2\mathrm{i}\widetilde{\varphi}_2} + (\widetilde{r}^{*}_{2,1}\,\widetilde{r}_{2,3}\,\mathrm{e}^{2\mathrm{i}\widetilde{\varphi}_2})^2 + \ldots] \\ &= \widetilde{r}_{1,2} + \frac{\widetilde{t}_{1,2}\,\widetilde{t}^{*}_{2,1}\,\widetilde{r}_{2,3}\,\mathrm{e}^{2\mathrm{i}\widetilde{\varphi}_2}}{1 - \widetilde{r}^{*}_{2,1}\,\widetilde{r}_{2,3}\,\mathrm{e}^{2\mathrm{i}\widetilde{\varphi}_2}} = \frac{\widetilde{r}_{1,2} + \widetilde{r}_{2,3}\,\mathrm{e}^{2\mathrm{i}\widetilde{\varphi}_2}}{1 + \widetilde{r}_{1,2}\,\widetilde{r}_{2,3}\,\mathrm{e}^{2\mathrm{i}\widetilde{\varphi}_2}}. \qquad (3.140)\end{aligned}$$

The last transformation was performed by using the reversibility conditions 3.118 and 3.119. The complex phase change for a one-way traversing of layer 2 is

$$\widetilde{\varphi}_2 = (2\pi d_2/\lambda)\widetilde{n}_2\cos\widetilde{\theta}_2. \qquad (3.141)$$

Similarly, summing the partial waves from all transmissions into medium 3, Airy obtained the total transmission coefficient for layer 2, sandwiched between media 1 and 3:

$$\begin{aligned} \widetilde{t}_{1-3} &= \widetilde{t}_{1,2}\,\widetilde{t}_{2,3}\,[1 + \widetilde{r}_{2,3}\,\widetilde{r}^{*}_{2,1}\,\mathrm{e}^{2\mathrm{i}\,\widetilde{\varphi}_2} + (\widetilde{r}_{2,3}\,\widetilde{r}^{*}_{2,1}\,\mathrm{e}^{2\mathrm{i}\,\widetilde{\varphi}_2})^2 + \ldots]\,\mathrm{e}^{\mathrm{i}\,\widetilde{\varphi}_2} \\ &= \frac{\widetilde{t}_{1,2}\,\widetilde{t}_{2,3}\,\mathrm{e}^{\mathrm{i}\,\widetilde{\varphi}_2}}{1 - \widetilde{r}^{*}_{2,1}\,\widetilde{r}_{2,3}\,\mathrm{e}^{2\mathrm{i}\,\widetilde{\varphi}_2}} = \frac{\widetilde{t}_{1,2}\,\widetilde{t}_{2,3}\,\mathrm{e}^{\mathrm{i}\,\widetilde{\varphi}_2}}{1 + \widetilde{r}_{1,2}\,\widetilde{r}_{2,3}\,\mathrm{e}^{2\mathrm{i}\,\widetilde{\varphi}_2}}. \end{aligned} \tag{3.142}$$

Equations 3.140 and 3.142 apply for both normal and oblique incidence, provided the respective Fresnel coefficients are substituted into these equations.

After using the expressions above to calculate the complex reflection and transmission coefficients, they can be represented in polar form

$$\widetilde{r}_{1-3} = |\widetilde{r}_{1-3}|\,e^{\mathrm{i}\,\varphi^{(r)}_{1-3}}; \qquad \widetilde{t}_{1-3} = \left|\widetilde{t}_{1-3}\right|\,e^{\mathrm{i}\,\varphi^{(t)}_{1-3}}, \tag{3.143}$$

which allows determination of the phase change $\varphi^{(r)}_{1-3}$ upon reflection from, or $\varphi^{(t)}_{1-3}$ upon transmission through layer 2, sandwiched between media 1 and 3.

From expressions 3.140 and 3.142 it can be seen that $\widetilde{r}_{1-3}$ and $\widetilde{t}_{1-3}$ are periodic functions of the phase change[15] φ_2 from a one-way trip across layer 2 with period π and 2π, respectively. Therefore, if the thickness of layer 2 d_2 is such that $\varphi_2 = \pi$

$$\lim_{\varphi_2 \to \pi} \widetilde{r}_{1-3} = \widetilde{r}_{1,3}; \qquad \lim_{\varphi_2 \to \pi} \mathcal{R}_{1-3} = \mathcal{R}_{1,3}, \tag{3.144}$$

$$\lim_{\varphi_2 \to \pi} \widetilde{t}_{1-3} = -\widetilde{t}_{1,3}; \qquad \lim_{\varphi_2 \to \pi} \mathcal{T}_{1-3} = \mathcal{T}_{1,3}. \tag{3.145}$$

This explains why a layer 2 with thickness $d_2 = \lambda/(2n_3)$ would be "invisible". Such layers are called half-λ, or latent layers.

---

[15] Here for simplicity the phase is taken real which is equivalent to a non-absorbing medium.

As can be expected, when the thickness of layer 2 $d_2 \rightarrow 0$, or equivalently, when the phase change for a one-way trip across layer 2 $\varphi_2 \rightarrow 0$

$$\lim_{\varphi_2 \to 0} \widetilde{r}_{1-3} = \widetilde{r}_{1,3}; \qquad \lim_{\varphi_2 \to 0} \widetilde{t}_{1-3} = \widetilde{t}_{1,3}. \tag{3.146}$$

This means that if layer 2 is removed we return to the results for a single interface between media 1 and 3.

3.4.1.2 Reflectance, transmittance and absorptance

Once we have calculated $\widetilde{r}_{1-3}$ and $\widetilde{t}_{1-3}$, the reflectance and transmittance can be obtained using expressions that are analogous to 3.114–3.117

$$\mathcal{R}_{1-3} = \left| \frac{\hat{\mathbf{n}}_{2,1} \cdot \widetilde{\boldsymbol{S}}_1^+}{\hat{\mathbf{n}}_{2,1} \cdot \widetilde{\boldsymbol{S}}_1^-} \right| = \left| \widetilde{r}_{1-3} \right|^2 = \widetilde{r}_{1-3} \, \widetilde{r}^*_{1-3} \tag{3.147}$$

$$= \frac{\left|\widetilde{r}_{1,2}\right|^2 + \left|\widetilde{r}_{2,3}\right|^2 + 2\mathrm{Re}\left\{\widetilde{r}_{1,2} \, \widetilde{r}_{2,3} \, \mathrm{e}^{2\mathrm{i}\,\widetilde{\varphi}_2}\right\}}{1 + \left|\widetilde{r}_{1,2} \, \widetilde{r}_{2,3}\right|^2 + 2\mathrm{Re}\left\{\widetilde{r}_{1,2} \, \widetilde{r}_{2,3} \, \mathrm{e}^{2\mathrm{i}\,\widetilde{\varphi}_2}\right\}}, \tag{3.148}$$

$$\mathcal{T}_{1-3} = \left| \frac{\hat{\mathbf{n}}_{2,1} \cdot \widetilde{\boldsymbol{S}}_3^+}{\hat{\mathbf{n}}_{2,1} \cdot \widetilde{\boldsymbol{S}}_1^+} \right| = \left| \frac{\widetilde{n}_3 \cos \widetilde{\theta}_3}{\widetilde{n}_1 \cos \widetilde{\theta}_1} \right| \left| \widetilde{t}_{1-3} \right|^2 \tag{3.149}$$

$$= \sqrt{\frac{\widetilde{n}_3 \cos \widetilde{\theta}_3}{\widetilde{n}_1 \cos \widetilde{\theta}_1} \frac{\widetilde{n}^*_3 \cos \widetilde{\theta}^*_3}{\widetilde{n}^*_1 \cos \widetilde{\theta}^*_1}} \; \widetilde{t}_{1-3} \, \widetilde{t}^*_{1-3} \tag{3.150}$$

$$= \left| \frac{\widetilde{n}_3 \cos \widetilde{\theta}_3}{\widetilde{n}_1 \cos \widetilde{\theta}_1} \right| \frac{\left|\widetilde{t}_{1,2} \, \widetilde{t}_{2,3}\right|^2 \mathrm{e}^{2\varphi''_2}}{1 + \left|\widetilde{r}_{1,2} \, \widetilde{r}_{2,3}\right|^2 + 2\mathrm{Re}\left\{\widetilde{r}_{1,2} \, \widetilde{r}_{2,3} \, \mathrm{e}^{2\mathrm{i}\,\widetilde{\varphi}_2}\right\}}. \tag{3.151}$$

The latter two expressions replace the incorrect ones given by Heavens [30, equations 4(48) and 4(49)].

It should be reminded that if medium 1 is absorbing then $\mathcal{R}_{1-3}$ is a strictly correct expression for the reflectance only in the infinitely thin layer of medium 1 adjacent to the interface 1-2. As the wave propagates further back into medium 1 it is damped continuously due to absorption in medium 1.

Similarly, if medium 3 is absorbing then $\mathcal{T}_{1-3}$ is a strictly correct expression for the transmittance only in the infinitely thin layer of medium 3 adjacent to the interface 2-3. As the wave propagates further forward into medium 3 it is damped continuously due to absorption in medium 3.

Finally, the conservation of energy gives the absorption within layer 2:

$$\mathcal{A}_2 = 1 - \mathcal{R}_{1-3} - \mathcal{T}_{1-3} \tag{3.152}$$

Let us introduce the polar representations of the Fresnel coefficients

$$\widetilde{r}_{1,2} = r_{1,2}\, e^{i\varphi_{1,2}}; \qquad \widetilde{r}_{2,3} = r_{2,3}\, e^{i\varphi_{2,3}}, \tag{3.153}$$

$$\widetilde{t}_{1,2} = t_{1,2}\, e^{i\phi_{1,2}}; \qquad \widetilde{t}_{2,3} = t_{2,3}\, e^{i\phi_{2,3}}, \tag{3.154}$$

where $$r_{j,j+1} = \left|\widetilde{r}_{j,j+1}\right|; \qquad t_{j,j+1} = \left|\widetilde{t}_{j,j+1}\right|. \tag{3.155}$$

From the left-side reversibility relation 3.118 it follows that

$$\varphi_{j+1,j} = -\varphi_{j,j+1} \pm \pi, \text{ rad} \qquad \phi_{j+1,j} = -\phi_{j,j+1} \pm \pi, \text{ rad} \tag{3.156}$$

The phase changes $\varphi_{j,j+1}$ and $\phi_{j,j+1}$ are real provided there are no losses upon reflection from and transmission through the interface between media j and $j+1$, respectively. Here $j = 1$ or 2.

Using equations 3.153–3.155, the reflectance 3.148 and transmittance 3.151 can be reduced to

$$\mathcal{R}_{1-3} \;=\; \frac{r_{1,2}^2 \,+\, r_{2,3}^2 \,+\, 2r_{1,2}\, r_{2,3}\, \mathrm{Re}\left\{\mathrm{e}^{\mathrm{i}\,(2\widetilde{\varphi}_2 \,+\, \varphi_{1,2} \,+\, \varphi_{2,3})}\right\}}{1 \,+\, (r_{1,2}\, r_{2,3})^2 \,+\, 2r_{2,1}\, r_{2,3}\, \mathrm{Re}\left\{\mathrm{e}^{\mathrm{i}\,(2\widetilde{\varphi}_2 \,+\, \varphi_{2,1} \,+\, \varphi_{2,3})}\right\}}, \qquad (3.157)$$

$$\mathcal{T}_{1-3} \;=\; \left|\frac{\widetilde{n}_3 \cos\widetilde{\theta}_3}{\widetilde{n}_1 \cos\widetilde{\theta}_1}\right| \frac{(t_{1,2}\, t_{2,3})^2\, \mathrm{e}^{2\varphi_2''}}{1 \,+\, (r_{1,2}\, r_{2,3})^2 \,+\, 2r_{1,2}\, r_{2,3}\, \mathrm{Re}\left\{\mathrm{e}^{\mathrm{i}\,(2\widetilde{\varphi}_2 \,+\, \varphi_{1,2} \,+\, \varphi_{2,3})}\right\}}. \qquad (3.158)$$

The latter two equations can be expressed in terms of the single interface reflectance and transmittance

$$\mathcal{R}_{1-3} \;=\; \frac{\mathcal{R}_{1,2} \,+\, \mathcal{R}_{2,3} \,+\, 2\sqrt{\mathcal{R}_{1,2}\, \mathcal{R}_{2,3}}\, \mathrm{Re}\left\{\mathrm{e}^{\mathrm{i}\,(2\widetilde{\varphi}_2 \,+\, \varphi_{1,2} \,+\, \varphi_{2,3})}\right\}}{1 \,+\, \mathcal{R}_{1,2}\, \mathcal{R}_{2,3} \,+\, 2\sqrt{\mathcal{R}_{1,2}\, \mathcal{R}_{2,3}}\, \mathrm{Re}\left\{\mathrm{e}^{\mathrm{i}\,(2\widetilde{\varphi}_2 \,+\, \varphi_{1,2} \,+\, \varphi_{2,3})}\right\}}, \qquad (3.159)$$

$$\mathcal{T}_{1-3} \;=\; \frac{\mathcal{T}_{1,2}\, \mathcal{T}_{2,3} \mathrm{e}^{2\varphi_2''}}{1 \,+\, \mathcal{R}_{1,2}\, \mathcal{R}_{2,3} \,+\, 2\sqrt{\mathcal{R}_{1,2}\, \mathcal{R}_{2,3}}\, \mathrm{Re}\left\{\mathrm{e}^{\mathrm{i}\,(2\widetilde{\varphi}_2 \,+\, \varphi_{1,2} \,+\, \varphi_{2,3})}\right\}}. \qquad (3.160)$$

The imaginary part of the complex phase $\widetilde{\varphi}_2$ accounts for absorption within layer 2. In equations 3.157–3.160 we can take the real-part operations:

$$\mathrm{Re}\left\{\mathrm{e}^{\mathrm{i}\,(2\widetilde{\varphi}_2 \,+\, \varphi_{1,2} \,+\, \varphi_{2,3})}\right\} \;=\; \cos\left(2\varphi_2' \,+\, \varphi_{1,2} \,+\, \varphi_{2,3}\right) \mathrm{e}^{-2\varphi_2''} \qquad (3.161)$$

If medium 2 is only very weakly absorbing, ignoring the imaginary part of the phase, further reduces equations 3.159 and 3.160 to

$$\mathcal{R}_{1-3} \;=\; \frac{\mathcal{R}_{1,2} \,+\, \mathcal{R}_{2,3} \,+\, 2\sqrt{\mathcal{R}_{1,2}\, \mathcal{R}_{2,3}}\, \cos\left(2\varphi_2' \,+\, \varphi_{1,2} \,+\, \varphi_{2,3}\right)}{1 \,+\, \mathcal{R}_{1,2}\, \mathcal{R}_{2,3} \,+\, 2\sqrt{\mathcal{R}_{1,2}\, \mathcal{R}_{2,3}}\, \cos\left(2\varphi_2' \,+\, \varphi_{1,2} \,+\, \varphi_{2,3}\right)}, \qquad (3.162)$$

$$\mathcal{T}_{1-3} \;=\; \frac{\mathcal{T}_{1,2}\, \mathcal{T}_{2,3}}{1 \,+\, \mathcal{R}_{1,2}\, \mathcal{R}_{2,3} \,+\, 2\sqrt{\mathcal{R}_{2,1}\, \mathcal{R}_{2,3}}\, \cos\left(2\varphi_2' \,+\, \varphi_{1,2} \,+\, \varphi_{2,3}\right)}. \qquad (3.163)$$

Often the ambient media 1 and 3 are the same (most often vacuum, or air). These expressions are applicable to two types of such cases:

- the realistic, completely symmetric case. Then the symmetry relations $\mathcal{R}_{2,3} = \mathcal{R}_{2,1}$, and $\mathcal{T}_{2,3} = \mathcal{T}_{2,1}$ hold true;
- the imaginary asymmetric case: regardless of the fact that the single layer is surrounded symmetrically by media 1 and 3, i.e., here we assume that the two interfaces are different though the two ambient media are the equivalent.

The latter case, even though unrealistic, is interesting as a starting point for treating of asymmetric Fabry-Perot resonators.

3.4.1.3 Fabry-Perot resonance

Here the Fabry-Perot resonance is described briefly. The basic theory of Fabry-Perot resonators is covered in more detail in section 3.5.

From Airy's formulas it is clear that the coefficients $\widetilde{r}_{1-3}$ and $\widetilde{t}_{1-3}$, and hence the reflectance and transmittance as well, are periodic functions of the phase φ_2 for non-absorbing media, and damped oscillating functions of the phase for absorbing media.

For normal incidence, the phase depends linearly on the layer thickness and the wave number $\breve{\nu} = 1/\lambda$. If either of them is varied, the transmittance and reflectance will manifest the periodical fringes characteristic for the Fabry-Perot resonance.

Let us imagine that such a structure is illuminated with a continuous spectrum within a range $\Delta\breve{\nu}$, e.g., the polychromatic radiation from the source of a Fourier-transform interferometer. Due to the non-monochromatic character of the source, there will be a corresponding spread $\Delta\phi_2$ of the phase change ϕ_2 that occurs while the wave travels within medium 2. When the corresponding phase range is $\Delta\phi_2 = \pi$, or the thickness of medium 2 is $d_2 = (2n_2\Delta\breve{\nu})^{-1}$ there is a complete overlap of the fringes from two adjacent orders that correspond to the two ends of the spectral range. Above that threshold the reflectance and transmittance will no longer have periodic character. Therefore, the Fabry-Perot resonance will be observable provided layer 2 is thin enough

$$d_2 < (2n_2\Delta\breve{\nu})^{-1} \tag{3.164}$$

which is the condition for incomplete overlap of the fringes from two adjacent orders for the two ends of the covered spectral range. Naturally, the stronger the inequality, the better the observability of the resonance will be.

When the opposite inequality holds true

$$d_2 > (2n_2\Delta\breve{\nu})^{-1}, \tag{3.165}$$

layer 2 is thick and the fringes are lost [18, p. 98].

If one needs to calculate the reflectance from or transmittance through a thick layer, elimination of the fringes by spectral averaging of the data must be performed.

3.4.1.4 Single absorbing layer, normal incidence.

Here the incident beam is normal to the interface. We are interested in the reflection from and the transmission through an absorbing layer sandwiched between two absorbing semi-infinite media. Applying equation 3.124 and 3.125 for the two interfaces, we have

$$\widetilde{r}_{1,2} = \frac{\widetilde{n}_1 - \widetilde{n}_2}{\widetilde{n}_1 + \widetilde{n}_2}; \qquad \widetilde{t}_{1,2} = \frac{2\widetilde{n}_1}{\widetilde{n}_1 + \widetilde{n}_2}, \tag{3.166}$$

$$\widetilde{r}_{2,3} = \frac{\widetilde{n}_2 - \widetilde{n}_3}{\widetilde{n}_2 + \widetilde{n}_3}; \qquad \widetilde{t}_{2,3} = \frac{2\widetilde{n}_2}{\widetilde{n}_2 + \widetilde{n}_3}. \tag{3.167}$$

Substituting these four equations into the Airy sums 3.140 and 3.142

$$\widetilde{r}_{1-3} = \frac{(\widetilde{n}_1 - \widetilde{n}_2)(\widetilde{n}_2 + \widetilde{n}_3)\mathrm{e}^{-\mathrm{i}\widetilde{\varphi}_2} + (\widetilde{n}_1 + \widetilde{n}_2)(\widetilde{n}_2 - \widetilde{n}_3)\mathrm{e}^{\mathrm{i}\widetilde{\varphi}_2}}{(\widetilde{n}_1 + \widetilde{n}_2)(\widetilde{n}_2 + \widetilde{n}_3)\mathrm{e}^{-\mathrm{i}\widetilde{\varphi}_2} + (\widetilde{n}_1 - \widetilde{n}_2)(\widetilde{n}_2 - \widetilde{n}_3)\mathrm{e}^{+\mathrm{i}\widetilde{\varphi}_2}}, \tag{3.168}$$

$$\widetilde{t}_{1-3} = \frac{4\widetilde{n}_1\widetilde{n}_2}{(\widetilde{n}_1 + \widetilde{n}_2)(\widetilde{n}_2 + \widetilde{n}_3)\mathrm{e}^{-\mathrm{i}\widetilde{\varphi}_2} + (\widetilde{n}_1 - \widetilde{n}_2)(\widetilde{n}_2 - \widetilde{n}_3)\mathrm{e}^{+\mathrm{i}\widetilde{\varphi}_2}}. \tag{3.169}$$

Finally, substituting the latter two equations into expressions 3.147 and 3.150, we get the reflectance and transmittance for the special case of normal incidence

$$\mathcal{R}_{1-3} = \frac{\mathcal{N}_a + \mathcal{N}_b}{\mathcal{N}_c + \mathcal{N}_d}; \qquad \mathcal{T}_{1-3} = \frac{16\,|\widetilde{n}_1\widetilde{n}_3|\,|\widetilde{n}_2|^2}{\mathcal{N}_c + \mathcal{N}_d}, \tag{3.170}$$

where

$$\mathcal{N}_a = |(\widetilde{n}_1 - \widetilde{n}_2)(\widetilde{n}_2 + \widetilde{n}_3)|^2 + |(\widetilde{n}_1 + \widetilde{n}_2)(\widetilde{n}_2 - \widetilde{n}_3)|^2, \tag{3.171}$$

$$\mathcal{N}_b = 2\mathrm{Re}\left\{(\widetilde{n}_1^* - \widetilde{n}_2^*)(\widetilde{n}_2^* + \widetilde{n}_3^*)(\widetilde{n}_1 + \widetilde{n}_2)(\widetilde{n}_2 - \widetilde{n}_3)\mathrm{e}^{2\mathrm{i}\widetilde{\varphi}_2}\right\}, \tag{3.172}$$

$$\mathcal{N}_c = |(\widetilde{n}_1 + \widetilde{n}_2)(\widetilde{n}_2 + \widetilde{n}_3)|^2 + |(\widetilde{n}_1 - \widetilde{n}_2)(\widetilde{n}_2 - \widetilde{n}_3)|^2, \tag{3.173}$$

$$\mathcal{N}_d = 2\mathrm{Re}\left\{(\widetilde{n}_1^* + \widetilde{n}_2^*)(\widetilde{n}_2^* + \widetilde{n}_3^*)(\widetilde{n}_1 - \widetilde{n}_2)(\widetilde{n}_2 - \widetilde{n}_3)\mathrm{e}^{2\mathrm{i}\widetilde{\varphi}_2}\right\}. \tag{3.174}$$

Equations 3.170 with the partial expressions (macros?) 3.171-3.172 must replace the wrong ones given by Heavens [30, eqs. 4(54) and 4(55)].

3.4.2 Reflection and Transmission by Two Layers

This case involves a stack of two layers bound by three interfaces, surrounded by two, possibly different, media. It will be used as an illustration for two of the recursive methods. Such a structure is presented in Fig. 3.3. Only the primary reflection and transmission for each layer are shown. (Alternately, this could be an illustration for the direct application of the boundary conditions, with a forward- and a backward-propagating wave in each medium.)

From equations 3.140 and 3.142 we get

$$\widetilde{r}_{1-3} = \frac{\widetilde{r}_{1,2} + \widetilde{r}_{2,3}\,\mathrm{e}^{2\mathrm{i}\widetilde{\varphi}_2}}{1 + \widetilde{r}_{1,2}\,\widetilde{r}_{2,3}\,\mathrm{e}^{2\mathrm{i}\widetilde{\varphi}_2}}; \qquad \widetilde{t}_{1-3} = \frac{\widetilde{t}_{1,2}\,\widetilde{t}_{2,3}\,\mathrm{e}^{\mathrm{i}\widetilde{\varphi}_2}}{1 + \widetilde{r}_{1,2}\,\widetilde{r}_{2,3}\,\mathrm{e}^{2\mathrm{i}\widetilde{\varphi}_2}}, \tag{3.175}$$

$$\widetilde{r}_{2-4} = \frac{\widetilde{r}_{2,3} + \widetilde{r}_{3,4}\,\mathrm{e}^{2\mathrm{i}\widetilde{\varphi}_3}}{1 + \widetilde{r}_{2,3}\,\widetilde{r}_{3,4}\,\mathrm{e}^{2\mathrm{i}\widetilde{\varphi}_3}}; \qquad \widetilde{t}_{2-4} = \frac{\widetilde{t}_{2,3}\,\widetilde{t}_{3,4}\,\mathrm{e}^{\mathrm{i}\widetilde{\varphi}_3}}{1 + \widetilde{r}_{2,3}\,\widetilde{r}_{3,4}\,\mathrm{e}^{2\mathrm{i}\widetilde{\varphi}_3}}. \tag{3.176}$$

Naturally, the complex phase change for a one-way traversing of layer j is

$$\widetilde{\varphi}_j = (2\pi d_j/\lambda)\widetilde{n}_j \cos\widetilde{\theta}_j; \quad j = 2, 3. \tag{3.177}$$

The method of Pierre Rouard [34,30] prescribes that $\widetilde{r}_{2,3}$ and $\widetilde{t}_{2,3}$ in equations 3.175 be replaced by the expressions for $\widetilde{r}_{2-4}$ and $\widetilde{t}_{2-4}$ given by equations 3.176, in order to get $\widetilde{r}_{1-4}$ and $\widetilde{t}_{1-4}$, respectively.

Vice versa, the method of Antonín Vašíček (pronounced "Vashichek") [35,30] prescribes that $\widetilde{r}_{2,3}$ and $\widetilde{t}_{2,3}$ in equations 3.176 be replaced by the expressions for $\widetilde{r}_{1-3}$ and $\widetilde{t}_{1-3}$ given by equations 3.175, in order to get $\widetilde{r}_{1-4}$ and $\widetilde{t}_{1-4}$, respectively.

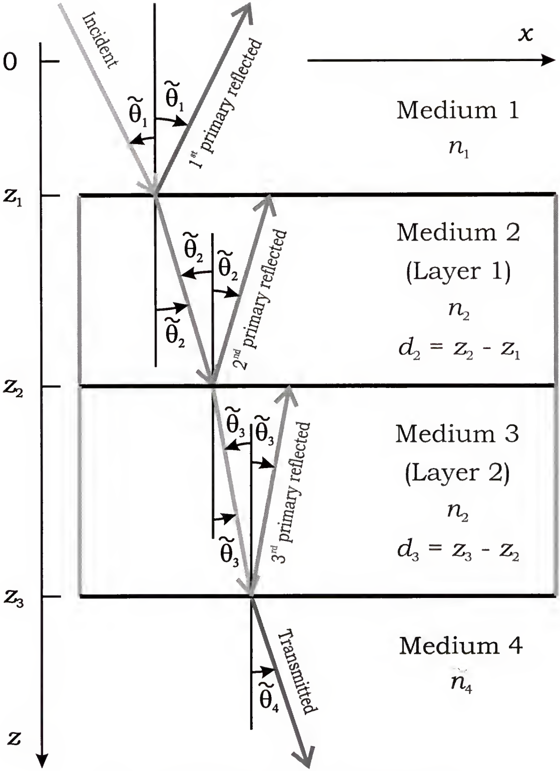

Figure 3.3: Reflection and transmission by two layers.

In both cases the results are the same:

$$\widetilde{r}_{1-4} = \frac{\widetilde{r}_{1,2} + \widetilde{r}_{2,3}\,\mathrm{e}^{2\mathrm{i}\,\widetilde{\varphi}_2} + \widetilde{r}_{3,4}\,\mathrm{e}^{2\mathrm{i}\,(\widetilde{\varphi}_2 + \widetilde{\varphi}_3)} + \widetilde{r}_{1,2}\,\widetilde{r}_{2,3}\,\widetilde{r}_{3,4}\,\mathrm{e}^{2\mathrm{i}\,\widetilde{\varphi}_3}}{1 + \widetilde{r}_{1,2}\,\widetilde{r}_{2,3}\,\mathrm{e}^{2\mathrm{i}\,\widetilde{\varphi}_2} + \widetilde{r}_{1,2}\,\widetilde{r}_{3,4}\,\mathrm{e}^{2\mathrm{i}\,(\widetilde{\varphi}_2 + \widetilde{\varphi}_3)} + \widetilde{r}_{2,3}\,\widetilde{r}_{3,4}\,\mathrm{e}^{2\mathrm{i}\,\widetilde{\varphi}_3}}, \qquad (3.178)$$

$$\widetilde{t}_{1-4} = \frac{\widetilde{t}_{1,2}\,\widetilde{t}_{2,3}\,\widetilde{t}_{3,4}\,\mathrm{e}^{\mathrm{i}\,(\widetilde{\varphi}_2 + \widetilde{\varphi}_3)}}{1 + \widetilde{r}_{1,2}\,\widetilde{r}_{2,3}\,\mathrm{e}^{2\mathrm{i}\,\widetilde{\varphi}_2} + \widetilde{r}_{1,2}\,\widetilde{r}_{3,4}\,\mathrm{e}^{2\mathrm{i}\,(\widetilde{\varphi}_2 + \widetilde{\varphi}_3)} + \widetilde{r}_{2,3}\,\widetilde{r}_{3,4}\,\mathrm{e}^{2\mathrm{i}\,\widetilde{\varphi}_3}}. \qquad (3.179)$$

In order to do practical calculations, it is convenient to represent all complex quantities in polar form, perform all the operations, and in the end, separate the real and imaginary parts.

For non-absorbing media, all quantities in the equations above, except for the exponential factors, become real.

3.4.3 Reflection and Transmission by Many Layers

More than two layers impose the use of computers, even though the latter are useful for the simpler cases, too. The equations get more complicated, but since they are solved iteratively it becomes a pointless exercise to write them in full even if the sheet were wide enough.

The methods of Pierre Rouard [34,30], and Antonín Vašíček [35,30], illustrated through a simple example in the previous subsection, can be easily generalized for an arbitrary number of layers.

The general method using the boundary conditions also works, especially if the amplitudes are expressed in terms of Fresnel coefficients following Abelès [33]. This procedure is especially convenient for absorbing media [30].

Another method that is suitable for multi-layered structures is the matrix method. A brief presentation of the matrix method follows.

3.4.4 Reflection and Transmission Using Matrix Method

Let the normal to the interface is in the $\hat{\mathbf{z}} = \hat{\mathbf{n}}_{1,2}$ direction. Since medium j (for any j) is uniform in the $\hat{\mathbf{x}}$–$\hat{\mathbf{y}}$ plane, if the plane of incidence is xOz, the electric field will be of the form [18]:

$$\widetilde{\boldsymbol{E}}_j^{(s)}(x,y,z) \;=\; \widetilde{E}_j^{(s)}(z)\,\mathrm{e}^{\mathrm{i}\,(\widetilde{k}_{jx}x\,-\,\omega t)}\,\hat{\mathbf{y}}, \tag{3.180}$$

$$\widetilde{\boldsymbol{E}}_j^{(p)}(x,y,z) \;=\; \widetilde{E}_j^{(p)}(z)\,\mathrm{e}^{\mathrm{i}\,(\widetilde{k}_{jx}x\,-\,\omega t)}\,(\cos\widetilde{\theta}_j\,\hat{\mathbf{x}} \;-\; \sin\widetilde{\theta}_j\,\hat{\mathbf{z}}). \tag{3.181}$$

Furthermore, in medium j (for any j) of the multi-layered optical structure, the electrical amplitude of an electromagnetic wave for both s- and p-polarizations can be decomposed into forward- and backward-propagating waves:

$$\widetilde{E}_j(z) \;=\; \widetilde{E}_j^{(+)}(z) \;+\; \widetilde{E}_j^{(-)}(z) \;=\; \widetilde{A}_{Fj}\mathrm{e}^{\mathrm{i}\widetilde{k}_{jz}z} \;+\; \widetilde{A}_{Bj}\mathrm{e}^{-\mathrm{i}\widetilde{k}_{jz}z}. \tag{3.182}$$

Even though the amplitude on the left side is a continuous function of z, its components on the right side can be discontinuous at each interface.

The relationship between the wave-vector components and the angle of incidence or refraction is

$$\widetilde{k}_{jx} \;=\; (\omega/c)\widetilde{n}_j\sin\widetilde{\theta}_j; \qquad\qquad \widetilde{k}_{jz} \;=\; (\omega/c)\widetilde{n}_j\cos\widetilde{\theta}_j. \tag{3.183}$$

Let us assume that the interface between medium j and medium $j+1$ is positioned at z_j, and hence the thickness of layer j is $d_j = z_{j+1} - z_j$. We can introduce the following abbreviations

$$\widetilde{A}_j = \widetilde{E}_j^{(+)}(z_j^-); \qquad \widetilde{B}_j = \widetilde{E}_j^{(-)}(z_j^-), \tag{3.184}$$

$$\widetilde{A}^{\dagger}_{j+1} = \widetilde{E}^{(+)}_{j+1}(z_j^+); \qquad \widetilde{B}^{\dagger}_{j+1} = \widetilde{E}^{(-)}_{j+1}(z_j^+). \tag{3.185}$$

where z_j^- (z_j^+) is the position of a plane just[16] before (after) the interface between medium j and medium $j+1$, respectively. Each A or B describes a forward- or backward-propagating wave, respectively.

The linear relationships resulting from applying the boundary conditions at interface j can be expressed conveniently with a matrix equation

$$\begin{pmatrix} \widetilde{A}_j \\ \\ \widetilde{B}_j \end{pmatrix} = \widetilde{\mathsf{D}}_j^{-1}\widetilde{\mathsf{D}}_{j+1} \begin{pmatrix} \widetilde{A}^{\dagger}_{j+1} \\ \\ \widetilde{B}^{\dagger}_{j+1} \end{pmatrix} = \widetilde{\mathsf{D}}_{j,j+1} \begin{pmatrix} \widetilde{A}^{\dagger}_{j+1} \\ \\ \widetilde{B}^{\dagger}_{j+1} \end{pmatrix}, \tag{3.186}$$

where the dynamical matrix of medium j, given for s- and p-polarization, is

$$\widetilde{\mathsf{D}}_j^{(s)} = \begin{pmatrix} 1 & 1 \\ \\ \widetilde{\mathcal{Z}}_j \cos\widetilde{\theta}_j & -\widetilde{\mathcal{Z}}_j \cos\widetilde{\theta}_j \end{pmatrix}; \quad \widetilde{\mathsf{D}}_j^{(p)} = \begin{pmatrix} \cos\widetilde{\theta}_j & \cos\widetilde{\theta}_j \\ \\ \widetilde{\mathcal{Z}}_j & -\widetilde{\mathcal{Z}}_j \end{pmatrix}, \tag{3.187}$$

$\widetilde{\mathsf{D}}_j^{-1}$ is the inverse of the dynamical matrix $\widetilde{\mathsf{D}}_j$, and $\widetilde{\mathsf{D}}_{j,j+1} = \widetilde{\mathsf{D}}_j^{-1}\widetilde{\mathsf{D}}_{j+1}$ is the transmission matrix for the interface between media j and $j+1$, which describes both the reflection and transmission of that interface:

---

[16] Infinitesimally close to the interface.

$$\widetilde{\mathsf{D}}^{(s)}_{j,j+1} = \frac{1}{2}\begin{pmatrix} 1 + \dfrac{\widetilde{\mathcal{Z}}_{j+1}\,\cos\widetilde{\theta}_{j+1}}{\widetilde{\mathcal{Z}}_j\,\cos\widetilde{\theta}_j} & 1 - \dfrac{\widetilde{\mathcal{Z}}_{j+1}\,\cos\widetilde{\theta}_{j+1}}{\widetilde{\mathcal{Z}}_j\,\cos\widetilde{\theta}_j} \\ \\ 1 - \dfrac{\widetilde{\mathcal{Z}}_{j+1}\,\cos\widetilde{\theta}_{j+1}}{\widetilde{\mathcal{Z}}_j\,\cos\widetilde{\theta}_j} & 1 + \dfrac{\widetilde{\mathcal{Z}}_{j+1}\,\cos\widetilde{\theta}_{j+1}}{\widetilde{\mathcal{Z}}_j\,\cos\widetilde{\theta}_j} \end{pmatrix}, \tag{3.188}$$

$$\widetilde{\mathsf{D}}^{(p)}_{j,j+1} = \frac{1}{2}\begin{pmatrix} \dfrac{\cos\widetilde{\theta}_{j+1}}{\cos\widetilde{\theta}_j} + \dfrac{\widetilde{\mathcal{Z}}_{j+1}}{\widetilde{\mathcal{Z}}_j} & \dfrac{\cos\widetilde{\theta}_{j+1}}{\cos\widetilde{\theta}_j} - \dfrac{\widetilde{\mathcal{Z}}_{j+1}}{\widetilde{\mathcal{Z}}_j} \\ \\ \dfrac{\cos\widetilde{\theta}_{j+1}}{\cos\widetilde{\theta}_j} - \dfrac{\widetilde{\mathcal{Z}}_{j+1}}{\widetilde{\mathcal{Z}}_j} & \dfrac{\cos\widetilde{\theta}_{j+1}}{\cos\widetilde{\theta}_j} + \dfrac{\widetilde{\mathcal{Z}}_{j+1}}{\widetilde{\mathcal{Z}}_j} \end{pmatrix}. \tag{3.189}$$

If we were to reduce the latter matrix to the form given by Yeh, a common factor of $\cos\widetilde{\theta}_{j+1}/\cos\widetilde{\theta}_j$ would have to appear in front of the matrix which is missing from equation 5.1-11 in [18]. Consequently, the expressions for the p-waves in equations 5.1-13 and 5.1-14 also seem to be wrong.

For both polarizations, the transmission matrix can be represented through the Fresnel coefficients in the form [18]

$$\widetilde{\mathsf{D}}_{j,j+1} = \frac{1}{\widetilde{t}_{j,j+1}}\begin{pmatrix} 1 & \widetilde{r}_{j,j+1} \\ \\ 1 & \widetilde{r}_{j,j+1} \end{pmatrix}. \tag{3.190}$$

The effect of layer j on a wave that is crossing it, is accounted for by the propagation matrix $\widetilde{\mathsf{P}}_j$

$$\begin{pmatrix} \widetilde{A}^{\dagger}_j \\ \\ \widetilde{B}^{\dagger}_j \end{pmatrix} = \widetilde{\mathsf{P}}_j \begin{pmatrix} \widetilde{A}_j \\ \\ \widetilde{B}_j \end{pmatrix} = \begin{pmatrix} \mathrm{e}^{\mathrm{i}\,\widetilde{\varphi}_j} & 0 \\ \\ 0 & \mathrm{e}^{\mathrm{i}\,\widetilde{\varphi}_j} \end{pmatrix}\begin{pmatrix} \widetilde{A}_j \\ \\ \widetilde{B}_j \end{pmatrix}. \tag{3.191}$$

By means of the introduced matrices, layered optical structures with an arbitrary number of layers can be considered. Thus, for a system consisting of N layers surrounded by media 1 and $N+2$ (the latter one could also be a very thick substrate or a completely opaque, that is strongly absorbing, substrate) we can write

$$\begin{aligned}\begin{pmatrix}\widetilde{A}_l\\ \\ \widetilde{B}_l\end{pmatrix} &= \widetilde{\mathsf{M}}^{(l)}\begin{pmatrix}\widetilde{A}^{\dagger}_{N+2}\\ \\ \widetilde{B}^{\dagger}_{N+2}\end{pmatrix}\\ &= \begin{pmatrix}\widetilde{\mathsf{M}}^{(l)}_{1,1} & \widetilde{\mathsf{M}}^{(l)}_{1,2}\\ \\ \widetilde{\mathsf{M}}^{(l)}_{2,1} & \widetilde{\mathsf{M}}^{(l)}_{2,2}\end{pmatrix}\begin{pmatrix}\widetilde{A}^{\dagger}_{N+2}\\ \\ \widetilde{B}^{\dagger}_{N+2}\end{pmatrix}, \quad l = 1, 2, 3, \ldots, N+1\end{aligned} \tag{3.192}$$

where the transfer matrix of the portion of the system from layer l to medium $N+2$ is

$$\widetilde{\mathsf{M}}^{(l)} = \prod_{j=l}^{N}\left[\widetilde{\mathsf{D}}_{j,j+1}\widetilde{\mathsf{P}}_{j+1}\right]\widetilde{\mathsf{D}}_{N+1,N+2} = \prod_{j=l}^{N}\left[\widetilde{\mathsf{D}}_{j}^{-1}\widetilde{\mathsf{D}}_{j+1}\widetilde{\mathsf{P}}_{j+1}\right]\widetilde{\mathsf{D}}_{N+1}^{-1}\widetilde{\mathsf{D}}_{N+2}. \tag{3.193}$$

Note that in the expression above, the propagation matrices $\widetilde{\mathsf{P}}_1$ and $\widetilde{\mathsf{P}}_{N+2}$ for the two ambient media are not included.

Once the transfer matrix for the whole system has been calculated, it is easy to find the reflection and transmission coefficients

$$\widetilde{r}_{1\to(N+2)} = \frac{\widetilde{B}_1}{\widetilde{A}_1} = \frac{\widetilde{\mathsf{M}}^{(1)}_{2,1}}{\widetilde{\mathsf{M}}^{(1)}_{1,1}}; \qquad \widetilde{t}_{1\to(N+2)} = \frac{\widetilde{A}_{N+2}}{\widetilde{A}_1} = \frac{1}{\widetilde{\mathsf{M}}^{(1)}_{1,1}}. \tag{3.194}$$

Finally, the reflectance and transmittance are

$$\mathcal{R}_{1\to(N+2)} = \left|\frac{\widetilde{\mathsf{M}}^{(1)}_{2,1}}{\widetilde{\mathsf{M}}^{(1)}_{1,1}}\right|^2 ; \qquad \mathcal{T}_{1\to(N+2)} = \left|\frac{\widetilde{n}_{N+2}\cos\widetilde{\theta}_{N+2}}{\widetilde{n}_1\cos\widetilde{\theta}_1}\right| \frac{1}{\left|\widetilde{\mathsf{M}}^{(1)}_{1,1}\right|^2}. \tag{3.195}$$

3.5 Theoretical Background of Flat Fabry-Perot Resonators

A simple plane Fabry-Perot resonator consists of two parallel flat mirrors separated by a gap, with their reflecting surfaces facing each other. However, it can be shown that any multi-layered resonator structure can be reduced to an effective simple resonator with two interface surfaces (see Chapter 8).

Thus, the transmittance through such a multi-layered resonator structure is given by equation 3.163. Straightforward algebraic transformations[17] lead to the following expression for the transmittance of the Fabry-Perot resonator [36]. Simultaneously the notation has been simplified in a self-explanatory manner, and we have allowed the two reflectors to be different from each other (asymmetric resonator) [37].

$$\mathcal{T} = \frac{T_I T_{II}\left(1 - \sqrt{R_I R_{II}}\right)^{-2}}{1 + 4\sqrt{R_I R_{II}}\left(1 - \sqrt{R_I R_{II}}\right)^{-2}\sin^2(\psi/2)}, \tag{3.196}$$

where T and R are the transmittance and the front-side[18] reflectance respectively, of the individual reflectors – denoted by Roman subscripts I and II, and ψ is the total phase change

---

[17] It is easier to do the derivation backwards: starting from equation 3.196, if one cancels the common denominators for the ratio, discloses the parentheses, and then uses the trigonometric identity $1 - 2\sin^2\psi/2 = \cos\psi$, one gets back to equation 3.163.

[18] Generally, if the reflector is a multi-layered structure, the reflectance from both of its sides is different, and one must distinguish between front-side and back-side reflectance.

$$\psi = \beta + \phi_I + \phi_{II}; \qquad \beta = 2\omega d/c. \tag{3.197}$$

Here $\beta = 2\varphi_1$ is the phase change of an electromagnetic wave, characterized by angular frequency ω, for one round trip inside the vacuum cavity (refractive index equal to one) of length d, and ϕ is the phase change upon reflection from the respective reflector (I or II).

Let us introduce the reflective finesse[19] [38,18]

$$\mathcal{F} = \frac{\pi\left(R_I R_{II}\right)^{1/4}}{1 - \sqrt{R_I R_{II}}}, \tag{3.198}$$

and the contrast factor [5,39,38]

$$C \equiv 1 + F = 1 + (2\mathcal{F}/\pi)^2, \tag{3.199}$$

which normally is a large number and is therefore approximately given by the F-parameter[20]

$$F = (2\mathcal{F}/\pi)^2 = 4\sqrt{R_I R_{II}}\left(1 - \sqrt{R_I R_{II}}\right)^{-2}, \tag{3.200}$$

By using these just introduced quantities, as well as the resonant transmittance

$$\mathcal{T}_{res} = \frac{T_I T_{II}}{\left(1 - \sqrt{R_I R_{II}}\right)^2}, \tag{3.201}$$

---

[19] Vaughan [36] calls $\mathcal{F}$ ideal-reflectivity finesse, and like Hernandez [38] denotes it by N_R.

[20] called so by Born and Wolf [5] and Hernandez [38]. Others [40,36] call it sloppily "finesse" which facilitates confusion. Even worse, Fowles [40] whose book in other respects is very good and clear, does not even mention the actual finesse given by equation3.198.

equation 3.196 for the transmittance of the Fabry-Perot resonator is reduced to

$$\mathcal{T} = \frac{\mathcal{T}_{res}}{1 + (2\mathcal{F}/\pi)^2 \sin^2 \psi/2} = \frac{\mathcal{T}_{res}}{1 + F \sin^2 \psi/2}. \tag{3.202}$$

By introducing the Airy shape function

$$\mathcal{A}(\psi) = \frac{1}{1 + (2\mathcal{F}/\pi)^2 \sin^2 \psi/2} = \frac{1}{1 + F \sin^2 \psi/2}, \tag{3.203}$$

the Fabry-Perot transmittance equation 3.202 can be ultimately reduced to

$$\mathcal{T} = \mathcal{T}_{res} \mathcal{A}(\psi). \tag{3.204}$$

Note that the relationship between the F-parameter and the finesse $\mathcal{F}$ is not linear. The former simplifies the appearance of equation 3.202 to a greater extent, whereas the latter one is the ratio of the free spectral range to the bandwidth (see equation 3.207).

Evidently when[21] $\psi = \psi_{min}^{(m)} = (2m + 1)\pi$ or $\psi = \psi_{max}^{(m)} = 2m\pi$, where m is an integer counting the interference fringes, the transmittance of the Fabry-Perot resonator reaches its minimum value $\mathcal{T}_{min} = \mathcal{T}_{res}\left[1 + (2\mathcal{F}/\pi)^2\right]^{-1}$ or maximum value $\mathcal{T}_{max} = \mathcal{T}_{res}$), respectively.

Assuming that the frequency variation of $\mathcal{T}_{res}$ is small, for the half maxima ($\mathcal{T}_{1/2} = \mathcal{T}_{res}/2$) the denominator in equation 3.202 must be set to 2, which gives

$$\mathcal{F}^2 \sin^2 (\psi_{1/2}/2) = (\pi/2)^2. \tag{3.205}$$

---

[21] The respective frequencies are masked within the expression for the phase through equation 3.197.

As the right side of this equationis small, and the square of the sine is bound by 1, assuming that the finesse $\mathcal{F}$ is large enough leads to the conclusion that the sine is small and therefore can be replaced by its argument in radians. Finally, taking into account that the sine function has a period of 2π, under all assumptions above, we get for the phase (see footnote 21) at the half maxima $\psi_{1/2}^{(m)} = 2m\pi \pm \pi/\mathcal{F}$.

If the phase (frequency) variations of ϕ_I and ϕ_{II} are neglected, then the phase bandwidth $\delta\psi$ of a single fringe is $2\pi/\mathcal{F} = \delta\psi = \delta\beta = 4\pi d\delta\omega$, or the frequency bandwidth of a single fringe, i.e., the full width at half maximum (FWHM), is

$$\delta\omega = (2d\mathcal{F})^{-1}. \tag{3.206}$$

Evidently, for a fixed vacuum-cavity length d, the finesse $\mathcal{F}$ is inversely proportional to the bandwidth $\delta\omega$. Remembering that the free spectral range is $\Delta\omega = (2d)^{-1}$, we can reach a second definition of the finesse as the ratio of the free spectral range to the frequency bandwidth:

$$\mathcal{F} = \Delta\omega/\delta\omega. \tag{3.207}$$

Note that the latter equation is consistent only with the finesse $\mathcal{F}$ as defined by equation 3.198, but not with the F-parameter as defined by equation 3.200.

CHAPTER 4
SUPERCONDUCTIVITY OF THE CUPRATES

4.1 Review of Early Studies on the Cuprates

Research in the field of high-temperature superconductivity is very active. It is not easy to summarize the work in this field briefly. The cuprates are complex compounds with interesting properties which are difficult to interpret. These challenging substances require the use of the whole arsenal of experimental methods developed by physicists. Reviews devoted to one or more of the various experimental techniques are published quite often.

Herein by necessity I will concentrate mainly on the infrared studies although other methods may be mentioned occasionally. My task is made somewhat easier by several related reviews that are available [23,25,41–44]. As the combined volume of these reviews is comparable or exceeding that of an average PhD dissertation, the review herein will inevitably omit a whole lot of important details. Any research "branches" that have proven to be dead-end will be "cut". My only hope is to be able to reconstruct at least the large-scale structure of the research developments.

The first review by Tanner and Timusk [23] covers the early studies (1986-1988) on polished and textured ceramic samples, as well as the pioneering studies of crystals and thin films. This review is the guideline for the next subsection.

4.1.1 Mid-Infrared Absorption

4.1.1.1 Ceramic samples

The first infrared measurements by Tajima et al. [45] were done on $La_{2-x}Sr_xCuO_4$ ($x = 0.18$), $La_{2-x}Ba_xCuO_4$ ($x = 0.10$), and La_2CuO_4 (the parent compound). The two doped samples had a reflectance minimum at $\lambda = 1.5\ \mu$m ($\mathfrak{E} = 0.83$ eV). The spectral position of the minimum did not change with doping. Such a minimum was not observed in the parent-compound reflectance. With increasing wavelength, the reflectance rises quickly, with the increase being steeper and the final reflectance magnitude being higher for the most-heavily doped sample. Three strong infrared-active phonons were observed for the parent compound. The softest one is absent from the doped-samples spectra. The authors discussed the results as manifesting a plasma edge and absorption by free carriers.

Soon thereafter Orenstein et al. [46] published room-temperature reflectance spectra of $La_{2-x}Sr_xCuO_4$ ($x = 0.175$), La_2CuO_4 and $YBa_2Cu_3O_{7-\delta}$, while Herr et al. [47] presented the reflectance spectra of $La_{2-x}Sr_xCuO_4$ ($x = 0.15$) measured at 4.2, 70, and 300 K. Both groups found that only the far-infrared optical properties could be described by a simple Drude model. They observed a strong, broad (ca. 1 eV) feature in the mid-infrared ($\mathfrak{E} = 0.44 - 0.45$ eV for $La_{2-x}Sr_xCuO_4$ and 0.65 eV for $YBa_2Cu_3O_{7-\delta}$). The Drude term contributed only a small part of its oscillator strength.

Orenstein et al. [46] modeled the spectra using a two-fluid Drude-Lorentz model, whereas Herr et al. [47] obtained the frequency dependence of conductivity by Kramers–Kronig analysis and found that the vibrational features (especially the one at 240 cm^{-1}) were anomalously strong.

Ceramic $YBa_2Cu_3O_{7-\delta}$ samples were studied in the mid- and far-infrared by Bonn et al. [48] and Kamarás et al. [49] Kramers–Kronig analysis produced a broad (almost 1 eV) mid-infrared band at $\mathfrak{E} = 0.37$ eV, observed in the superconducting ($\delta = 0.1$), but not in the non-superconducting ($\delta = 0.8$) sample. The authors attributed the absorption in the mid-infrared to a charge-transfer electronic excitation among strongly correlated, perhaps localized electrons. Such electrons were suggested by Varma et al. [50].

As Orenstein and Rapkine pointed out, the early measurements described above were inaccurate due to low quality of the inhomogeneous samples and ignoring the strong anisotropy of the cuprates [51].

Schlesinger et al. [52] realized that the mixing of *c*-axis phonon structure with *ab*-plane electronic absorption leads to the apparently anomalous oscillator strength which was determined by either Kramers–Kronig analysis [47,49], or fits using a model dielectric function [53]. Polarized measurements confirmed that claim.

Tajima et al. [45] found that the spectral position 6600 cm^{-1} ($\mathfrak{E} = 0.83$ eV) of the plasmon minimum $La_{2-x}Ba_xCuO_4$ did not depend on x when the latter was in the range from 0.06 to 0.18. This was confirmed by others [23, p. 364]. Etemad et al. [54,55] studied $La_{2-x}Sr_xCuO_4$with x in the range from 0 to 0.30 and found that though the low-frequency reflectance varied with doping level, still the spectral location of the reflectance minimum was invariably at $\mathfrak{E} = 0.9$ eV. This contradicts the Drude model according to which the square of the screened (since ε_∞ is present) plasma frequency is proportional to the carrier[1] concentration n_e:

$$\omega_p^\dagger = \sqrt{n_e e^2/(m^* \varepsilon_p \varepsilon_\infty)}. \tag{4.1}$$

By varying the doping level it was found that the oscillator strength of the mid-infrared band is correlated with the critical temperature T_c. In $YBa_2Cu_3O_{7-\delta}$ this was observed by Kamarás et al. [49,56], whereas in $La_{2-x}Sr_xCuO_4$ by Orenstein et al. [57] and by Etemad et al. [54,55].

---

[1] The subscript distinguishes the concentration from the refractive index.

An important detail is that the normal-state DC conductivity is not correlated with superconductivity. Indeed, in the overdoped samples [58] σ_{DC} continues to rise with x, contrary to the decreasing T_c.

Bonn et al. [59] showed that by using ceramic pellets of high density, annealed for sufficient time at high temperature, and by avoiding polishing or other mechanical processing, one can obtain textured ceramic samples. X-ray and electron-microscope analysis prove that about 80% of the surface is covered with fine crystals with their **c**-axes normal to the surface. Though such a surface appear to be quite rough compared to a polished one, after scattering correction the textured samples have a much higher reflectance than the polished ones.

The textured ceramics were studied [59–62] within a wide spectral range at temperatures within the range from 2 to 300 K. The conductivity obtained by Kramers–Kronig analysis of the reflectance has a relatively narrow Drude peak at low frequencies, six sharp phonon lines, and a broad mid-infrared wing. The normal-state data can be fit with the following dielectric function

$$\tilde{\varepsilon}(\omega) = \varepsilon_\infty - \frac{\omega_{pD}^2}{\omega^2 - \mathrm{i}\omega/\tau} + \frac{\omega_{pe}^2}{\omega_e^2 - \omega^2 - \mathrm{i}\omega\gamma_e} + \sum_{j=1}^{N_{ph}} \frac{S_j\omega_j^2}{\omega_j^2 - \omega^2 - \mathrm{i}\omega\gamma_j}. \quad (4.2)$$

The the four terms in this equation are as follows:

1. the first accounts for the high-frequency part $\varepsilon_\infty = 3.8$;
2. the second describes the Drude contribution, characterized by plasma frequency $\omega_{pD} = 0.74\ \mathrm{eV}/\hbar$ (5,900 cm^{-1}) and relaxation rate $1/\tau = 0.037\ \mathrm{eV}/\hbar$ (300 cm^{-1});

3. the third is a Lorentz term modeling the mid-infrared absorption and is characterized by strength $\omega_{pe} = 2.6$ eV/$\hbar$ (21,000 cm^{-1}), center frequency $\omega_e = 0.26$ eV/$\hbar$ (2,100 cm^{-1}), and a width of $\gamma_e = 1.0$ eV/$\hbar$ (8,400 cm^{-1});
4. the fourth is a sum of Lorentz oscillators representing the $N_{ph} = 6$ phonons whose parameters are given by Bonn et al. [59].

It is interesting that the mid-infrared term is so strong and wide, that even though centered at 0.26 eV (2,100 cm^{-1}), it takes over from the Drude term already at 0.06 eV (500 cm^{-1}).

The resistivity at 100 cm^{-1} follows, as expected [63,64] for high-quality samples, linear dependence

$$\rho = \rho_o + \alpha T, \tag{4.3}$$

where the zero-temperature intercept ρ_o is relatively small.

The real part $\varepsilon'(\omega)$ of the dielectric function is negative at low frequencies, as can be expected for a conductor, but is almost zero above 0.1 eV (800 cm^{-1}): within the spectral range from 800 to 2,000 cm$^{-1}\varepsilon'(\omega)$ is positive at 300 K, and negative at 100 K, but in both cases its absolute value is small. This small value of $\varepsilon'(\omega)$ is behind the steep plasmon-like drop of the reflectance in the far-infrared.

The superconducting-state data can be fit with the following dielectric function [62]

$$\widetilde{\varepsilon}(\omega) = \varepsilon_\infty - \frac{\omega_{ps}^2}{\omega^2} + \mathrm{i}\,\frac{\pi\omega_{ps}^2}{2\omega}\,\delta(\omega) + \frac{\omega_{pe}^2}{\omega_e^2 - \omega^2 - \mathrm{i}\omega\gamma_e} + \sum_{j=1}^{N_{ph}} \frac{S_j\omega_j^2}{\omega_j^2 - \omega^2 - \mathrm{i}\omega\gamma_j}. \tag{4.4}$$

Comparison with equation 4.2 shows that most terms are unchanged (even the values of the parameters in them remain almost the same), except for the Drude term which has been replaced by a complex London term in which $\omega_{ps} \propto \sqrt{n_s}$ is the plasma frequency (oscillator strength) of the superfluid electrons, proportional to the square root from the concentration n_s of superconducting electrons. The real part of the London term corresponds the inertial response at finite frequency, whereas the imaginary part includes the delta function that describes to the diverging DC conductivity of the superconductor.

4.1.1.2 Crystal samples and thin films

The mid-infrared absorption band has also been observed in the *ab*-plane spectra of $YBa_2Cu_3O_{7-\delta}$ crystals [60–62,65,66] and thin films [67].

The normal-state reflectance from crystals can also be fit with the dielectric function given by equation 4.2, but the parameters are slightly changed. At 100 K [60–62] the following values were found:

1. Drude plasma frequency $\omega_{pD} = 1.2$ eV/$\hbar$ (9,700 cm^{-1}) and relaxation rate $1/\tau = 0.030$ eV/$\hbar$ (240 cm^{-1});

2. mid-infrared strength $\omega_{pe} = 2.5$ eV/$\hbar$ (20,000 cm^{-1}), center frequency $\omega_e = 0.25$ eV/$\hbar$ (2,000 cm^{-1}), and a width of $\gamma_e = 0.6$ eV/$\hbar$ (5,000 cm^{-1}).

Phonons were observed, but because the crystals are small and have a much higher conductivity than the ceramics, the signal-to-noise ratio of the spectra is inadequate to produce reliable phonon parameters.

The Drude contribution to the dielectric function at 100 K leads to a value for the DC conductivity $\sigma_{DC} = 6500$ $(\Omega{\cdot}\mathrm{cm})^{-1}$, which agrees with the measured one.

Van der Marel et al. [67] measured the room-temperature reflectance of a thin $YBa_2Cu_3O_{7-\delta}$ film and by comparing the conductivity extracted from that measurements with the density of states obtained independently, they established that the low-energy bands observed in the conductivity spectra cannot be associated with interband transitions.

All measurements mentioned earlier, even when polarizeed, gave only averages for the *ab*-plane spectra of $YBa_2Cu_3O_{7-\delta}$, because of twinning of the crystals. Therefore Tanaka et al. [68,69] made an important breakthrough: they used a microscope to measure a single-domain, reflectance from an $EuBa_2Cu_3O_{7-\delta}$ crystal with the polarization along either a or b (the latter being the direction of the Cu-O chains. The spectra with these two polarizations are markedly different: for the *b*-polarization the reflectance is higher, the plasmon frequency is higher and the plasma edge is steeper, compared to those for the a-polarization.

Kramers–Kronig analysis shows that the conductivity and the electron loss function are also different for the two polarizations, but strong mid-infrared bands are present in both cases.

Large anisotropy between the *ab*-plane and *c*-axis was also reported for $La_{2-x}Sr_xCuO_4$ [70,71]. Even for compositions whose *ab*-plane has metallic appearance, the c axis is nevertheless insulating.

At photon energies above 1 eV, $La_{2-x}Sr_xCuO_4$ ceramics [47,54] and crystals [72] are characterized by doping-independent bands at 1.4, 2.7, and 5 eV, which are followed by strong absorption due to interband transitions.

Using ellipsometry, Etemad et al. [54] found in the parent compound La_2CuO_4 a strong band at 2 eV, which becomes weaker with doping, and disappears when $x > 0.10$.

Similarly, at photon energies above 1 eV, $YBa_2Cu_3O_{7-\delta}$ ceramics [49,73,74], films [67,75], and crystals [74], absorb at 2.5-2.7 and above 6 eV, the latter being followed by strong interband absorption.

Kelly et al. [74] found in the parent compound $YBa_2Cu_3O_{7-\delta}6$ two very narrow absorption bands at 1.7 and 4.1 eV which get weaker with doping and disappear when $\delta \lesssim 0.10$.

The early infrared studies of high-temperature superconductors devoted a lot of fruitless efforts to determine the superconducting energy gap [23].

4.2 Review of More Recent Studies on the Cuprates

The second review by Tanner and Timusk [25] covers the next period (1988-1990) of studies of the *ab*-plane conductivity of crystals and thin films. This review is the guideline for this subsection. Well-established facts at the time the review was written:

1. The parent compounds are charge-transfer insulators with a gap about 2 eV (16,000 cm^{-1}). The charge transfer gap is stabilized by the combination of:
    - a large Hubbard energy U on the Cu sites which prevents them from double-electron occupancy;
    - and the energy difference between the Cu $d_{x^2-y^2}$ state and the O p_x and p_y states.
2. In the doped compounds, the holes occupy oxygen sites in the CuO_2 layers, and act as mobile charge carriers in both the normal and superconducting regime.
3. The cuprates are "clean-limit" (the superconducting coherence length $\xi <$ the electronic mean free path ℓ), normal-skin-effect (the electronic mean free path $\ell <$ the penetration depth λ) superconductors. This is so because the cuprates have very low ξ, but their carrier concentrations (and hence conductivity) are relatively low, leading to higher λ in comparison with the metal elements. Conversely, many clean metal elements, known to be supercon-

ducting, are in the anomalous skin effect regime which according to Mattis and Bardeen [76] is equivalent to being "dirty limit" superconductors.

4.2.1 A Second Look at Mid-Infrared Absorption

4.2.1.1 $La_{2-x}Sr_xCuO_4$

With only one CuO_2 plane per formula unit (i.e., two per unit cell), $La_{2-x}Sr_xCuO_4$ is the simplest of the cuprate families. It allows doping in a wide region: from $x = 0$ (antiferromagnetic insulator), though $x = 0.15$ (optimally doped superconductor), to $x = 0.3$ (a very queer metal).

It is difficult to produce large, homogeneous $La_{2-x}Sr_xCuO_4$ single crystals. For this reason most early studies were done on low-quality samples with broad superconducting transitions or even on non-superconductingsamples. Uchida et al. [77,78] presented the first study on samples of a better quality. The composition x (doping) was within the range from 0 to 0.34. The sample with $x = 0.15$ had a very sharp superconducting transition at $T_c = 27$ K (which is below the expected 38 K for such a composition). The samples with $x = 0.10$ and $x = 0.20$ had $T_c = 18$ and 22 K, respectively.

The undoped sample ($x = 0$) has reflectance typical for an insulator: there is a high phonon peak about 700 cm^{-1} ($\approx .09$ eV), the mid-infrared reflectance is almost constantup to the Cu-O charge transfer band at 2 eV (16,000 cm^{-1}). Phonons at 140 and 360 cm^{-1} have also been found [70,71,79].

With doping, the mid-infrared portion rises, masking the phonons, and the charge-transfer band weakens. The plasmon minimum, however, is pinned at about 1 eV for most of the doping range. Only for heavily overdoped samples ($x = 0.34$) the plasmon minimum has a small red-shift which indicates a small reduction of the mid-infrared oscillator strength for strongly overdoped non-superconducting $La_{2-x}Sr_xCuO_4$ samples.

The conductivity spectrum, obtained by Kramers–Kronig analysis of the reflectance data, manifests these details even more clearly. For the undoped sample the conductivity below 1 eV is negligible (the negative values and the absence of the phonon contribution may be due to uncertainties, or to the chosen extrapolations outside the measured spectral range), and the absorption at 2 eV is clearly seen.

With doping the spectral weight (or oscillator strength) of the band decreases; but other features appear in the mid-infrared and in the vicinity of 1.5 eV. The mid-infrared band manifests as a maximum in the lightly doped samples which proves it is not related to the Drude absorption in the far-infrared. When $x = 0.02$ the mid-infrared maximum is about 0.5 eV (4,000 cm^{-1}), it shifts to 0.14 eV (1,100 cm^{-1}) for the $x = 0.10$ sample, but becomes only a shoulder for the $x = 0.15$ sample. In samples of higher doping than the latter one, the mid-infrared absorption is hard to discern: because of the high DC conductivity it is hidden by the Drude peak. However, the mid-infrared absorption can be seen clearly for all superconducting compositions.

The intensity of the phonon bands is almost constant with doping.

The DC conductivity quickly increases (resistivity decreases) with doping. It agrees with the far-infrared conductivity (resistivity) to within a factor of 2. E.g., for the $x = 0.10$ sample, the far-infrared resistivity $\rho_{FIR} = 1,700\ \mu\Omega\cdot\mathrm{cm}^{-1}$, whereas the four-probe-measured resistivity is $\rho_{DC} = 900\ \mu\Omega\cdot\mathrm{cm}^{-1}$. That portion of the discrepancy which cannot be attributed to the rms total uncertainty from the two measurements, may be due to unaccounted contribution of the mid-infrared band in the far-infrared.

For doped materials at low photon energies, the real part of the dielectric function is negative [77,78]. The zero-crossing for the lowest doping ($x = 0.02$) is in the phonon region of the spectrum. However, for x in the range from 0.10 to 0.34, $\varepsilon' = 0$ in the vicinity of 0.7 eV invariably, even though the high-frequency is decreasing with doping. The latter decrease is the result of oscillator-strength conversion from the charge-transfer band to the mid-infrared and Drude bands.

For either free or bound charge carriers, provided the binding energy of the latter carriers differs significantly from the plasmon energy of the former carriers, the spectral location of the zero crossing $\varepsilon' = 0$ is very close to the screened plasma frequency, given by equation 4.1. But if such analysis were correct, the insensitivity of the zero crossing to doping observed by Uchida et al. [77,78] would mean that the ratio n_e/m^* does not change (or increases slightly) with doping in the range from 0.10 to 0.34]. Similar conclusions can be reached from considering the electron loss function [25, p. 373].

Very different conclusions can be reached by using the partial sum rule, Eq. 3.80. The effective number $N_{eff}(\omega)$ of carriers is zero up to 1 eV for the undoped sample which can be expected for an insulator. As one moves to samples of increasing doping $N_{eff}(\omega)$ grows in the far-infrared, forms a sloped "plato" showing a vague tendency to "saturate" above 1 eV, but just below 2 eV the charge-transfer and other higher energy transitions take over and $N_{eff}(\omega)$ increases more rapidly. The "plato" raises quickly until $x = 0.1$ is reached, increases quite slowly in the range from 0.1 to 0.2, and experiences a slight decrease above $x = 0.2$. The fact that $N_{eff}(\omega) > x$, especially when $x < 0.1$, is a signal that some of the charge-transfer oscillator strength gets redistributed to the mid-infrared and Drude bands. The latter conclusion was made initially for the $\mathrm{Pr}_{2-x}\mathrm{Ce}_x\mathrm{CuO}_4$ by Cooper et al. [80,25].

More studies on the latter type of materials have been reviewed in [25, pp. 374–377], but will be omitted here for brevity.

4.2.1.2 Bi cuprates

The family of bismuth cuprates includes compounds with one, two, or three CuO_2 layers, separated by Bi-O layers or layers with Sr^{+2} ion and apical oxygen ions. These three sub-families can be denoted briefly as (2201), (2212) and (2223), respectively, where $(n_1 n_2 n_3 n_4)$ are the number of particular atoms in the formula unit $Bi_{n_1}Sr_{n_2}Ca_{n_3}Cu_{n_4}O_y$. In the two layer material $Bi_2Sr_2CaCu_2O_8$ ($YBa_2Cu_3O_{7-\delta}$), Ca (Y) occupies the site between the two CuO_2 planes. Thus, $Bi_2Sr_2CaCu_2O_8$ is a system very similar to $YBa_2Cu_3O_{7-\delta}$, except for the fact that the latter one has also a layer with quasi-one-dimensional Cu-O chains. The charge carriers in $Bi_2Sr_2CaCu_2O_8$ are holes. It is assumed that they originate from the Bi-O layer, either from defects or from charge transfer. Band structure calculations predict that the Bi-O layer should also be conducting [81–83]. But STM[2] [84] and EEL[3] [85] measurements have proven that actually the Bi-O layer has an energy gap of the order of 4 eV. The fact that this layer is an insulator has been further confirmed by photoelectron spectroscopy of well-annealed samples with very high T_c [86].

Maeda et al. [87] compared polycrystalline ceramic samples belonging to the three sub-families of Bi cuprates by measuring their infrared reflectance. The reflectance minimum shows a blue shift as the number of CuO_2 layers increases. It is roughly at about 7000, 9000, and 12000 $cm^{-1}$for the measured compositions with one (2.1,1.9,0,1), two (2,1.8,1.2,2), and three (1.85,$Pb_{0.35}$,2,1.2,3.1) CuO_2 layers per unit cell, respectively. Drude fits give the screened plasmon frequencies to be about 5500, 7400, and 8800 cm^{-1}, respectively. Tanner and Timusk [25, pp. 377] pointed out that these values must be multiplied by $\sqrt{\varepsilon_\infty}$ in order to get the actual plasma frequency.

---

[2] Scanning Tunneling Microscope

[3] Electron Energy Loss

$Bi_2Sr_2CaCu_2O_8$ doped with Y was studied, also [87]. If Ca^{2+} is replaced by Y^{3+}, the number of holes on the CuO_2 planes decreases. When about 50 % of the Ca is replaced by Y, the system becomes an insulator. The hole concentration changes with Y content whereas the plasmon frequency is pinned. Rather the far-infrared reflectance decreases as the Y doping is increased. Similar behaviour is familiar from $La_{2-x}Sr_xCuO_4$, and is a warning that estimating the carrier concentration from the reflectance minimum spectral location is unreliable.

Reedyk et al. [88] measured the temperature dependence of far-infrared reflectance from single-crystal $Bi_2Sr_2CaCu_2O_8$ samples with $T_c = 85$ K and calculated the optical conductivity by Kramers–Kronig analysis. Later, similar data were reported by others. [89–93]. Throughout the infrared spectral range the reflectance goes down steadily and reaches its minimum in the vicinity of 10000 cm^{-1}(1.3 eV). Above 1000 $cm^{-1}$the temperature dependence is negligible. A wide, but weak band with a maximum at about 16000 cm^{-1}(2 eV) is present and is interpreted as a charge-transfer band. A structure, whose appearance varies from sample to sample, spans the spectral range from 28 to 32×10^3 cm^{-1}(from 3.5 to 4.0 eV). Most probably it originates due to excitations of the Bi-O layer.

Forro et al. [94] showed that the micaceous layered structure of $Bi_2Sr_2CaCu_2O_8$ allows using of free standing flakes with thickness that can be as low as 100 nm, suitable for transmittance measurements. Romero et al. [95] studied the unpolarized transmittance through $Bi_2Sr_2CaCu_2O_8$ flakes within the temperature range from 20 to 300 K. Without an interfering substrate, they were able to cover a wide spectral range from 80 to 30,000 cm^{-1}. The transmittance is very low, and increases with frequency. As can be expected, the far-infrared portion has a pronounced temperature dependence. Below T_c the transmittance is negligible, and can be approximated with $\mathcal{T} \propto \omega^2$. In the normal state it has a finite DC intercept. The transmittance is quasi-linear with the frequency within the spectral range from 1000 to 2200 cm^{-1}(from 0.12 to 0.27 eV). At higher frequencies the slope is steeper. The transmittance has a maximum at 14000 cm^{-1}(1.8 eV) and another one at 25000 cm^{-1}(3.1 eV). Such a linear $\mathcal{T}(\omega)$ cannot be expected for a simple metal.

Indeed, Glover and Tinkham [96,97] obtained the approximate transmittance through a free-standing thin metallic film

$$\mathcal{T} = [(1 + Z_o\sigma' d/2)^2 + (Z_o\sigma'' d/2)^2]^{-1}, \tag{4.5}$$

where σ' and σ'', are the real and imaginary part of the conductivity (equation 2.112), the wave impedance of vacuum Z_o is given by equation 3.17, and d is the film thickness. When the transmittance is very low ($\mathcal{T} \ll 1$), the unity in the first term can be neglected, and equation 4.5 is reduced to

$$\mathcal{T} \approx 4\,|Z_o d\widetilde{\sigma}|^{-2}\,. \tag{4.6}$$

For a simple metal in the far-infrared $\sigma'' \ll \sigma'$. Therefore, in the normal state the DC intercept of $\mathcal{T}(\omega)$ is a direct measure of the DC conductivity. In the superconducting state the superfluid inductive response dominates ($\sigma' \ll \sigma''$) in the far-infrared.

The high-frequency ($\omega \gg 1/\tau$) limit of equation 3.51 leads to purely imaginary free-carrier conductivity

$$\widetilde{\sigma}(\omega) \approx \mathrm{i}\,\varepsilon_o\omega_p^2/\omega. \tag{4.7}$$

Substitution of this equation into equation 4.6 gives a quadratic frequency dependence

$$\mathcal{T} \approx 4\omega^2 \left(Z_o d \varepsilon_o \omega_p^2\right)^{-2} \propto \omega^2. \tag{4.8}$$

Therefore, the quasi-linear spectral dependence of the transmittance is a further proof that the mid-infrared conductivity cannot be attributed to Drude free carriers.

In the superconducting state, one can see a shoulder around 700 cm^{-1}(90 meV). This shoulder is related to both superconductivity and the mid-infrared absorption. A clear explanation of the latter connection is given by Tanner and Timusk [25, p. 381].

The Kramers–Kronig relations 3.130 and 3.133 between the reflectance and phase change upon reflection, can be adapted for transmittance and phase change upon transmission. Comparison of equations 3.147 and 3.149 shows that this can be done by the formal substitution

$$\mathcal{R} \rightarrow \left|\frac{\widetilde{n}_1 \cos\widetilde{\theta}_1}{\widetilde{n}_3 \cos\widetilde{\theta}_3}\right| \mathcal{T}; \qquad\qquad \varphi_r \rightarrow \varphi_t, \tag{4.9}$$

and if the film is surrounded by equivalent media on both sides ($\widetilde{n}_3 = \widetilde{n}_1$) this is simplified to

$$\mathcal{R} \rightarrow \mathcal{T}; \qquad\qquad \varphi_r \rightarrow \varphi_t. \tag{4.10}$$

Once the phase change $\varphi_t(\omega)$ upon transmission has been determined, the complex refractive index can be calculated by numerical solution of

$$\sqrt{\mathcal{T}} \mathrm{e}^{\mathrm{i}\,\varphi_t(\omega)} = \frac{4\widetilde{n}}{(\widetilde{n} + 1)^2 \mathrm{e}^{-\mathrm{i}\beta(\omega)} - (\widetilde{n} - 1)^2 \mathrm{e}^{\mathrm{i}\beta(\omega)}}, \tag{4.11}$$

where $\beta(\omega) = \omega d\widetilde{n}/c$ is the phase change for one trip through the film. Before the numerical solution, one must add the phase change $\beta_o(\omega) = \omega d/c$ the wave would have after propagating for a distance d through vacuum to $\varphi_t(\omega)$. After the complex refractive index has been found, one can calculate the complex dielectric function, and from its imaginary part the conductivity can be determined.

Romero et al. [98] and Tanner et al. [99] used Kramers–Kronig analysis in the manner described above to get the optical conductivity of $Bi_2Sr_2CaCu_2O_8$. The normal-state, low-frequency conductivity is approximately equal to the DC conductivity. Though it is a decreasing function of frequency as if it were from Drude free carriers, above 300 cm^{-1}, it changes more according to $\sigma' \propto \omega^{-1}$, rather than $\sigma' \propto \omega^{-2}$, expected for the Drude case. Moreover, the temperature dependence of $\sigma'(\omega)$ at higher frequencies is much smaller than at DC or in the far-infrared. In the superconducting state, $\sigma'(\omega)$ has a broad band with a maximum around 1000 cm^{-1}(0.15 eV), and some phonon structure. There is also a small minimum at 400 cm^{-1}(50 meV).

Martin et al. [100] noted that the conductivity of $Bi_2Sr_2CuO_6$ has a "metallic" temperature dependence, but the system either never becomes superconducting or otherwise $T_c < 5$ K. Romero et al. [98] studied this compound using the technique described above for $Bi_2Sr_2CaCu_2O_8$. The conductivity spectra of $Bi_2Sr_2CuO_6$ are very similar to those of the normal-state $Bi_2Sr_2CaCu_2O_8$. Both the magnitude and the temperature dependence of the far-infrared optical conductivity agree with the DC conductivity. The initial decrease of $\sigma'(\omega)$ with frequency is Drude-like, but at higher frequencies it switches to $\sigma' \propto \omega^{-1}$ and the temperature dependence becomes limited. These data have shown the important fact that the non-Drude behaviour is not necessarily correlated with a high T_c, but is due to the holes present in the CuO_2 layers.

4.2.1.3 Y cuprates

$YBa_2Cu_3O_{7-\delta}$ has been studied very extensively. It is one of the most complicated and interesting superconductors: it includes both Cu-O plains and chains, most samples are microtwinned and can provide only average values within the $a-b$-plane, and besides have a variable oxygen content [25]

The first complete measurements of $a-b$-plane reflectance were done by Schützmann et al. [101] who found that the reflectance drops steadily, but not quite linearly throughout the infrared range. They found two strong bands in the infrared at zero frequency (Drude) and in the mid-infrared around 500 cm^{-1}.

Thomas et al. [66], Cooper et al. [102], and Orenstein et al. [103] studied high quality twinned crystals with various δ. They measured reflectance exceeding 90 % below 500 cm^{-1}. Some samples have a shoulder around 500 cm^{-1}, and all samples have a plasmon minimum around 10000 cm^{-1}. Reducing the oxygen content substantially reduces the mid-infrared reflectance. Most of the temperature dependence is noticeable below 800 cm^{-1}.

Many groups, including Kamarás et al. [104], et al. [101], have used Kramers–Kronig analysis to determine the optical conductivity. In the normal state a Hagen-Rubens low-frequency extrapolation works well. The far-infrared conductivity has a strong temperature dependence, but the changes in the mid-infrared are small. There is a minimum around 430 cm^{-1} which is significantly more pronounced in the normal state.

As larger single crystals of higher quality became available many researchers studied the $a-b$-plane anisotropy due to the metallic Cu-O chains. Numerous references can be found in the second review article by Tanner and Timusk [25]

Before 1995 YBCO was the most studied material from among the cuprates. Later the attention shifted predominantly to other cuprates. In YBCO the studies continued on the c-axis optical properties as well as studies on the pseudogap. To avoid turning of this dissertation into a huge review article, at this point I'll refer the curious readers to the review articles listed in the beginning of this chapter. Do not forget to check if there are any new ones published since this dissertation was frozen, and finally plunge into the deep ocean of the original papers.

CHAPTER 5
INFRARED SPECTROSCOPY

5.1 Introduction

A spectrometer is any instrument that can produce a spectrum—that is the dependence of some quantity (spectral characteristic) on some spectroscopic variable. In this section the basic components of a spectrometer are listed and their function is described briefly (definitions of some terms and more details for selected components will be given later):

The source generates electromagnetic radiation. The collimating optical system consists of lenses[1] and/or mirrors and forms the source radiation into a beam of the desired geometry, direction and solid angle (f-number). A slit or aperture at a focal plane defines the effective source dimensions (height × width or diameter) forming the cross section of the beam to be a narrow rectangle or a circle, for the case of monochromators or interferometers, respectively.

Monochromators use either a dispersive prism or a diffraction grating to separate spatially the radiation components of various frequencies (or wavelengths). Modern high-quality monochromators are based exclusively on diffraction gratings. Nowadays prisms are only used for instructional purposes, or in cheap, not-very-accurate spectrometers. Scanning is accomplished by rotating the prism or grating (or sometimes a mirror) with a step motor.[2] Interferometers use either a beam-splitter for amplitude division, or a lamellar grating for wavefront splitting, in order to separate the beam coming from the source into two beams [105]. A scanning mechanism moves a mirror or a subset of lamellae either stepwise, or continuously. The scanner in a fast-scan interferometer is air-bearing driven [106]. A He-Ne laser is used to track the position of the moving mirror [107]. The internal optical system consists of lenses and/or mirrors that direct the beam along its path within the spectrometer.

---

[1] If the collimator is a lens, then the slit is in front of that lens.

[2] Step motors came into use around 1965-75. They were preceded by AC motors which have been used in monochromators since 1940-45. Earlier than that the operator used to turn a knob manually and record data point-by-point in a notebook without batteries!

The sample-mounting device could be within a cryostat to enable spectroscopic measurements at cryogenic temperatures. The cryostat must be furnished with suitable windows, transparent for the spectral region of interest. Interferometers often need high-pass and/or low-pass optical filters to cut out a frequency range of interest, thereby allowing adequate accuracy while preventing aliasing.[3] The filters can be positioned at any convenient plane crossing the beam between the source and the detector. However, if the source is very bright and the beam-splitter is with small area, a low-pass optical filter must be placed between the source and the beam splitter to protect the latter from overheating by cutting the intensive visible and ultraviolet portions of the radiation. In fast-scan interferometers this is the main function of the optical filter, because aliasing is suppressed by electronic filters.

The condenser optics (again lenses and/or mirrors) projects an image of the previous optical component (illuminated part of the sample, beam splitter, prism, or grating) onto the detector. All optical components within any spectrometer have appropriate mechanical adjustments used for proper alignment of the beam. The radiation detector transforms the electromagnetic radiation into electric signal and may be combined with a preamplifier in order to preserve a high signal-to-noise ratio.

---

[3] Aliasing is described later.

Finally the data acquisition system includes an ADC (an analog-to-digital converter to digitize the analog signal coming from the detector), a processor (to control the spectrometer, to store in its RAM, to process, and to output the data), plus any combination of long-term storage devices (floppy drive, hard disc, CD-R,[4] CD-RW,[5] MO,[6] or removable drive) and/or output devices (a chart recorder, display, printer, plotter). A network connection may be useful for on-line data exchange, processing, or transfers. Naturally, since the system is computer-based, it also needs some suitable software for data acquisition, manipulation, and modeling. When one has to overcome small signal-to-noise ratios, a chopper and a lock-in nanovoltmeter are added to accomplish phase sensitive detection in a narrow frequency range tuned to the chopping frequency and phase. A chopper can also be used for filtering [105]. With fast-scanning interferometers detection is synchronized with the scanner and so chopping the radiation is not needed.

Universal spectrometers able to cover the whole known electromagnetic spectrum do not exist today, and are unlikely to be possible even in the distant future. Hence, various types of sources, detectors, prisms, gratings, beam splitters, lenses, and mirrors are used in different spectral regions. Any wide-range spectra are measured initially for narrow regions and later the various sections are merged together by custom application software.

E.g., a spectrometer with a rich set of exchangeable components can cover the whole optical region including ultraviolet, visible, and infrared. Only the visible region, which is relatively very narrow can be covered by a single instrument without changing some components.[7] The other two regions are subdivided further. For example, as was mentioned in chapter 2, the infrared is subdivided into near, mid, and far-infrared. Specific instruments exist for each of these regions. Measurements are hardest in the far-infrared which has to be subdivided further into smaller regions usually named after the beam-splitters used to cover them. Naturally this is not a universal subdivision, but rather a instrument-dependent one.

---

[4] recordable compact disc player

[5] rewritable compact disc player

[6] magneto-optical drive

Note that it is possible to measure several of the infrared sub-regions on the same instrument, but in order to accomplish that, one cannot avoid the necessity to change beam splitters or gratings, and/or sources, and/or detectors.

In its infancy spectroscopy has provided information about the various spectral regions themselves. Then it is has been used to study the sources, spectral elements, and detectors employed for generating, transforming, and detecting of electromagnetic radiation in optical equipment, including spectrometers themselves. Simultaneously, spectroscopy has obtained valuable information about the interaction of electromagnetic radiation with matter. A wide and diverse group of samples can be studied with pertinent spectroscopic methods.

In most cases the effects of the spectrometer and environment are divided out. First a spectrum with the sample in place is measured, then a second (background or reference) spectrum is taken without the sample, and the respective ordinates for each point are divided.

For samples that are highly reflective in a particular spectral region, one usually measures reflectance. In the other extreme case—almost transparent samples—one usually measures transmittance. In the majority of intermediate cases, especially with thin-film samples, one can measure both reflectance and transmittance, giving additional information about the samples. Moreover, as we have shown in chapter 6 [108], when the samples are flat, parallel plates with more-than-one layer, the reflectance can be measured from both the front and back sides of the sample.

---

[7] In order to enable covering a wider spectral range any of all of the following components can be changed: the grating or beamsplitter, the filters, the sources, and the detectors.

Microscope-monochromators exist for measuring small samples, or small spots of larger samples in the near infrared. Similar tasks can be accomplished in the mid and far-infrared by using microscopic attachments to far-mid infrared spectrometers.

Optical spectroscopy (UV, VIS, and IR) in general, and IR spectroscopy as its special case, often provide rich data about the studied objects or materials. However, in most cases it is necessary to combine their results with those provided by other experimental methods: Raman spectroscopy, diffraction of neutrons, electrons, or x-rays, magnetic resonance methods, mass spectrometry, methods for studying transport properties, etc. [106].

In this chapter, the spectrum variables and their units will be covered first. Then spectroscopic methods for the optical region of the electromagnetic region will be mentioned briefly, followed by a more detailed treatment of the infrared techniques, especially those suitable for the far-infrared region. Finally, I describe the instruments and other enabling equipment that were used in our experiments.

5.1.1 Spectrum Variables and Units

Due to historical reasons, suitability for particular spectral regions, or other considerations, a number of spectrum variables are used in the various regions of the electromagnetic spectrum.

For the shortest waves (gamma rays) most convenient is the photon energy given by equation 2.135 $\mathfrak{E} = h\nu$, measured in electronvolts [eV]. In the x-ray region the wavelength $\lambda = c/\nu$, measured in ångströms [Å] is the spectral variable of choice most often, as x-ray diffraction is used to determine lattice constants.

For the UV and VIS regions the wavelength in nanometers [nm] seems to be the most popular. Within the infrared range non-physicists tend to use the wavelength in micrometers [μm], while physicists, and especially spectroscopists, normally use the spectroscopic wave number $\breve{\nu} = 1/\lambda$, measured in reciprocal centimeters[8] [cm^{-1}].

For microwaves and radio waves the frequency ν (often denoted with f) measured in tera- or giga-, and mega-, or kiloHertz [THz, GHz, MHz, kHz] is standard.

When thermally excited processes (e.g., phonons, magnons, and their interactions with photons) are considered the thermal energy of a photon $k_BT = h\nu$ becomes important. So, sometimes the absolute temperature T measured in Kelvin [K] is used as spectrum variable. Similarly if magnetic interactions (e.g., optical studies of magnons in magnetic fields) are present the magnetic energy $\mu_B B = h\nu$ of a photon allows using of the magnetic-induction magnitude B measured in Tesla [T] as the spectrum variable. In the latter equation μ_B is the Bohr magneton.

In theoretical treatments the angular frequency $\omega = 2\pi\nu$ measured in radians per second [rad/s], and the wave number $k = 2\pi/\lambda = 2\pi\breve{\nu}$ measured in radians per meter [rad/m] are most convenient.

Due to the fundamental importance of energy conservation for all types of processes, physicists in general prefer the energy, or quantities proportional to energy. Wavelength often seems more straightforward to people from other fields and even to less experienced physicists.

---

[8] The reciprocal centimeter is commonly known as wave number, but I try to stay away from jargon using the same word for both the quantity and the unit. Also, usually the spectroscopic wave number is denoted simply by ν and is even called simply frequency, which can be mistaken for the regular frequency c/λ. Sometimes the spectroscopic wave number is denoted with tilde, but herein tilde is reserved for complex quantities. As a result, breve is used to denote the spectroscopic wave number $\breve{\nu}$.

Using the equations relating the various quantities, it is easy to obtain the conversion factors given in Table 5.1. These conversion factors have been calculated with the latest recommended values of the fundamental constants, taken from the web site of NIST (`www.nist.org`). All stable (certain) significant digits have been kept though such a high precision is rarely needed. All quantities proportional to photon energy, including frequency, spectroscopic wave number, temperature, magnetic induction, can be conveniently converted among each other using that table. Note that the g-factor has not been taken into account in the table, that is, the column for B, T should be divided by two. Care is necessary with the last line, as the wavelength is inversely proportional to all other quantities in the table, and therefore the factors for the wave number become divisors for the wavelength as the two quantities are proportional.

Table 5.1: Conversion Factors Between the Various Spectroscopic Units.

Quantity, Unit	E, meV	ν, THz	$\breve{\nu}$, cm^{-1}	T, K	B, T
E, meV	1	0.2417989	8.065545	11.604506	17.275988
ν, GHz	4.135667	1	33.35640952	47.9924	71.447728
$\breve{\nu}$, cm^{-1}	0.1239842	0.0299792458	1	1.43878	2.1419490
T, K	0.086173	0.0208366	0.695036	1	1.4887
B, T	0.057883817	0.013996246	0.46686452	0.67171	1
$\lambda = \breve{\nu}^{-1}$, cm	0.1239842	0.0299792458	1	1.43878	2.1419490

5.1.2 Optical Conductance

Between the source and detector of any spectrometer there is a series of imaging (lenses, mirrors, gratings) and/or optically-conducting elements (diaphragms, light pipes, fibers). Samples interact with radiation and—depending on their specific nature—can be considered either imaging, or conducting or any combination in between. Such an optical system transports electromagnetic radiation with radiant flux Φ from the source to the detector:

$$\Phi := \; L\, G\, \tau, \tag{5.1}$$

where L is the radiance of the light source measured in [W/(sr·cm^2)],[9] G the optical conductance in [sr·cm^2], and τ is the transmission factor of the system [109].

Let us consider two successive components of an optical system. The one that is closer to the source is denoted by subscript 1, and the other one by subscript 2, respectively. The two optical components have active areas A_1 and A_2. Neglecting losses to absorption or scattering, the portion of the whole optical system between these two components will have an optical conductance given by

$$G \,=\, n^2 \int_{A_1} \mathrm{d}A_1 \int_{A_2} \mathrm{d}A_2 \, \frac{\cos\alpha_1 \cos\alpha_2}{d_{1,2}^2}, \tag{5.2}$$

where $\mathrm{d}A_j$ is a differential element of the area A_j ($j = 1, 2$), $d_{1,2}$ stands for the distance between the two surface elements $\mathrm{d}A_1$ and $\mathrm{d}A_2$, α_j is the angle between the normal to the surface element $\mathrm{d}A_j$ and the straight section connecting the two surface elements, and n is the refractive index of the medium between the two surfaces.

If $A_j \ll d_{1,2}^2$ we can consider that $d_{1,2}^2$ is constant, and pulling it out of the integrals, the latter can be taken trivially:

$$G \approx n^2 A_1 A_2 / d_{1,2}^2. \tag{5.3}$$

---

[9] Here W stands for watt, and sr is steradian.

Using the solid angles with vertex on surface 1 or 2, respectively

$$\Omega_1 = A_2/d_{1,2}^2; \qquad \Omega_2 = A_1/d_{1,2}^2, \tag{5.4}$$

we get the optical conductance of the two optical components

$$G_1 = n^2 A_1 \Omega_1; \qquad G_2 = n^2 A_2 \Omega_2, \tag{5.5}$$

where the left-side equation is for the component with area A_1 radiating within a solid angle Ω_1, whereas the right-side equation is for the component with area A_2 being irradiated from a solid angle Ω_2.

Assuming the solid angle can be represented by a cone with an apex angle of 2Θ

$$\Omega = 2\pi(1 - \cos\Theta) = 4\pi \sin^2(\Theta/2). \tag{5.6}$$

Small solid angles can be approximated with

$$\Omega \approx \pi \sin^2 \Theta, \tag{5.7}$$

and substituting this in equation 5.5 we get an approximation for the optical conductance of an optical component

$$G \approx n^2 A \pi \sin^2 \Theta = \pi A A_N^2, \tag{5.8}$$

where $A_N = n \sin\Theta$ is the numerical aperture.

In a well designed instrument the optical conductance must be the same for any pair of successive optical elements. This will ensure invariant radiance for any cross section of the optical path, provided we ignore the losses due to unwanted reflection, absorption, or scattering. Should there be a “weak link” in the optical "chain" due to theoretical or technical limitations, it will act as a bottleneck no matter how perfect the rest of the optical system is. Depending on the particular region of the electromagnetic spectrum or the specifics of the sample, almost any component (the source, detector, dispersive or interferometric element, and even the sample itself) can act as such a limiting element. E.g., in the FIR the sources are the weak link (their longwave tail has to be exploited), while in the MIR the detectors have a maximum noise equivalent power, or a minimum detectivity [109].

The medium in spectrometers is most often vacuum, dry nitrogen, or air, and then $n = 1$.

5.1.3 Spectrometers

5.1.3.1 Monochromators

Monochromators can select a narrow spectral range of radiation. An entry slit initially forms a narrow image of the source. The beam is collimated using either concave mirrors preceding the slit, or lenses after the slit. Next, either a dispersive prism or a diffraction grating is used to separate spatially the various spectral frequencies. Finally the needed narrow spectral region is selected with an exit slit. The radiation from this narrow spectral region is either transmitted through or reflected by the sample and focused on the detector. Scanning of the whole covered region of the spectrum is accomplished by rotating the dispersive/diffracting element stepwise (or in rare cases continuously). In the past this used to be done manually, but in recent decades this task has been delegated to stepper motors controlled by computers which don't get bored easily, offer greater spectral accuracy and contribute to better optical resolution.

Prism monochromators are nowadays cheap instruments for the visible part of the spectrum used for educational purposes or when low-accuracy measurements are adequate. Furthermore, prisms for the near and mid infrared must be made from alkali halides which are easily damaged by moisture. As a result, grating monochromators are used predominantly.

5.1.3.2 Interferometers

Interferometers split the beam coming from the source into two or more coherent parts which cover different optical paths before being recombined to interfere. Depending on the optical path difference the interference can be constructive, destructive, or with any value within the continuous range between the two extreme values. The recombined beams are either reflected by or transmitted through the sample and then reach the detector. By scanning stepwise (or continuously) various optical path differences and sampling the signal at every step (or sampling periodically—when scanning continuously) one gets an interferogram. It combines the interference effects of the whole covered frequency range. A processor applies fast Fourier transformation (FFT) to the interferogram and the result is a single-beam spectrum. The processing must include phase correction, but may also do additionally apodization, convolution or deconvolution, digital filtering, etc. Some of these operations will be covered briefly later in this chapter. The sample single-beam spectrum is divided by the background single-beam spectrum in order to get the reflectance or transmittance power spectrum, respectively. That is why this method is called power FTS (Fourier Transform Spectroscopy).

More rarely amplitude FTS is used: the sample is placed between the beam splitter and the fixed mirror (transmission), or replaces the fixed mirror (reflection). This method allows both the modulus and phase of the electric amplitude to be determined [[105].

Separation of the source beam into two parts can be achieved in two ways:

Lamellar reflecting gratings consist of two alternating sets of lamellae positioned in two parallel planes, and so the incident beam is separated into two reflected beams with optical path difference equal to the doubled spacing between these two planes.

Beam splitters are either semitransparent films (acting as Fabry-Perot resonators) or wire meshes.[10] The ideal beam-splitter is not-absorbing, reflects 50% of the incident radiation flux, and transmits the other 50%. Real beam splitters meet these requirements only partially. They are optimized for a particular frequency and are applicable in a certain range about that center frequency. Moving away from the central frequency of a beam-splitter inevitably leads to decreasing its efficiency— the ratio of separation is 50:50 only at the central frequency. In order to cover a wide spectral region one has to use a set of several beam splitters.

5.1.3.3 Comparison of monochromators and interferometers

- Monochromator advantages: Simple construction, no need for mathematical processing of the data, simpler theory and hence less stringent requirements to the education of their operators. In dual-beam[11] versions the background spectrum is taken simultaneously with the sample one, thus eliminating the effect of fluctuations or drifting of the source, environment, or some electronic components.

- Monochromator drawbacks: The narrow slits cause lower throughput and hence lower signal-to-noise ratio especially in the far-infrared, no multiplex advantage—slow monochromatic sampling, unsuitable for studying fast processes.

---

[10] In the past semitransparent silver mirrors have been used, but later were abandoned due to high losses.

[11] Traditionally here the term "double-beam" is used. I prefer to reserve it for the interferometers.

- Interferometer advantages: Jaquinot (throughput or étendue) advantage—circular apertures have higher throughput than the narrow slits necessary for monochromators to separate a spectral region that is small enough. Fellgett (multiplex) advantage—all frequencies are sampled simultaneously, the signal-to-noise ratio is higher and sampling is faster.

- Interferometer disadvantages: Interferometric spectroscopy is a single-beam (this is unfortunate terminology as from another point of view interferometers use double-beam interference.) technique—the sample and the background are measured separately rather than simultaneously. The Fellgett advantage only applies for the far and midinfrared regions where performance is limited by detector noise. At higher frequencies photon "shot" noise becomes dominant and the Fellgett advantage is buried in it. Also, the needed FFT is sometimes prone to introducing errors. Care is needed to avoid such errors and to interpret the results correctly. The more involved theory requires operators with higher education or deeper knowledge.

5.2 Fourier Transform Spectroscopy

5.2.1 Generic Michelson Interferometer

Not only was the Michelson interferometer historically the first double-beam interferometer used in commercial instruments for IR FTS, but some of its variations is behind most interferometers currently in use. Furthermore, its basic theory applies for interferometers of any design in general. Consider the simplified diagram of the essential[12] optical part of a generic Michelson interferometer shown in FigureIt consists of four arms: one with the IR source Σ, the second with a fixed mirror M_α, the third with a moving mirror M_β, and the fourth is directed to the sample S and the detector D. At the intersection of the four arms is the beam splitter B [106]. Ideally it should be non-absorbent and would split the zeroth-order beam with intensity I_Σ coming from the source into two first-generation partial beams with halved intensity $I_\Sigma/2$.

The sample S can be mounted in four configurations: for either power measurement of reflectance/transmittance, or amplitude-phase measurement of reflectivity/transmissivity. For power measurements the sample S is mounted in a sample compartment between the beam splitter B and the detector D. For transmittance ($\mathcal{T} = \widetilde{tt}^*$) measurement the sample $\mathrm{S}_\mathcal{T}$ is simply placed in the beam at right angle (normal incidence). For reflectance ($\mathcal{R} = \widetilde{rr}^*$) measurements a reflectance stage (Figure) is added into the sample compartment. This stage uses mirrors to deflect the beam into a "W"-shaped detour. The top cusp of "W" is the position for the reflecting sample $\mathrm{S}_\mathcal{R}$ or reference mirror $\mathrm{M}_\mathcal{R}$ (Au or Ag). The incidence is almost normal, that is the angle of incidence is close to zero. For amplitude-phase measurements the sample is mounted in the path of one of the partial beams: for reflection-coefficient ($\widetilde{r}$) measurement the sample S_r replaces the fixed mirror M_α, and for transmission-coefficient ($\widetilde{t}$) measurement the sample S_t is placed normally in the beam path between the beam splitter B and the fixed mirror M_α.

Measuring a background (reference) spectrum allows one to divide out (or very rarely subtract) any spectral effects of the equipment, and, in some cases, of the environment. E.g., for express, not-very-accurate measurements, the sample compartment may not be evacuated, but just flushed with dry nitrogen, or even left with air).

---

[12] The collimating or condensing optical systems have been omitted. Flat mirrors are shown and the ray-tracing diagram is only schematic. As a result the electromagnetic waves within the interferometer are plane.

To measure the reference for transmittance or transmissivity, the sample is simply removed from the path of the beam. The sample holder can have an "L"-shaped cross-section with two wings. Each of the two wings has a hole of identical diameter in the middle. The sample is mounted over one of the holes while the other is used for the reference measurement. Thus, switching forth and back between the sample and reference position can be accomplished by simply turning the sample holder through $\pm 90^o$.

To measure the reference for reflectance or reflectivity, the sample must be replaced by a reference mirror. A sample holder with C_{2v} symmetry can be used. The sample and mirror are glued to the back of their plates over identical conically-tapered holes. The two plates are mounted to the sample holder opposite to each other facing outward. In this case switching forth and back between the sample and reference position can be accomplished by simply turning the sample holder through $\pm 180^o$.

Let us assume initially that the interferometer is set up for a reference measurement, i.e., a sample S is mounted neither in the sample compartment, nor within the interferometer.[13] The source emits electromagnetic waves. I'll concentrate on their electric-field component as it is dominating the interaction with matter. The IR beam $\Sigma \rightarrow$B emitted by the source Σ travels the distance $L_{\Sigma \rightarrow B}$ to the beam splitter B. This beam is characterized by the following electric field[14] spectrum (in complex notation):

---

[13] The rest of this section is based on a series of lectures given by D. B. Tanner in 1994 and 1999 as well as on treatments found in the literature [105,110,111,107,112,113].

[14] For simplicity only magnitudes of the field vectors will be used.

$$\widetilde{E}_{\Sigma}(k,t) \;=\; \widetilde{E}_{\Sigma o}(k)\exp i(\boldsymbol{k}\cdot\boldsymbol{L} \;-\; \omega t). \tag{5.9}$$

where $E_{\Sigma o}(k)$ is the complex electric field amplitude at wave vector frequency k and $\boldsymbol{L}$ is a vector describing the displacement of a photon moving from the source along the beam path. Naturally, at the source $\boldsymbol{L} = 0$. The intensity of the beam at angular frequency ω is:

$$I_{\Sigma}(k) \;=\; (c/n)(\varepsilon\varepsilon_o/2)\widetilde{E}_{\Sigma o}(k)\widetilde{E}^{*}_{\Sigma o}(k). \tag{5.10}$$

Within the interferometer $n = 1 = \varepsilon$.

One can get rid of the time-dependence by assuming that the rest of our derivation is for $t = 0$. Additionally, since all distances are measured along the beam path, the vector notation in the exponents will be dropped.

The beam splitter B is characterized by complex reflectivity $\widetilde{r}_B(k) = r_B(k)\exp i\phi_B(k)$ and complex transmissivity $\widetilde{t}_B(k) = t_B(k)\exp i\varphi_B(k)$. The reflected beam B→M$_\alpha$ goes a distance $L_{B\to\alpha}$ to the fixed mirror M$_\alpha$ characterized by complex reflection coefficient $\widetilde{r}_\alpha = r_\alpha \exp i\phi_\alpha$ with modulus r_α and phase ϕ_α; the transmitted beam goes a variable distance $L_{B\to\beta}$ to the moving mirror M$_\beta$ characterized by complex reflection coefficient $\widetilde{r}_\beta = r_\beta \exp i\phi_\beta$ with modulus r_β and phase ϕ_β. Then the two beams return to the beam splitter B, and again each of them is split in two second-generation partial beams giving a total of four such beams. Two of them are directed back to the source, while the other two recombine and interfere just after their second interaction with the beam splitter B, as they are leaving it to begin their trip to the detector D spaced $L_{B\to D}$ apart.

Our treatment will be slightly simplified, but the result will not be affected if we assume that the two second-generation beams travel independently to recombine and interfere only when they reach the detector D. In such a case these two beams reach the detector characterized by their electric fields:

$$\widetilde{E}_{D1}(k,\omega) \;=\; \widetilde{E}_o(k)e^{ikL_{\Sigma\to B}}\,\widetilde{r}_B e^{ikL_{B\to\alpha}}\,r_\alpha e^{i\phi_\alpha}e^{ikL_{B\to\alpha}}\,\widetilde{t}_B e^{ikL_{B\to D}} \tag{5.11}$$

$$\widetilde{E}_{D2}(k,\omega) \;=\; \widetilde{E}_o(k)e^{ikL_{\Sigma\to B}}\,\widetilde{t}_B e^{ikL_{B\to\beta}}\,r_\beta e^{i\phi_\beta}e^{ikL_{B\to\beta}}\,\widetilde{r}_B e^{ikL_{B\to D}} \tag{5.12}$$

Applying the principle of superposition, the total electric field at angular frequency ω that reaches the detector is:

$$\begin{aligned}\widetilde{E}_D(k) \;&=\; \widetilde{E}_{D1}(k) \;+\; \widetilde{E}_{D2}(k)\\ &=\; \widetilde{E}_o(k)\,\widetilde{r}_B(k)\,\widetilde{t}_B(k)\,e^{i\Phi(k)}\left\{r_\alpha(k) \;+\; r_\beta(k)\,e^{i[kd\,+\,\phi(k)]}\right\},\end{aligned} \tag{5.13}$$

where the following three equations have been used:

$$\phi(k) \;=\; \phi_\beta(k) \;-\; \phi_\alpha(k), \tag{5.14}$$

$$\Phi(k) \;=\; k\,[L_{\Sigma\to B} \;+\; L_{B\to D} \;+\; 2\,L_{B\to\alpha} \;+\; \phi_\alpha(k)]. \tag{5.15}$$

$$d \;=\; L_{B\to\beta} \;-\; L_{B\to\alpha}, \tag{5.16}$$

Here d is the displacement of the moving mirror referred to the fixed mirror position.

In fact the detector responds not to the electric field of the radiation, but to its intensity. The spectral density of the intensity incident on the detector is:

$$\begin{aligned}
S_D(k) &= (c\,\varepsilon_o/2)\,\widetilde{E}_D(k)\,\widetilde{E}_D^*(k) \\
&= (c\,\varepsilon_o/2)\,|\widetilde{E}_o(k)|^2\,|\widetilde{r}_B(k)|^2\,|\widetilde{t}_B(k)|^2\,\left|\left\{r_\alpha(k)\;+\;r_\beta(k)\,e^{\mathrm{i}\,[k\,d\,+\,\phi(k)]}\right\}\right|^2 \\
&= (c\,\varepsilon_o/2)\,|\widetilde{E}_o(k)|^2\,\mathcal{R}_B(k)\,\mathcal{T}_B(k)\,\left\{r_\alpha^2(k)\;+\;r_\beta^2(k)\right. \qquad (5.17) \\
&\qquad \left. +\,2\,r_\alpha(k)\,r_\beta(k)\,\cos\left[k\,d\;+\;\phi(k)\right]\right\}.
\end{aligned}$$

Let us consider the product of the beam-splitter reflectance and transmittance and apply the energy conservation relation 3.152 to it we get

$$\begin{aligned}
\mathcal{R}_B(k)\,\mathcal{T}_B(k) &= \mathcal{R}_B(k)\,[1-\mathcal{R}_B(k)-\mathcal{A}_B(k)] \qquad (5.18) \\
&= \begin{cases} 0 \quad (\text{min}) \quad \text{if} \quad \mathcal{R}_B(k)=0 \quad \text{or if} \quad \mathcal{R}_B(k)=1-\mathcal{A}_B(k), \\[2ex] [1-\mathcal{A}_B(k)]^2/4 \quad (\text{max}) \quad \text{if} \quad \mathcal{R}_B(k)=[1-\mathcal{A}_B(k)]/2. \end{cases}
\end{aligned}$$

This equation hints that the product of the beam-splitter reflectance and transmittance characterizes how good the beam-splitter is for a particular spectral range. Therefore we can define two varieties of beam-splitter efficiency: amplitude $\widetilde{\epsilon}_B(k)$

which is complex, and power $\mathcal{E}_B(k)$.

$$\widetilde{\epsilon}_B(k) \;=\; 2\,\widetilde{r}_B(k)\,\widetilde{t}_B(k), \tag{5.19}$$

$$\mathcal{E}_B(k) \;=\; |\widetilde{\epsilon}_B(k)|^2 \;=\; 4\,\mathcal{R}_B(k)\;\mathcal{T}_B(k). \tag{5.20}$$

The spectral power density of the source is

$$S_o(k) = |\widetilde{E}_o(k)|^2 \tag{5.21}$$

At this point it is convenient to switch from the "theoretical" variables (ω and k) to the "experimental" variables (ν and $\breve{\nu}$). Combining equations 5.17, 5.18, and 5.19, and integrating over the whole spectrum we get the total intensity incident onto the detector.

$$I_D(d) \;=\; \frac{1}{4}\int_0^\infty S_o\,(\breve{\nu})\,\mathcal{E}_B(\breve{\nu})\;\left\{r_\alpha^2(\breve{\nu}) \;+\; r_\beta^2(\breve{\nu})\right. \tag{5.22}$$

$$\left. +\,2\,r_\alpha(\breve{\nu})\,r_\beta(\breve{\nu})\,\cos\left[\breve{\nu}\,d \;+\; \phi(\breve{\nu})\right]\right\}\;\mathrm{d}\breve{\nu}$$

As the displacement d of the moving mirror increases, the cosine oscillates faster and faster and if d could grow to infinity the cosine would vanish at its average value.

$$I_\infty = \lim_{d\to\infty} I_D(d) = \frac{1}{4}\int_0^\infty S_o\,(\breve{\nu})\,\mathcal{E}_B(\breve{\nu})\;\left[r_\alpha^2(\breve{\nu}) \;+\; r_\beta^2(\breve{\nu})\right]\;\mathrm{d}\breve{\nu} \tag{5.23}$$

Another special case is when both d and ϕ, and it is called "zero path difference" or "white-light position" of the moving mirror

$$I_o \;=\; I_D(0) = \frac{1}{4}\int_0^\infty S_o\,(\breve{\nu})\,\mathcal{E}_B(\breve{\nu})\;[r_\alpha(\breve{\nu}) \;+\; r_\beta(\breve{\nu})]^2\;\mathrm{d}\breve{\nu} \tag{5.24}$$

If the two mirrors were perfect, then $r_\alpha(\breve{\nu}) = -1 = r_\beta(\breve{\nu})$ and the immediate consequence would be $I_o = 2I_\infty$. For good mirrors this relationship is approximately true.

The quantity that is actually measured by the detector of a Fourier-transform interferometer is the interferogram, that is, the deviation of the intensity $I_D(d)$ from the average intensity I_∞ for each position d of the moving mirror.

$$\begin{aligned}\gamma(d) = I_D(d) - I_\infty \;&=\; \frac{1}{2}\int_0^\infty S_o\,(\breve{\nu})\,\mathcal{E}_B(\breve{\nu})\,r_\alpha(\breve{\nu})\,r_\beta(\breve{\nu})\,\cos\left[\breve{\nu}\,d \;+\; \phi(\breve{\nu})\right]\mathrm{d}\breve{\nu}\\ &=\; \frac{1}{2}\int_0^\infty \mathfrak{S}_D(\breve{\nu})\,\cos\left[\breve{\nu}\,d \;+\; \phi(\breve{\nu})\right]\mathrm{d}\breve{\nu} \end{aligned}\tag{5.25}$$

where, as the various factors clearly indicate, the spectrum $\mathfrak{S}_D(\breve{\nu})$, "seen" by the detector, combines information about the light source, the beam-splitter, the two mirrors, and if a sample is mounted anywhere in the path of the beam, then there will be another spectral-density factor to account for the sample effect, as well

$$\mathfrak{S}_D(\breve{\nu}) = S_o\,(\breve{\nu})\,\mathcal{E}_B(\breve{\nu})\,r_\alpha(\breve{\nu})\,r_\beta(\breve{\nu}) \tag{5.26}$$

In some spectrometers when measuring reflectance, the sample can replace one of the mirrors (usually the fixed one). Such a configuration yields not only information about the amplitude, but also about the phase of the complex reflection constant.

The response $\gamma(d)$ will be real, provided the spectrum at the detector is hermitian, and if that is the case, by representing the cosine as a sum of two exponential functions $\cos[\breve{\nu}\, d + \phi(\breve{\nu})] = \{e^{\mathrm{i}\,[\breve{\nu}\, d + \phi(\breve{\nu})]} + e^{-\mathrm{i}\,[\breve{\nu}\, d + \phi(\breve{\nu})]}\}/2$ we can make a transition from the cosine Fourier transformation (equation 5.25) to the exponential Fourier transformation.

$$\gamma(d) = \frac{1}{4} \int_{-\infty}^{\infty} \mathfrak{S}_D(\breve{\nu})\, \mathrm{e}^{\mathrm{i}\,[\phi(\breve{\nu})\, +\, \breve{\nu}\, d]}\, \mathrm{d}\breve{\nu} \tag{5.27}$$

From equations 5.25 and 5.27 it is clear that the spectrum is the Fourier transform of the interferogram, and vice versa. Indeed, taking the inverse Fourier transformation on both sides of equation 5.27, we get

$$\mathfrak{S}_D(\breve{\nu})\, \mathrm{e}^{\mathrm{i}\,\phi(\breve{\nu})} = \frac{2}{\pi} \int_{-\infty}^{\infty} \gamma(d) \mathrm{e}^{-\mathrm{i}\,\breve{\nu}\, d}\, \mathrm{d}d \tag{5.28}$$

Now it is clear that if we measure the interferogram $\gamma(d)$ and want to get the spectrum $\mathfrak{S}_D(\breve{\nu})$ we may get the product of the spectrum and an exponential phase factor. Various precautions must be taken to avoid such phase errors. Care must be taken to align the spectrometer and the sample properly. On a slow-scan interferometer a check can be done by ensuring that $I_o = 2I_\infty$. One way of phase correction is to multiply the product obtained from equation 5.28 by the reciprocal exponential function $\mathrm{e}^{-\mathrm{i}\,\phi(\breve{\nu})}$.

Another type of error is due to the discrete sampling. Ideally one of the sampled points must be at the zero path difference or white-light position, but this is extremely hard to accomplish. Mathematically speaking a discrete sampling is equivalent to multiplying the continuous spectrum by a finite sum of Dirac $\delta(d)$ functions that are shifted step-wise with a one-dimensional spatial period of l called a "shah"-function. Therefore a sampled interferogram will be

$$\gamma_s(d) = \gamma(d) \sum_{j=\infty}^{\infty} \delta(d - jl - \xi). \tag{5.29}$$

where l is the sampling interval. Then the inverse transformation will result in

$$\mathfrak{S}_D(\breve{\nu})\,\mathrm{e}^{\mathrm{i}\,\phi(\breve{\nu})} = \frac{2}{\pi}\sum_{j=\infty}^{\infty}\delta(jl-\xi)\mathrm{e}^{-\mathrm{i}\,\breve{\nu}\,[jl+\xi]}. \tag{5.30}$$

Clearly the discrete character of the sampling imposes another phase correction needed to restore the spectrum

$$\mathfrak{S}_D(\breve{\nu}) = \frac{2}{\pi}\,\mathrm{e}^{-\mathrm{i}\,[\phi(\breve{\nu})+\breve{\nu}\xi]}\sum_{j=\infty}^{\infty}\delta(jl-\xi)\mathrm{e}^{-\mathrm{i}\,\breve{\nu}\,jl}. \tag{5.31}$$

Two important results can be deducted from these transformations: the discrete sampling brings another phase factor $\mathrm{e}^{-\mathrm{i}\,\breve{\nu}\xi}$ which must be taken care of, and additionally, the spectrum is rendered periodic which can lead to aliasing and folding.

A third unavoidable source of error is the finite scanning range for the moving mirror. This inevitably imposes a "box-car" ("top hat") apodization, as if an imaginary ideal interferogram with an infinite scanning range has been truncated by multiplication with the following apodization function

$$A(x) = \begin{cases} 0 & \text{for } x < -L_1 \\ 1 & \text{for } -L_1 \le x \le L_2 \\ 0 & \text{for } x > L_2 \end{cases} \tag{5.32}$$

where L_1 is the distance covered by the moving mirror on one side of the white-light position, whereas L_2 is the distance covered by the moving mirror on the other side of the white-light position.

Transforming the product of the ideal interferogram and the apodization function is the reason why now the spectrum is actually the convolution of the "real" spectrum with the apodization function. The Fourier transform of the boxcar apodization, $A(x)$ is a $\mathrm{sinc}(x)$ function [$\mathrm{sinc}(x) = \sin(x)/x$.] The characteristic width of the latter function is $1/L_2$. If a single sine wave of wave number $\breve{\nu}_1$ were convolved with a boxcar apodization characterized by a maximum length L_2, the resultant spectrum would be a sinc(x) function centered at $\breve{\nu}_1$ with width $1/L_2$. Thus, the resolution is limited to $\Delta\breve{\nu} \approx 1/L_2$. An additional drawback is that the convolution also introduces "ghost" side lobes near sharp features in the spectrum. These side lobes may be reduced by multiplying the interferogram by using a different apodization function but this will come at the cost of a further reduction in resolution.

5.2.2 Details of FT-IRS

Further details on Fourier-transform infrared spectroscopy can be found in the three articles Herres and Gronholtz [107,112,113], as well as in several specialized books [105,110,111,114,115]. Some of the interesting points covered therein include

- picket fence effect and zero filling;
- aliasing and undersampling;
- leakage, apodization, and reduced resolution;
- phase correction;
- fringes, thickness determination, and elimination;
- apodization and smoothing;
- deconvolution;
- various types of interferometers and details about their components.

5.3 Equipment

5.3.1 Bruker FT-IR Interferometer. Reflection Stage.

The commercial Fourier-transform interferometer 113v manufactured by Bruker company, which was used for most of our measurements, is shown in Figure 5.1. This is a fast-scan instrument which consists of six major chambers and two auxiliary used for switching of the two channels:

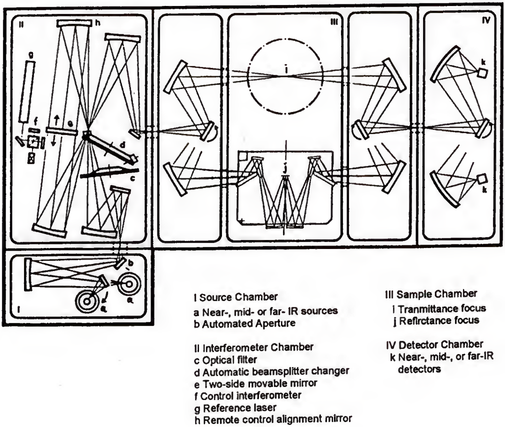

Figure 5.1: Schematic diagram of Bruker 113v Fourier-transform infrared interferometer. The bottom channel is furnished with a reflection stage used to measure reflectance.

1. source chamber (bottom, left),

2. interferometer chamber

3. sample chamber
4. detector chamber

To avoid the infrared bands of water vapor, CO_2, the spectrometer is evacuated most of the time, except for servicing, changing samples and alignment. This instrument has two symmetrical channels. We have furnished the bottom channel with a custom-made reflection stage suitable for our reflectance measurements. In the far-infrared a mercury arc lamp is used as the source of light.

5.3.2 Bolometer

In order to take data with a high signal-to-noise ratio we have used an external silicon bolometer, cooled with liquid helium and pre-cooled with liquid nitrogen. A schematic diagram of this bolometer is shown on Figure 5.2. Within the housing there are a top dewar for liquid nitrogen, which extends down into a thermally-shielding jacket for the lower dewar which is for helium. On the bottom of the helium dewar, from below, the silicon detector is mounted. Additionally, on the side a preamplifier is mounted which picks up the tiny signals and saves them from the background noise. There is window for the signal as well a choice of three filters.

The other interferometer that we have used is a custom made slow-scan Michelson interferometer. This interferometers, as well as sample-holders, cryogenic, and vacuum equipment, have been described by recent graduate students—now all of them are PhDs—of Dr. Tanner in their dissertations. Some of these students (Mr. Gao, Mr. Quijada, Mr. Yoon, Ms. Tache, Mr. Kumar) also studied cuprates [116–120], whereas others (Ms. John, Mr. LaVeigne, and Mr. Hwang) studied different materials [121–123], but have used the same equipment and sim-

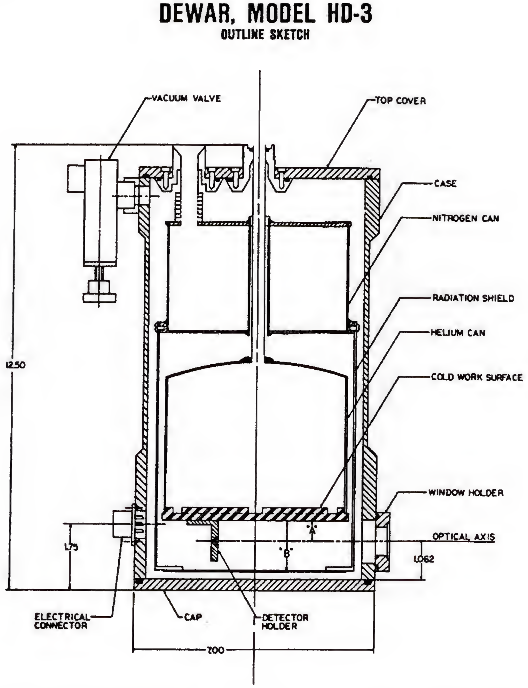

Figure 5.2: Schematic diagram of a silicon bolometer, cooled with liquid helium.

ilar experimental techniques. A reference to their descriptions allows me not to dwell on such matters herein.

5.4 Samples

The samples we studied and their preparation has been described in our papers [124,108,125,37], and in the dissertation of my collaborator A. Ravi Kumar [120]. The basics of using laser ablation for preparation of thin cuprate films are given in the dissertation of Dr. Tache [119].

For transmittance measurements it is irrelevant whether the incidence is onto the back surface or onto the front surface of the sample. However, unless we are dealing with a single, flat-plate layer, the reflectance from the front-side is, in general (provided the layers are not ordered symmetrically), different from the back-side reflectance.

The nominal structure of Sample NIST 255 is presented in Figure 5.3, which also illustrates the sample configuration used for measurement of back-side reflectance. In order to avoid unnecessary complication of the picture, only first-order reflections from each interface are shown on the figure. The beam[15] reflected from the back-side of the sample is the result of superposition of all partial beams generated due to multiple-beam interference.

The nominal structure of Sample NIST 256 is presented in Figure 5.4, which also illustrates the sample configuration used for measurement of front-side reflectance. In order to avoid unnecessary complication of the picture, only first-order reflections from each interface are shown on the figure. The beam reflected from the front-side of the sample is the result of superposition of all partial beams generated due to multiple-beam interference.

---

[15] For simplicity any beam is represented with a single ray denoted by an arrow which indicates the direction of propagation.

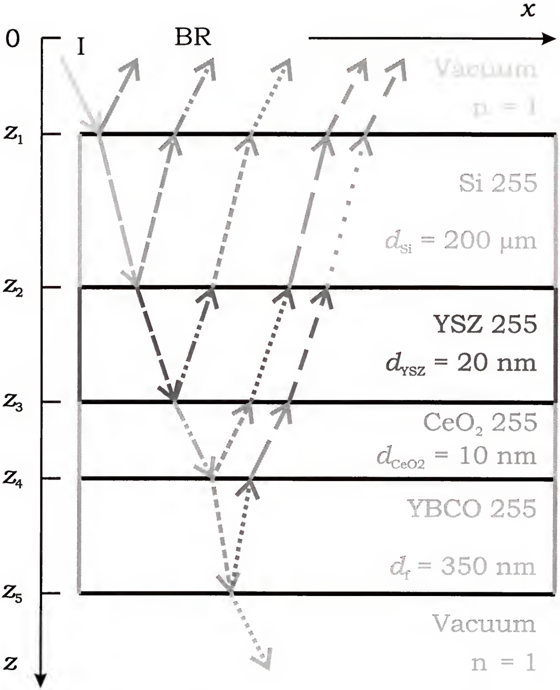

Figure 5.3: Structure of Sample NIST 255 and its configuration in back-side reflectance measurements.

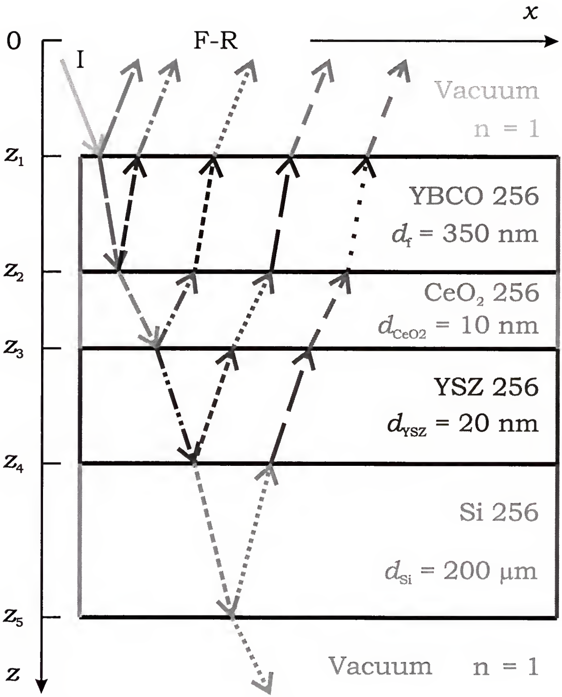

Figure 5.4: Structure of Sample NIST 256 and its configuration in front-side reflectance measurements.

The nominal structure of Sample NIST 256 is presented once more in Figure 5.5, which also illustrates the sample configuration used for measurement of transmittance. In order to avoid unnecessary complication of the picture, only first- and second-order reflections within each layer, that is, one reflection from each side of any interface, are shown on the figure, and the picture is "unfolded" by shifting all beams after the reflected-back primary beam to the left, parallel to the interface.

The nominal structure of Sample NIST 73 is presented in Figure 5.6, which also illustrates the sample configuration used for measurement of back-side reflectance. In order to avoid unnecessary complication of the picture, only first-order reflections from each interface are shown on the figure. The beam reflected from the back-side of the sample is the result of superposition of all partial beams generated due to multiple-beam interference.

The nominal structure of Sample NIST 74 is presented in Figure 5.7, which also illustrates the sample configuration used for measurement of front-side reflectance. In order to avoid unnecessary complication of the picture, only first-order reflections from each interface are shown on the figure. The beam reflected from the front-side of the sample is the result of superposition of all partial beams generated due to multiple-beam interference.

The nominal structure of Sample NIST 73 is presented once more in Figure 5.8, which also illustrates the sample configuration used for measurement of transmittance. In order to avoid unnecessary complication of the picture, only first- and second-order reflections within each layer, that is, one reflection from each side of any interface, are shown on the figure, and the picture is "unfolded" by shifting all beams after the reflected-back primary beam to the left, parallel to the interface.

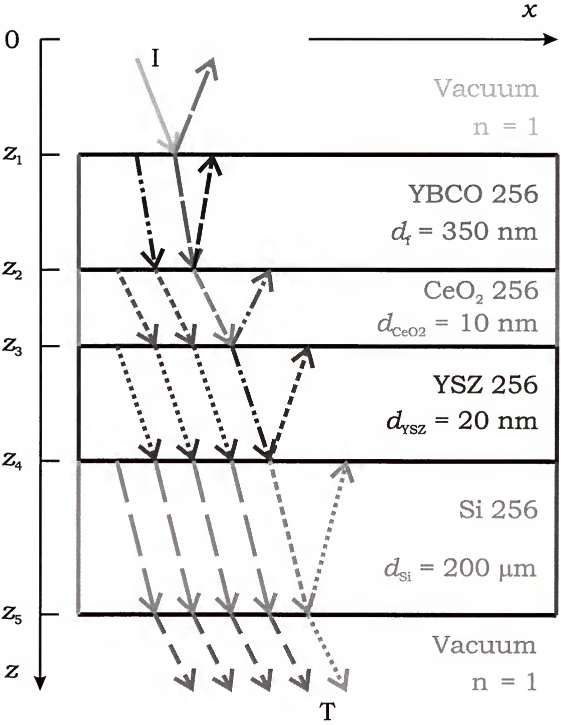

Figure 5.5: Structure of Sample NIST 256 and its configuration in transmittance measurements.

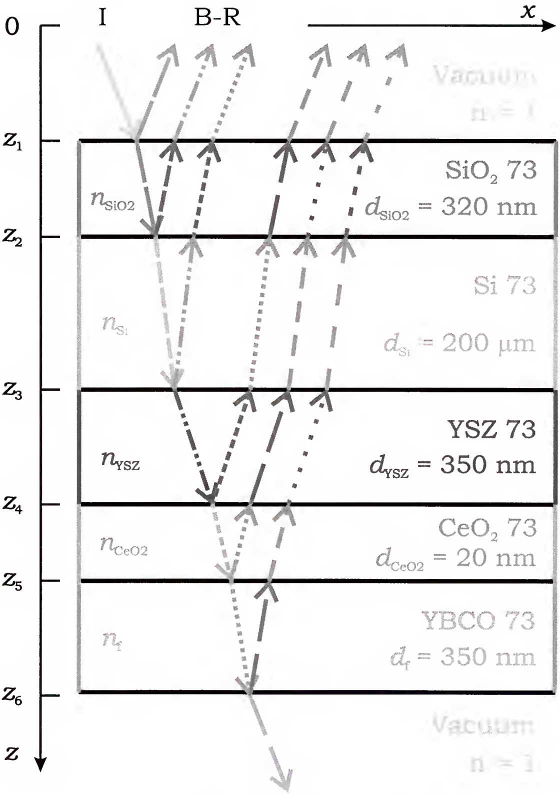

Figure 5.6: Structure of Sample NIST 73 and its configuration in back-side reflectance measurements.

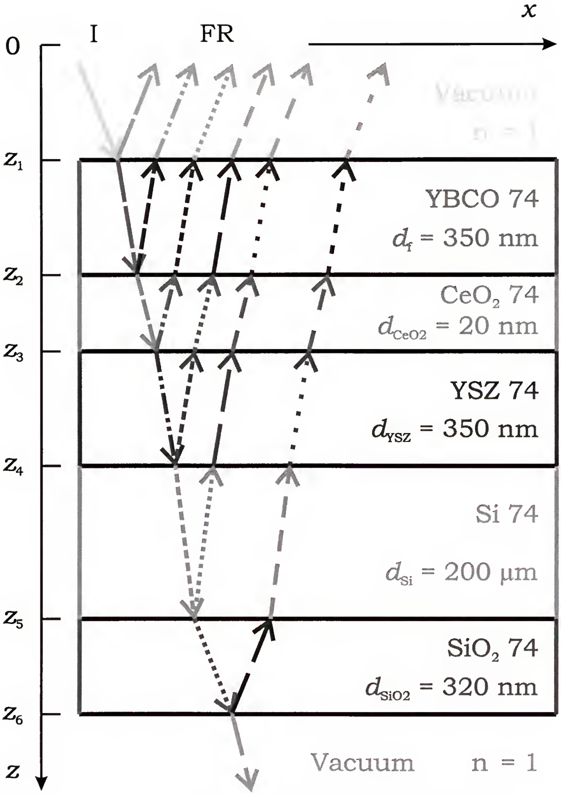

Figure 5.7: Structure of Sample NIST 74 and its configuration in front-side reflectance measurements.

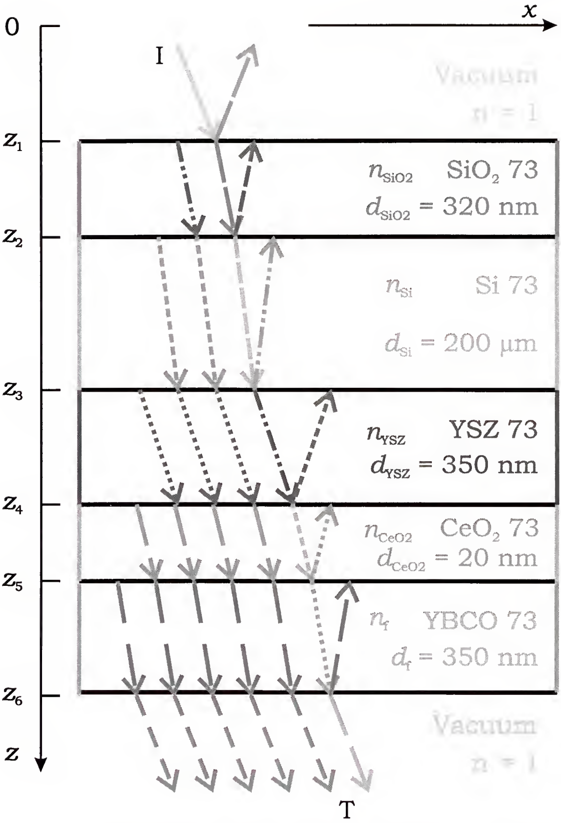

Figure 5.8: Structure of Sample NIST 73 and its configuration in transmittance measurements.

Above, the structure of any of the four $YBa_2Cu_3O_{7-\delta}$ samples has been shown at least once, and every one of the three possible configurations (for measuring front-side reflectance, back-side reflectance, and transmittance) is shown twice, with two different samples.

CHAPTER 6
TRANSMITTANCE AND REFLECTANCE

6.1 Introduction

This chapter includes a description of our transmittance and reflectance measurements, the experimental data, as well as analysis of the data and discussion of the results. Generally, the reflectance would be reversible only for the case of a single layer. If two or more layers are present, such a symmetry is no longer present. That is why we have measured both front-side[1] and back-side[2] reflectance.

We have measured two batches of $YBa_2Cu_3O_{7-\delta}$ on Si substrates with buffer layers of YSZ[3] and CeO_2. This dissertation presents data taken on the best[4] two samples from each batch: Samples NIST 255 and NIST 256 from the earlier batch, and Samples NIST 73 and NIST 74 from the more recent batch. The samples from the latter batch had five layers: SiO_2, Si substrate, two buffer layers (YSZ and CeO_2), and $YBa_2Cu_3O_{7-\delta}$-film. The samples from the first batch had their SiO_2 layer removed, and additionally their buffer layers were thinner, especially the YSZ layer whose thickness differed by an order of magnitude. The thicker buffer layers of the second batch were meant to allow deposition of higher-quality $YBa_2Cu_3O_{7-\delta}$–films.

---

[1] Front-side reflectance is measured with the incident ray coming from the side of the top layer. For Samples NIST 255, NIST 256, NIST 73 and NIST 74 the top layer is the $YBa_2Cu_3O_{7-\delta}$ film; for Samples NIST 02 (a substrate only) and NIST 39 (a substrate with buffer layers, but without an YBCO film) the top layer is Silicon and CeO_2, respectively.

[2] Back-side reflectance is measured with the incident ray coming from the SiO_2 side, or, in case the oxide layer has been removed, from the Si side.

[3] yttria-stabilized zirconia, i.e., ZrO_2 stabilized with about 5 % Y_2O_3

[4] Actually, NIST 256 was the second best match for NIST 255, but it had to replace the former best match which was broken due to mechanical stress caused by the thermal gradient within the sample holder.

The transmittance through the first group of samples, including Samples NIST 255 and NIST 256, was measured within the spectral range from 10 to 100 cm^{-1} on a slow-scan Michelson interferometer, and the front-side and back-side reflectance from these samples were measured on a fast-scan Bruker interferometer within the spectral range from 20 to 600 cm^{-1}. While analyzing the data for this first batch of samples, we were concerned with the low-frequency region (below 100 cm^{-1}) only, even though the reflectance measurements covered a wider spectral range. This restriction allowed us to ignore excitations at medium or high frequencies and simplified our analysis significantly. Concentrating our attention on the low-frequency region, we were able to use only one beam-splitter with the slow-scan Michelson interferometer. This saves a lot of time, because not only the measurements on our Michelson interferometer last approximately four times longer than respective measurements on the fast-scan Bruker interferometer, but the changing and aligning of the beam splitter in the Michelson interferometer is manual, unlike the computer-controlled changes of beam splitters in the Bruker. The beam splitter we used gradually loses its efficiency below about 20 cm^{-1} or above ca. 80 cm^{-1} which adds random noise to the data in these two regions, especially when the signal is small. The noisiest portions of the transmittance data have been removed.

During the measurements the temperature was kept fixed at one of five different values: two corresponding to the $YBa_2Cu_3O_{7-\delta}$ film in the superconducting state (10 and 50 K), and three in the normal state (100, 200, and 300 K). Before studying the $YBa_2Cu_3O_{7-\delta}$ films on Si substrates, we started with measuring a couple of the silicon plates with neither buffer layers nor an $YBa_2Cu_3O_{7-\delta}$ film deposited on top. These measurements on Si allowed us to study the effect of temperature on the optical thickness of Si, and to check for any spectral offsets between the two spectrometers we were using.

The second batch of samples, including Samples NIST 73 and NIST 74, was measured on a fast-scan Bruker interferometer within the spectral range from 20 to 600 cm^{-1}. The measurements were done at all temperatures mentioned above, and additionally at 20 K. The measurements at 10 K and 20 K turned out to be almost identical, to within the experimental uncertainty and background noise. Later, Si plates with a thin layer of SiO_2 on the bottom side, including Sample NIST 02, were measured, as well as such substrates covered with the two buffer layers of yttria-stabilized zirconia and CeO_2, including Sample NIST 39. These measurements of structures with reduced number of layers were meant to help us fit the five-layered structures more accurately—by gradually increasing the number of layers to be fit.

The thickness of the $YBa_2Cu_3O_{7-\delta}$ films was about 35 nm. Thus, the films were quite transparent at all temperatures. This allowed us to observe the interference fringes associated with multiple reflections within the Si substrate. Therefore, in our analysis of the data, we have assumed that we are dealing with a thin film on a thin substrate. Background information about the classical models we have used for fitting of the transmittance and reflectance of the samples is presented in subsection 3.1.5. The Drude-Lorentz model, equations 3.67, 3.68, and 3.48, applied for the dielectric function of high-temperature superconductors in general, and $YBa_2Cu_3O_{7-\delta}$ in particular, in the normal state leads to equation 4.2 [23, p. 367] in which the contribution of a single mid-infrared oscillator describing electron transitions is taken out of the Lorentz sum, and what is left of that sum accounts for the several infrared-active phonon oscillators. This equation can be generalized further by replacing the single mid-infrared term with a sum of several such terms (a number which increases from one to two or three with increasing the upper bound of the studied spectral range). Thus the Lorentz term is rendered into the following form: describing phonons.

$$\begin{aligned}\widetilde{\varepsilon}_L &= \sum_{\substack{i=1\\ \omega_{ei}\neq 0}}^{3} \frac{S_{ei}\omega_{ei}^2}{\omega_{ei}^2 - \omega^2 - \mathrm{i}\,\Gamma_{ei}\omega} + \sum_{\substack{j=1\\ \omega_{pj}\neq 0}}^{\mathcal{N}} \frac{S_j\omega_j^2}{\omega_j^2 - \omega^2 - \mathrm{i}\,\Gamma_j\omega} \\ &= \sum_{\substack{i=1\\ \omega_{ei}\neq 0}}^{3} \frac{\omega_{pei}^2}{\omega_{ei}^2 - \omega^2 - \mathrm{i}\,\Gamma_{ei}\omega} + \sum_{\substack{j=1\\ \omega_{pj}\neq 0}}^{\mathcal{N}} \frac{\omega_{pj}^2}{\omega_j^2 - \omega^2 - \mathrm{i}\,\Gamma_j\omega}, \end{aligned} \tag{6.1}$$

where S_{ei} is the oscillator strength, ω_{pei} the plasma angular frequency, ω_{ei} the central angular frequency, and Γ_{ei} the width for the i^{th} mid-infrared oscillator describing electronic transitions; similarly, S_j is the oscillator strength, ω_{pj} the plasma angular frequency, ω_j the central angular frequency, and Γ_j the width for the j^{th} phonon oscillator, respectively.

In the superconducting state, applying the two-fluid model to equation 4.4 leads to the following result for the dielectric function:

$$\begin{aligned}\widetilde{\varepsilon}(\omega) = \varepsilon_\infty - (1 - f_s)\frac{\omega_p^2}{\omega(\omega + \mathrm{i}/\tau)} - f_s\frac{\omega_{ps}^2}{\omega^2} + \mathrm{i}\, f_s\frac{\pi\omega_{ps}^2}{2\omega}\,\delta(\omega) + \\ \sum_{\substack{i=1\\ \omega_{ei}\neq 0}}^{3} \frac{\omega_{pei}^2}{\omega_{ei}^2 - \omega^2 - \mathrm{i}\,\Gamma_{ei}\omega} + \sum_{\substack{j=1\\ \omega_{pj}\neq 0}}^{\mathcal{N}_{ph}} \frac{\omega_{pj}^2}{\omega_j^2 - \omega^2 - \mathrm{i}\,\Gamma_j\omega}. \end{aligned} \tag{6.2}$$

where f_s is the fraction of superconducting charge carriers, and hence $(1-f_s)$ is the complementary fraction of normal charge carriers. The term with the $(1-f_s)$ factor is the Drude contribution of the normal fluid, whereas the terms multiplied by f_s are the contribution of the superconducting fluid which includes the Dirac $\delta(\omega)$-function. The latter describes the infinite DC conductivity of the superconducting fluid. By substituting formally $f_s = 0$ into equation refE:EpsDLz2fluid we can return to the Drude-Lorentz model for the normal state.

For our earlier results the Si substrate, which is transparent in the far-infrared region (below 400 cm^{-1}), was modelled with a simple refractive index, constant with frequency, but with a slight temperature dependence.

Presented, analyzed and discussed within this chapter are the measured spectra and the fits to these spectra, the parameters that were associated with the best fits, the calculated spectral dependencies of the $YBa_2Cu_3O_{7-\delta}$ complex refractive index, complex dielectric function and complex conductivity, as well as the antireflection and resonance effects. Since the second batch of samples was measured within a wider spectral range, we had to include into our model not only the three mid-infrared band of $YBa_2Cu_3O_{7-\delta}$, but also some of the well-known phonons in four of the five layers: the thin SiO_2 layer on the back side of the substrate, the Si substrate, the inner, YSZ buffer layer, and the $YBa_2Cu_3O_{7-\delta}$ film. Another reason requiring that approach was the presence of a significantly thicker YSZ buffer layer. For the second batch of samples this layer was 200 nm, compared to 20 nm for the earlier samples. But we were still able to ignore the phonons of the outer buffer layer of CeO_2 which though thicker by 50 % than previously is still thin enough and does not absorb within the covered spectral range. However, in order to improve the accuracy of the fits for these samples, the CeO_2 layer was modelled by a plain dielectric constant, whereas for the earlier samples that layer had been ignored totally.

Preceding the results for the $YBa_2Cu_3O_{7-\delta}$ films, some data for the Si substrates and their analysis are presented below. For the first batch of samples, the transmittance through a naked Si substrate was measured at 10 K, 100 K, and 300 K and the reflectance was measured at those three temperatures and additionally at 50 K and 200 K. For the more recent batch of samples, Si substrates both without buffer layers (only with 320 nm SiO_2 on the back side—Sample NIST 02) and with buffer layers (Sample NIST 39), were measured at 10 K, 20 K, 50 K, 100 K, 200 K, and 300 K.

It should be pointed out that as a rule at any fixed temperature, the same fitting parameters have been used for all three sets of spectra: transmittance, front-side reflectance, and back-side reflectance.[5] Furthermore, most parameters were temperature independent. Weak temperature dependencies of the phonon oscillators were ignored. Only the temperature dependence of the optical thickness of Si, as well as the Drude scattering rate and the fraction of the superconducting electrons in the $YBa_2Cu_3O_{7-\delta}$ film were taken into account.

6.2 Measurements of Silicon Substrates

6.2.1 Naked Silicon Substrates

The transmittance and reflectance of the Si substrate were measured at different fixed temperatures in order to evaluate the optical thickness of Si (the product refractive index n_{Si} times thickness d_{Si} of Si), as well as the uncertainty of the measurements. The refractive index of single-crystal Si has been studied in detail for the needs of the semiconductor industry. In order to eliminate any absorption in the substrate we have used intrinsic single-crystal Si of high-resistivity.

We have measured the transmittance through and reflectance from a bare Si substrate (whose SiO_2 layer has been stripped mechanically) Figure 6.1 presents the measured reflectance and transmittance of a Si substrate at 300 K. It can be seen clearly, that the transmittance maxima coincide with the reflectance minima, as one would expect. This fact holds true for any fixed temperature, even though the curves do have a temperature dependence.

---

[5] Several exceptions are mentioned later and are specifically designated as alternate fits.

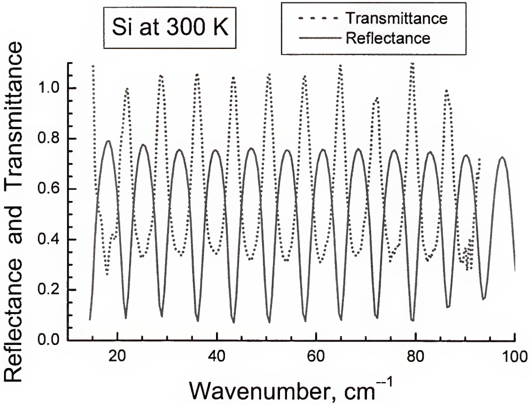

Figure 6.1: Room temperature transmittance through and reflectance from a Si substrate whose SiO_2 layer has been removed mechanically.

The transmittance through a bare Si substrate measured at 10, 100 and 300 K is presented in Figure 6.2 where the curves are overlayed for an easy comparison. The same transmittance data, with the fits to them, are shown in Figure 6.3.

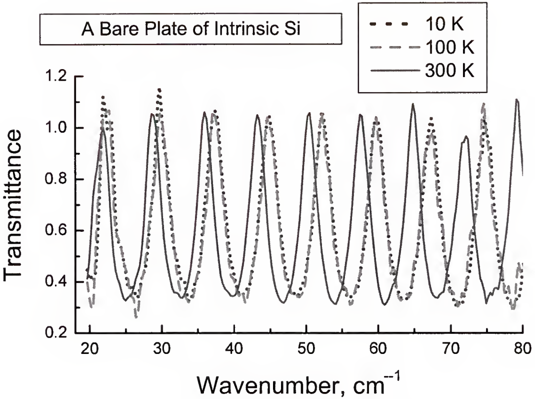

Figure 6.2: Temperature dependence of the transmittance through a Si substrate whose SiO_2 layer has been removed mechanically.

The alignment for the transmittance configuration is more straight-forward and less prone to inaccuracy than the alignment for the reflectance configuration. Additionally, the transmittance measurement is free from the parasitic effect discussed earlier, and therefore produces the most accurate and reliable data. The envelopes of the curves do not depend on temperature. There is only a slight temperature dependence of the refractive index of Si which causes a slight temperature variation of the free spectral range at high temperatures, but below 50 K it is virtually constant.

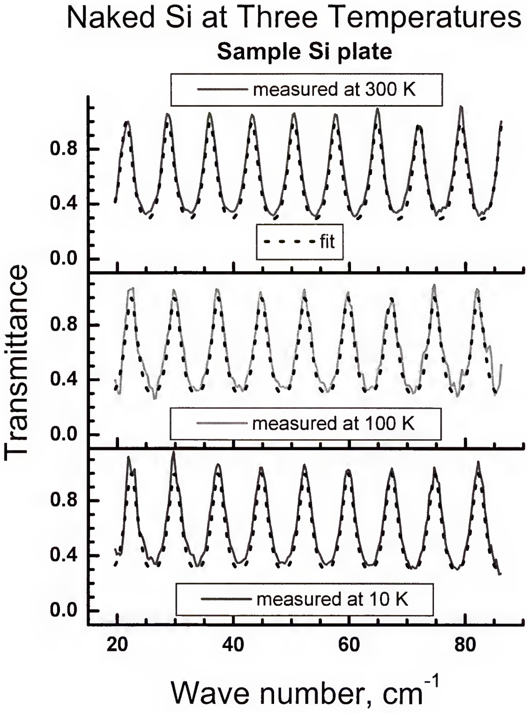

Figure 6.3: Measured temperature dependence and fits of the transmittance through a Si substrate whose SiO_2 layer has been removed mechanically.

In the case of a naked Si substrate, however, we are most interested in the spectral positions of the fringes, which allow us to determine the optical thickness of of the silicon plate and from it to derive the refractive index and permittivity of the Si plate. For such a purpose the reflectance data are as good.

The measured spectra of reflectance from a naked Si substrate, with the fits to them, are shown in Figure 6.4 (at 300 K, 200 K, and 100 K) and Figure 6.5 (at 50 K and 10 K).

A thin Si plate comprises essentially a Fabry-Perot resonator. Such resonators are the subject of Chapter 8 and the related terminology is introduced therein. The free spectral range is the interval of some spectral variable, (e.g., the wave length, wave number, frequency), between two interference maxima. It is related to the optical thickness of Si by the equation[6]

$$\Delta\omega = (2n_{Si}d_{Si})^{-1}. \tag{6.3}$$

And indeed, the data show the typical Fabry-Perot interference patterns, characterized in our case with maxima $T_{max} \lesssim 1$, minima $T_{min} \approx 0.3$, and a free spectral range $\Delta\omega \approx 7$ cm^{-1}. E.g., the 300 K curve is characterized by seven minima within the spectral range from 25 to 75 cm^{-1}which gives a free spectral range of 7.14 with two significant digits.

Even though the fringe positions are in an excellent agreement, the values of the extrema do not match quite as well. E.g., near the spectral lower and upper bounds, the maxima values for the transmittance vary between 0.95 and 1.05 or even more. This is probably due to imperfect alignment of the interferometer: the

---

[6] Note that in the equations we use the angular frequency, whereas everywhere in the plots we are dealing with the spectroscopic wave number $\tilde{\nu}$ measured in cm^{-1}. The two quantities are proportional with a factor of $2\pi c$. In the plots of our papers [124,108,125,37], due to the jargon strongly-rooted among people working in the infrared field, the spectroscopic wave number is labeled as frequency.

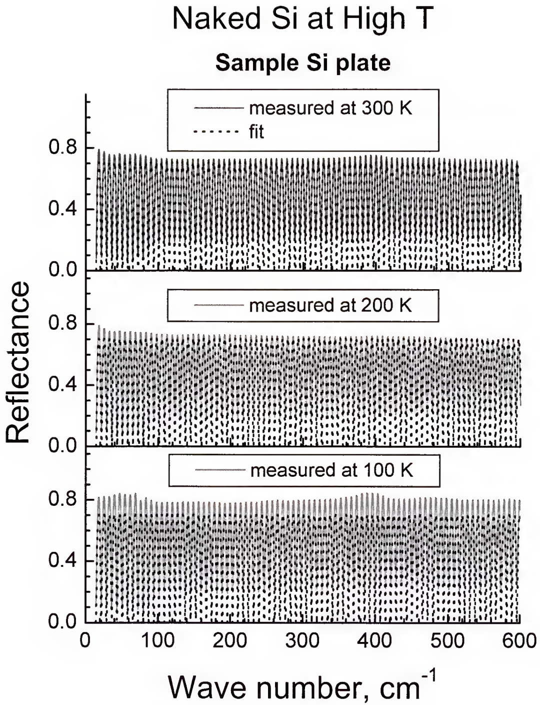

Figure 6.4: Measured reflectance from a naked Si substrate and fits at three high temperatures.

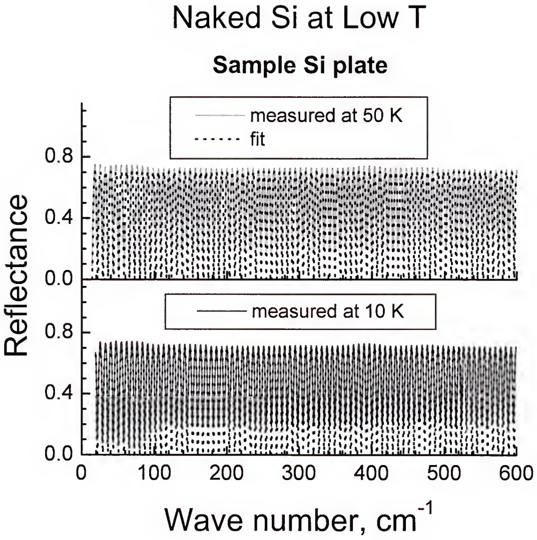

Figure 6.5: Measured reflectance from a naked Si substrate and fits at two low temperatures.

Si substrates are highly transparent in the far-infrared and therefore the multiple-beam interference is very important. Theoretically, the transmittance through Si at all far-infrared maxima should be unity. Thus, a tiny angular deviation of the plate with the reference hole from axial incidence can reduce slightly the background signal and cause the transmittance to exceed 1. However, being only interested in the spectral positions of the fringes, we decided these early data of ours are good enough for our purpose.

Additionally, the reflectance minima never quite reach zero. In the past we had attributed that fact to insufficient spectral resolution. But later measurements with higher resolution disproved that assumption. The root-mean-square difference between the measured and the calculated values gave us a standard uncertainty of about 0.05 in both the transmittance and reflectance. Based on this, the uncertainty was estimated to be bound from above by 10 % for any of our measurements. Such uncertainty is large upon comparison to measurements without sharp interference fringes. It could be due to a variety of reasons: detector nonlinearity, misalignment, phase error, and multiple reflections between the sample, windows, and the beam splitter [111]. Luckily, it turned out that we have overestimated our uncertainty: the number given above is for the substrate measurements only and is caused by a systematic error about which we were unaware at the time.

While writing this dissertation, the repetitive character of reflectance data slightly shifted up with respect to the fits, as well as sum of reflectance and transmittance exceeding unity prompted me to reconsider our initial conclusions. Finally, I realized that some parasitic reflectance is responsible for these anomalies: the sample holder (with the backs of the sample and the reference mirror facing each other) that we have been using is meant to be used with opaque samples; if significant transmittance is present, the transmitted beam is reflected back from the rear side of the reference mirror and is recycled through the sample. Depending on the phase of the parasitic light, it could lead either to increased (for non-absorbing samples) resultant reflectance, or also to decreased (for absorbing samples) resultant reflectance. Unfortunately, this realization came too late, but at least students that work after me will be able to avoid it by appropriately blocking this "channel" which is causing systematic errors. The more transparent the sample is, the larger this parasitic effect will be. A simple way to avoid it is to use a strongly absorbing or dispersive element to separate optically the backs of the sample and the reference mirror.

By fitting the measured reflectance[7] through a naked Si substrate, we have determined the temperature dependence of the far-infrared refractive index and dielectric constant of Si. These results apply for the spectral range from 10 to 100 cm^{-1} and are shown in Table 6.1.

Table 6.1: Refractive index and permittivity of Silicon vs. temperature, optimized for the spectral range 10 to 100 cm^{-1}.

T, K	n_{Si}	$\varepsilon_{\infty}^{(Si)}$
300	3.4161	11.67
200	3.40065 ± 0.00014	11.56445 ± 0.00095
100	3.39032 ± 0.00041	11.4943 ± 0.0028
50	3.38784 ± 0.00016	11.47745 ± 0.00105
10	3.38743 ± 0.00016	11.47465 ± 0.00105

All parameters herein have been determined by finding their respective range which minimizes χ^2 of the fits. The values of the parameters are set to the central point of their range, and half of that range is specified as the uncertainty. This is the very reason why the uncertainties occasionally have more than two digits. The number of digits in the uncertainty must not be thought to imply that ten to the power of double that number scan have been accumulated, as is common in the field of errors and uncertainty statistics. Rather is shows both how "flat" the bottom of the χ^2 parabola for the respective parameter is and where that parabola happens to be intersected by a particular measurement.

---

[7] We chose the to use the reflectance data, because we had a more complete set, measured on a fast-scan instrument at five temperatures in a six-fold wider spectral range, whereas the transmittance was measured on a slow-scan instrument only at three temperatures.

In order to determine these "constants", we have used as reference point the refractive index of Si at 300 K. For simplicity, this value is assumed to be accurate and therefore no uncertainty is specified for it. The refractive index of Si has a very slight frequency dependence: according to Loewenstein et al. [126] n_{Si} increases from 3.4155 at 30 cm^{-1}, through 3.4185 at 100 cm^{-1}, to 3.4200 at 270 cm^{-1}, and remains constant within the spectral range from 270 to 350 cm^{-1}. At 275 meV (2220 cm^{-1}) n_{Si} is 3.423 [127], [128], still not significantly changed. Linear extrapolation of low-wave-number data from Loewenstein et al. [126] leads to n_{Si} = 3.4145 at 10 cm^{-1}. Therefore, from 10 to 100 cm^{-1} n_{Si} increases by only 0.088 %. Linear interpolation between 350 and 2220 cm^{-1}gives n_{Si} = 3.4204 at 600 cm^{-1}. Thus, from 10 to 600 cm^{-1}n_{Si} increases by only 0.17 %. For our purposes, such small spectral variations of n_{Si} can safely be neglected. Because of the above considerations we have assumed that the refractive index of Si depends only on the temperature. Indeed, the 100 cm^{-1} value of n_{Si} grows from 3.3842 at 1.5 K to 3.4185 at 300 K [126], a change of 1.0%. This thermal dependence of n_{Si} is attributed to the weak phonon contribution.

Because silicon is characterized by very low absorption over the spectral range of our interest, we can safely assume that

$$\varepsilon_{\infty}^{(Si)} \approx n_{Si}^2. \tag{6.4}$$

Whenever a large number of fringes is observed within the measured spectral range, even small variations in the optical thickness of Si can be detected. At 300 K, taking $n_{Si} = 3.4165$ (the average of the values at 10 and 100 cm^{-1} [126]) or $\varepsilon_{\infty}^{(Si)} = 11.67$ within the spectral range from 10 to 100 cm^{-1}, from the free spectral range we can determine the Si thickness. For Sample NIST 255 the apparent thickness of Si determined from the transmittance, back-side reflectance, and front-side reflectance data is 205.0, 204.6, and 203.5 μm, respectively. This is not a random variation, and we believe it is due to the fact that the interfaces between the separate layers are not sharp, as it is assumed in our simple model and film-fitting software. While such considerations would account for different effective thickness of Si obtained from the front-side and back-side reflectance data, we would expect the value determined from the transmittance data to be between the other two values. At this moment we do not have a good explanation why the observed values do not agree with that expectation. The average of the three values for the Si layer thickness of Sample NIST 255 is 204.37 μm. To avoid any misunderstanding: the thicknesses mentioned above are determined from data shown later. From the transmittance shown in Fig. 6.2 we can determine the thickness of the blank Si substrate that we have measured, which in general can be slightly different.

We have assumed that the transmittance is measured at normal incidence. Actually, the angles of incidence vary $\pm 9^{o}$ due to divergence of the beam coming out of the light pipe used in our custom-built Michelson interferometer. Nevertheless, the relatively high refractive index of silicon causes the angle of refraction to be small. Therefore, the change in the free spectral range due to non-normal incidence is less than 0.5 %.

Loewenstein et al. [126] pointed that lowering the temperature from 300 to 0 K would cause a thermal contraction of Si by only 2.4×10^{-3} %. According to our data, the free spectral range increases with lowering the temperature. Neglecting the thermal variation of Si thickness, we can confirm that the refractive index of Si decreases as temperature is lowered which is caused by the decreasing contribution of several weak infrared-active phonons.

6.2.2 Bufferless Silicon Substrates (Sample NIST 02)

Recently some more detailed and accurate measurements of the Si substrates were done in a wider spectral range 15–600 cm^{-1}. At first a bufferless Si substrate (Sample NIST 02), with only a thin (320 nm) SiO_2 film on its back side, was measured. The feature that dominates these spectra is the wide oscillator in the SiO_2 layer at about 449 cm^{-1}.

6.2.2.1 Transmittance through Sample NIST 02

The transmittance through Sample NIST 02 is shown in Figures 6.6 (high temperature) and 6.7 (low temperature).

All calculated curves based on the models we are using are shown in black dotted lines. In all cases we found that our data measured at 10 K and at 20 K practically almost coincide. The transmittance measurement is free from the parasitic effect discussed earlier, and therefore produces the most accurate and reliable data. The envelopes of the curves do not depend on temperature. There is only a slight temperature dependence of the refractive index of Si which causes a slight temperature variation of the free spectral range at high temperatures, but below 50 K it is virtually constant as the phonons are mostly "frozen".

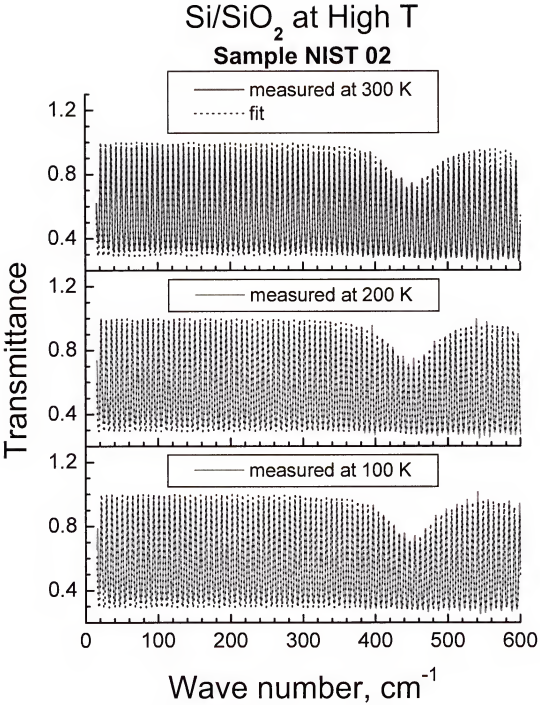

Figure 6.6: High-temperature transmittance through Sample NIST 02: a Si substrate with a thin SiO_2 film on its back side.

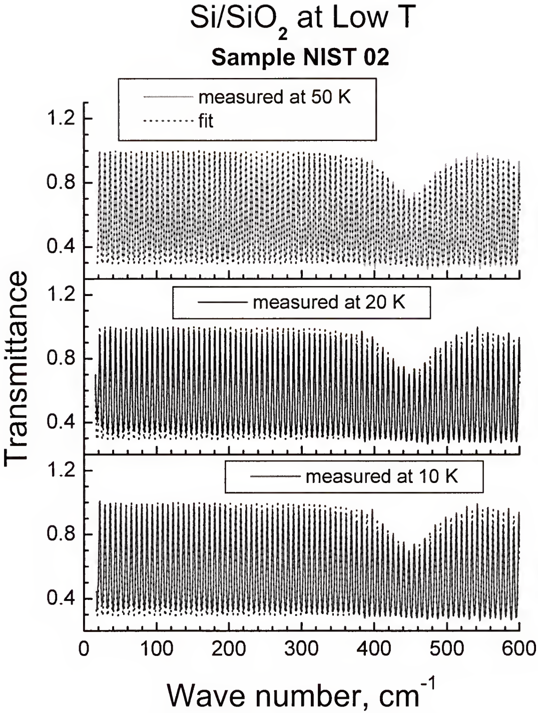

Figure 6.7: Low-temperature transmittance through Sample NIST 02: a Si substrate with a thin SiO_2 film on its back side.

6.2.2.2 Front-side reflectance from Sample NIST 02

The front-side reflectance from Sample NIST 02 is shown in Figures 6.8 (high temperature) and 6.9 (low temperature). The slight shift of 0.02 to 0.04 between the measured and the calculated reflectance curves is most likely due to the parasitic reflectance mentioned earlier.

6.2.2.3 Back-side reflectance from Sample NIST 02

The back-side reflectance from Sample NIST 02 is shown in Figures 6.10 (high temperature) and 6.11 (low temperature).

6.2.2.4 Results for Sample NIST 02 and discussion

Because these later measurements were in a wider spectral range, from 20 to 600 cm^{-1}, at 300 K, we took[8] $n_{Si} = 3.4200$ which is exact for the more than a half of the studied spectral range (from 270 to 600 cm^{-1}) and is quite accurate down to 200 cm^{-1} [126], but is also a reasonably good approximation for the spectral range from 20 to 200 cm^{-1}. Si does not absorb in the far-infrared spectral range except for a few very weak phonon bands, and so we can safely assume that $\varepsilon_{\infty}^{Si} \approx n_{Si}^2$ which gives at room temperature $\varepsilon_{\infty}^{Si} = 11.6964$. Using the latter value, by fitting the spectral positions of the fringes in the measured transmittance at room temperature, we can determine the thickness of the Si layer. Similarly, by fitting the spectral positions of the fringes in the measured transmittance at temperatures below 300 K, we determined (ignoring the small temperature dependence of the thickness of Si) the refractive index of Si at different temperatures. These results

---

[8] The larger number of fringes allows us to use higher precision, hence the couple of extra digits for these more recent measurements.

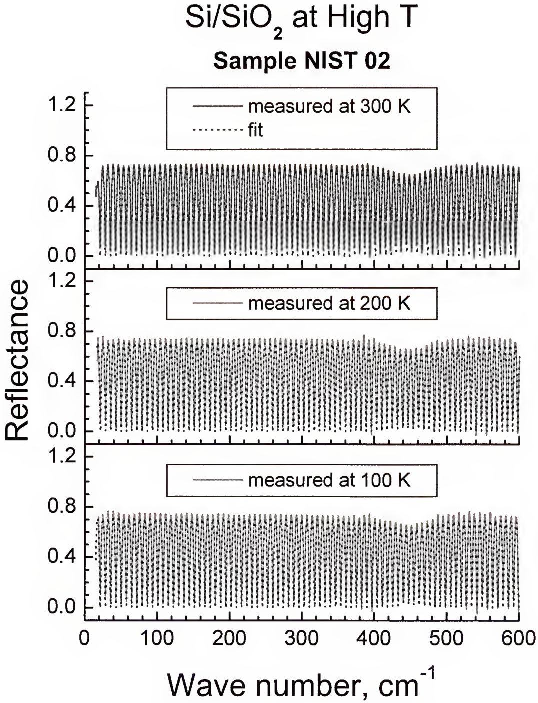

Figure 6.8: Front-side reflectance from Sample NIST 02: a Si substrate with a thin SiO_2 film on its back side at high temperatures.

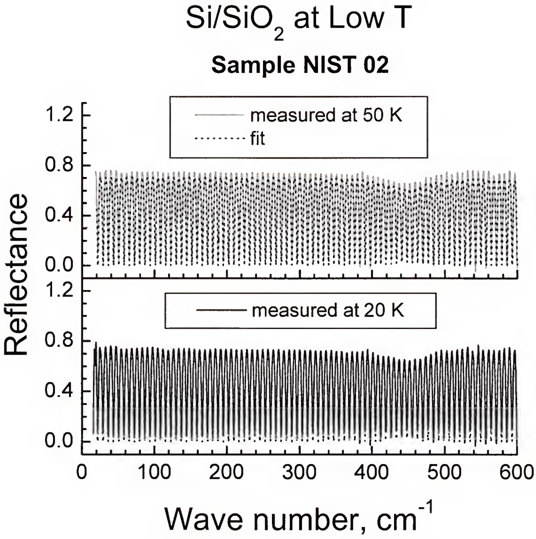

Figure 6.9: Front-side reflectance from Sample NIST 02: a Si substrate with a thin SiO_2 film on its back side at low temperatures.

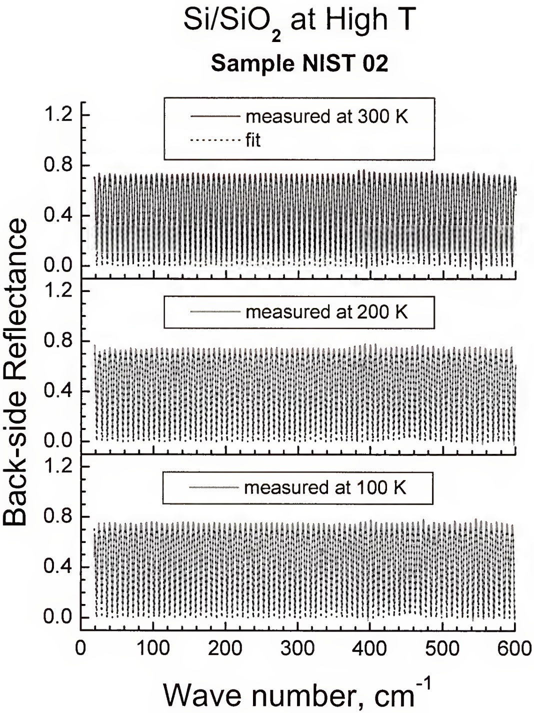

Figure 6.10: Back-side reflectance from Sample NIST 02: a Si substrate with a thin SiO_2 film on its back side at high temperatures.

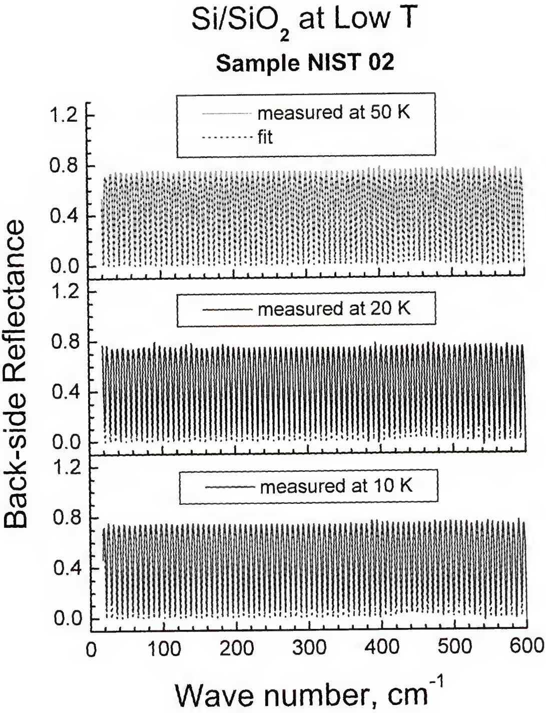

Figure 6.11: Back-side reflectance from Sample NIST 02: a Si substrate with a thin SiO_2 film on its back side at low temperatures.

are shown in Table 6.2, and were obtained by modelling[9] the spectra of both Sample NIST 02 (Si substrate with a SiO_2 layer only) and Sample NIST 39 (a substrate with two buffer layers whose spectra are shown next). These values of the dielectric constants are most suitable for the spectral range from about 200 to 600 cm^{-1}. Because of the wider spectral range that was used to calculate them, they have a couple of more significant digits than the results shown earlier in Table 6.1. The room-temperature values have been used as a reference point and so no uncertainty has been estimated for them.

Table 6.2: Refractive index and ε_∞ of Silicon vs. temperature optimized for the spectral range from 200 to 600 cm^{-1}.

T, K	n_{Si}	$\varepsilon_\infty^{(Si)}$
300	3.4200	11.6964
200	3.4063 ± 0.00010	11.6027 ± 0.0002
100	3.3962 ± 0.0004	11.5344 ± 0.0007
50	3.3942 ± 0.0003	11.5205 ± 0.0005
20	3.3938 ± 0.0003	11.5182 ± 0.0005
10	3.3938 ± 0.0002	11.5181 ± 0.0004

Of course, our measurements only give the optical thickness of silicon. The lower precision of our earlier measurements of a naked Si substrate allowed us to consider its thickness to be independent of temperature. Now, however, we had to take into account the thermal expansion of silicon. Initially, we tried to use the known values summarized in some handbooks [129–131]. However, we found that if we use those tabulated values of the thermal expansion for Sample NIST 02, and derive the values of $\varepsilon_\infty^{(Si)}$, then applying the latter for Sample NIST 39 (considered next) would result in the opposite sign of the thermal coefficient of silicon. This was an indication that thermal contraction of the cryostat–sample holder assembly probably caused a slight misalignment that was increasing as temperature was lowered. Additionally, that contraction resulted in shifting the spot, that was being probed, down the sample, and the latter could be slightly wedged. Faced with such inconsistencies, we chose to fit the spectra of Samples NIST 02 and NIST 39 in such a way that both samples would have as close thermal expansion to each other as possible. Having the spectra of two silicon plates at a several fixed temperatures, one can in principle obtain the temperature dependence of both the thickness and the dielectric constant (or refractive index), except for the degenerate case when the thicknesses of the two plates are exactly equal. Unfortunately, our two samples were quite close in thickness and we were dealing with the almost degenerate case which presented some additional difficulty. That is the story behind the values we have reported in Tables 6.2, 6.3, and 6.5. Table 6.3 presents the temperature dependence of the apparent thickness of the Si layer of Sample NIST 02 as determined from transmittance (superscript $\mathcal{T}$), front-side reflectance (superscript $\mathcal{R}$), and back-side reflectance (superscript $b\mathcal{R}$).

---

[9] The modelling of multi-layered structures was done using the program "flmfit" from the custom data-processing package created by Charles Porter and David Tanner.

One glance at Table 6.3 will convince you that at each temperature the three spectra result in three different values of the apparent thickness of the Si layer, and that the values produced by fitting the two reflectance spectra are much closer to each other than to the apparent thickness derived from the transmittance data. We tentatively attribute that fact to the somewhat gradual character of the transitions between the separate layers at the interface between them, rather than the sharp interfaces that are implied in our models (or possibly to an effect which is analogous to the Goos–Hänchen effect for the case of total internal reflection).

Table 6.3: Temperature dependence of the apparent thickness of the Si layer of Sample NIST 02 as determined from transmittance ($\mathcal{T}$), front-side reflectance ($\mathcal{R}$), and back-side reflectance ($b\mathcal{R}$).

T, K	$d_{Si}^{(\mathcal{T})}$, nm	$d_{Si}^{(\mathcal{R})}$, nm	$d_{Si}^{(b\mathcal{R})}$, nm
300	204111.4 ± 5.6	203799.0 ± 2.0	203830.5 ± 7.5
200	204032.5 ± 2.5	203719.0 ± 7.0	203732.5 ± 2.5
100	204016.5 ± 8.5	203708.0 ± 6.0	203689.5 ± 3.5
50	203979.0 ± 3.0	203702.5 ± 7.5	203669.5 ± 5.5
20	203982.5 ± 6.5	203700.4 ± 1.3	203675.0 ± 6.0
10	203982.5 ± 7.9	—	203668.5 ± 6.5

The large number of fringes allows us to determine the free spectral range with a high precision. E.g., from the transmittance at 300 K shown in Fig. 6.6 with 81.0 minima between 20 and 600 cm^{-1} we get a free spectral range of 7.160 cm^{-1} with three significant digits. Interpolation of the fits in order to determine the spectral position of the extrema more accurately could add another couple of digits.

It is interesting to note that the transmittance spectrum is characterized by a higher finesse than the front-side and back-side reflectance. Indeed, the transmittance curves are characterized by maxima that are narrower than the minima, whereas for the reflectance curves the situation is exactly the opposite.

In order to model all curves measured on Sample NIST 02, we have taken into account one phonon in each of the Si and SiO$_2$ layers. Initially we started with as many oscillators as we could find in various literature sources [132–134], or that we could approximately derive from plots [135,136]. The calculations matched to data taken on Sample NIST 02 are not sensitive to all of these phonons. However it was possible that some of these phonons could interact with close-in-frequency phonons from other layers in structures with more layers (Samples NIST 39, NIST 73, NIST 74), which are described later. That is the reason why initially we included all phonons. A reasonably-good eye-ball fit was used as a starting point. Because of the large number of parameters and the effects of partial coherence, often the least-square fitting procedure was not converging to a better fit. Therefore, each parameter was varied separately, with all the rest fixed, in order to determine the range for that parameter within which the χ^2 of the fit is minimum. That parameter was set to the middle of the range and half of that range was used as an estimation for the uncertainty of that parameter. After a similar procedure has been performed for every parameter, a single iteration has been completed for one particular spectrum on a specific sample. A lot of going forth and back between the various spectra and samples had to be done until the final values of the fitting parameters that optimize all measured spectra could be "distilled". Because of the large number of parameters and curves for several samples, the above-described fitting procedure was very slowly converging and a large number of such semi-manual iterations were necessary in order to reach the final results. Those parameters that affected the calculated spectra were varied until we reached a good agreement of the calculated curves with the measured data. Other parameters, mainly those characterizing the weak phonon bands in Si to which data taken on Sample NIST 02 were insensitive, were adjusted during fitting the experimental data taken on Sample NIST 39 described later. Later Occam's razor was applied and we were left with only a fraction of the oscillators with which we had started initially.

The phonon parameters (plasma wave number $\breve{\nu}_{pj}$, central wave number $\breve{\nu}_j$, and bandwidth $\varGamma_j$ of the j^{th} band) for Si and SiO_2 that were determined in this way are given in Table 6.4.

Table 6.4: Si and SiO_2 Model Parameters.

layer	$\breve{\nu}_{pj}$, cm^{-1}	$\breve{\nu}_j$, cm^{-1}	Γ_j, cm^{-1}
Si	10.5 ± 0.2	612.8 ± 0.4	20.4 ± 0.4
SiO_2	340 ± 6	449.1 ± 2.3	60.0 ± 3.6

For SiO_2 we have used a thickness[10] of $d_{SiO_2} = 320$ nm and $\varepsilon_\infty = 2.37$. The latter value is the average of the ε_∞ values given for the ordinary and extraordinary rays by Russell and Bell [132]. Averaging of the ordinary and extraordinary ε_∞ corresponds to the fact that the SiO_2 layer of our samples is amorphous rather than crystalline. Indeed, the very wide phonon band centered about 449 $cm^{-1}$is a clear indication that the SiO_2 layer on the bottom of the Si substrate is amorphous. To be on the safe side, initially we had even included phonon bands centered at frequencies exceeding the upper bound of our measurements by up to 30%, though they are likely to have any effect only if they are either centered close to the measured range, and/or are sufficiently wide.

Here we must note that because the absorption of SiO_2 in the far-infrared is not negligible, we should not use the approximation given by equation 6.4. Indeed, with $n_{SiO_2} = 2.154$ (the average of the ordinary and extraordinary values 2.132 and 2.176 at 100 cm^{-1}given by Loewenstein et al. [126]) equation 6.4 would lead us to the overestimated $\varepsilon_\infty^{(SiO_2)} = 4.640$.

No temperature dependence of the fitting parameters characterizing Si and SiO_2 (except for the optical thickness of Si) was found. For simplicity we have ignored the temperature dependence of the phonon bands. Because the structures we have studied are complicated, with multiple layers (except for the naked Si plate and Sample NIST 02 which has only two layers), such a simplification does not seem to be a problem. Most pronounced are two broad phonon bands in two amorphous layers. We have dealt with one of these two features—widened by chaotical long-range order—which is manifested strongly in the transmittance (Figs. 6.6 and 6.7) and more weakly in the front-side reflectance (Figs. 6.8 and 6.9) of Sample NIST 02. The other broad phonon band will appear in the spectra of all samples that have a thick YSZ amorphous layer, starting with the coming-next Sample NIST 39. The samples to follow, NIST 73 and NIST 74, that have an YBCO layer, are characterized furthermore by three mid-infrared bands which are also fairly wide. None of these broad features shows a significant temperature dependence anyway.

---

[10] This nominal thickness value was given to us by Leila Vale from NIST who has produced our samples.

6.2.3 Buffered Silicon Substrates (Sample NIST 39)

Measured next was a Si substrate (Sample NIST 39), similar to Sample NIST 02 which has additionally been covered with the two buffer layers. Besides the thin SiO_2 film on its back side, a YSZ, and CeO_2 buffer layers were deposited on its front side. The features that dominate these spectra are the two wide oscillators in the YSZ layer at about 156 cm^{-1} and 181 cm^{-1}, as well as the wide oscillator in the SiO_2 layer at about 449 cm^{-1} which is shaped further by four phonons of the YSZ layer that lie within the spectral range from 350 to 450 cm^{-1}.

6.2.3.1 Transmittance through Sample NIST 39

The transmittance through Sample NIST 39 is shown in Figures 6.12 (high temperature) and 6.13 (low temperature). As promised, in these curves another wide oscillator due to the yttria-stabilized zirconia layer is present. Again, it proves that this layer is also amorphous or at least somewhat inhomogeneous. The purpose

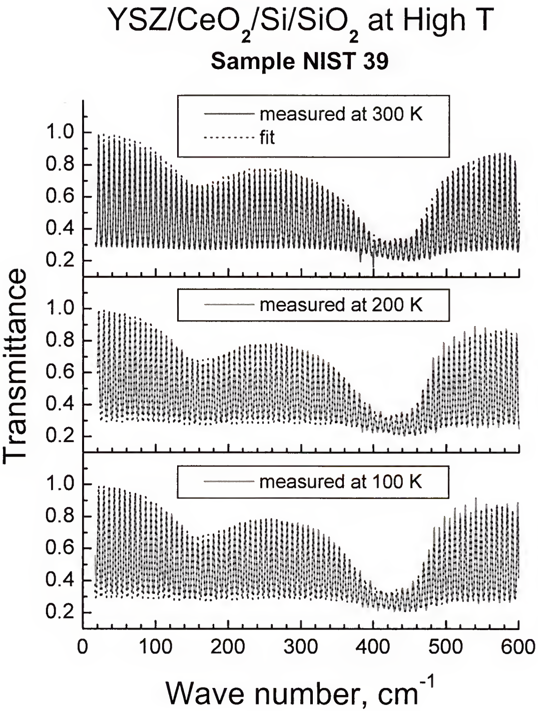

Figure 6.12: High-temperature transmittance through Sample NIST 39: a Si substrate with a thin SiO_2 film on its back side and a YSZ and CeO_2 buffer layers on its front side.

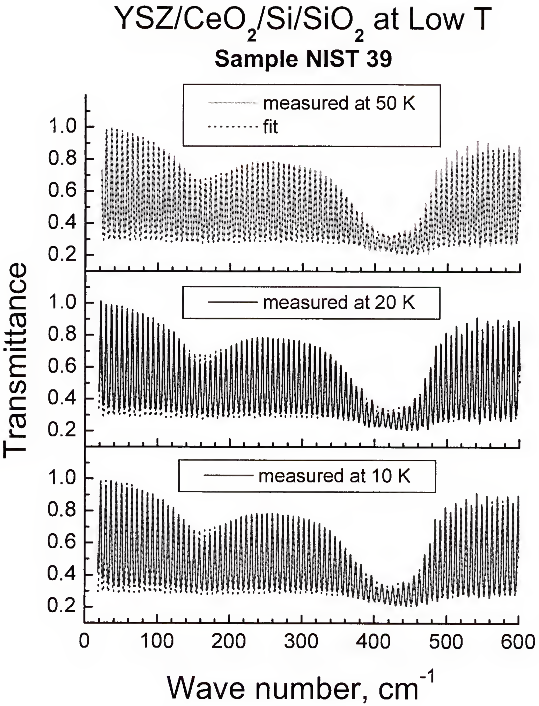

Figure 6.13: Low-temperature transmittance through Sample NIST 39: a Si substrate with a thin SiO_2 film on its back side and a YSZ and CeO_2 buffer layers on its front side.

of the yttria-stabilized zirconia layer, indeed, is to compensate some of the stress due to the lattice mismatch between the substrate and the film (and to prevent any slow chemical interaction between an YBCO film and the Si substrate which would cause premature aging of the samples). But the stress gradient makes this layer inhomogeneous, which, combined with the chaotic long-range order, causes widening of the oscillator absorption band.

In the spectral range below about 100 cm^{-1} the top envelope of the transmittance at 300 K is slightly wavy. We believe that this effect is due to the fact that accidentally the thicknesses of the Si layer of the sample and the beam splitter used within that spectral range (or the cryostat window) are such that the sample and the beam splitter become coupled, forming a composite Fabry-Perot resonator. This effect is also present in the front-side reflectance from Sample NIST 39 at 300 K (top panel of Figure 6.14) as well as in the back-side reflectance from Sample NIST 39 at 300 K (top panel of Figure 6.16), and there are traces of such an effect even at lower temperatures.

6.2.3.2 Front-side reflectance from Sample NIST 39

The front-side reflectance from Sample NIST 39 is shown in Figures 6.14 (high temperature) and 6.15 (low temperature). With all of its four layers, Sample NIST 39 is still quite transparent within the studied spectral range. Hence, this is another instance for which there is some shift between the measured data and the calculated curves, due to parasitic reflectance.

The broad band of the YSZ layer is not manifested in the reflectance spectra, but interestingly the presence of the buffer layers makes somewhat more pronounced the wide band of the SiO_2 layer, compared to the reflectance from the bufferless Sample NIST 02 (compare Figs. 6.14 and 6.15 to Figs. 6.8 and 6.9, respectively). In the spectral range from about 480 to 600 cm^{-1} both the top and

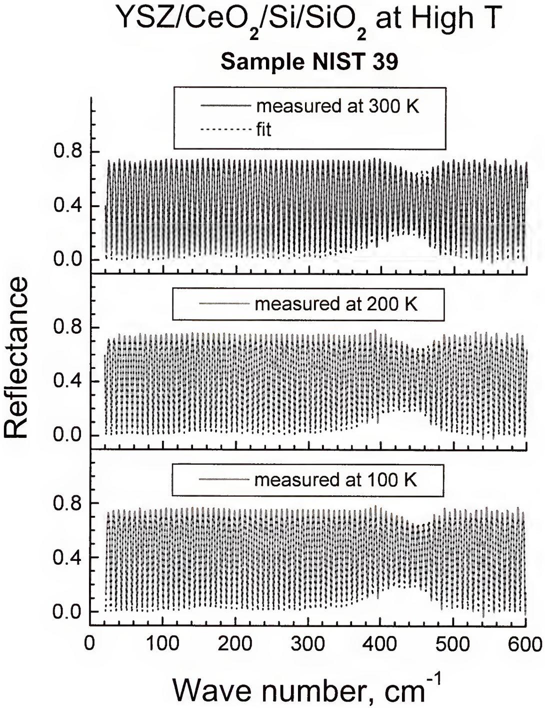

Figure 6.14: Front-side reflectance from Sample NIST 39: a Si substrate with a thin SiO_2 film on its back side and a YSZ and CeO_2 buffer layers on its front side at high temperatures.

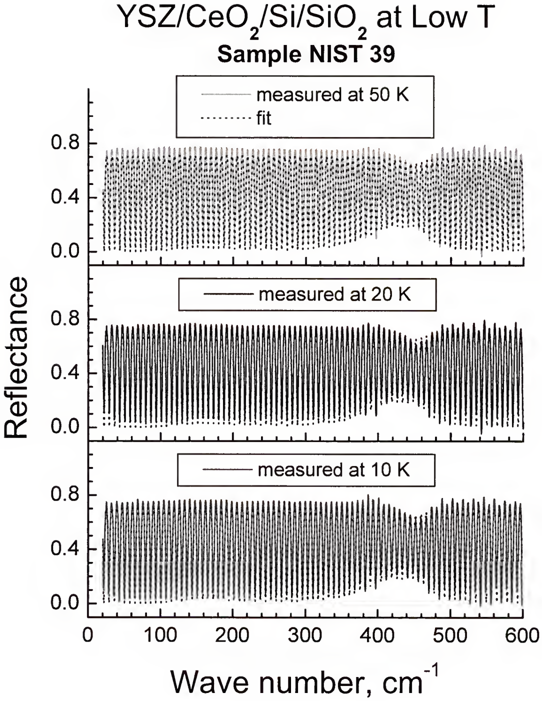

Figure 6.15: Front-side reflectance from Sample NIST 39: a Si substrate with a thin SiO_2 film on its back side and a YSZ and CeO_2 buffer layers on its front side at low temperatures.

bottom envelopes of the reflectance oscillate creating the impression of "hair" and "beard" respectively. This effect is due to the fact that accidentally the thicknesses of the Si layer of the sample and the beam splitter used within that spectral range (or the cryostat window) are such that the sample and the beam splitter become coupled, forming a composite Fabry-Perot resonator.

6.2.3.3 Back-side reflectance from Sample NIST 39

The back-side reflectance from Sample NIST 39 is shown in Figures 6.16 (high temperature) and 6.17 (low temperature).

The broad band of the YSZ layer can also be seen in the back-side reflectance spectra, and what is even more interesting is that the presence of the buffer layers is acting “similarly” to a photo-developer: it makes visible the wide band of the SiO_2 layer which was not at all discernible in the back-side reflectance from the bufferless Sample NIST 02 (compare Figs. 6.16 and 6.17 to Figs. 6.10 and 6.11, respectively).

6.2.3.4 Results for Sample NIST 39 and discussion

To model all curves measured on Sample NIST 39, initially we had taken into account phonons in all four layers. For the SiO_2 and Si layers we used the parameters determined previously on Sample NIST 02. Of course, one cannot expect that the thicknesses of these two layers can be exactly the same. Nevertheless, the oxide-layer thickness was kept at its nominal value for lack of a better knowledge.

Table 6.5 presents the temperature dependence of the apparent thickness of the Si layer of Sample NIST 39 as determined by fitting the measured transmittance (superscript $\mathcal{T}$), front-side reflectance (superscript $\mathcal{R}$), and back-side reflectance (superscript $b\mathcal{R}$).

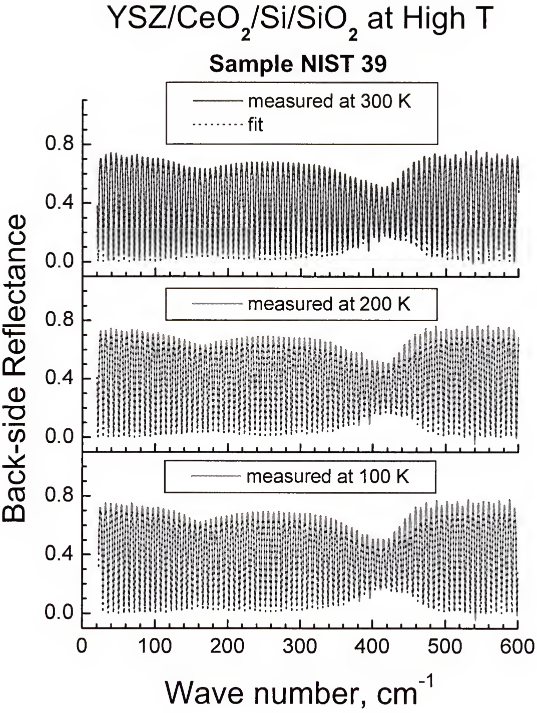

Figure 6.16: Back-side reflectance from Sample NIST 39: a Si substrate with a thin SiO_2 film on its back side and a YSZ and CeO_2 buffer layers on its front side at high temperatures.

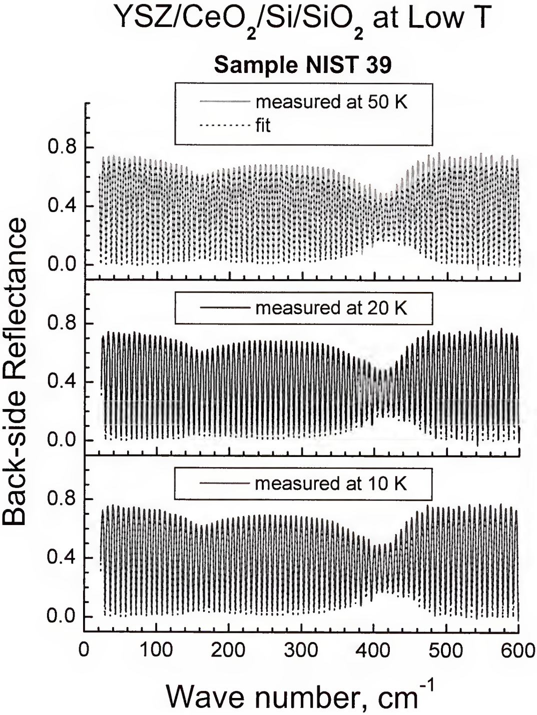

Figure 6.17: Back-side reflectance from Sample NIST 39: a Si substrate with a thin SiO_2 film on its back side and a YSZ and CeO_2 buffer layers on its front side at low temperatures.

Table 6.5: Temperature dependence of the apparent thickness of the Si layer of Sample NIST 39 as determined from transmittance ($\mathcal{T}$), front-side ($\mathcal{R}$), and back-side reflectance ($b\mathcal{R}$).

T, K	$d_{Si}^{(\mathcal{T})}$, nm	$d_{Si}^{(\mathcal{R})}$, nm	$d_{Si}^{(b\mathcal{R})}$, nm
300	204239.6 ± 32.8	203911.5 ± 7.0	204005.0 ± 9.0
200	204200.6 ± 1.7	203827.5 ± 6.5	203938.0 ± 9.0
100	204192.5 ± 10.5	203813.5 ± 5.5	203924.5 ± 5.5
50	203173.5 ± 3.5	203814.5 ± 6.5	203910.0 ± 4.0
20	204174.5 ± 4.0	203823.5 ± 7.5	203913.5 ± 4.5
10	204184.5 ± 12.5	203804.5 ± 8.5	203909.0 ± 6.0

The thicknesses of the YSZ and CeO_2 layers were fixed at $d_{YSZ} = 350$ nm and $d_{CeO_2} = 20$ nm, respectively, which are the nominal values reported to us by our sample supplier, Leila Vale from NIST. Again, for these two new layers we started with as many parameters as we could find in various literature sources, e.g. [134], or that we could approximately derive from plots [135,136]. Then the parameters for the two new layers were varied until we reached a good agreement of the calculated curves with the measured data. Eventually it became clear that all phonon bands of the CeO_2 can be omitted safely, as this layer is still thin enough and quite transparent within the studied spectral range. Therefore CeO_2 was modelled[11] with a plain constant $\varepsilon_\infty^{(CeO_2)} = 2.1 \pm 1.6$. This value is not very reliable or conclusive, because the large uncertainty shows that our results were not sensitive to this parameter. The respective constant for YSZ is $\varepsilon_\infty^{(YSZ)} = 2.80 \pm 0.08$.

Our values for $\varepsilon_\infty^{(YSZ)}$ and $\varepsilon_\infty^{(CeO_2)}$ are significantly lower than the known total far-infrared permittivity of YSZ (25) and CeO_2 (17), respectively [137,138]. Comparable values for YSZ in the microwave spectral range which is adjacent to the far-infrared are presented graphically by Grischkowsky and Keiding [139]. The difference for YSZ can be accounted by the contribution of the phonon bands given in Table 6.6. No similar explanation is possible for the CeO_2 layer, but as mentioned before our data are quite insensitive to $\varepsilon_{\infty}^{(CeO_2)}$.

---

[11] The only reason this layer was not ignored completely is to account for its "spacer" effect, which helps to keep thickness of the silicon layer more accurate.

The phonon parameters for yttria-stabilized zirconia that were determined as described above are given in Table 6.6.

Table 6.6: Yttria-stabilized zirconia model parameters.

$\breve{\nu}_{pj}$, cm^{-1}	$\breve{\nu}_j$, cm^{-1}	Γ_j, cm^{-1}
322 ± 4	155.9 ± 1.6	86.5 ± 3.5
335.5 ± 5.5	181.4 ± 2.9	157 ± 10
416.5 ± 5.5	349.7 ± 2.0	138.0 ± 5.5
294.5 ± 5.5	385.0 ± 1.3	42.0 ± 2.5
110 ± 12	400.0 ± 1.2	16.0 ± 1.5
407 ± 5	418.8 ± 1.5	42.9 ± 1.8
288.5 ± 5.5	450.70 ± 0.45	33.6 ± 2.5

Any temperature dependence of these parameters has been ignored without causing a significant deviation of the fits from the measured spectra. The wide oscillator in the yttria-stabilized zirconia layer is an indication that either this layer is amorphous, or it is inhomogeneous because of the stress gradient, or both.

After all the needed iterations of the fitting procedure had been done, for each parameter we had a range in which χ^2 (to within three digits) is minimum, provided all the rest parameters were at their optimum values. We set each parameter to the center of its corresponding range, and specified half of that range as the uncertainty. This is the very reason why, contrary to the common[12] practice, the uncertainties herein are often given with two or even more digits, especially when the range in question happens to be odd. Therefore, in no case should one assume an uncertainty with n digits to imply that 10^{2n} scans have been taken. Of course, it is very easy to round the numbers in the end, but because the correlations among some of the parameters lowering the precision of tuning of several of them could affect the range of other parameters.

6.3 YBCO Films on Buffered Si Substrates

The spectra of the two best samples (NIST 255 and NIST 256) from the first batch of $YBa_2Cu_3O_{7-\delta}$ films on Si substrates are shown next.[13]

6.3.1 Sample NIST 255

6.3.1.1 Transmittance through Sample NIST 255

The transmittance of the first batch of $YBa_2Cu_3O_{7-\delta}$ films on Si substrates was measured using the slow-scan Michelson interferometer. The transmittance through Sample NIST 255 is shown in Figures 6.18 (at three temperatures with YBCO in the normal state) and 6.19 (at two temperatures with YBCO in the superconducting state). The transmittance spectra again show the typical Fabry-Perot fringes due to multiple-beam interference within the Si substrate. The fits are in a good agreement with the measured data: the χ^2 is within 0.003 in most cases. At 300 K we can count 7.00 minima between 25.11 and 75.20 cm^{-1} and

---

[12] Actually, it seems that increasingly often the practice is to omit the uncertainties as if their only purpose is to torment undergraduate physics-lab students.

[13] Unfortunately, a better match for Sample NIST 255 than NIST 256 was broken due to thermal stress before we had started using springs to ensure thermal contact with the sample holder.

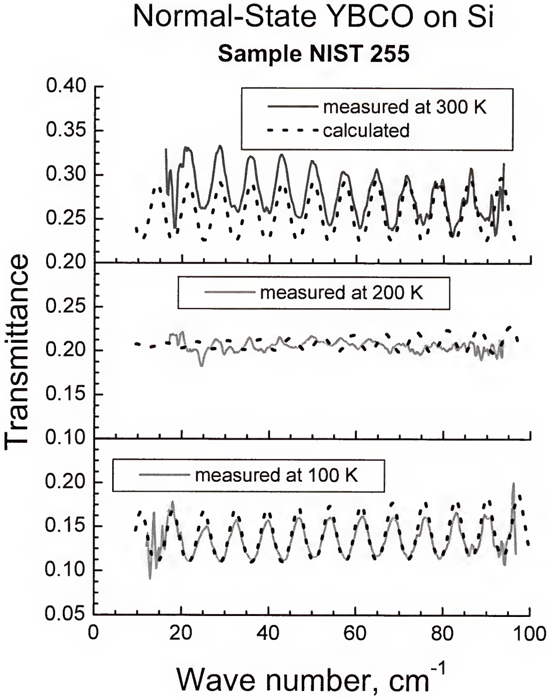

Figure 6.18: Transmittance through Sample NIST 255: an $YBa_2Cu_3O_{7-\delta}$ film deposited onto a Si substrate with YSZ and CeO_2 buffer layers, and with a thin SiO_2 film on its back side, at three temperatures in the normal state.

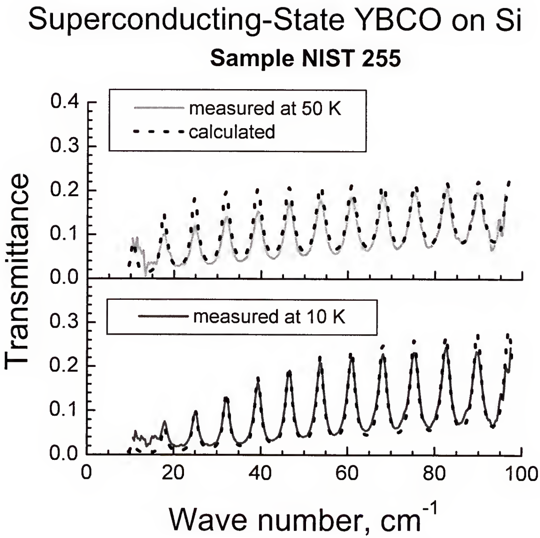

Figure 6.19: Transmittance through Sample NIST 255: an $YBa_2Cu_3O_{7-\delta}$ film deposited onto a Si substrate with YSZ and CeO_2 buffer layers, and with a thin SiO_2 film on its back side, at two temperatures in the superconducting state.

hence the free spectral range in this case is about 7.156 cm^{-1} with three significant digits.

The fringe-averaged transmittance is defined by

$$\langle \mathcal{T}(\omega)\rangle = \frac{1}{\delta\omega}\int_{\omega-\delta\omega/2}^{\omega+\delta\omega/2} \mathcal{T}(\Omega)\,\mathrm{d}\Omega, \tag{6.5}$$

where $\mathcal{T}(\Omega)$ is the transmittance measured at angular frequency Ω, which is the dummy integration variable. In most cases the fringe-averaged transmittance (or reflectance) can be approximated crudely by visualizing a smooth central line between the top and bottom envelope. Such a visualization will convince you that in the normal state the fringe-averaged transmittance is nearly uniform within the covered spectral range at any given temperature, but gradually decreases as the temperature is lowered. This decrease in the transmittance is the result of increased electrical conductivity of the $\mathrm{YBa_2Cu_3O_{7-\delta}}$ film at low temperatures.

At any fixed temperature, the interference pattern is quite periodic within the covered spectral range, but has a strong temperature dependence, especially in the normal state (300, 200, 100 K): even though the values of the maxima vary only slightly with temperature (i.e., the top envelope does not have a significant temperature dependence), the fringe contrast

$$\mathcal{C}_{fr} = (\mathcal{T}_{max} - \mathcal{T}_{min})/(\mathcal{T}_{max} + \mathcal{T}_{min}) \tag{6.6}$$

changes significantly with temperature. Also, there is a phase shift of π rad between the 300 K and 100 K data. It is manifested in the fact that the transmittance maxima at the former temperature correspond to the transmittance minima at the latter one. Evidently, in the case of Sample NIST 255 the phase switch occurs at a temperature very close to 200 K. Additionally, the fringe contrast for Sample

NIST 255 almost vanishes at 200 K, because the Si substrate acts as an antireflective "coating" for the $YBa_2Cu_3O_{7-\delta}$ film. Such a phase shift has been observed earlier by Hadni et al. [140], but they were not sure if it was real and hence refrained from any explanations. A similar effect can be observed in Figures 6.25 and 6.26 for Sample NIST 256 at some temperature between 200 and 300 K. Furthermore, that temperature is most likely about 250 K if we assume that the temperature dependence of the transmittance is roughly linear within the range from 200 to 300 K. Naturally, as the temperature is varied, small changes of the spectral positions of the extrema can also be observed. These temperature shifts are due to the temperature dependence of the optical thickness of the Si substrate.

In the superconducting state, the fringe-averaged transmittance increases with frequency. The fringe contrast for the transmittance is higher at lower temperatures. This can be explained by the effect of optical resonance within the YBCO film-substrate composite, as well as by lower absorptance losses within the YBCO film.

Here it was mentioned briefly how the antireflection effect affects the interference pattern, and how the optical resonance affects the transmittance fringe contrast in the superconducting state. More details are given later.

6.3.1.2 Results for NIST 255 and discussion

Table 6.7 presents the temperature dependence of the free spectral range $\Delta\breve{\nu}$ determined from the transmittance (denoted by a superscript $\mathcal{T}$), from the front-side reflectance[14] (denoted by a superscript $\mathcal{R}$), and form the back-side reflectance(denoted by a superscript $b\mathcal{R}$), respectively. Table 6.7 is just a show-

---

[14] The parameters corresponding to front-side reflectance and back-side reflectance are also included in this and many other tables, even though the respective spectra will be shown later, after the transmittance data.

Table 6.7: Temperature dependence of the free spectral range characterizing the multiple beam interference in the Si substrate of Sample NIST 255, determined from transmittance ($\mathcal{T}$), front-side reflectance ($\mathcal{R}$), and back-side reflectance ($b\mathcal{R}$).

T, K	$\Delta\breve{\nu}_{Si}^{(\mathcal{T})}$, cm^{-1}	$\Delta\breve{\nu}_{Si}^{(\mathcal{R})}$, cm^{-1}	$\Delta\breve{\nu}_{Si}^{(b\mathcal{R})}$, cm^{-1}
300	$7.16434 \pm 2.6E-4$	$7.1973 \pm 3.3E-3$	$7.17820 \pm 2.5E-4$
200	—	$7.2326 \pm 5.3E-3$	—
100	$7.20654 \pm 8.0E-4$	$7.267 \pm 1.4E-2$	$7.22466 \pm 2.8E-4$
50	$7.220 \pm 1.6E-2$	—	$7.2424 \pm 1.1E-2$
10	$7.1819 \pm 3.3E-3$	—	$7.194 \pm 1.1E-2$

case. If necessary, such a table can be made for each of the measured samples. At about 200 K there is a phase change related to the antireflection effect which will be described in more detail later. Because of this antireflection effect, at 200 K the amplitude of the fringes in the transmittance and back-side reflectance has almost vanished and it is impossible to get any reliable value for the free spectral range. The values at 50 K and 10 K that should have been obtained from reflectance are also missing because we were not successful with these measurements. In order to determine the free spectral range as accurately as possible the following procedure was used: the "exact" spectral position of three extrema at both sides of the covered spectral range was found by means of a fine interpolation.[15] on the fit data[16] Then the free spectral range was obtained as the average of its values for the four combinations including extrema which were separated spectrally as far as possible. The uncertainty for some of the values is artificially large (overestimated), because only four values have been averaged. If necessary, this problem can be readily resolved by using all nine combinations that are possible, or even considering more (and even all) extrema and combinations of couples among them.

---

[15] by the "interp" program from Dr. Tanner's lab package.

[16] The optimized fits have fringes at the same spectral positions as the measured data, but, unlike the latter, the fits are free of background noise.

Because of the narrow spectral range in which the measurements of Sample NIST 255 and the coming-next Sample NIST 256 were done, only the Drude band has been considered for the normal state of the $YBa_2Cu_3O_{7-\delta}$ film, that is, all other terms of equation 6.2 have been neglected and besides $f_s = 0$. When the film is in the superconducting state a Dirac δ-function takes over some spectral weight from the Drude band which simply means that in equation 6.2 $0 < f_s \leq 1$ (the equality being only possible in high-quality bulk samples at very low temperatures). The simplicity of this oscillator model for the $YBa_2Cu_3O_{7-\delta}$ film of Sample NIST 255 and Sample NIST 256 is summarized in Table 6.8, where[17] $\breve{\nu}_{pj}$ is the plasma wave number of the j^{th} oscillator, $\breve{\nu}_j$ the central wave number of the j^{th} oscillator, and $\mathit{\Gamma}_j$ the width of the j^{th} oscillator, all three measured in cm^{-1}.

Table 6.8: Two fluid model for the $YBa_2Cu_3O_{7-\delta}$ film of Samples NIST 255 and NIST 256.

$\breve{\nu}_{pj}$, cm^{-1}	$\breve{\nu}_j$, cm^{-1}	$\mathit{\Gamma}_j$, cm^{-1}	Band
$\alpha(T)$	0	0	$\delta(\omega)$
$\beta(T)$	0	$\mathit{\Gamma}(T)$	Drude

More specifically, $\beta(T)$ is the Drude plasma wave number, $\mathit{\Gamma}(T)$ is nothing else, but the Drude scattering rate $1/\tau(T)$ ($\tau(T)$ is the Drude relaxation time), and $\alpha(T)$ is the wave-number weight of the $\delta(\omega)$-function. The temperature dependence of these parameters for Sample NIST 255 is presented in Table 6.9. Actually, two of these three parameters are not independent. Indeed, the fraction of normal or

---

[17] The notation here may seem to be an overkill, but it will come handy when models with more oscillators are considered for some samples that have been measured in a wider spectral range.

Table 6.9: Temperature dependence of the model parameters for the $YBa_2Cu_3O_{7-\delta}$ film of Sample NIST 255.

T K	$\Gamma(T)$, cm^{-1}	$\alpha(T)$, cm^{-1}	$\beta(T)$, cm^{-1}
300	630 ± 50	0	7000 ± 300
200	448 ± 51	0	7000 ± 300
100	265 ± 11	0	7000 ± 300
50	220 ± 11	3051 ± 131	6300 ± 270
10	220 ± 7	4454 ± 191	5400 ± 232

superconducting carriers is related to the fitting parameters α and β:

$$f_n(T) \;=\; \frac{\beta^2(T)}{\alpha^2(T) \;+\; \beta^2(T)}; \qquad\qquad f_s(T) \;=\; \frac{\alpha^2(T)}{\alpha^2(T) \;+\; \beta^2(T)}, \tag{6.7}$$

and evidently these equations meet the self-explanatory condition

$$f_n(T) \;+\; f_s(T) \;=\; 1. \tag{6.8}$$

Furthermore, because in superconductors there is no thermal generation of quasi-free charge carriers, the denominators in equations 6.7 are temperature independent:

$$\alpha^2(T) \;+\; \beta^2(T) \;=\; \mathrm{const}(T) \;=\; \beta^2(300\ \mathrm{K}). \tag{6.9}$$

Hence after $\beta(300\ \mathrm{K})$ has been determined by fitting the room-temperature data, the parameters α and β at any other fixed temperature must be varied in a correlated manner, so that the condition 6.9 is met at all times.

In the normal state of $YBa_2Cu_3O_{7-\delta}$, both the scattering rate and the DC resistivity decrease almost linearly with lowering temperature. Above the critical temperature T_c, the dominating scattering mechanism is the temperature-dependent electronic scattering. This is the reason why both the scattering rate and the resistivity are characterized by a linear temperature dependence.

For convenience, the temperature dependencies of the superconducting fluid fraction and the DC-conductivity for the $YBa_2Cu_3O_{7-\delta}$ film of Sample NIST 255, which correspond to the parameter values given in Table 6.9, are presented in Table 6.10. From equation 3.52 we can derive an equation for estimation of the uncertainty $\Delta\sigma_{DC}$ of the DC-conductivity

Table 6.10: Temperature dependence of some transport characteristics for the $YBa_2Cu_3O_{7-\delta}$ film of Sample NIST 255.

T, K	$f_s(T)$, %	σ_{DC}, $(\Omega{\cdot}\mathrm{cm})^{-1}$
300	0	1296 ± 130
200	0	1823 ± 235
100	0	3082 ± 226
50	$19.0 \pm .8$	∞
10	40.5 ± 1.7	∞

$$\Delta\sigma_{DC} = \sigma_{DC}\sqrt{2\left(\frac{\Delta\omega_p}{\omega_p}\right)^2 + \left(\frac{\Delta(1/\tau)}{1/\tau}\right)^2} = \sigma_{DC}\sqrt{2\left(\frac{\Delta\beta}{\beta}\right)^2 + \left(\frac{\Delta\Gamma}{\Gamma}\right)^2}. \tag{6.10}$$

6.3.1.3 Front-side reflectance from Sample NIST 255

The front-side reflectance from the two best samples of the first batch are shown herein. In spite of the fact that Samples NIST 255 and NIST 256 were the best, many of our front-side and back-side reflectance measurements from them were not very successful. Still we present these data here, because Samples NIST 255 and NIST 256 were very important for our studies of two Fabry-Perot resonators made with those two samples. These two resonators are covered in Chapter 8. For any unsuccessful measurement the dotted line on the plot gives the predicted or calculated curve rather than a fit. Fits were done only for the spectra that we deemed as successfully measured. Priority was always given to the transmittance data as the alignment for the transmittance configuration is more straightforward and reliable.

The reason for the low quality of the earlier data for reflectance from Samples NIST 255 and NIST 256 is most likely human errors due to inexperience. Normally we have two temperature sensors, one mounted in the cold finger of the cryostat and another attached to the sample-holder. When a good thermal contact between the cold finger has been obtained below nitrogen temperatures the two sensors differ by less than a Kelvin. Occasionally some of the many users of the cryostat would damage the thin wires of the sample holder temperature sensor and until a replacement diode was received and installed, the measurements continued "blindly", with the hope that a good thermal contact had been obtained. Unfortunately, evidently this was not always the case. Indeed, for some measurements there is almost no difference between the reflectance data at 10 K and 50 K, and sometimes even 100 K. This is a clear indication that only the cold finger was as cold as measured, whereas the sample was probably at a much higher temperature.

Attempts were done to repeat the unsuccessful measurements after several months. However, we found that the two samples had changed their properties. E.g., the reflectance of Sample NIST 255 was measured with a delay of eight months. At that time the measured reflectance in the superconducting state was significantly lower than the calculations based on our model for the transmittance data. The properties of the $YBa_2Cu_3O_{7-\delta}$ film are very sensitive to the oxygen content. Oxidation of the films over a period of time may lead to a degradation of their superconducting properties which would lower the reflectance. However, in this particular case the use of unsuitable solvent to remove the glue with which the samples were attached to the sample holder for the previous measurements most likely had caused degradation of the superconducting properties.

The front-side reflectance in the superconducting state, was measured for several other samples. These measurements confirmed the expected differences between the front-side and back-side reflectance. In the superconducting state, the fringe contrast for the front-side reflectance is much smaller than that for the back-side reflectance.

The front-side reflectance from Sample NIST 255 is shown in Figures 6.20 (normal state) and 6.21 (superconducting state). Evidently, the front-side reflectance from Sample NIST 255, with YBCO in the normal state was measured successfully which is not true for the superconducting case.

The fringe contrast and the fringe-averaged front-side reflectance are larger in comparison with those for the back-side reflectance. No antireflection effect can be seen at any of the temperatures at which we have measured the reflectance. In this case the infrared beam coming from a low-optical-density medium (vacuum) is mostly reflected by the $YBa_2Cu_3O_{7-\delta}$ layer. The YBCO layer is characterized by the highest refractive index compared to vacuum and Si, whereas anti-reflecting effect (admittance matching) is only possible when the middle layer has intermediate refractive index compared to the two adjacent two media.

6.3.1.4 Back-side reflectance from Sample NIST 255

The back-side reflectance from Sample NIST 255 is shown at first with the interference fringes in Figures 6.22 (normal state) and 6.23 (superconducting state).

The fringe contrast and the fringe-averaged back-side reflectance are larger in comparison with those for the front-side reflectance. In the normal state it

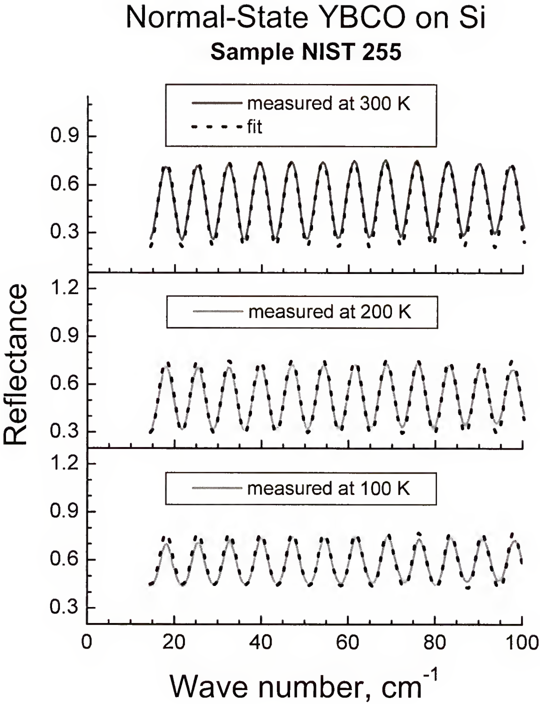

Figure 6.20: Front-side reflectance from Sample NIST 255: an $YBa_2Cu_3O_{7-\delta}$ film on a Si substrate with YSZ and CeO_2 buffer layers, and with a thin SiO_2 film on its back side at three temperatures in the normal state.

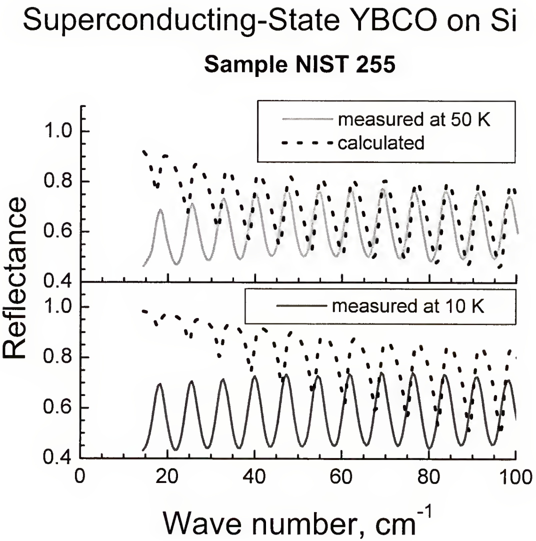

Figure 6.21: Front-side reflectance from Sample NIST 255: an $YBa_2Cu_3O_{7-\delta}$ film on a Si substrate with YSZ and CeO_2 buffer layers, and with a thin SiO_2 film on its back side at two temperatures in the superconducting state.

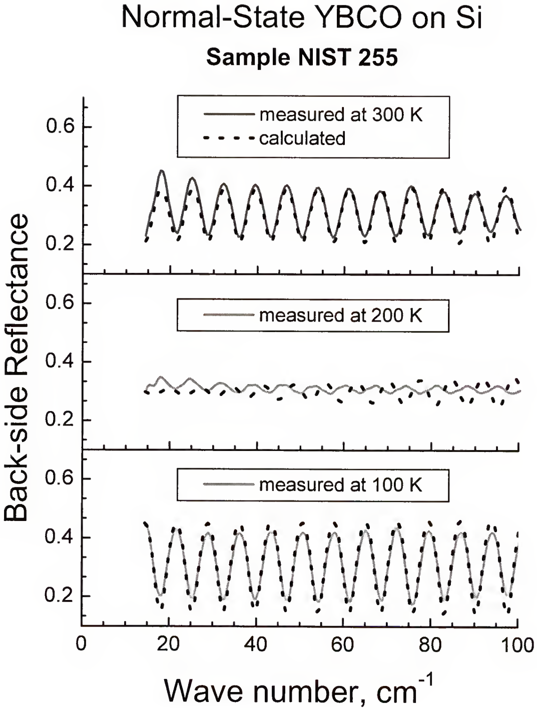

Figure 6.22: Back-side reflectance from Sample NIST 255: an $YBa_2Cu_3O_{7-\delta}$ film on a Si substrate with YSZ and CeO_2 buffer layers, and with a thin SiO_2 film on its back side at three temperatures in the normal state.

can clearly be seen that antireflection is in effect at about 200 K. This is now possible because the Si substrate has intermediate refractive index and can act as an antireflecting coating for the YBCO layer. This indeed is the case at a temperature close to 200 K where the Si impedance (admittance) happens to be matched: the square of the Si wave impedance is equal to the product of the wave impedances of YBCO and free space.

The picture is complemented by Figure 6.24 which shows the filtered back-side reflectance from Sample NIST 25 within the spectral range from 10 to 600 cm^{-1}, including three curves in the normal state and two curves in the superconducting state. The curves are filtered by using the program "fts" (Fourier-transform smoothing) which takes the Fourier transform of the spectrum to be smoothed, the signatures of over-represented fringes can be isolated and restricted and the inverse Fourier transformation produces the smoothed spectrum. As a result most of the fringes are eliminated, and so the filtered spectrum can be used as a convenient first approximation for fringe averaging.

From Figure 6.24 it can be seen again, that the back-side reflectance in the superconducting state exceeds significantly that in the normal state, especially below 100 cm^{-1}. The reflectance increases sharply as the temperature gets below the critical temperature T_c, and continues to increase more slowly as the temperature is reduced further, until it gets saturated at temperatures below $\gtrsim$ 20 K. (The latter fact was found from more recent measurements on Samples NIST 73 and NIST 74 from another batch. Their spectra are practically the same at both 10 and 20 K.)

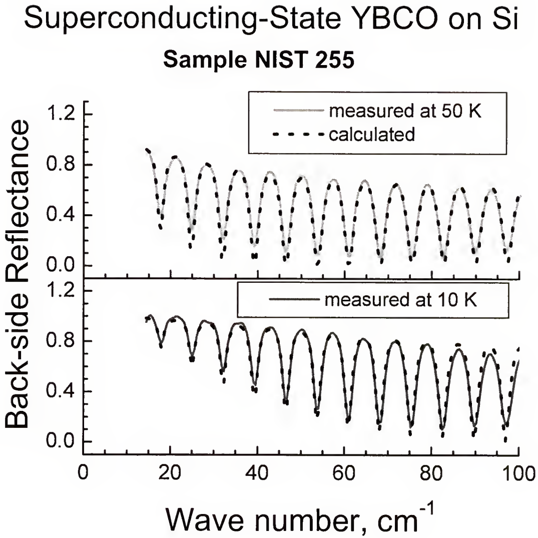

Figure 6.23: Back-side reflectance from Sample NIST 255: an $YBa_2Cu_3O_{7-\delta}$ film on a Si substrate with YSZ and CeO_2 buffer layers, and with a thin SiO_2 film on its back side at three temperatures in the superconducting state.

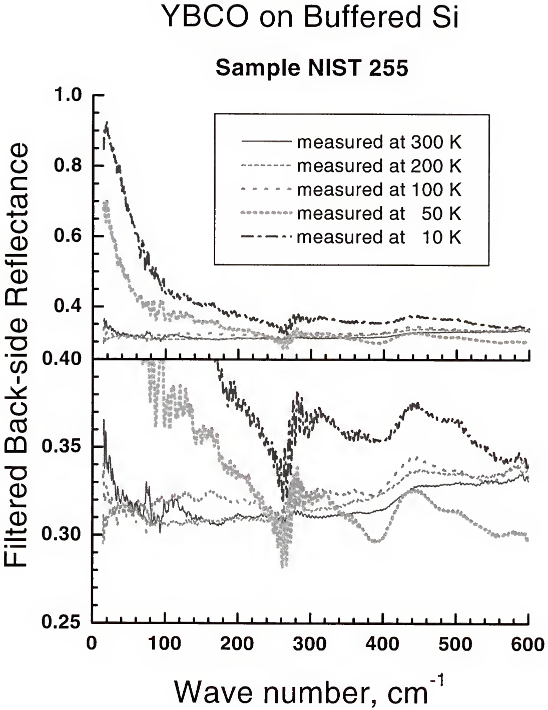

Figure 6.24: Filtered back-side reflectance from Sample NIST 255: an $YBa_2Cu_3O_{7-\delta}$ film on a Si substrate with YSZ and CeO_2 buffer layers, and with a thin SiO_2 film on its back side at three temperatures in the normal state.

6.3.2 Sample NIST 256

6.3.2.1 Transmittance through Sample NIST 256

The measured transmittance through Sample NIST 256 and the corresponding fits are shown in Figures 6.25 (at three temperatures with YBCO in the normal state) and 6.26 (at two temperatures with YBCO in the superconducting state).

As can be expected, the transmittance spectra of Sample NIST 256 also show the typical Fabry-Perot fringes due to multiple-beam interference within the Si substrate. At 300 K we can count 7.00 minima between 25.11 and 75.20 cm^{-1} and hence the free spectral range in this case is about 7.156 cm^{-1} with three significant digits.

The transmittance fits at 100 and 300 K agree well with the measured spectra. However, at 200 K the measured transmittance, rather than being in the middle between the curves at 100 K and 300 K, is shifted by about 0.05 down along the transmittance axis from the respective fit. We believe some human error lead to a systematic error in this particular case. Most probably, when measuring the single-beam spectrum through Sample NIST 256, the sample had not been aligned at the optimum angle, which resulted in a slight asymmetry between the incident and the reflected beams and lead to a reduced signal from the sample. Indeed, boosting the transmittance measured at 200 K by 20 % leads to a good agreement with the fit obtained by averaging the parameters for the 100 K and 300 K fits (assuming linear dependence of the scattering rate and the DC conductivity, the curve obtained in the way described above should represent a 200 K fit). Unfortunately, at the time when we found this imperfection in our data, the sample had been damaged and such a measurement could not be reproduced on the same sample.

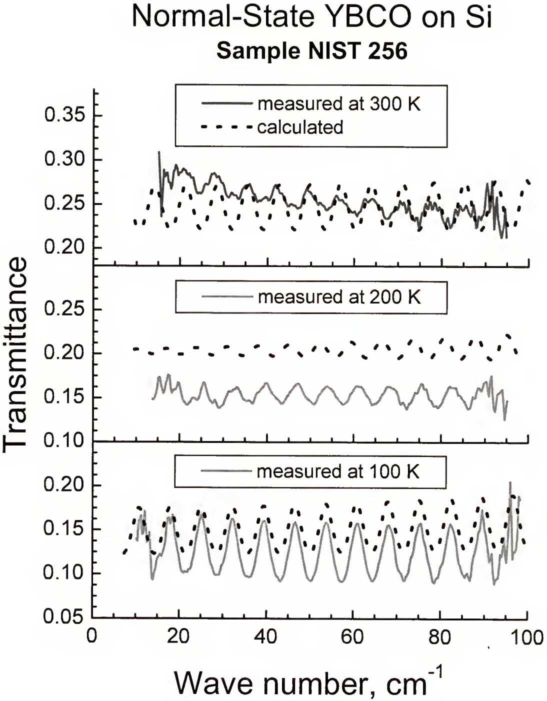

Figure 6.25: Transmittance through Sample NIST 256: an $YBa_2Cu_3O_{7-\delta}$ film deposited onto a Si substrate with YSZ and CeO_2 buffer layers, and with a thin SiO_2 film on its back side, at three temperatures in the normal state.

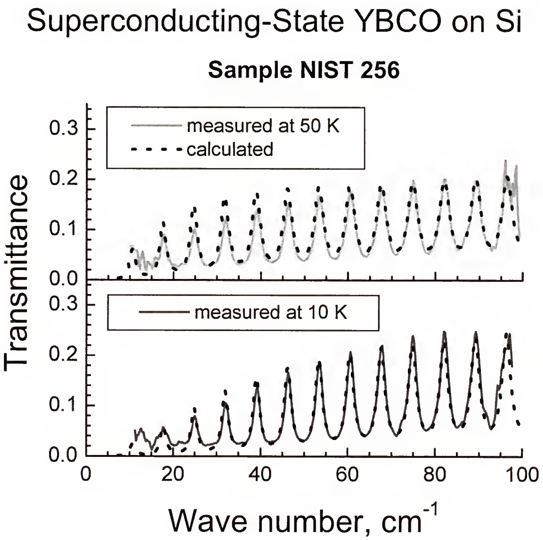

Figure 6.26: Transmittance through Sample NIST 256: an $YBa_2Cu_3O_{7-\delta}$ film deposited onto a Si substrate with YSZ and CeO_2 buffer layers, and with a thin SiO_2 film on its back side, at two temperatures in the superconducting state.

6.3.2.2 Results for Sample NIST 256 and discussion

The temperature dependencies of the parameters $\alpha(T)$, $\beta(T)$, and $\Gamma(T)$ for Sample NIST 256 are presented in Table 6.11. Equations 6.7, 6.8, and 6.9 apply for Sample NIST 256, too.

Table 6.11: Temperature dependence of the model parameters for the $YBa_2Cu_3O_{7-\delta}$ film of Sample NIST 256.

T, K	$\Gamma(T)$, cm^{-1}	$\alpha(T)$, cm^{-1}	$\beta(T)$, cm^{-1}
300	635 ± 50	0	7300 ± 312
200	476 ± 54	0	7300 ± 312
100	317 ± 13	0	7300 ± 312
50	200 ± 10	3323 ± 142	6500 ± 278
10	200.0 ± 6.4	4433 ± 190	5800 ± 248

For convenience, the temperature dependencies of the superconducting fluid fraction and the DC-conductivity for the $YBa_2Cu_3O_{7-\delta}$ film of Sample NIST 256, which correspond to the parameter values given in Table 6.11, are presented in Table 6.12.

Table 6.12: Temperature dependence of some transport characteristics for the $YBa_2Cu_3O_{7-\delta}$ film of Sample NIST 256.

T, K	$f_s(T)$, %	σ_{DC} $(\Omega\cdot\text{cm})^{-1}$
300	0	1399 ± 139
200	0	1866 ± 240
100	0	2802 ± 205
50	20.7 ± 0.9	∞
10	36.9 ± 1.6	∞

6.3.2.3 Front-side reflectance from Sample NIST 256

The front-side reflectance from Sample NIST 256 is shown in Figures 6.27 (normal state) and 6.28 (superconducting state). Again the measurement in the normal state was successful, whereas that in the superconducting was not perfect, but it still was better than the respective reflectance measurement from Sample NIST 255. Indeed, the low-frequency reflectance increases significantly as the temperature is lowered, although not quite as much as predicted by the parameters of the transmittance fit. The discrepancy is especially strong for the reflectance at 50 K.

6.3.2.4 Back-side reflectance from Sample NIST 256

Our measurements of the back-side reflectance from Sample NIST 256 were not very successful. The spectra are shown at first with the interference fringes in Figures 6.29 (normal state) and 6.30 (superconducting state).

The measured back-side reflectance at 10 K is very similar to that at 50 K. The maxima of the calculated spectra are significantly higher, especially at the lowest wave number. These facts clearly indicate that most likely the recorded temperatures did not correspond to the actual temperatures of the sample. Bad thermal contact to the colt finger of the cryostat is the suspect.

Note, that the fringe contrast in the superconducting state of YBCO is much higher than the one in the normal state. Similarly to the transmittance case, the fringe contrast at 200 K is much smaller in comparison with that at 100 and 300 K. Furthermore, comparison between the transmittance and back-side reflectance plots shows that the frequencies of transmittance maxima coincide with those of reflectance minima.

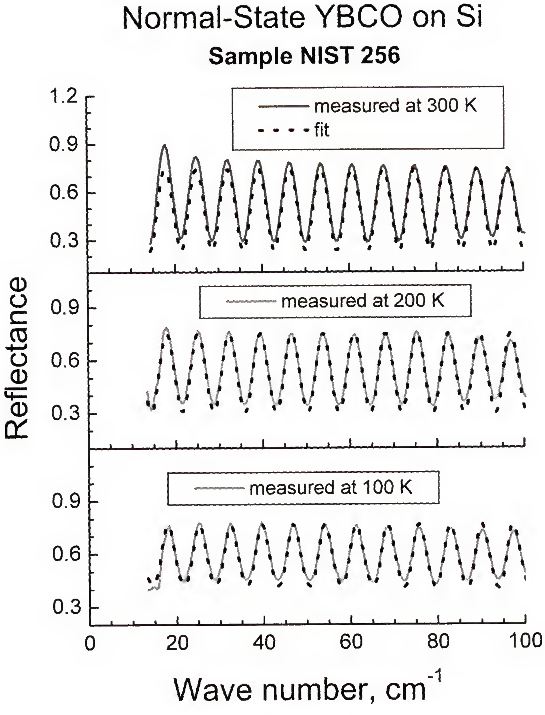

Figure 6.27: Front-side reflectance from Sample NIST 256: an $YBa_2Cu_3O_{7-\delta}$ film on a Si substrate with YSZ and CeO_2 buffer layers, and with a thin SiO_2 film on its back side at three temperatures in the normal state.

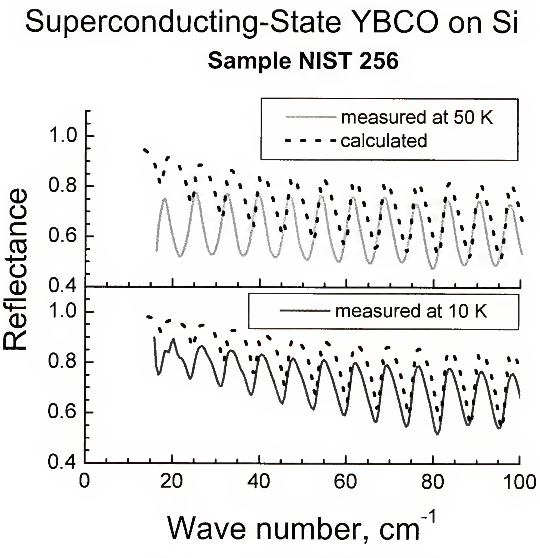

Figure 6.28: Front-side reflectance from Sample NIST 256: an $YBa_2Cu_3O_{7-\delta}$ film on a Si substrate with YSZ and CeO_2 buffer layers, and with a thin SiO_2 film on its back side at two temperatures in the superconducting state.

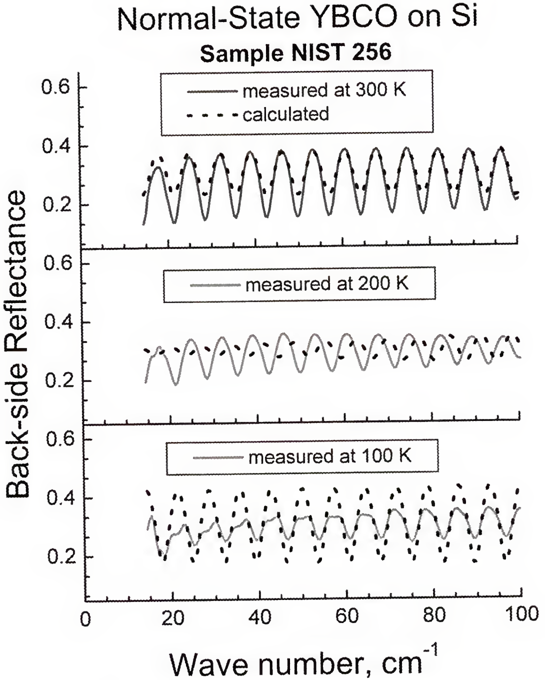

Figure 6.29: Back-side reflectance from Sample NIST 256: an $YBa_2Cu_3O_{7-\delta}$ film on a Si substrate with YSZ and CeO_2 buffer layers, and with a thin SiO_2 film on its back side at three temperatures in the normal state.

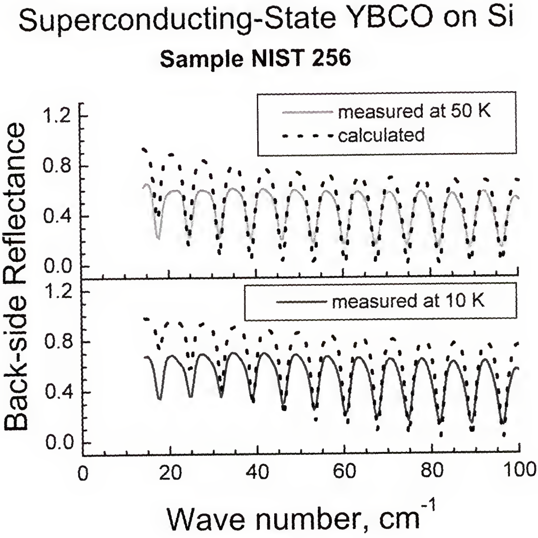

Figure 6.30: Back-side reflectance from Sample NIST 256: an $YBa_2Cu_3O_{7-\delta}$ film on a Si substrate with YSZ and CeO_2 buffer layers, and with a thin SiO_2 film on its back side at three temperatures in the superconducting state.

Temperature modulation of the $YBa_2Cu_3O_{7-\delta}$ films on Si substrate about the critical temperature would cause alternation between the normal and superconducting states of the $YBa_2Cu_3O_{7-\delta}$, which would lead to a large change in the back-side reflectance at particular frequencies.[18] This is an experimental demonstration of the fact that in the future HTSC films can be applied for far-infrared intensity modulation [108].

It is evident that the fringe-averaged back-side reflectance is virtually constant with frequency in the normal state, as well as above about 150 cm^{-1} in the superconducting state. Only when the frequency is lowered below the latter value, the fringe-averaged back-side reflectance increases. Thus 150 cm^{-1} corresponds to the superconducting gap. Above the gap the fringe-averaged back-side reflectance is essentially constant with both frequency and temperature.

6.3.3 Sample NIST 73

Recently some more detailed measurements on a second batch of $YBa_2Cu_3O_{7-\delta}$ films were done in a wider spectral range from 20 to 600 cm^{-1}. These films were deposited onto Si substrates that had a multi-layered structure just like that of Sample NIST 39: with the two buffer layers described earlier on top of the Si, and a SiO_2 layer on its back. The spectra of the two best Samples (NIST 73 and NIST 74) from this batch are shown herein. The features that dominate these spectra are the $YBa_2Cu_3O_{7-\delta}$ phonon about 270 cm^{-1}, the two wide oscillators in the YSZ layer at about 156 cm^{-1} and 181 cm^{-1}, as well as the wide oscillator in the SiO_2 layer at about 449 cm^{-1} which is shaped further by four phonons of the YSZ layer that lie within the spectral range from 350 to 450 cm^{-1}.

---

[18] In practice it is easier to modulate the critical temperature by current pulses with magnitude exceeding the critical current which is enough to destroy the superconducting state temporarily, provided the sample is kept below T_c, but close to it, practically done by using nitrogen.

6.3.3.1 Transmittance through Sample NIST 73

The transmittance through Sample NIST 73 is shown in Figures 6.31 (normal state) and 6.32 (superconducting state). The fringe-averaged far-infrared transmittance decreases monotonically as the temperature is lowered, as expected. In the normal state, this behavior corresponds to the increasing DC conductivity, whereas in the superconducting state it is due to the increasing fraction of the superconducting fluid (i.e., increasing weight of the Dirac $\delta(\omega)$-function).

The far-infrared transmittance of Sample NIST 73 at 100 K is an example of the antireflection effect which has suppressed the interference fringes almost completely. Hence the total suppression should be at some temperature close above 100 K.

In the narrow spectral range between 380 and 400 cm^{-1} several oscillators from different layers interact strongly, the phase changes in a complicated manner, and the fringes become somewhat chaotic.

6.3.3.2 Results for Sample NIST 73 and discussion

Table 6.13 presents the temperature dependence of the apparent thickness of the Si layer of Sample NIST 73 as determined from transmittance (superscript $\mathcal{T}$), front-side reflectance[19] (superscript $\mathcal{R}$), and back-side reflectance (superscript $b\mathcal{R}$). The values marked with "ar" ("abr") correspond to an alternate fit optimized specifically for the front-side (back-side) reflectance summarized in Table 6.13 and described in more detail later.

Once again, Table 6.13 demonstrates that at each temperature the three spectra result in three different values of the apparent thickness of the Si layer. However,

---

[19] The parameters corresponding to front-side reflectance and back-side reflectance are also included in this and many other tables, even though the respective spectra will be shown later, after the transmittance data.

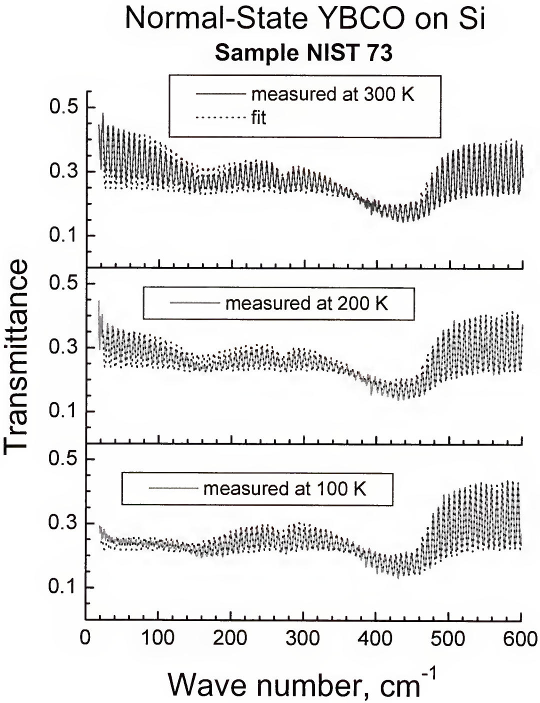

Figure 6.31: Transmittance through Sample NIST 73: an $YBa_2Cu_3O_{7-\delta}$ film deposited onto a Si substrate with YSZ and CeO_2 buffer layers, and with a thin SiO_2 film on its back side at three temperatures in the normal state.

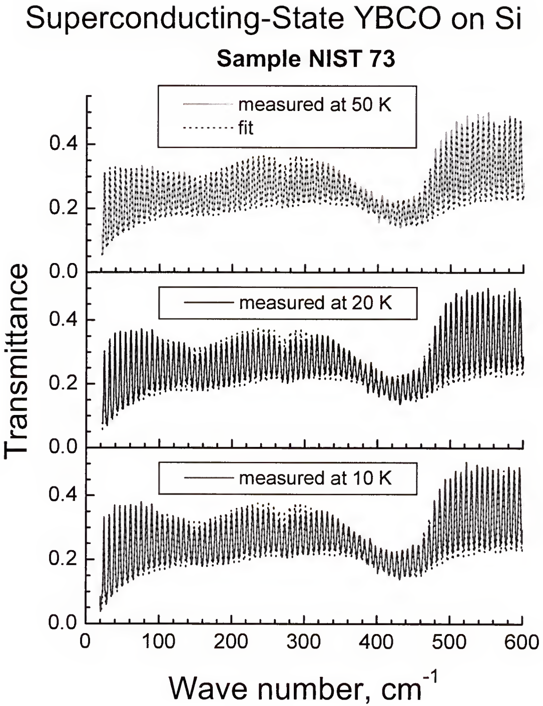

Figure 6.32: Transmittance through Sample NIST 73: an $YBa_2Cu_3O_{7-\delta}$ film on a Si substrate with YSZ and CeO_2 buffer layers, and with a thin SiO_2 film on its back side at three temperatures in the superconducting state.

Table 6.13: Temperature dependence of the apparent thickness of the Si layer of Sample NIST 73 as determined from transmittance ($\mathcal{T}$), front-side reflectance ($\mathcal{R}$), and back-side reflectance ($b\mathcal{R}$).

T, K	$d_{Si}^{(\mathcal{T})}$, nm	$d_{Si}^{(\mathcal{R})}$, nm	$d_{Si}^{(b\mathcal{R})}$, nm
300	200451.5 ± 9.0	198364.5 ± 10.5	200671.0 ± 5.0
200	200438.5 ± 8.5	198418 ± 12	200459.5 ± 11.5
100	200445.0 ± 12.0	198527 ± 12	200257 ± 15
50	200480.0 ± 4.0	198620.0 ± 5.0	200200 ± 13
50		198670 ± 10 ar	200217.0 ± 2.5 abr
20	200484.5 ± 6.5	198682.5 ± 5.5	200174.5 ± 12.5
20		198740.5 ± 6.5 ar	abr
10	200450.5 ± 2.5	198685 ± 8	200173.5 ± 6.5
10		198741 ± 13 ar	abr

for the case of Sample NIST 73, the silicon thickness corresponding to the transmittance is within the range bound by the two values for the thickness of Si which were produced by fitting the front-side and back-side reflectance, just as one can expect.

To model all curves measured on Sample NIST 73 and the coming-next Sample NIST 74, initially we took into account phonons in all five layers, but later we found that it is possible to omit many of these phonons, including all phonons of the CeO_2 layer. Our modelling procedure was already explained when we described how we have processed the data for Samples NIST 02 and NIST 39. For the four layers (SiO_2, Si substrate and the two buffer layers) we used the parameters determined previously[20] on Samples NIST 02 and NIST 39. For the $YBa_2Cu_3O_{7-\delta}$ film we started with the parameters from our previous studies, using the Drude model for the normal state, and the two fluid model for the superconducting state. In the normal state the Drude relaxation rate decreases linearly as the temperature is lowered. In the superconducting state the relaxation rate is constant, but some of the Drude quasi-free carriers condense into Cooper pairs. This is manifested in reducing of the spectral weight of the Drude band and simultaneous increasing of the spectral weight of a Dirac δ-function, corresponding to the condensed (superconducting) electrons. Thus, below T_c, the fraction of superconducting electrons increases monotonically as temperature is lowered. Because of the wider spectral range of these measurements we added all three mid-infrared bands reported by Kamarás et al. [104,141]. Next we added the five reliably-determined phonon bands that have been published in various literature sources [142–146]. Especially useful is the review article by Feile [147]. Then all parameters for the $YBa_2Cu_3O_{7-\delta}$ layer were varied until we reached a good agreement of the calculated curves with the measured data. The oscillator parameters of the $YBa_2Cu_3O_{7-\delta}$ film that were determined in this way for Sample NIST 73 are given in Table 6.14. For sim-

---

[20] Actually, each fitting iteration was performed on all four samples, before we proceeded with the next iteration. Therefore "previously" must be regarded to be just a figure of speech.

Table 6.14: $YBa_2Cu_3O_{7-\delta}$ Model Parameters for Sample NIST 73.

$\breve{\nu}_{pj}$, cm^{-1}	$\breve{\nu}_j$, cm^{-1}	Γ_j, cm^{-1}	Band
$\alpha(T)$	0	0	$\delta(\omega)$
$\beta(T)$	0	$\Gamma(T)$	Drude
1305 ± 20	310 ± 7	329 ± 54	mid-IR
4987 ± 98	730 ± 18	1820.5 ± 102.5	mid-IR
17270 ± 760	3300 ± 80	12605 ± 1765	mid-IR
425.5 ± 25.5	270.8 ± 1.5	16.55 ± 3.35	phonon
638 ± 70	351.7 ± 2.1	68 ± 22	phonon
309.5 ± 57.5	565.8 ± 2.6	22 ± 10	phonon

plicity we have ignored both the asymmetry and the temperature dependence of the phonon bands. We have taken into account the effect of temperature on three essential parameters, and their temperature dependence for Sample NIST 73 is presented in Table 6.15. Equations 6.7, 6.8, and 6.9 apply for Sample NIST 73, too.

Table 6.15: Temperature dependence of some model parameters for the $YBa_2Cu_3O_{7-\delta}$ film of Sample NIST 73.

T K	$\Gamma(T)$, cm^{-1}	$\alpha(T)$, cm^{-1}	$\beta(T)$, cm^{-1}	Applicable to
300	542.5 ± 3.5	0	5006.5 ± 19.5	all
200	410.5 ± 3.5	0	5006.5 ± 19.5	all
100	273.5 ± 3.5	0	5006.5 ± 19.5	all
50	197.9 ± 1.7	2512.0 ± 18.5	4330.7 ± 10.7	$\mathcal{T}$
	197.9 ± 1.7	3655 ± 43	3421.41 ± 4.05	$\mathcal{R}$
	197.9 ± 1.7	1774.0 ± 13.5	4681.66 ± 5.15	$b\mathcal{R}$
20	210.4 ± 2.8	2783.0 ± 24.5	4161.7 ± 16.4	$\mathcal{T}, b\mathcal{R}$
20	210.4 ± 2.8	3899.0 ± 27.5	3140.52 ± 34.15	$\mathcal{R}$
10	209.25 ± 1.15	2808 ± 7	4144.90 ± 4.75	$\mathcal{T}, b\mathcal{R}$
10	209.25 ± 1.15	3891.0 ± 50.5	3150.4 ± 62.4	$\mathcal{R}$

For convenience, the temperature dependencies of the superconducting fluid fraction and the DC-conductivity[21] for the $YBa_2Cu_3O_{7-\delta}$ film of Sample NIST 73, which correspond to the parameter values given in Table 6.15, are presented in Table 6.16. The uncertainties in $\Delta\sigma_{DC}$ of the DC-conductivity reported in Table 6.16 have been determined by using equation 6.10.

---

[21] The DC-conductivity σ_{DC} was calculated in the "*.dru" files generated by the program "dlcalc" from the custom data-processing package created by Charles Porter and David Tanner.

Table 6.16: Temperature dependence of some transport characteristics for the $YBa_2Cu_3O_{7-\delta}$ film of Sample NIST 73.

T, K	$f_s(T)$, %	σ_{DC}, $(\Omega\cdot\text{cm})^{-1}$	Applicable to
300	0	770.0 ± 6.6	all
200	0	1018 ± 10	all
100	0	1527 ± 21	all
50	25.18 ± 0.37	∞	$\mathcal{T}$
	53.30 ± 0.63	∞	$\mathcal{R}$
	12.56 ± 0.19	∞	$b\mathcal{R}$
20	30.90 ± 0.28	∞	$\mathcal{T}, b\mathcal{R}$
20	60.65 ± 0.43	∞	$\mathcal{R}$
10	41.36 ± 0.16	∞	$\mathcal{T}, b\mathcal{R}$
10	60.40 ± 0.78	∞	$\mathcal{R}$

6.3.3.3 Front-side reflectance from Sample NIST 73

The front-side reflectance from the two best Samples (NIST 73 and NIST 74) of the second batch measured recently are shown herein. Clearly, these results are much better than the earlier measurements on Samples NIST 255 and NIST 256. The reflectance spectra are dominated by the same features that were listed for the transmittance, but here they are more weakly "pronounced", and mostly affect the bottom envelope of the curves. The front-side reflectance from Sample NIST 73 is shown in Figures 6.33 (normal state) and 6.34 (superconducting state). The top and bottom envelopes of the fits generally follow the shape of the corresponding envelopes for the measured reflectance. However, the top-fit envelope is slightly higher than the top-data envelope, and even more pronounced is the down shift of the bottom-fit envelope with respect to the bottom-data envelope. These shifts are present for the reflectance spectra at all temperatures, in both the normal

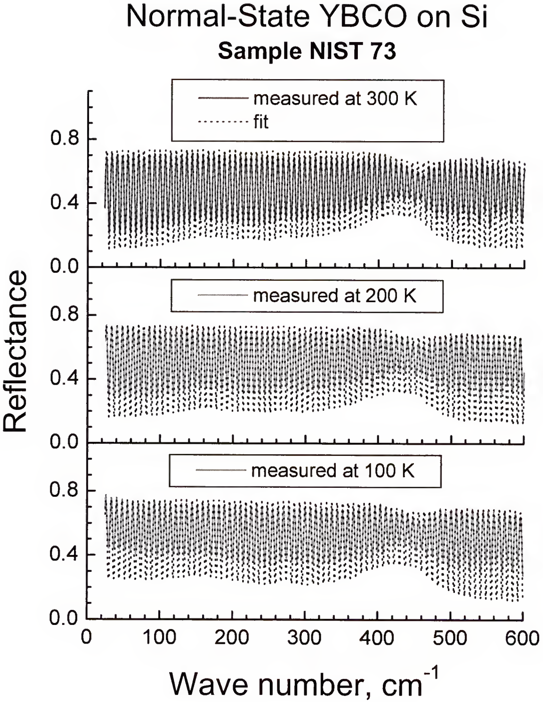

Figure 6.33: Front-side reflectance from Sample NIST 73: an $YBa_2Cu_3O_{7-\delta}$ film on a Si substrate with YSZ and CeO_2 buffer layers, and with a thin SiO_2 film on its back side at three temperatures in the normal state.

and the superconducting state of the $YBa_2Cu_3O_{7-\delta}$ film. In part this higher amplitude[22] of the fits compared to the measured data is due to partial coherence which can be caused by small parasitic wedging of either the Si substrate or the $YBa_2Cu_3O_{7-\delta}$ film. But we believe that some of it is due to the inhomogeneity of the $YBa_2Cu_3O_{7-\delta}$ film along the normal to film plane. An indication leading to that conclusion is the fact that as the temperature is lowered, with the YBCO in the superconducting state, the far-infrared reflectance from Sample NIST 73 is growing fast, but the fits using the parameters optimized for the transmittance, are lagging behind, as can be seen in Figure 6.34 Therefore, based on these and other similar results that we have, it can be argued that the film can roughly be subdivided into three sub-layers: outer—adjacent to the vacuum interface, inner—adjacent to the top buffer layer (CeO_2), and central—in between the former two transitional sub-layers. Thus we had to assume that in the presence of a superconducting fluid, the front-side reflectance probes mostly the outer YBCO-film sub-layer and its close vicinity, whereas the back-side reflectance probes mostly the inner YBCO sub-layer and its close vicinity. The transmittance probes more or less the entire depth of the sample without discrimination, and is thus equivalent to an effective averaging of the parameters characterizing the various sub-layers of the film. Thus, for Sample NIST 73 the fraction f_s of the superconducting electrons for the central and inner sub-layers of the $YBa_2Cu_3O_{7-\delta}$ film is lagging behind f_s for the outer sub-layers as the temperature is lowered in the superconducting state. Therefore, the crudest way to account for the observed discrepancies is to allow the values of f_s for the front-side and back-side reflectance to be generally different than that for the transmittance spectra at those temperatures. This lead as to the

---

[22] Here the term "amplitude" is generalized to mean half of the difference between the top and bottom envelopes, and is a function of the spectral variable—the wave number.

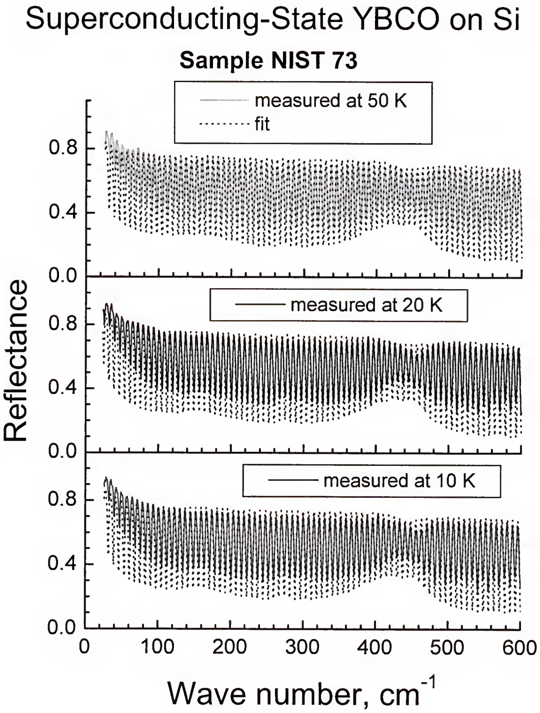

Figure 6.34: Front-side reflectance from Sample NIST 73: an $YBa_2Cu_3O_{7-\delta}$ film on a Si substrate with YSZ and CeO_2 buffer layers, and with a thin SiO_2 film on its back side at three temperatures in the superconducting state.

alternate fits with parameters optimized specifically for the front-side reflectance or back-side reflectance.

The front-side reflectance from Sample NIST 73 with alternate fits is shown in Figure 6.35 (superconducting state).

The apparent thickness of Si corresponding to the alternate fit optimized specifically for the front-side reflectance are marked with "ar" in Table 6.13. The three essential parameters, presented in Table 6.15, correspond to the alternate fit optimized specifically for the front-side reflectance whenever they are on a line marked with $\mathcal{R}$, but not marked with $\mathcal{T}$. The same applies for the two transport parameters given in Table 6.16.

It should be noted also that the far-infrared at 100 K is higher than the fit (see Figure 6.33). We can call this effect advancing. The observed advancing might imply that superconducting fluctuations begin to appear even above the critical temperature T_c. In high T_c materials superconducting fluctuations are known (believed) to be present up to temperature $T \sim 2T_c$. We tried to model the superconducting stripes or islands caused by such fluctuations in two different ways: by including a premature $\delta(\omega)$-function, or by considering two Drude bands with different scattering rate. In both attempts the iterations converged to the original fit. But using either of these two approaches, it is possible to obtain a fit that is visually more pleasing even though it has a higher χ^2. It seems the reason for that is the problem with partial coherence which causes the amplitude of the fits to be higher compared to that of the measured data. This can cause the much wider spectral range above the pseudogap to dominate the χ^2-parameter of the fits.

As the temperature is lowered, it seems that the superconducting state initially appears about some imaginary surface (ideally a plane) which is likely to be within the middle sub-layer. We can call it nucleating surface. The position of that sur-

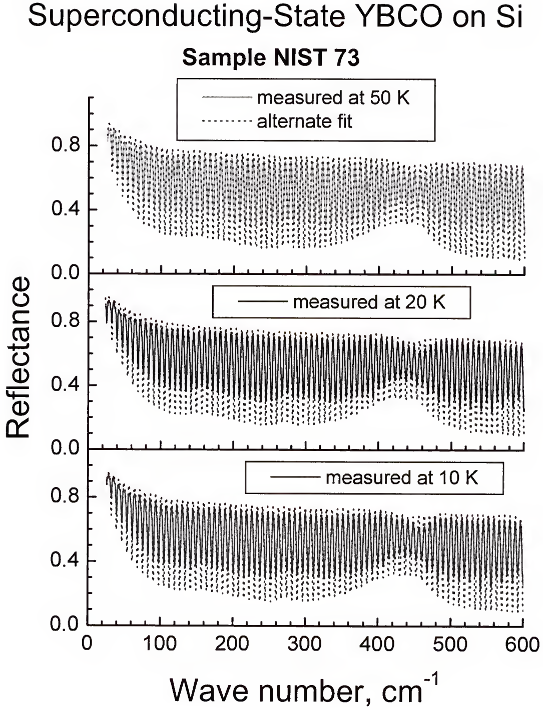

Figure 6.35: Front-side reflectance from Sample NIST 73: an $YBa_2Cu_3O_{7-\delta}$ film on a Si substrate with YSZ and CeO_2 buffer layers, and with a thin SiO_2 film on its back side at three temperatures in the superconducting state.

face may vary from sample to sample due to the manufacturing conditions which can differ even for samples from the same batch which were in different locations within the reactor. Because of the observed advancing of the reflectance from Sample NIST 73, for that particular sample the nucleating surface must be much closer to the outer sub-layer than to the inner sub-layer. As the temperature is lowered below T_c, two demarcation surfaces (ideally two parallel planes) separating the superconducting and normal state (with possibly some fluctuations) "march", one of them inward, deeper into the cuprate film, and the other outward towards the free surface, until almost the entire film is already superconducting at temperatures below some temperature between 50 K and 20 K, most likely closer to 20 K. With data at 50, 20, and 10 K, we can safely conclude only that the of the superconducting fluid reaches saturation below about 20 K. The demarcation planes have a higher temperature speed $\mathrm{d}x/\mathrm{d}T$ within the central sub-layer, but are gradually "slowed" down as they enter the outer or inner layer, respectively, where they meet a higher "resistance". Thus, the superconducting transition within the central sub-layer is sharp similarly to the bulk case, but the superconducting transition of the outer sub-layer and/or inner sub-layer may be spread within a wide temperature range, even though the transition in each differentially-thin sub-sub-layer is sharp as usual.

Indeed, the alternate fitting parameters for the front-side reflectance imply that below 100 K or even below some temperature exceeding 100 K, the outer sub-layer of the YBCO film always has a higher density of the superfluid than the rest of the film, whereas the alternate fitting parameters for the back-side reflectance (covered in the next subsubsection) imply that the inner-most sub-layer of the YBCO film at 50 K has a lower density of the superfluid than the rest of the film, but at about 20 K the inner-most sub-layer has an average superfluid density.

As can be seen in Table 6.16, at 50 K the front-side reflectance, transmittance, and back-side reflectance, are best fit by the highest (0.533), intermediate (0.252), and lowest (0.126) value of f_s, respectively. At 20 K the transmittance and back-side reflectance share the same $f_s = 0.309$, whereas the front-side reflectance can be fit well with $f_s = 0.606$. And finally, at 10 K the transmittance and back-side reflectance share the same $f_s = 0.414$, whereas the front-side reflectance can be fit well with $f_s = 0.604$.

Furthermore, at 100 K the transmittance and back-side reflectance can be fit well with $f_s = 0$, but visually the front-side reflectance requires a non-zero value ($f_s = 0.126$) in order to model the far-infrared increase. Because the latter visual fit is not supported by the χ^2 criterion, we have not presented it herein.

A more refined approach for handling the above issues was suggested to me by Dr. Zhuomin Zhang (personal communication): rather than artificially assigning different parameters of the YBCO layer for transmittance, front-side and back-side reflectance, one can substitute the monotonic variation of the film's properties as a function of depth with an effective step function, that is one can represent the film by two (or three) sub-layers, outer, (middle), and inner, characterized by different effective superfluid densities. Naturally, this introduces one (two) sub-layer thickness(es) as additional parameters, and so this approach was not used.

6.3.3.4 Back-side reflectance from Sample NIST 73

The back-side reflectance from Sample NIST 73 is shown in Figures 6.36 (normal state) and 6.37 (superconducting state). The prominent features affect both the top and the bottom envelopes, making the curves almost symmetric with respect to the fringe-averaged central line.[23]

---

[23] If one were to imagine that the curves are rotated clockwise by 90deg, one would be able to see nice artistic "vases". They could be interpreted to be symbolizing that our research was

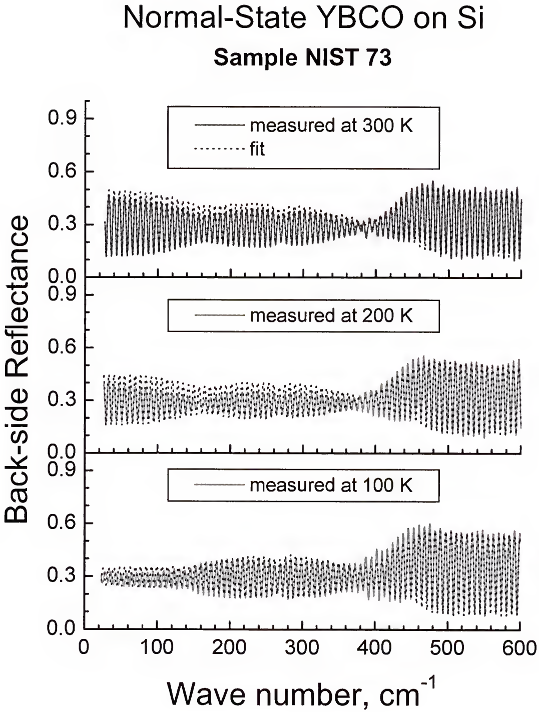

Figure 6.36: Back-side reflectance from Sample NIST 73: an $YBa_2Cu_3O_{7-\delta}$ film on a Si substrate with YSZ and CeO_2 buffer layers, and with a thin SiO_2 film on its back side at three temperatures in the normal state.

The curve measured at 100 K shows the far-infrared antireflection effect, and the curve at 200 K is close to having the antireflection effect within the spectral range from 160 to 380 cm^{-1}. The far-infrared back-side reflectance increases sharply in the superconducting state, as expected.

6.3.4 Sample NIST 74

6.3.4.1 Transmittance through Sample NIST 74

The transmittance through Sample NIST 74 is shown in Figures 6.38 (normal state) and 6.39 (superconducting state). The transmittance through Sample NIST 74 is very similar in its general appearance to that of Sample NIST 73 (compare Figures 6.38 and 6.39 to Figures 6.31 and 6.32, respectively. One major exception is that for Sample NIST 74 the far-infrared antireflection effect is at a temperature close to and below 200 K, rather than close to and above 100 K as was observed for Sample NIST 73. Additionally, Sample NIST 74 is characterized by antireflection effect within the spectral range from 160 to 360 cm^{-1}at some temperature close to 300 K. A similar spectral shift of the antireflection effect with temperature should be present for Sample NIST 73, too. The respective temperature does not seem to be very close to 200 K, though the presence of some shrinking in the difference between the top and bottom envelope for the spectral range from 160 to 360 cm^{-1} implies that the antireflection effect for that spectral range may be either above 200 K (e.g., from 230 to 240 K), or below 200 K (e.g., from 160 to 170 K).

---

done under the hat of the College of Liberal Arts and Sciences.

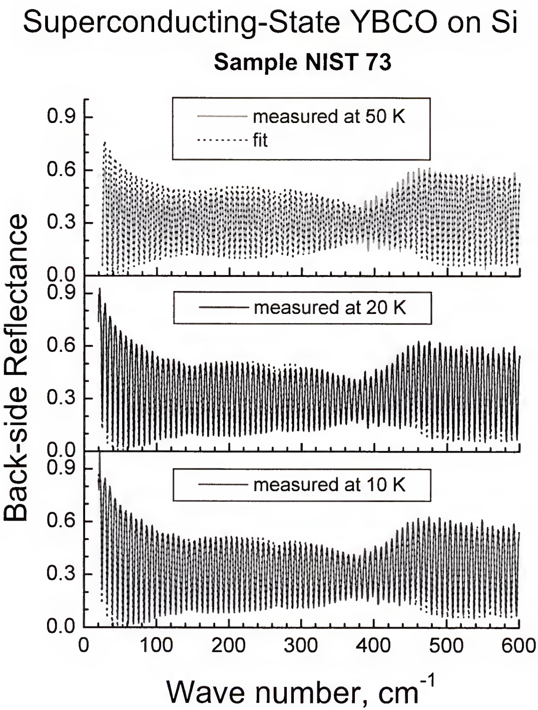

Figure 6.37: Back-side reflectance from Sample NIST 73: an $YBa_2Cu_3O_{7-\delta}$ film on a Si substrate with YSZ and CeO_2 buffer layers, and with a thin SiO_2 film on its back side at three temperatures in the superconducting state.

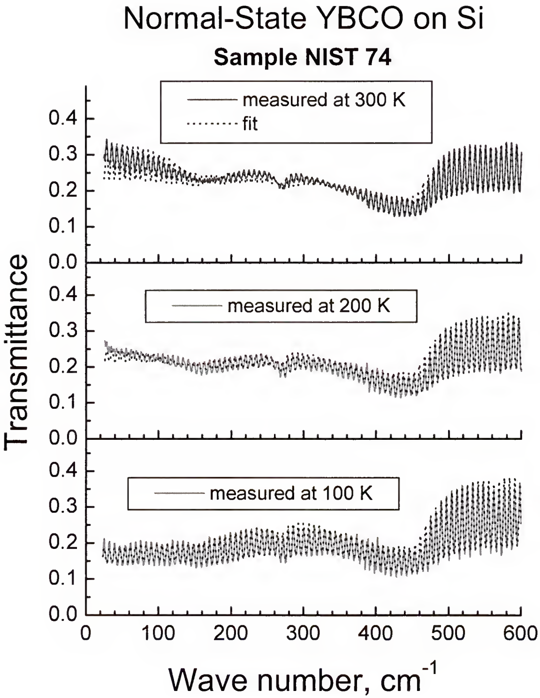

Figure 6.38: Transmittance through Sample NIST 74: an $YBa_2Cu_3O_{7-\delta}$ film on a Si substrate with YSZ and CeO_2 buffer layers, and with a thin SiO_2 film on its back side at three temperatures in the normal state.

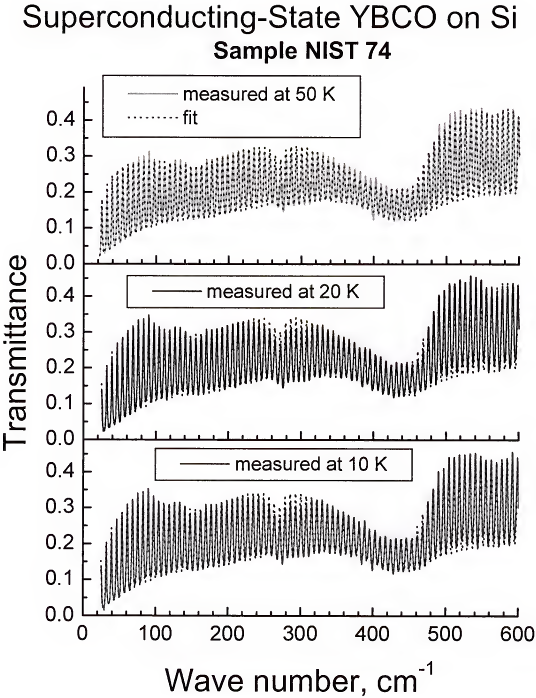

Figure 6.39: Transmittance through Sample NIST 74: an $YBa_2Cu_3O_{7-\delta}$ film on a Si substrate with YSZ and CeO_2 buffer layers, and with a thin SiO_2 film on its back side at three temperatures in the superconducting state.

6.3.4.2 Results for Sample NIST 74 and discussion

Table 6.17 presents the temperature dependence of the apparent thickness of the Si layer of Sample NIST 74 as determined from transmittance (superscript $\mathcal{T}$), front-side reflectance[24] (superscript $\mathcal{R}$), and back-side reflectance (superscript $b\mathcal{R}$). The values marked with "ar" ("abr") correspond to an alternate fit optimized specifically for the front-side (back-side) reflectance, respectively, summarized in Table 6.19, and described in more detail later.

Table 6.17: Temperature dependence of the apparent thickness of the Si layer of Sample NIST 74 as determined from transmittance ($\mathcal{T}$), front-side reflectance ($\mathcal{R}$), and back-side reflectance ($b\mathcal{R}$).

T, K	$d_{Si}^{(\mathcal{T})}$, nm	$d_{Si}^{(\mathcal{R})}$, nm	$d_{Si}^{(b\mathcal{R})}$, nm
300	202142.0 ± 18.5	202125.5 ± 6.5	202204.5 ± 10.0
200	201982.0 ± 10.0	202052.0 ± 8.0	202102.0 ± 3.0
100	201917.5 ± 12.5	202034.0 ± 5.0	202027.5 ± 15.5
50	201913.0 ± 9.0	202032.5 ± 5.5	202018.0 ± 24.0
50		201993.5 ± 11.5 ar	202050.5 ± 11.5 abr
20	201913.5 ± 2.5	202024.0 ± 11.0	201993.5 ± 8.5
20		201985.2 ± 4.0 ar	202016.0 ± 12.0 abr
10	201911.5 ± 9.5	202021.0 ± 7.0	201984.0 ± 11.0
10		201981.0 ± 8.0 ar	202004.0 ± 7.0 abr

Once again, Table 6.17 demonstrates that at each temperature the three spectra result in three different values of the apparent thickness of the Si layer. For the case of Sample NIST 74, the silicon thickness corresponding to the transmittance is within the range bound by the other two values for the thickness of Si only at

---

[24] The parameters corresponding to front-side reflectance and back-side reflectance from Sample NIST 73 are also included in this table.

300 K. However, at all lower temperatures the silicon thickness corresponding to the transmittance is the lowest of the three values which seems to be anomalous and is probably due to slight misalignment due to the temperature gradient in the sample holder.

The oscillator model parameters for the $YBa_2Cu_3O_{7-\delta}$ film of Sample NIST 74 are given in Table 6.18.

Table 6.18: $YBa_2Cu_3O_{7-\delta}$ Model Parameters for Sample NIST 74.

$\breve{\nu}_{pj}$, cm^{-1}	$\breve{\nu}_j$, cm^{-1}	$\mathit{\Gamma}_j$, cm^{-1}	Band
$\alpha(T)$	0	0	$\delta(\omega)$
$\beta(T)$	0	$\mathit{\Gamma}(T)$	Drude
1716 ± 70	261 ± 19	343.5 ± 46.5	mid-IR
5451 ± 115	719.5 ± 22.5	1736 ± 79	mid-IR
21126 ± 808	3241.5 ± 16.5	10319 ± 1058	mid-IR
515.5 ± 52.5	269.95 ± 0.95	15.05 ± 3.55	phonon
653.5 ± 85.5	349.65 ± 4.15	47.75 ± 12.25	phonon
302 ± 75	564.55 ± 3.15	18.1 ± 7.3	phonon

For convenience, the temperature dependencies of the superconducting fluid fraction and the DC-conductivity for the $YBa_2Cu_3O_{7-\delta}$ film of Sample NIST 74, which correspond to the parameter values given in Table 6.19, are presented in Table 6.20. Equations 6.7, 6.8, and 6.9 apply for Sample NIST 74, too.

For convenience, the temperature dependencies of the superconducting fluid fraction and the DC-conductivity for the $YBa_2Cu_3O_{7-\delta}$ film of Sample NIST 74 are presented in Figure 6.20.

Table 6.19: Temperature dependence of some model parameters for the $YBa_2Cu_3O_{7-\delta}$ film of Sample NIST 74.

T, K	$\Gamma(T)$, cm^{-1}	$\alpha(T)$, cm^{-1}	$\beta(T)$, cm^{-1}	Applicable to
300	563.5 ± 4.5	0	6094.5 ± 18.5	all
200	403.35 ± 3.15	0	6094.5 ± 18.5	all
100	250.75 ± 3.05	0	6094.5 ± 18.5	all
50	196.2 ± 3.8	3582.0 ± 43.5	4930.7 ± 31.6	$\mathcal{T}$
	196.2 ± 3.8	2474 ± 84	5569.8 ± 37.3	$\mathcal{R}$
	196.2 ± 3.8	1841 ± 71	5809.8 ± 22.5	$b\mathcal{R}$
20	206.3 ± 1.3	3911.0 ± 11.5	4674.08 ± 9.65	$\mathcal{T}$
	206.3 ± 1.3	2759 ± 50	5434 ± 25	$\mathcal{R}$
	206.3 ± 1.3	3001 ± 2	5304.42 ± 1.15	$b\mathcal{R}$
10	207.95 ± 4.75	3946 ± 42	4644.6 ± 35.7	$\mathcal{T}$
	207.95 ± 4.75	3053.0 ± 45.5	5274.7 ± 26.3	$\mathcal{R}$
	207.95 ± 4.75	2914.0 ± 27.5	5352.7 ± 14.9	$b\mathcal{R}$

Table 6.20: Temperature dependence of some transport characteristics for the $YBa_2Cu_3O_{7-\delta}$ film of Sample NIST 74.

T, K	$f_s(T)$, %	σ_{DC}, $(\Omega\cdot\text{cm})^{-1}$	Applicable to
300	0	1099 ± 10	all
200	0	1535 ± 14	all
100	0	2469 ± 32	all
50	34.54 ± 0.84	∞	$\mathcal{T}$
	16.48 ± 1.12	∞	$\mathcal{R}$
	9.13 ± 0.70	∞	$b\mathcal{R}$
20	41.18 ± 0.24	∞	$\mathcal{T}$
	24.247 ± 0.032	∞	$\mathcal{R}$
	20.49 ± 0.74	∞	$b\mathcal{R}$
10	41.92 ± 0.89	∞	$\mathcal{T}$
	25.09 ± 0.75	∞	$\mathcal{R}$
	22.86 ± 0.43	∞	$b\mathcal{R}$

6.3.4.3 Front-side reflectance from Sample NIST 74

The front-side reflectance through Sample NIST 74 is shown in Figures 6.40 (normal state) and 6.41 (superconducting state). Here the fit at 300 K with parameters optimized for the transmittance, is shifted up from the measured data by about 0.1. As the temperature is decreased the corresponding up-shift of the fit decreases The far-infrared up-shift in the superconducting state is another story: it seems to imply that the outer YBCO-sub-layer of Sample NIST 74 has worse superconducting properties than the central sub-layer, whereas for Sample NIST 73 we observed exactly the opposite: the outer sub-layer seemed to have better superconducting properties than the central sub-layer (compare Figure 6.41 to Figure 6.34.

The front-side reflectance from Sample NIST 74 with alternate fits is shown in Figure 6.42 (superconducting state).

The apparent thickness of Si corresponding to the alternate fit optimized specifically for the front-side reflectance are marked with "ar" in Table 6.17. The three essential parameters, presented in Table 6.19, correspond to the alternate fit optimized specifically for the front-side reflectance whenever they are on a line marked with $\mathcal{R}$, but not marked with $\mathcal{T}$. The same applies for the two transport parameters given in Table 6.20.

It should be noted also that the far-infrared reflectance is depressed compared to the fit at all six temperatures (see Figures 6.40 and 6.41). This seems to be the opposite effect to what we called advancing superconducting transition, and so we can call this effect retarding superconducting transition. The observed retarding might imply that the outer sub-layer is "dead" and presents a much higher temperature "resistance" to the outer demarcation plane. Because of the observed retarding in the reflectance from Sample NIST 74, for that particular sample the

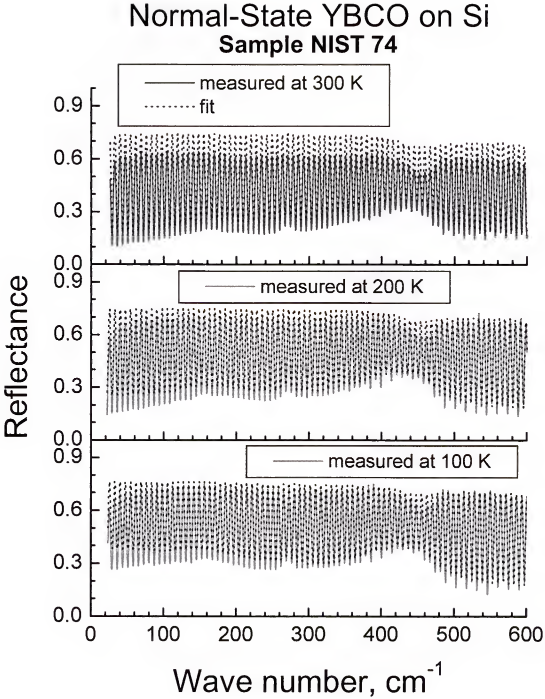

Figure 6.40: Front-side reflectance from Sample NIST 74: an $YBa_2Cu_3O_{7-\delta}$ film on a Si substrate with YSZ and CeO_2 buffer layers, and with a thin SiO_2 film on its back side at three temperatures in the normal state.

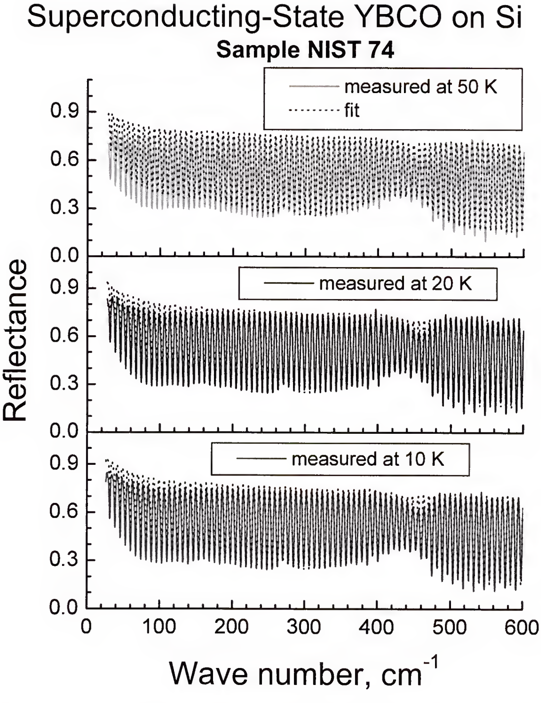

Figure 6.41: Front-side reflectance from Sample NIST 74: an $YBa_2Cu_3O_{7-\delta}$ film on a Si substrate with YSZ and CeO_2 buffer layers, and with a thin SiO_2 film on its back side at three temperatures in the superconducting state.

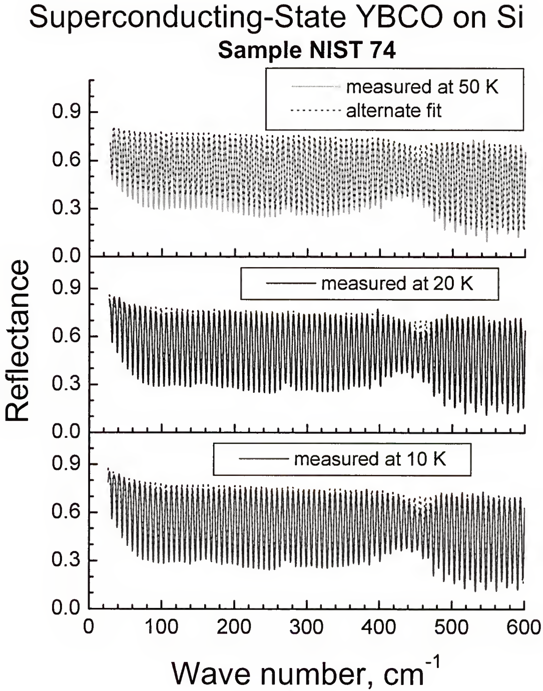

Figure 6.42: Front-side reflectance from Sample NIST 73: an $YBa_2Cu_3O_{7-\delta}$ film on a Si substrate with YSZ and CeO_2 buffer layers, and with a thin SiO_2 film on its back side at three temperatures in the superconducting state.

nucleating surface must be much closer to the inner sub-layer than to the outer sub-layer.

Indeed, the alternate fitting parameters for the front-side reflectance imply that below 100 K or more, the outer sub-layer of the YBCO film always has a lower density of the superfluid than the central sub-layer of the film, just as the alternate fitting parameters for the back-side reflectance (covered in the next subsubsection) imply that the inner-most sub-layer of the YBCO film at all superconducting-state temperatures also has a lower density of the superfluid than the central sub-layer of the film.

As can be seen in Table 6.20, at 50 K the transmittance, front-side reflectance, and back-side reflectance, are best fit by the highest (0.345), intermediate (0.165), and lowest (0.0913) value of f_s, respectively. At 20 K the transmittance, front-side reflectance, and back-side reflectance, are best fit by the highest (0.412), intermediate (0.243), and lowest (0.205) value of f_s, respectively. And finally, at 10 K the transmittance, front-side reflectance, and back-side reflectance, are best fit by the highest (0.419), intermediate (0.251), and lowest (0.229) value of f_s, respectively.

6.3.4.4 Back-side reflectance from Sample NIST 74

The back-side reflectance through Sample NIST 74 is shown in Figures 6.43 (normal state) and 6.44 (superconducting state). Qualitatively, these back-side reflectance spectra are very similar to those of Sample NIST 73. But the fits with parameters optimized for the transmittance are not quite as good in this case. This is an indication that the inner sub-layer of this sample differs more significantly from the central one than is the case for sample NIST 73. Notably, the far-infrared back-side reflectance from Sample NIST 74 at 50 K is significantly lower than the calculated with parameters optimized for the transmittance. At all the three temperatures with YBCO in the superconducting state, the fits amplitude

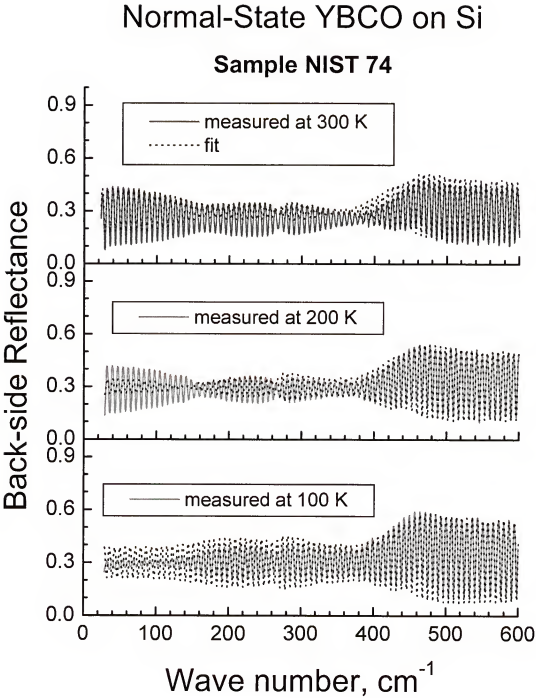

Figure 6.43: Back-side reflectance from Sample NIST 74: an $YBa_2Cu_3O_{7-\delta}$ film on a Si substrate with YSZ and CeO_2 buffer layers, and with a thin SiO_2 film on its back side at three temperatures in the normal state.

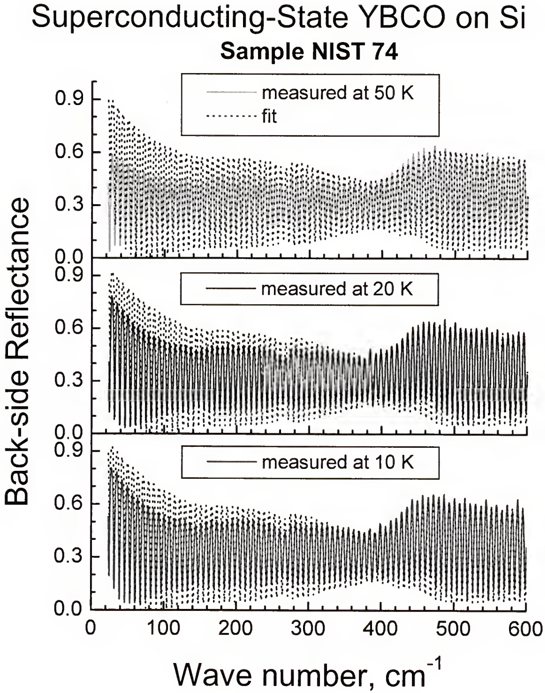

Figure 6.44: Back-side reflectance from Sample NIST 74: a $YBa_2Cu_3O_{7-\delta}$ film on a Si substrate with YSZ and CeO_2 buffer layers, and with a thin SiO_2 film on its back side at three temperatures in the superconducting state.

significantly exceeds the amplitude of the measured spectrum in the spectral range below 360 cm^{-1}. The difference in these amplitudes decreases somewhat as the temperature is lowered.

6.4 Analysis of the Transmittance and Reflectance

The fact, that the far-infrared wavelengths are roughly comparable to the Si substrate thickness, explains the presence of interference fringes in our spectra. The thin $YBa_2Cu_3O_{7-\delta}$ films (35 nm) we have used are transparent enough in the far-infrared spectral range, so that the fringes due to multiple-beam interference within the Si substrate are there not only for measurements of "naked" substrates, but also in the spectra of $YBa_2Cu_3O_{7-\delta}$ film-substrate composites.

6.4.1 Fitting Procedure

The most important facts about the fitting procedure have already been mentioned as the various spectra were presented and described. Here some more detail will be added.

The multi-layered samples that we have measured were described in the previous chapter. Various methods for calculating the optical properties of such structures exist, some of which are presented in sections 3.2 and 3.4. My collaborator A. Ravi Kumar [120] has used the matrix method for some of his calculations. I have processed our data using custom-made software by Charles Porter that can be found on Dr. David Tanner's web-page at `www.ufl.phys.edu/~ tanner/` (click on "Data analysis programs"). The package includes a film-fitting program "flmfit" based on the method of P. Rouard: assuming downward incidence, the bottom two layers are replaced by one effective layer, and by iterating the same procedure from the bottom layer to the top one, the multi-layered case is reduced to the simple plate-in-a-medium problem.

The result of the calculation is the complex refractive index which allows calculation of either transmittance or reflectance. The calculated curves can be compared to the measured spectra. The fitting procedure involves an appropriate modelling of the optical properties of each individual layer. The model parameters for all layers are varied until the root-mean-square difference from the measured spectrum is minimized. The spectrum calculated with the parameters, optimized in this way, is the best fit. Naturally, the optimized parameters that correspond to the best fit, characterize the optical properties of the whole multi-layered structure, and a specific subset of those parameters characterizes each individual layer.

As a first approximation, dielectric layers with low absorption within the spectral range of interest are modelled by a simple real dielectric constant and thickness. The spectra might indicate also the presence of phonons which are accounted for by Lorentz oscillators. Summing the contribution of all oscillators gives the complex dielectric function of the particular layer from which the complex refractive index can be calculated. For layers with "free" charge carriers, a Drude term must be added to the Lorentz ones. With these assumptions the complex refractive index for each layer can be calculated. The latter, together with the respective layer thickness serve as feeding information for the Rouard's iterative procedure mentioned in sections 3.4.2 and 3.4.3.

Since our earlier measurements covered a narrower spectral range from 10 to 100 cm^{-1}, we were able to ignore the two thin dielectric layers used as buffers, namely CeO_2, and yttria-stabilized zirconia. These substances are characterized by a very weak absorption in the far-infrared spectral range, and besides the thickest of the layers (yttria-stabilized zirconia) was only 20 nm. In the far-infrared and short-wave microwave spectral range the dielectric constants of yttria-stabilized zirconia and CeO_2 are 25 and 17, respectively [138,139]. Thus, we found that the presence of the SiO_2, yttria-stabilized zirconia, and CeO_2 layers has no detectable effect on the calculated transmittance and reflectance for the case of our earlier measurements. Therefore, we were ignoring those layers, which reduced the problem to a two-layered structure: a thin $YBa_2Cu_3O_{7-\delta}$ film on a thin Si substrate.

Because the alignment of the transmittance configuration is much less demanding than that of the reflectance configuration, the transmittance data are always more reliable than the reflectance data. Additionally, for our earlier measurements, the transmittance spectra (taken on the Michelson interferometer) have a better spectral resolution than the reflectance spectra (taken on the Bruker interferometer). This is especially important for spectra with sharp interference features. Finally, we recently realized that when a sample is characterized by a significant transmittance, the sample holder for reflectance measurements in the Bruker interferometer allows some parasitic light to be reflected from the back of the reference mirror. The recycled parasitic light takes part in the multiple beam interference within the Si substrate, and will lead to shifting the reflectance data up or down, depending on the phase of the parasitic light. Therefore, we always start by fitting the transmittance spectra. Of course, the model parameters were also tested with the front-side and back-side reflectance data whenever such were available and deemed reliable.

The normal state of $YBa_2Cu_3O_{7-\delta}$ was modelled using the Drude-Lorentz model. The relatively weak effect of the Lorentz term in the far-infrared spectral range allows the use of a single oscillator. My collaborator Dr. Kumar used as a starting point the values for the parameters recommended by Zhang et al. [148]: $\omega_e = 1800\ \text{cm}^{-1}$, $\omega_{pe} = 18000\ \text{cm}^{-1}$, and $\gamma_e = 5400\ \text{cm}^{-1}$. Since in the far-infrared spectral range $\omega \ll \omega_e$, this mid-infrared band leads to an essentially real dielectric constant

$$\varepsilon_L \approx (\omega_{pe}/\omega_e)^2 \tag{6.11}$$

Not only its effect within the spectral range from 10 to 100 cm^{-1} is very weak, but it is quite insensitive to the specific values for the parameters, too. E.g., Dr. Kumar found that the following set of Lorentz parameters ω_e = 1800 cm^{-1}, ω_{pe} = 24150 cm^{-1}, and γ_e = 7500 cm^{-1} [149], does not lead to any significant changes in the transmittance and reflectance spectra.

The plasma frequency ω_{pe} was determined by fitting the room-temperature data. The square of plasma frequency is proportional to the total "free" electron density (see equation 3.40), or the DC conductivity(see equation 3.52), and for superconductors is typically constant with temperature [104,141,25]. Therefore, for spectra at other temperatures in the normal state of $YBa_2Cu_3O_{7-\delta}$, only the scattering rate is used as an adjustable parameter.

In the superconducting state of $YBa_2Cu_3O_{7-\delta}$, the fraction of superconducting electrons f_s is added as another adjustable parameter along with the scattering rate $1/\tau$. Because unlike the semiconductor case, in superconductors there are generally no thermally generated charge carriers, the Drude and δ-function plasma frequencies added in quadrature should be equal to the square of the normal state plasma frequency.

The "free" carriers in the normal state of $YBa_2Cu_3O_{7-\delta}$ are accounted for by the Drude term. Its adjustable parameters are the plasma frequency ω_p (or DC conductivity σ_{DC}), and the scattering rate, i.e., the inverse relaxation time $1/\tau$ for the carriers. Varying the fitting parameters has shown that the optical properties depend much more strongly on σ_{DC}, rather than on $1/\tau$. This implies that our values for the scattering rate have a larger uncertainty compared to that for the DC conductivity.

When the root-mean-square difference is not very sensitive to the parameters, one can also use the differences in the fringe-averaged transmittance and the peak transmittance in order to determine the best fit.

In order to improve the quality of the $YBa_2Cu_3O_{7-\delta}$ film, the later batch of samples that we have measured had thicker buffer layers than those for the earlier batch. The CeO_2 layer was twice thicker and the yttria-stabilized zirconia layer was about an order of magnitude thicker than those in the earlier samples. Additionally, our more recent measurements were done in a wider spectral range from 20 to 600 cm^{-1}. As a consequence of these facts, we found that the above mentioned simplification was not justifiable any more. Initially we had to include a number of phonons within all five layers into consideration. Later it turned out that our data are not sensitive to all of them and many of them were dropped, including all phonons for the CeO_2 layer. Each of the phonons that were left is characterized by its central wave number $\breve{\nu}_j$, its plasma wave number $\breve{\nu}_{pj}$, and its linewidth Γ_j. All of these parameters are summarized in Tables in the preceding subsections.

6.4.2 Transmittance

For comparison the most essential fitting parameters for both sample films from our earlier measurements are shown in Table 6.21. The values presented in the table are derived from the transmittance measurements which we deem as most reliable and representative. Indeed, the alignment for transmittance is less critical and therefore is not as prone to errors. Furthermore, the normal incidence makes these measurements much less sensitive to the effects of partial coherence which have been described by e.g., Zhang [150] and others. In the table head the critical temperature T_c, the Drude plasma frequency ω_p, and the thickness d_{Si} of the Si substrate are listed. The thermal expansion of Si is negligible and has been ignored during the analysis of our earlier measurements. Any effect it might have, has been "absorbed" by the refractive index of Si that we have used. Given in the table body is the temperature dependence of the refractive index n_{Si} of Si and three parameters characterizing the $YBa_2Cu_3O_{7-\delta}$ film: the DC conductivity σ_{DC}^{-1}, the Drude scattering rate $1/\tau$, and the fraction f_s of superconducting electrons.

Table 6.21: Essential parameters characterizing Samples NIST 255 and NIST 256. Estimated maximum uncertainties: 0.03 % in n_{Si}, 10 % in σ_{DC}^{-1}, 11 % in τ^{-1}, and 15 % in f_s.

		Sample NIST 255 $T_c = 81.5 \pm 0.2$ K $\omega_p = 7000 \pm 100$ cm^{-1} $d_{Si} = 203.7 \pm 0.1$ μm			Sample NIST 256 $T_c = 80.2 \pm 0.2$ K $\omega_p = 7300 \pm 100$ cm^{-1} $d_{Si} = 205.3 \pm 0.1$ μm		
T, (K)	n_{Si}	σ_{DC}^{-1}, ($\mu\Omega$·cm)	$1/\tau$, (cm^{-1})	f_s	σ_{DC}^{-1}, ($\mu\Omega$·cm)	$1/\tau$, (cm^{-1})	f_s
300	3.416	771.6	630	0	714.8	635	0
200	3.401	548.5	448	0	535.9	476	0
100	3.391	324.5	265	0	356.9	317	0
50	3.386	0	220	0.190	0	200	0.207
10	3.386	0	220	0.405	0	200	0.369

The difference in the respective values for the two samples may be caused by slight variations in the film deposition conditions at different locations within the deposition chamber.

In the superconducting state, only the temperature-independent scattering due to impurities and lattice defects remains [149]. Thus, the corresponding scattering rate should be constant at low temperatures. And eventually we obtained the best agreement between the measured and calculated transmittance for both samples with the same scattering rate at 50 K and 10 K. Bonn et al. [151] have shown that due to the rapid reduction of the density of thermally activated quasiparticles, as the temperature is reduced below T_c, the scattering rate of $YBa_2Cu_3O_{7-\delta}$ decreases drastically. Even though their results are for single-crystal $YBa_2Cu_3O_{7-\delta}$ of extremely high quality (with $f_s \lessapprox 1$ at very low temperatures), we expect they should also apply for thin $YBa_2Cu_3O_{7-\delta}$ films.

For the case of thin $YBa_2Cu_3O_{7-\delta}$ films, there is a large fraction ($f_n = 1 - f_s$) of normal-state electrons even at the lowest temperatures. Conversely, for conventional superconductors or bulk high-T_c superconductors, f_n is zero at temperatures $T \ll T_c$. The definition of f_s for high-temperature-superconducting materials can be quite ambiguous. Some researchers have obtained higher values for f_s by assuming that a portion (known as "dead" layer) of the $YBa_2Cu_3O_{7-\delta}$ film is not superconducting [41,140]. For our earlier measurements, the fraction of superconducting electrons is calculated without the assumption that a "dead" layer is present. This is one of the reasons why our values of f_s are small. Another reason might be the higher DC resistivity $1/\sigma_{DC}$ of $YBa_2Cu_3O_{7-\delta}$ films in the normal state. The DC resistivity of such films is affected strongly by the choice of the substrate and buffer layers, as well as by the thicknesses of all the layers [152]. The damage caused by the stripping procedure which is part of the sample preparation technique may have reduced f_s further.

Finally, Sample NIST 255 had a slightly higher critical temperature than Sample NIST 256, and at 10 K is the former sample had a slightly higher fraction of superconducting electrons than the latter sample. Furthermore, in the normal state Sample NIST 255 had a higher electrical resistivity than Sample NIST 256. All of these facts are in agreement, confirming that Sample NIST 255 has an edge over Sample NIST 256 as far as the superconducting characteristics are concerned.

A similar comparison can be made for Samples NIST 73 and NIST 74. The detailed results for these two samples were presented earlier. Here, for the purpose of comparison only the most essential fitting parameters for both sample films from our more recent measurements are juxtaposed in Table 6.22. All values presented in the table are determined from the transmittance measurements which we deem as most reliable and accurate. In the table head the Drude plasma frequency ω_p and the thickness d_{Si} of the Si substrate at 300 K are listed. An attempt has been made to account for the thermal expansion of Si which, even though small, has some effect on the refractive index of Si due to the higher precision of these measurements compared to the earlier data. Given in the table body is the temperature dependence of the refractive index n_{Si} of Si and three parameters characterizing the $YBa_2Cu_3O_{7-\delta}$ film: the DC conductivity σ_{DC}^{-1}, the Drude scattering rate $1/\tau$, and the fraction f_s of superconducting electrons. The uncertainties for these four parameters, which are maximum from among both

Table 6.22: Essential parameters characterizing Samples NIST 73 and NIST 74. Estimated maximum uncertainties: 0.005 % in n_{Si}, 2.0 % in σ_{DC}^{-1}, 1.9 % in τ^{-1}, and 2.4 % in f_s.

		Sample NIST 73 $\omega_p = 5006.5 \pm 19.5$ cm^{-1} $d_{Si} = 200.452 \pm 0.009$ μm			Sample NIST 74 $\omega_p = 6094.5 \pm 18.5$ cm^{-1} $d_{Si} = 202.142 \pm 0.018$ μm		
T, (K)	n_{Si}	σ_{DC}^{-1}, ($\mu\Omega$·cm)	$1/\tau$, (cm^{-1})	f_s	σ_{DC}^{-1}, ($\mu\Omega$·cm)	$1/\tau$, (cm^{-1})	f_s
300	3.4200	1298	542	0	909.9	564	0
200	3.4063	982.3	410	0	651.5	403	0
100	3.3962	654.9	274	0	405.0	251	0
50	3.3938	0	198	0.252	0	196	0.345
20	3.3938	0	210	0.309	0	206	0.412
10	3.386	0	209	0.414	0	208	0.419

samples at all six temperatures, are given in the figure caption. On the average, the uncertainties for characteristics of Samples NIST 73 and NIST 74 are about six times smaller than the respective uncertainties in the parameters of Samples NIST 255 and NIST 256.

Again, the small difference in the respective values for the two samples from the same batch are caused by slight variations in the film deposition conditions at different locations within the deposition chamber.

In the superconducting state the scattering rate is virtually constant, but still there seems to be a very shallow minimum in the vicinity of 50 K. Sample NIST 74 is characterized with a higher superfluid density than Sample NIST 73 at all temperatures below T_c, although at very low temperatures the difference between the two samples has "melted" almost completely. This hints that Sample NIST 74 must have a higher critical temperature. Unfortunately, we do not have information about the critical temperature of these two samples. Indirectly, because they came from the same source as the earlier Samples NIST 255 and NIST 256, we can assume that the two more recent samples have T_c of the same order, maybe slightly higher, taking into account the fact that they show higher superfluid concentrations.

Our reflectance data show some proof for the presence of layers adjacent to the interfaces, whose properties differ from those of the central section of the film. But nevertheless, we have not included into consideration a "dead" layer. Rather we are letting the transmittance to do some averaging for us.

6.4.3 Optical Characteristics of the $YBa_2Cu_3O_{7-\delta}$ Films

The spectra of the optical characteristic of the $YBa_2Cu_3O_{7-\delta}$ films were calculated using the complex dielectric function obtained from the fitting procedure by means of the program "dlcalc", using the parameter files (.prm) generated by the program "flmfit".

6.4.3.1 Samples NIST 255 and NIST 256

Figures 6.45 and 6.46 present the complex refractive index spectra of the $YBa_2Cu_3O_{7-\delta}$ film for Sample NIST 255 and Sample NIST 256, respectively, at five fixed temperatures. The top panels give the real refractive index n'_f of the $YBa_2Cu_3O_{7-\delta}$ film, whereas the bottom panels present its extinction coefficient n''_f. In the normal state, $n'_f \approx n''_f$, as can be expected for any metallic film, and both have a temperature dependence with a negative slope, but positive curvature which is significant in the lowest third of the covered spectral range. At 300 K, 200 K, and 100 K, the real refractive index $n'_f(10\ \mathrm{cm}^{-1})$ is increasing approximately to 62.0, 72.9, and 94.4, respectively, whereas $n'_f(90\ \mathrm{cm}^{-1})$ is increasing approximately to 19.5, 22.1, and 25.9. The respective numbers for the extinction coefficient $n''_f(10\ \mathrm{cm}^{-1})$ are 62.7, 74.6, and 97.7, whereas $n''_f(90\ \mathrm{cm}^{-1})$ these numbers are 21.7, 26.4, and 35.6.

As the $YBa_2Cu_3O_{7-\delta}$ film becomes superconducting, in the far-infrared spectral range n'_f falls sharply, whereas n''_f grows abruptly and its curvature also increases, especially at the very low frequencies. This tendency continues, even though the change is more gradual, as the temperature is reduced further from 50 K to 10 K. Thus, below T_c, $n'_f \ll n''_f$ and to a large extent the response of the $YBa_2Cu_3O_{7-\delta}$ film is inductive. Indeed, at 50 K and 10 K $n'_f(10\ \mathrm{cm}^{-1})$ drops approximately to 29.2 and 14.8, respectively, whereas $n'_f(90\ \mathrm{cm}^{-1})$ go down to approximately 18.5 and 11.4. The respective numbers for the extinction coefficient $n''_f(10\ \mathrm{cm}^{-1})$ shoot up to 308 and 445, whereas for $n''_f(90\ \mathrm{cm}^{-1})$ these numbers go up to 46.5 and 55.3, respectively. The descriptions above apply quantitatively to Sample NIST 255 only, but qualitatively to Sample NIST 256, as well.

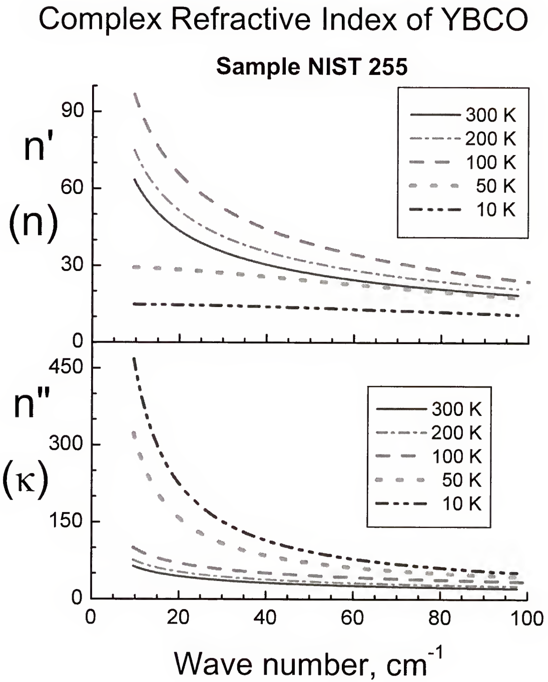

Figure 6.45: Complex refractive index for the $YBa_2Cu_3O_{7-\delta}$ layer of Sample NIST 255: refractive index/extinction on top/bottom panel, respectively.

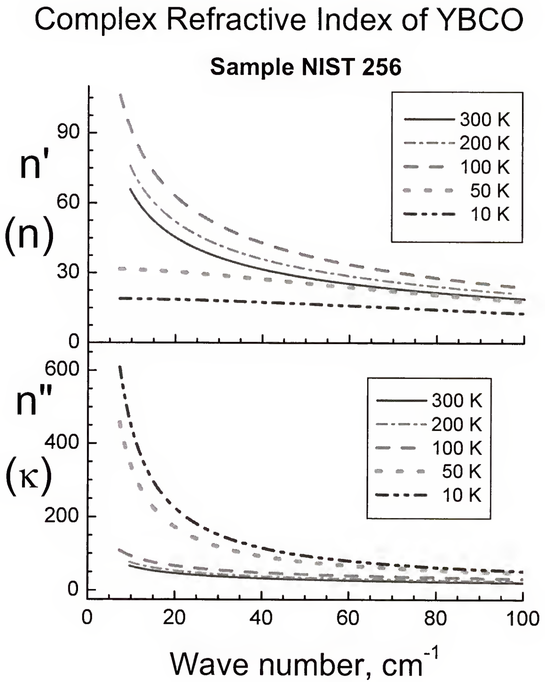

Figure 6.46: Complex refractive index for the $YBa_2Cu_3O_{7-\delta}$ layer of Sample NIST 256: refractive index/extinction on top/bottom panel, respectively.

In the superconducting state, Sample NIST 255 is characterized by an approximately equal to slightly higher n''_f and somewhat lower n'_f than the respective values for Sample NIST 256. To get a rough estimate for the batch variation of the complex refractive index, one can compare the refractive index at 10 K for Sample NIST 255 $\langle n'_f(10\ \mathrm{cm}^{-1}) \approx 14.8$, $n'_f(90\ \mathrm{cm}^{-1}) \approx 11.4$, $n''_f(10\ \mathrm{cm}^{-1}) \approx 445$, $n''_f(90\ \mathrm{cm}^{-1}) \approx 55.3\rangle$ and Sample NIST 256 $\langle n'_f(10\ \mathrm{cm}^{-1}) \approx 18.9$, $n'_f(90\ \mathrm{cm}^{-1}) \approx 13.6$, $n''_f(10\ \mathrm{cm}^{-1}) \approx 444$, $n''_f(90\ \mathrm{cm}^{-1}) \approx 57.3\rangle$. Evidently, this difference between the refractive index of the two samples from the same batch must be due to a somewhat larger fraction of the superconducting electrons in Sample NIST 255 compared to that for Sample NIST 255, as can be seen in Table 6.10 and Table 6.12. This is contrary to the conclusion which Dr. Kumar had reached earlier [124,120], and proves that a $YBa_2Cu_3O_{7-\delta}$ film of a higher quality is deposited onto Sample NIST 255 rather than onto Sample NIST 256.

Although this is redundant, for convenience the complex conductivity and dielectric function were calculated as well.

Figures 6.47 and 6.48 present the complex-conductivity spectra of the $YBa_2Cu_3O_{7-\delta}$ film for Sample NIST 255 and Sample NIST 256, respectively, at five fixed temperatures. The top panels give the real part of the $YBa_2Cu_3O_{7-\delta}$-film conductivity σ'_f, whereas the middle (normal state) panels and the bottom (superconducting state) panels present the imaginary part of the $YBa_2Cu_3O_{7-\delta}$-film conductivity σ''_f.

At 300 K the real part of the $YBa_2Cu_3O_{7-\delta}$-film conductivity σ'_f is almost constant in the far-infrared spectral range. Indeed, $\sigma'_f(10\ \mathrm{cm}^{-1}) \approx 1296$ and $\sigma'_f(90\ \mathrm{cm}^{-1}) \approx 1270$. At 200 K σ'_f is still almost constant, but increased by about 40 %. Indeed, $\sigma'_f(10\ \mathrm{cm}^{-1}) \approx 1822$ and $\sigma'_f(90\ \mathrm{cm}^{-1}) \approx 1752$. Lowering the temperature from 200 K to 100 K causes an increase of $\sigma'_f(10\ \mathrm{cm}^{-1})$ to 3077 (by about 69 %) below 50 cm^{-1}, but with increasing the wave number the change in

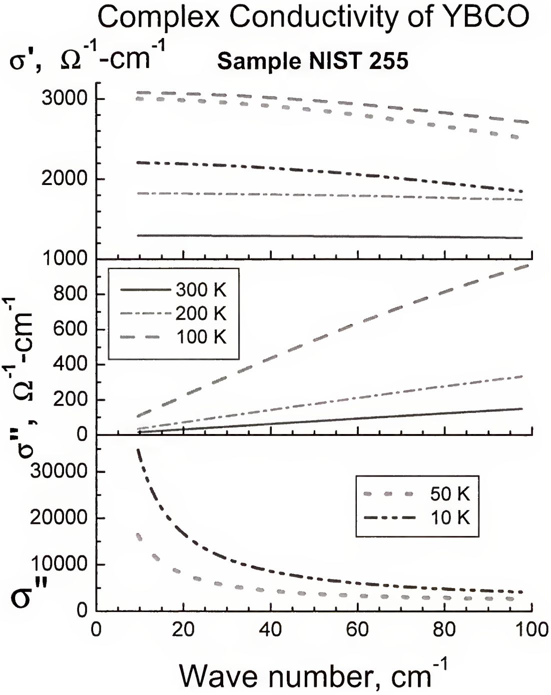

Figure 6.47: Complex conductivity for the $YBa_2Cu_3O_{7-\delta}$ layer of Sample NIST 255: real/imaginary part (normal/superconducting) state on top/middle/bottom panel, respectively.

σ'_f becomes smaller. E.g., at 90 $\text{cm}^{-1}$the increase is only to 2763 (by about 58 %). Therefore the line at 100 K has a small negative curvature. Upon further lowering the temperature from 100 K to 50 K, σ'_f decreases a little and its negative curvature is increased in magnitude only slightly: $\sigma'_f(10\ \text{cm}^{-1}) \approx 3001$ and $\sigma'_f(90\ \text{cm}^{-1}) \approx 2575$. Cooling from 50 K to 10 K causes a larger further decrease, such that the negative curvature of σ'_f at 10 K is almost the same as that at 100 K: $\sigma'_f(10\ \text{cm}^{-1}) \approx 2204$ and $\sigma'_f(90\ \text{cm}^{-1}) \approx 1892$.

In the normal state σ''_f is almost linear, with a positive slope and an intercept close to zero. At 300 K the slope is about 1.53 Ω^{-1} and increases to about 3.43 Ω^{-1} and 9.94 Ω^{-1} at 200 K and 100 K, respectively. The three lines appear as an unfolding fan, centered at the origin. As the superconducting state is reached, σ''_f jumps sharply to much higher values, and the jump is extremely high at the lowest wave numbers. Actually, σ''_f is characterized by a large positive curvature, especially within the lowest third of the covered spectral range and seems to diverge when extrapolated to DC. At 50 K and 10 K $\sigma''_f(10\ \text{cm}^{-1})$ is about 15.4 and 33.1 $(\text{m}\Omega\cdot\text{cm})^{-1}$, respectively, whereas these values for $\sigma''_f(90\ \text{cm}^{-1})$ are about 2.73 and 4.40 $(\text{m}\Omega\cdot\text{cm})^{-1}$. The numbers given above refer to Sample NIST 255, but qualitatively the description is valid for Sample NIST 256, too, except for the fact that below about 50 cm^{-1} the curves of σ'_f at 100 K and 10 K come relatively close and almost merge: $\sigma'_f(10\ \text{cm}^{-1}) \approx 2799$ at 100 K and $\sigma'_f(10\ \text{cm}^{-1}) \approx 2796$ at 10 K.

Figures 6.49 and 6.50 present the complex dielectric-function spectra of the $\text{YBa}_2\text{Cu}_3\text{O}_{7-\delta}$ film for Sample NIST 255 and Sample NIST 256, respectively, at five fixed temperatures. The top (normal state) panels and middle (superconducting state) panels give the real part of the $\text{YBa}_2\text{Cu}_3\text{O}_{7-\delta}$-film relative permittivity ε'_f, whereas the bottom panels present the imaginary part of the $\text{YBa}_2\text{Cu}_3\text{O}_{7-\delta}$-film relative permittivity ε''_f. At 300 K the real part of the $\text{YBa}_2\text{Cu}_3\text{O}_{7-\delta}$-film relative

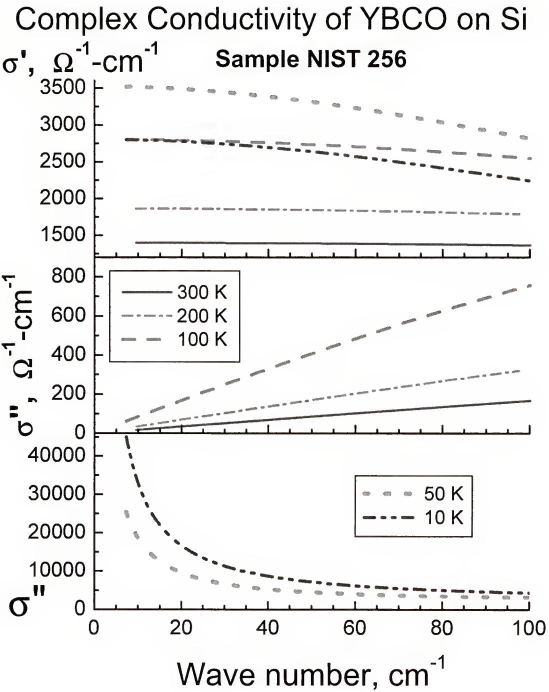

Figure 6.48: Complex conductivity for the $YBa_2Cu_3O_{7-\delta}$ layer of Sample NIST 256: real/imaginary part (normal/superconducting) state on top/middle/bottom panel, respectively.

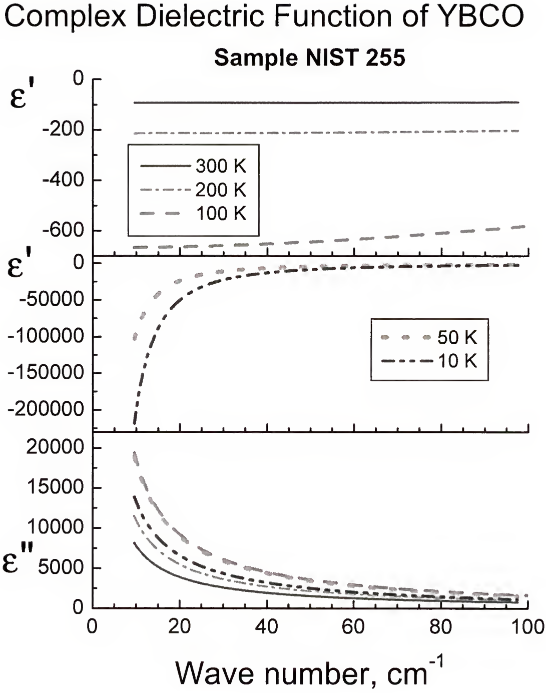

Figure 6.49: Complex dielectric function for the $YBa_2Cu_3O_{7-\delta}$ layer of Sample NIST 255: real (normal/superconducting) state/imaginary part on top/middle/bottom panel, respectively.

permittivity ε'_f is roughly constant and negative in the far-infrared, close to -92. At 200 K ε'_f is still almost constant and negative in the far-infrared, close to -210. At 100 K $\varepsilon'_f(10\ \mathrm{cm}^{-1}) \approx -667$, $\varepsilon'_f(90\ \mathrm{cm}^{-1}) \approx -595$, and there is a slight positive curvature. As the superconducting state is reached, ε'_f drops sharply to much lower values, and the jump is extremely impressive at the lowest wave numbers. Actually, σ''_f is characterized by a significantly large negative curvature, especially within the lowest third of the covered spectral range and seems to diverge to $-\infty$ when extrapolated to DC. At 50 K and 10 K $\varepsilon'_f(10\ \mathrm{cm}^{-1})$ is about -94000 and -199000, respectively, whereas these values for $\varepsilon'_f(90\ \mathrm{cm}^{-1})$ are -1820 and -2930. The latter two values appear to merge on the plot due to the large scale.

The imaginary part of the $\mathrm{YBa_2Cu_3O_{7-\delta}}$-film relative permittivity ε''_f at all temperatures is positive, with a large positive curvature, especially within the lowest third of the covered spectral range, and at higher wave numbers all the curves seem to be merging as they become almost horizontal. Towards DC all curves seem to diverge. With decreasing of the temperature ε''_f grows. In the superconducting state that growth is almost saturated.

6.4.3.2 Samples NIST 73 and NIST 74

Within this subsection the top panels give the whole picture for the refractive index of the $\mathrm{YBa_2Cu_3O_{7-\delta}}$ film, whereas the bottom panels magnify the scale to zoom into some more details. In the spectral range below 100 cm^{-1} the results are qualitatively similar to those for Samples NIST 255 and NIST 256, presented on the previous several pages. This behaviour is dominated by the Drude band in the normal state, whereas as the temperature is lowered in the superconducting state some of the spectral weight of the Drude band is taken over by the $\delta(\omega)$ function band describing the superfluid. At higher frequencies the signatures of three prominent oscillators are clearly visible: the phonons in the vicinity of 270 cm^{-1},

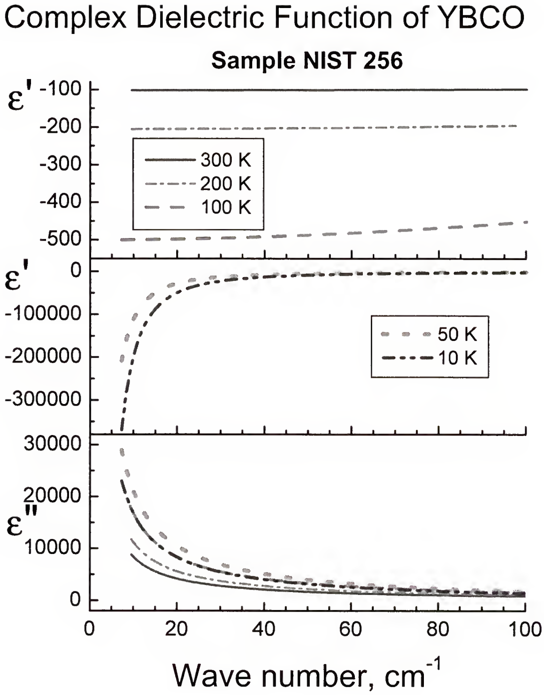

Figure 6.50: Complex dielectric function for the $YBa_2Cu_3O_{7-\delta}$ layer of Sample NIST 256: real (normal/superconducting) state/imaginary part on top/middle/bottom panel, respectively.

350 cm^{-1}, and 565 cm^{-1}. Although the three mid-infrared band are taken into account, too, they are too wide in order to be discernible on these plots.

Figures 6.51 and 6.52 present the refractive index n'_f spectra of the $YBa_2Cu_3O_{7-\delta}$ film for Sample NIST 73 and Sample NIST 74, respectively, at six fixed temperatures. Notably, in the vicinity of 160 cm^{-1} the three curves in the normal state cross and have the opposite order on both sides of that spectral point. The two curves at 10 K and 20 K almost coincide over the whole studied spectral range. Above about 500 cm^{-1}the 50 K curve is merging together with the other two curves in the superconducting state. With increasing the wave number the refractive index curves at all temperatures come closer to each other, but the three normal-state curves are far from merging either among themselves, or with the three merged superconducting curves, as can be seen from the magnified bottom panel.

Figures 6.53 and 6.54 present the extinction coefficient n''_f spectra of the $YBa_2Cu_3O_{7-\delta}$ film for Sample NIST 73 and Sample NIST 74, respectively, at six fixed temperatures. The three extinction-coefficient curves in the superconducting state (at 10, 20, and 50 K) almost coincide over the entire spectral range. With increasing the wave number the extinction-coefficient curves at all temperatures come closer to each other, and seem to be about to merge even on the magnified bottom panel.

To get a rough estimate for the sample variation of the complex refractive index, one can compare its far-infrared values for Sample NIST 73 ($n'_f(25\ \mathrm{cm}^{-1}) \approx 14.19$, $n'_f(100\ \mathrm{cm}^{-1}) \approx 10.56$, $n''_f(25\ \mathrm{cm}^{-1}) \approx 114.0$, $n''_f(100\ \mathrm{cm}^{-1}) \approx 32.79$) and Sample NIST 74 ($n'_f(25\ \mathrm{cm}^{-1}) \approx 12.87$, $n'_f(100\ \mathrm{cm}^{-1}) \approx 10.24$, $n''_f(25\ \mathrm{cm}^{-1}) \approx 158.8$, $n''_f(100\ \mathrm{cm}^{-1}) \approx 43.31$) at 10 K. Such a comparison shows that in the superconducting state, Sample NIST 73 is characterized by a lower n''_f and a slightly higher n'_f than those of Sample NIST 74. Evidently, this is due to a somewhat

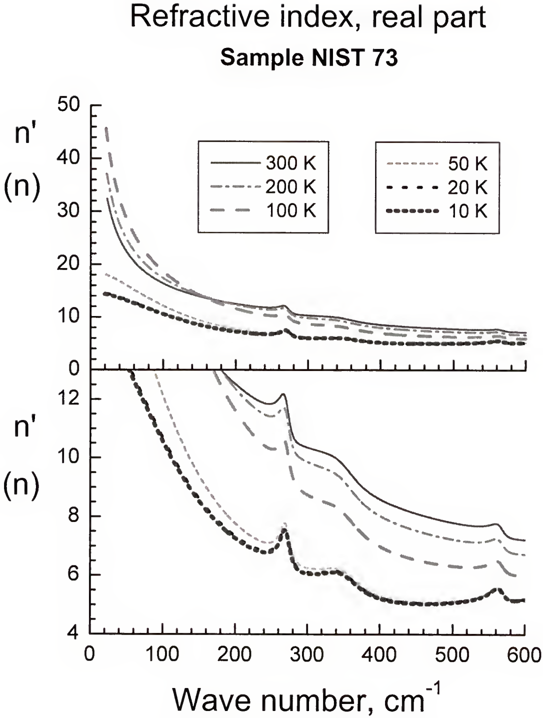

Figure 6.51: Refractive index for the $YBa_2Cu_3O_{7-\delta}$ layer of Sample NIST 73, magnified bottom panel.

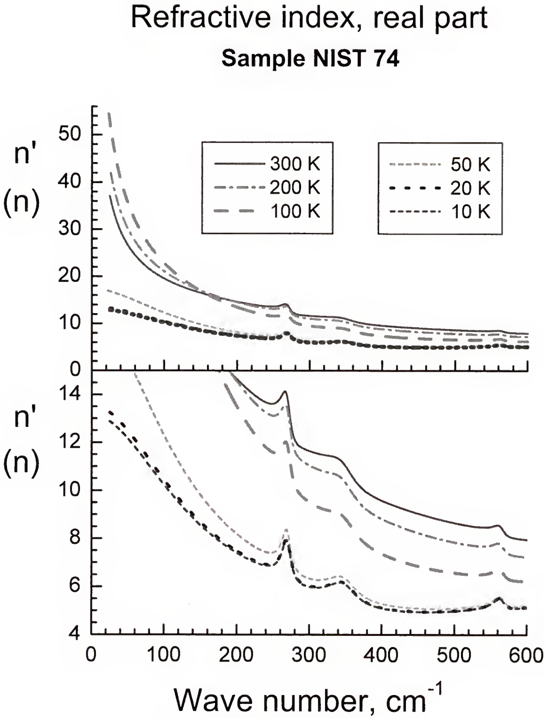

Figure 6.52: Refractive index for the $YBa_2Cu_3O_{7-\delta}$ layer of Sample NIST 74, magnified bottom panel.

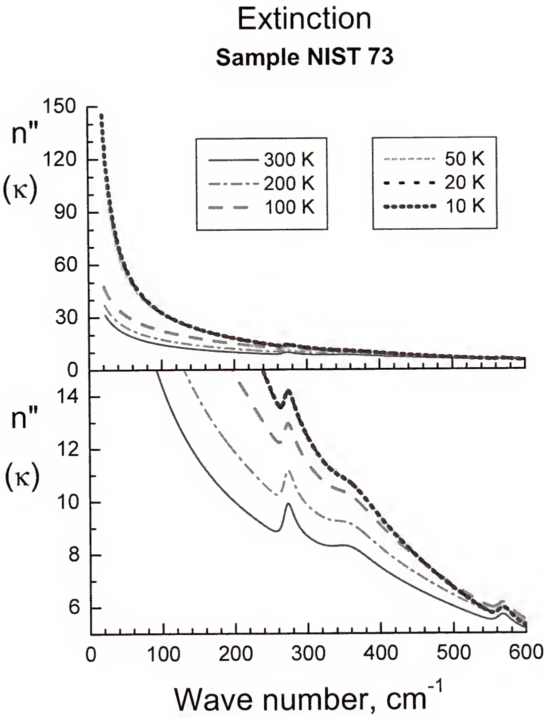

Figure 6.53: Extinction coefficient for the $YBa_2Cu_3O_{7-\delta}$ layer of Sample NIST 73 magnified bottom panel.

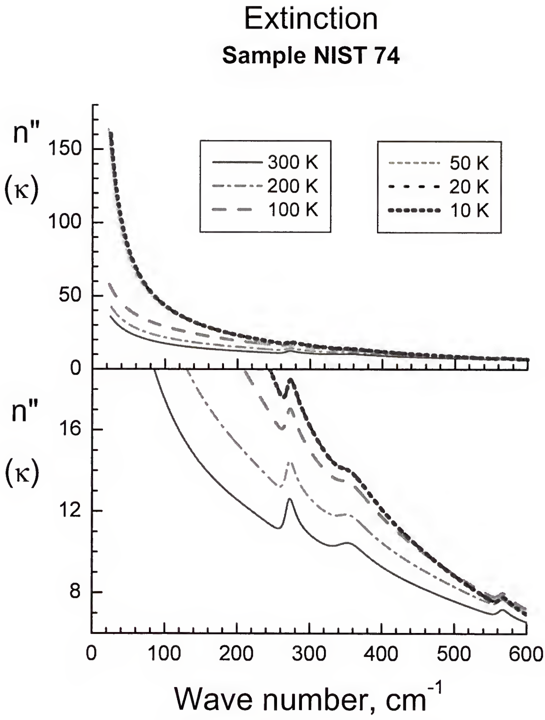

Figure 6.54: Extinction coefficient for the $YBa_2Cu_3O_{7-\delta}$ layer of Sample NIST 74 magnified bottom panel.

larger fraction of the superconducting electrons in Sample NIST 74 compared to that for Sample NIST 73, as can be seen in Table 6.16 and Table 6.20.

Although this is redundant, for convenience the complex conductivity and dielectric function were calculated as well.

Figures 6.55 and 6.56 present the real part σ'_f of the complex conductivity spectra for the $YBa_2Cu_3O_{7-\delta}$ film of Sample NIST 73 and Sample NIST 74, respectively, at six fixed temperatures. In the normal state, as the temperature is lowered the Drude scattering rate decreases and therefore the low-wave number optical conductivity increases as expected. With further decreasing of the temperature the low-wave number optical conductivity decreases somewhat as some of its spectral weight is taken over by the $\delta(\omega)$-function. The low-wave number portion (below about 240 cm^{-1}) has a small positive slope at 300 K, a small negative slope at 200 K, a large negative slope at 100 K. The curve at 50 K is characterized by the highest negative slope in its low-wave number portion, and the coinciding curves at 10 and 20 K have the second highest negative slope. The latter decrease is associated with the increasing power of the $\delta(\omega)$ contribution to the DC conductivity. Due to these differing slopes the curves at various temperatures cross at several points and change their order which can be traced most easily on the plots. But the three curves in the superconducting state do not cross, but rather tend merge at the highest studied wave numbers.

Figures 6.57 and 6.58 present the imaginary part σ''_f of the complex conductivity spectra for the $YBa_2Cu_3O_{7-\delta}$ film of Sample NIST 73 and Sample NIST 74, respectively, at six fixed temperatures. Interestingly, the curve at 300 K, and most of the curve at 200 K (except the highest portions of two phonon signatures) are negative. This could mean that the wide mid-infrared bands "bury" the Drude

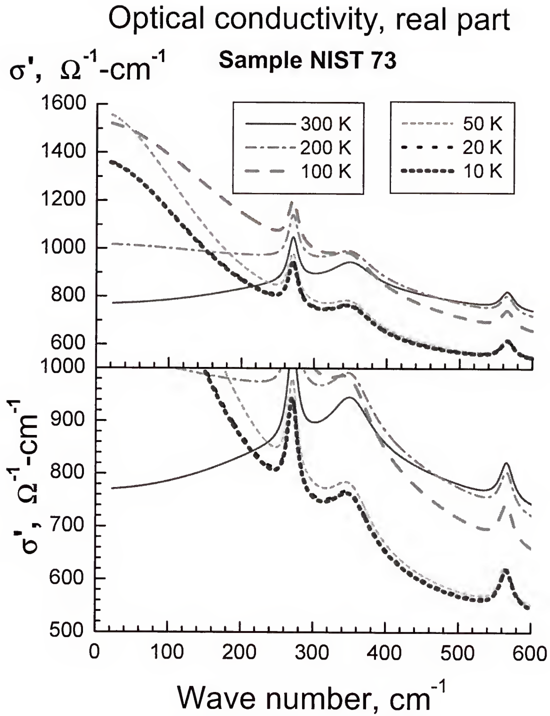

Figure 6.55: Real part of the conductivity for the $YBa_2Cu_3O_{7-\delta}$ layer of Sample NIST 73, magnified bottom panel.

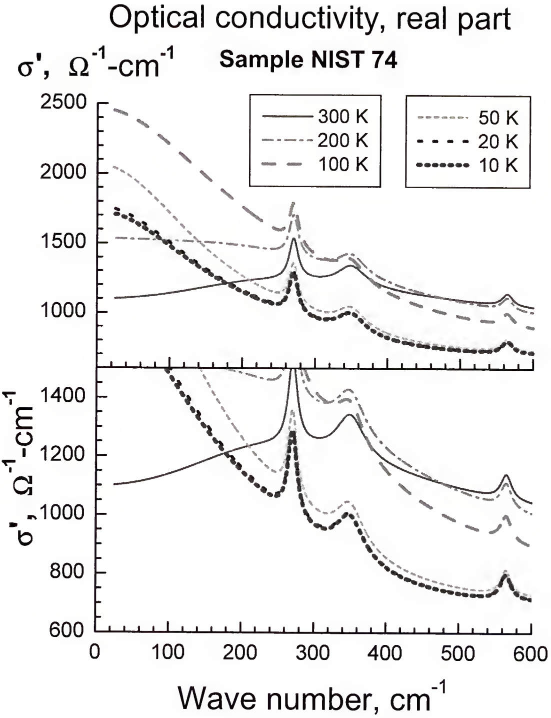

Figure 6.56: Real part of the conductivity for the $YBa_2Cu_3O_{7-\delta}$ layer of Sample NIST 74, magnified bottom panel.

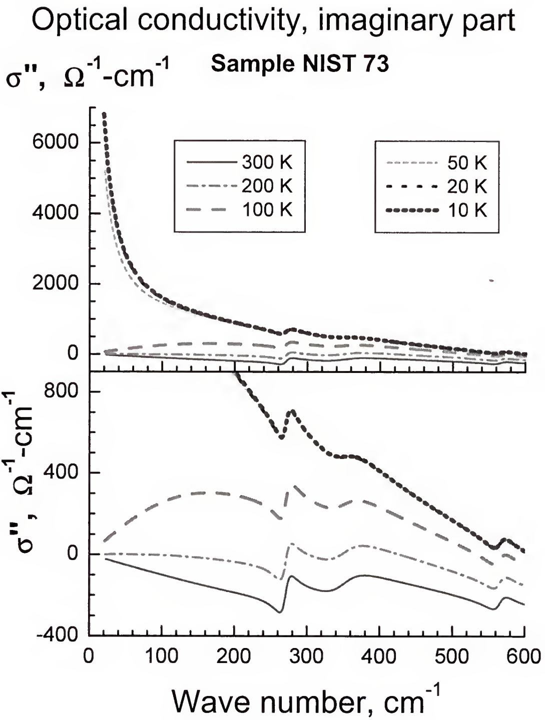

Figure 6.57: Imaginary part of the conductivity for the $YBa_2Cu_3O_{7-\delta}$ layer of Sample NIST 73, magnified bottom panel.

contribution.[25] The two curves at 10 K and 20 K practically coincide over the entire studied spectral range, and as early as above 200 cm^{-1} they get merged with the curve at 50 K.

Figures 6.59 and 6.60 present the real part of the relative permittivity (complex dielectric-function) ε'_f spectra of the $YBa_2Cu_3O_{7-\delta}$ film for Sample NIST 73 and Sample NIST 74, respectively, at six fixed temperatures. The contrast between the normal and the superconducting state curve here is so large that on the top panel the three normal-state curves seem to coincide, as do the three superconducting-state curves. The bottom panel shows that at least above 200 cm^{-1} the three superconducting-state curves really coincide. In the low-wave number portion all curves are characterized by a negative slope whose magnitude is increasing as the temperature is lowered until it gets saturated in the superconducting state. Curiously, the low-wave number portion of the curve at 300 K and a small portion (in the vicinity of a phonon signature) of the curve at 200 K are positive. This corresponds to the anomaly observed in the σ'' spectra.

Figures 6.61 and 6.62 present the imaginary part of the complex dielectric-function ε''_f spectra of the $YBa_2Cu_3O_{7-\delta}$ film for Sample NIST 73 and Sample NIST 74, respectively, at six fixed temperatures. Essentially, these curves provide the same information as ε' curves, but in a much less convenient form. Indeed the phonon signatures are superimposed on these steeply sloped curves and a lot of the sensitivity to those features is lost.

6.4.4 Reflectance

Generally, for calculating the reflectance spectra we have used the same parameters that gave optimum results for the transmittance.

---

[25] Private communication by David Tanner.

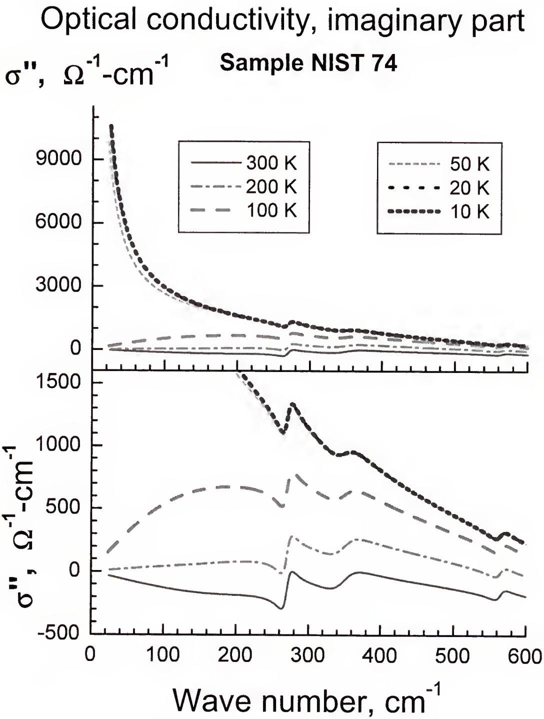

Figure 6.58: Imaginary part of the conductivity for the $YBa_2Cu_3O_{7-\delta}$ layer of Sample NIST 74, magnified bottom panel.

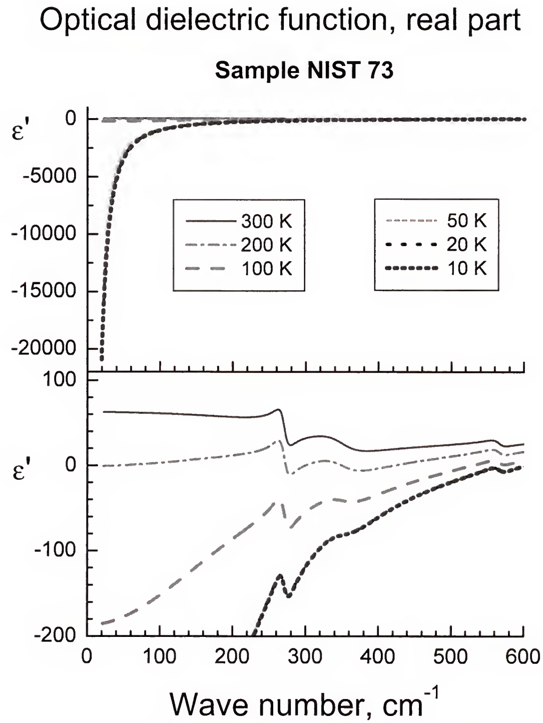

Figure 6.59: Real part of the complex dielectric function for the $YBa_2Cu_3O_{7-\delta}$ layer of Sample NIST 73, magnified bottom panel.

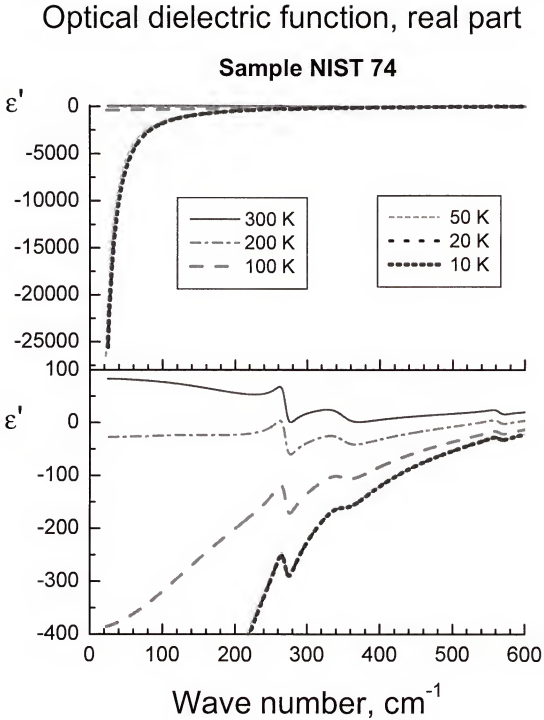

Figure 6.60: Real part of the complex dielectric function for the $YBa_2Cu_3O_{7-\delta}$ layer of Sample NIST 74, magnified bottom panel.

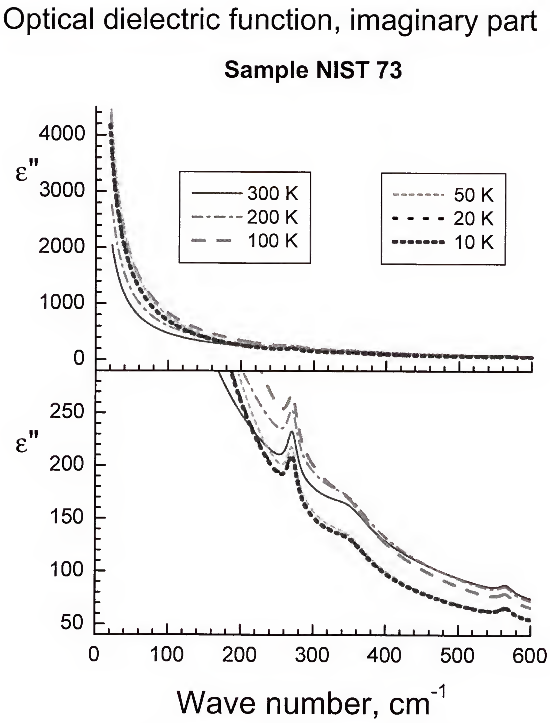

Figure 6.61: Imaginary part of the complex dielectric function for the $YBa_2Cu_3O_{7-\delta}$ layer of Sample NIST 73, magnified bottom panel.

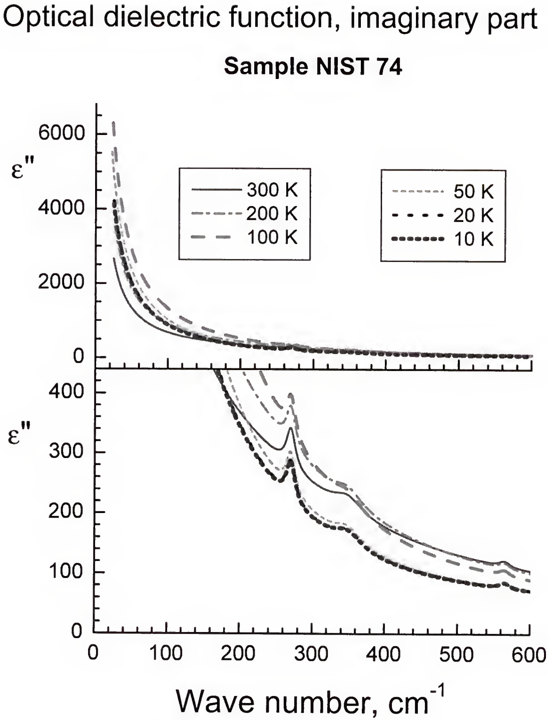

Figure 6.62: Imaginary part of the complex dielectric function for the $YBa_2Cu_3O_{7-\delta}$ layer of Sample NIST 74, magnified bottom panel.

The measured and calculated front-side reflectance spectra for Sample NIST 255 at room temperature are given in Fig. 6.20 (normal state) and Fig. 6.21 (superconducting state). The measured and calculated back-side reflectance spectra for Sample NIST 255 at room temperature are given in Fig. 6.22 (normal state) and Fig. 6.23 (superconducting state).

Less successful were the measurements of reflectance from Sample NIST 256. The measured and calculated front-side reflectance spectra for Sample NIST 256 at room temperature are given in Fig. 6.27 (normal state) and Fig. 6.28 (superconducting state). The measured and calculated back-side reflectance spectra for Sample NIST 256 at room temperature are given in Fig. 6.29 (normal state) and Fig. 6.30 (superconducting state).

Clearly, at room temperature the agreement between the calculated and measured reflectance is much better than the agreement in the superconducting state is. For that reason, as mentioned earlier, we believe the sample-holder was not in a good thermal contact with the cold finger of the cryostat and instead of at 50 K and 10 K, the reflectance measurements were actually done at temperatures above T_c.

The calculated front-side reflectance curves are shown for all temperatures at which we have done measurements with dotted lines. There is some temperature dependence of the spectral positions of the extrema. Within the temperature ranges where the $YBa_2Cu_3O_{7-\delta}$ layer is either in the superconducting or in the normal state, that temperature dependence is moderate. However, it becomes more significant if the temperature range includes the critical temperature, that is, if the $YBa_2Cu_3O_{7-\delta}$ changes its state from normal to superconducting, or vice versa. The fringe contrast is reduced significantly at lower temperatures, which can be expected since the penetration depth of electromagnetic radiation within the

$YBa_2Cu_3O_{7-\delta}$ film has a positive-slope temperature dependence, and is especially small in the superconducting state.

For the back-side reflectance (the incident beam is coming from the Si substrate side) with the $YBa_2Cu_3O_{7-\delta}$ layer in the superconducting state, the measured and calculated curves agree to a reasonable degree, but the calculated minima are sharper and significantly lower than the measured values. This discrepancy may be due to inadequate spectral resolution of the measurements, to divergence of the beam within the interferometer, or to ignoring the contribution of some of the dielectric layers.

Our more recent measurements on Sample NIST 73 and Sample NIST 74 are in a much better agreement. The measured and calculated front-side reflectance spectra for Sample NIST 73 at room temperature are given in Fig. 6.33 (normal state) and Fig. 6.34 (superconducting state). The measured and calculated back-side reflectance spectra for Sample NIST 73 at room temperature are given in Fig. 6.36 (normal state) and Fig. 6.37 (superconducting state).

Due to the effects of partial coherence, the amplitude of the reflectance fits always exceeds the measured data. The reflectance measurements are more sensitive to partial coherence, because non-normal incidence is used, whereas the transmittance measurements always use nominally[26] normal incidence.

The measured and calculated front-side reflectance spectra for Sample NIST 74 at room temperature are given in Fig. 6.40 (normal state) and Fig. 6.41 (superconducting state). The measured and calculated back-side reflectance spectra for Sample NIST 74 at room temperature are given in Fig. 6.43 (normal state) and Fig. 6.44 (superconducting state).

---

[26] Divergence of the beam can cause the outer cone of the beam to deviate from normal incidence, but in practice this parasitic effect is very small.

6.5 Discussion

6.5.1 Antireflection Effect

As was said earlier, we have observed a phase change in the transmittance within the approximate temperature range from 200 to 250 K. In particular, for Sample NIST 255, the phase change occurs at a temperature very close to 200 K as the curve measured at 200 K has only hints for fringes, almost buried in the noise. Furthermore, to within the spectral uncertainty, the spectral positions of the transmittance minima at 300 K correspond to those of the maxima at 100 K, 50 K, and 10 K. This interesting interference phenomenon can be explained by the antireflection effect, as can be seen from the following analysis.

Let us assume that the infrared beam is incident upon the Si substrate, traverses it, and is partially reflected by the film. The sample configuration for this case is shown in Figure5.3. From equation 3.140 applied to the case that is being considered, the complex Fresnel reflection coefficient for back-side incidence:

$$\widetilde{r} = \frac{-\widetilde{r}_{2,3} + \widetilde{r}_{2,1}\mathrm{e}^{\mathrm{i}\,2\widetilde{\delta}_f}}{1 - \widetilde{r}_{2,3}\widetilde{r}_{2,1}\mathrm{e}^{\mathrm{i}\,2\widetilde{\delta}_f}}. \tag{6.12}$$

Here the subscripts "1", "2", and "3" correspond to vacuum, $YBa_2Cu_3O_{7-\delta}$, and Si, respectively. To simplify the analysis the vacuum behind the $YBa_2Cu_3O_{7-\delta}$ film has been neglected in equationE:r. For the simple case of normal incidence

$$\widetilde{r}_{j,k} = \frac{\widetilde{n}_j - \widetilde{n}_k}{\widetilde{n}_j + \widetilde{n}_k}; \qquad (j,k) = (2,1),(2,3); \tag{6.13}$$

$$\widetilde{\delta}_f = \omega d_f \widetilde{n}_2 / c. \tag{6.14}$$

The former line gives the complex Fresnel reflection coefficient for the respective interface, and the latter line is the complex phase change accumulated while the beam makes a "round trip" within the $YBa_2Cu_3O_{7-\delta}$ film. Furthermore, the refractive indices of vacuum, the film, and the Si substrate are

$$\widetilde{n}_1 = 1; \qquad \widetilde{n}_2 = \widetilde{n}_f; \qquad \widetilde{n}_3 = n_{Si}, \tag{6.15}$$

respectively, and c is the speed of light in vacuum.

For the thin $YBa_2Cu_3O_{7-\delta}$ film in the normal state $2\left|\widetilde{\delta}_f\right| \ll 1$, with real part $d_f \ll \lambda/(4\pi n'_f)$, and imaginary part $d_f \ll \lambda/(4\pi n''_f)$. The latter condition simply means that the $YBa_2Cu_3O_{7-\delta}$ film thickness is much smaller than the electromagnetic-radiation penetration depth in the $YBa_2Cu_3O_{7-\delta}$ film. Above $\lambda = 2\pi c/\omega$ is the wavelength in vacuum.

The condition mentioned above means that in the normal state of $YBa_2Cu_3O_{7-\delta}$ we can use $e^{i2\widetilde{\delta}_f} \approx 1 + i\,2\widetilde{\delta}_f$. Substituting this approximation, as well as equation 6.13 into equation 6.12, after simplification, we get

$$\widetilde{r} \approx \frac{\widetilde{n}_3 - \widetilde{n}_1 + i\,\widetilde{\delta}_f\widetilde{n}_2(1 + \widetilde{n}_3/\widetilde{n}_2)(1 - \widetilde{n}_1/\widetilde{n}_2)}{\widetilde{n}_3 + \widetilde{n}_1 - i\,\widetilde{\delta}_f\widetilde{n}_2(1 - \widetilde{n}_3/\widetilde{n}_2)(1 - \widetilde{n}_1/\widetilde{n}_2)}. \tag{6.16}$$

In the normal state, $YBa_2Cu_3O_{7-\delta}$ behaves as a metal, and therefore its n'_f and n''_f are much higher than those for any dielectric layer or vacuum. We can then conclude that $|\widetilde{n}_3/\widetilde{n}_2| \ll 1$ and $|\widetilde{n}_1/\widetilde{n}_2| \ll 1$, which leads to a further simplification of equation 6.16:

$$\widetilde{r} \approx \frac{\widetilde{n}_3 - \widetilde{n}_1 + i\,\widetilde{\delta}_f\widetilde{n}_2}{\widetilde{n}_3 + \widetilde{n}_1 - i\,\widetilde{\delta}_f\widetilde{n}_2}. \tag{6.17}$$

This equationis the same as the one derived by McKnight et al. [153], but unlike them, Kumar [120] obtained it directly from Maxwell's equations without assuming that the film is infinitely thin.

It is convenient to define a dimensionless admittance of the $YBa_2Cu_3O_{7-\delta}$ film

$$\widetilde{y}_f = -\mathrm{i}\widetilde{\delta}_f\widetilde{n}_f. \tag{6.18}$$

which is complex in the general case. Using this equation and equation 6.15 allows reduction of equation 6.17 to

$$\widetilde{r} \approx \frac{n_{Si} - 1 - \widetilde{y}_f}{n_{Si} + 1 + \widetilde{y}_f}. \tag{6.19}$$

Substituting equation 6.14 into equation 6.18 we get

$$\widetilde{y}_f = -\mathrm{i}\omega d_f \widetilde{n}_f^2/c. \tag{6.20}$$

As was mentioned earlier, in the normal state of $YBa_2Cu_3O_{7-\delta}$ its dielectric function is dominated by the Drude term. At low frequencies ($\omega\tau \ll 1$), i.e., when the angular frequency is significantly smaller that the scattering rate, the Drude term becomes purely imaginary:

$$\widetilde{n}_f^2 = \widetilde{\varepsilon}_f = -\mathrm{i}\sigma_{DC}/(\omega\varepsilon_o), \tag{6.21}$$

whereupon the dimensionless admittance becomes practically real in the very far-infrared

$$\widetilde{y}_f = y_f = \sigma_{DC}d_f/(c\varepsilon_o). \tag{6.22}$$

Knowing that the dimensionless admittance is a positive constant, it is clear that if the following condition is met

$$\sigma_{DC}d_f/(c\varepsilon_o) = y_f = n_{Si} - 1, \tag{6.23}$$

then the numerator of equation 6.17 vanishes and the result is antireflection, also called impedance (admittance) matching. Substituting $n_{Si} = 3.4$, and the value of $c\varepsilon_o$, the antireflection condition is reduced to

$$(\sigma_{DC} d_f)^{-1} \approx 157\Omega. \tag{6.24}$$

Finally, the DC resistivity of a $YBa_2Cu_3O_{7-\delta}$ film with $d_f = 35$ nm, at which antireflection should occur is $\sigma_{DC}^{-1} \approx 550\mu\Omega$·cm. The DC resistivity obtained from the 200 K transmittance fit is $548.5\mu\Omega$·cm, which is a very good agreement, especially taking into account that several approximations have been made above.

The presence of residual interference fringes in the transmittance through Sample NIST 255 at 200 K is due to the fact that either 200 K is not the exact temperature at which the antireflection is complete, or one of the conditions above is not met perfectly—the scattering rate at 200 K is slightly lower (448 cm^{-1} for Sample NIST 255), or somewhat higher (476 cm^{-1} for Sample NIST 256) (see Table 6.21) from the optimum value, and the lowest frequency at which we have measured is 10 to 20 cm^{-1}.

The DC resistivity varies with temperature. As σ_{DC}^{-1} passes through the value at which the reflection vanishes, the Fresnel reflection coefficient (equation 6.17) changes its sign. This is equivalent to a phase change of π rad, and explains why the central frequencies of the transmittance maxima at 300 K correspond to the frequencies of transmittance minima at 100 K, and vice versa.

The calculated transmittance and reflectance agree very well with the measured data as far as the interference patterns at most temperatures are concerned A slight exception is made by Sample NIST 255 at 200 K for which the fit oscillates out of phase with the measured spectrum. The reason for this may be that in the vicinity of the temperature at which the phase switch occurs, the small contributions from the two buffer layers that we have neglected may become important. Also, under such conditions the phase becomes very sensitive to even small uncertainties in the fit parameters. Hence, in this case the fitting procedure is very unstable. Moreover, the transmittance at 200 K is not quite zero which is due to the fact that the approximations that were made above are only that—approximations. Hence the dimensionless admittance is only approximately real, and its small imaginary part is responsible for the deviation of the reflectance from zero, that is, the antireflection effect is not perfect. Another way to interpret the discrepancy under discussion is to assume that the scattering rate is a complex, frequency-dependent quantity. Modified Drude models using such a scattering rate have been suggested for the study of HTSC materials [154,155,41,156]. It is possible that such models could be applicable to thin $YBa_2Cu_3O_{7-\delta}$ films on Si substrates, too. However, with the data we have now, no definitive conclusion is possible at this moment.

There is some, relatively small, difference between the optical properties of Sample NIST 255 and Sample NIST 256. From the data we have (Figures 6.18, 6.25, and Table 6.21), for Sample NIST 256 we can estimate that antireflection, corresponding to the minimum fringe contrast, would occur at some temperature within the range from 200 to 300 K, and most likely in the vicinity of 208 K, where its DC electric resistivity is about[27] 550 $\mu\Omega$-cm. Furthermore, from equation 6.24, it is clear that by increasing the film thickness, at least in theory, it is possible to design a silicon antireflection substrate with an $YBa_2Cu_3O_{7-\delta}$film absorber on top of it, such that it is impedance-matched at room temperature. Further studies are needed in order to determine if the antireflection effect of Si substrate with high-temperature-superconducting films can find practical applications.

---

[27] Estimated by linear interpolation.

6.5.2 The Effect of Optical Resonance

For both Sample NIST 255 and Sample NIST 256, the transmittance maxima and reflectance minima measured in the superconducting state are sharper than the respective features measured in the normal state. Moreover, the peak transmittance at 10 K even exceeds that at 50 K. At first this is counterintuitive: one expects that as the temperature is lowered, the conductivity of the $YBa_2Cu_3O_{7-\delta}$ film increases and therefore the transmittance should decrease. The unexpected higher peak transmittance at lower temperatures only in narrow spectral bands is evidently the result of an optical resonance in the film-substrate composite.

A plain Fabry-Perot optical resonator is a thin (compared to the wavelength) dielectric plate coated with (or vaccum surrounded by) highly reflecting films on both sides. Such a structure would transmit only in narrow spectral ranges centered about periodical resonance frequencies, determined by the optical thickness of the dielectric plate. By varying the reflection coefficient at both or one of the interfaces, the transmittance spectrum of the resonator can be modified within a wide range of possibilities. Such Fabry-Perot multiple-beam resonances can lead to impressively high transmittance values, but only at certain frequencies.

Our samples are actually asymmetric optical resonators, with the $YBa_2Cu_3O_{7-\delta}$ film acting as one of the reflectors, the Si substrate is the dielectric plate, and its uncoated side acting as the second reflector. As the $YBa_2Cu_3O_{7-\delta}$ reflector gets more superconducting at low temperatures, its reflection coefficient increases significantly. This, combined with the multiple-beam interference within the Si substrate, can lead to sharp transmittance peaks at certain resonance frequencies. The resonance effects, observed by others [157–159] before us, demonstrate that $YBa_2Cu_3O_{7-\delta}$ films on Si substrates are good candidates for the development, design, and construction of Fabry-Perot resonators. Detailed studies of such resonance structures are presented in chapter 8.

6.5.3 Fitting Parameters

Our fitting parameters for Sample NIST 255 and Sample NIST 256 are summarized in Table 6.21). For our earlier measurements, we would start with fitting the measured transmittance. Then the fit parameters were tested and fine-tuned, if necessary, on the front-side and back-side reflectance whenever such data were available and deemed reliable.

In the far-infrared spectral range, only two parameters—the DC resistivity and the scattering rate—are sufficient to model the dielectric function of an $YBa_2Cu_3O_{7-\delta}$ film in the normal state. In Table 6.23, our latest values for the parameters characterizing Samples NIST 73, NIST 74, NIST 255, and NIST 256 at 300 K and 100 K, respectively, are compared with the previously-reported-by-us [124] parameters,[28] that were obtained from the same measurements of Samples NIST 255 and NIST 256, as well as to the parameters reported by several other groups that have done similar studies.

Due to the various substrates, buffer layers, as well as deposition techniques, that have been used, and possibly because of different quality of the samples, these values vary in a wide range with the upper bound exceeding the lower one by up to a factor of four. Our studies have shown that the optical properties of the $YBa_2Cu_3O_{7-\delta}$ layer depend more strongly on the DC resistivity $1/\sigma_{DC}$, than on the scattering rate $1/\tau$ which is confirmed by the fact that our fractional uncertainty for $1/\tau$ exceeds that for $1/\sigma_{DC}$.

---

[28] Those earlier estimations are superseded by our current values, presented herein. We believe that the latter are more accurate and reliable than the former.

Table 6.23: DC resistivity and Drude scattering rate of $YBa_2Cu_3O_{7-\delta}$ films as reported by various researchers.

Reference	Substrate	d_f, nm	ρ_{DC}, $\mu\Omega$·cm		$1/\tau$, cm^{-1}	
			300 K	100 K	300 K	100 K
NIST 73	Si	35	1298	654.9	542	274
NIST 74	Si	35	909.9	405.0	564	251
NIST 255	Si	35	771	324	630	265
NIST 256	Si	35	715	357	635	317
[124]	Si	35	800	306	600	230
[160]	MgO	48	555	165	550	175
[149]	$LaAlO_3$	10	880	-	300	-
		25	420	-	400	-
[161]	MgO	50	390	150	480	180
[162]	MgO	35	860	-	270	-

This can be visualized if the best fits are compared to the spectra calculated with one of those parameters offset from its optimum value by a certain percentage. Such a comparison for Sample NIST 256 at 100 K was made by Kumar in his dissertation [120, Figure 5.17]. It presents the best-fit transmittance juxtaposed to the calculated transmittance with $1/\tau$ offset by ±20 % (top panel), or $1/\sigma_{DC}$ offset by ±5 % (bottom panel). Evidently, even a relatively large variation in the scattering rate has only a small effect on the transmittance which implies that the scattering range obtained from the fits has a large uncertainty. Conversely, the transmittance is quite sensitive to the DC resistivity. A relatively small offset of this quantity from its optimum value can lead to a significant deviation of the transmittance from its best fit.

In the superconducting state, at a temperature as low as 10 K, our best fits produced a fraction of superconducting electrons f_s within the range from 0.19 to

0.42. This means that in high-temperature-superconducting thin films a significant fraction of all electrons remain normal even at very low temperatures. The latter fact has been noticed by many authors already [25]. Gao et al. [160] obtained $f_s \approx 0.5$ at 10 K for an $YBa_2Cu_3O_{7-\delta}$ film of thickness 48 nm. A similar result was obtained by Flik et al. [149] for a set of films with thickness within the range from 10 to 200 nm).

On the other hand, single crystals, as well as thick films, at temperatures much lower than the critical temperature T_c are characterized by f_s within the range from 0.70 to 0.85 [148]. This could be a hint that as the art for depositing $YBa_2Cu_3O_{7-\delta}$-films onto Si substrates continues to mature, the quality of the high-temperature-superconducting thin films could be increased further.

CHAPTER 7
ABSORPTANCE OF $YBa_2Cu_3O_{7-\delta}$ THIN FILMS

7.1 Introduction

This chapter presents the absorptance of $YBa_2Cu_3O_{7-\delta}$ films for the same samples whose reflectance and transmittance was presented in the previous chapter. For Samples NIST 255 and NIST 256 we have measured and calculated the absorptance within the spectral range from 10 to 90 cm^{-1} [125], whereas for Samples NIST 73 and NIST 74 the respective spectral range is from 20 to 600 cm^{-1}. The absorptance is calculated using the energy conservation relationship

$$\mathcal{A} = 1 - \mathcal{T} - \mathcal{R}. \tag{7.1}$$

If the measured or calculated transmittance and reflectance are substituted into this equation, one gets the measured or calculated[1] absorptance, respectively, which can be either front-side, or back-side, depending on which type of reflectance data have been used. As could be seen in the previous chapter, the front-side and back-side reflectance differ significantly. Naturally, this difference is inherited by the absorptance spectra, as well.

Exactly one reflectance spectrum and one transmittance spectrum are needed for calculating of each "measured" absorptance spectrum. This self-evident fact has the unfortunate consequence that if at least one of the needed two spectra has not been determined reliably then calculation of a trustworthy absorptance spectrum becomes impossible. For this reason we have not presented any measured front-side absorptance spectra for Sample NIST 255 with its YBCO layer in the superconducting state, nor any measured absorptance spectra for Sample NIST 256 regardless of both the side of incidence and the state of the YBCO layer for the latter sample.

---

[1] In other words, the "measured" absorptance is actually calculated using the measured reflectance and transmittance, whereas the "calculated" absorptance is obtained from the fits to the measured reflectance and transmittance.

Keeping all parameters set to their values determined by fitting the transmittance, front-side, and back-side reflectance, and varying the $YBa_2Cu_3O_{7-\delta}$-film thickness only, we have calculated[2] the variation of these three spectra (and subsequently of the front-side and back-side absorptance, as well) vs. the thickness of the YBCO film. For brevity this calculations were done only for Sample NIST 255 at 100 K, but there are no obstacles to expand the same procedure over all samples with an YBCO film that we have studied, and at any temperature at which reliably determined fitting parameters for each layer of the respective sample are available.

Our absorptance studies are aimed at collecting data that would be useful for designing of infrared-radiation detectors with high sensitivity. Detectors using $YBa_2Cu_3O_{7-\delta}$ thin films can operate above 77 K (the temperature of liquid nitrogen).

A higher absorptance leads to a higher responsitivity and detectivity as well as a smaller noise equivalent power [163,164]. The absorptance of the $YBa_2Cu_3O_{7-\delta}$ film depends on various factors such as: the wavelength of the incident radiation, the temperature of the sample, the thickness of the $YBa_2Cu_3O_{7-\delta}$ film, and the properties of the substrate. The back-side absorptance is higher than the front-side one. Silicon has been proven to be an excellent substrate for $YBa_2Cu_3O_{7-\delta}$ bolometers: it has a high thermal conductivity and is quite transparent in the far-infrared spectral range. Phelan et al. [162] have investigated the thickness-dependent absorptance of YBCO films on MgO substrates in the spectral range from 100 to 200 cm^{-1}. Unexpectedly, the absorptance by some thicker films is smaller than that of thin films. Actually, for relatively thin films (thickness below 500 nm) there is an optimum thickness for which the absorptance by the film-substrate composite is maximum [125]. Naturally, films thicker than about 500 nm again restore their “leadership”.

---

[2] Again, these calculations were done by running multiple times the program 'flmfit".

7.2 Sample NIST 255

7.2.1 Absorptance in the Normal State

7.2.1.1 Front-side absorptance of Sample NIST 255

The measured and calculated front-side absorptance for the $\mathrm{YBa_2Cu_3O_{7-\delta}}$ film of Sample NIST 255 at three temperatures, with the YBCO film in the normal state, is given in Figure 7.1 (at 300 K on the top panel, at 200 K on the middle panel, and at 100 K on the bottom panel). The match between the measured and calculated front-side absorptance spectra is to within the experimental uncertainty, combined for both the respective reflectance and transmittance data.

7.2.1.2 Back-side absorptance of Sample NIST 255

The measured and calculated back-side absorptance for the $\mathrm{YBa_2Cu_3O_{7-\delta}}$ film of Sample NIST 255 at three temperatures, with the YBCO film in the normal state, is shown in Figure 7.2. At room temperature the back-side absorptance shows a tendency to decrease as the frequency is lowered below 50 cm^{-1}. This corresponds to an increase of both the transmittance (Figure 6.18, top panel), and back-side reflectance (Figure 6.22, top panel) at lower frequencies. The match

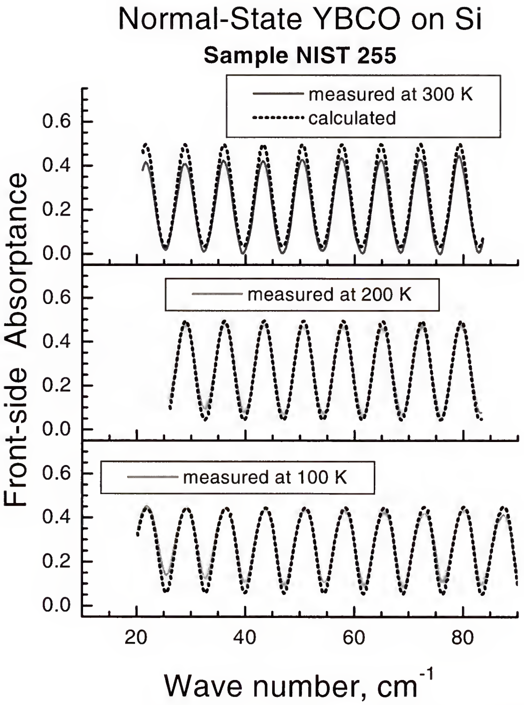

Figure 7.1: Front-side absorptance for the $YBa_2Cu_3O_{7-\delta}$ film of Sample NIST 255 at three temperatures in the normal state.

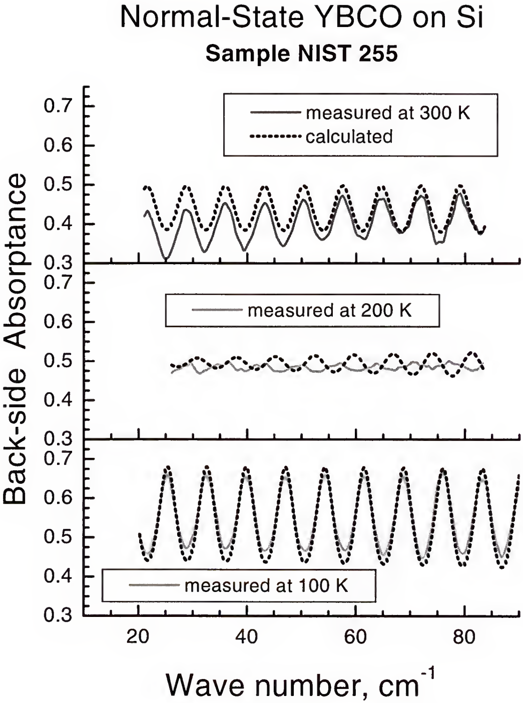

Figure 7.2: Back-side absorptance for the $YBa_2Cu_3O_{7-\delta}$ film of Sample NIST 255 at three temperatures in the normal state.

between the measured and calculated back-side absorptance spectra in the normal state is to within the experimental uncertainty except for the back-side absorptance at 200 K. In the vicinity of the phase-switch temperature the phase is unstable and hard to model, as it is very sensitive to even small uncertainties in a number of parameters. Inadequacy of our initial model (e.g., ignoring of all thin dielectric layers), and even losses in the Si substrate could also be blamed. In any case, I do not share Kumar's opinion [120, p. 93], that experimental noise can cause the calculated back-side absorptance at 200 K to be out of phase with the measured one. Noise is random and therefore cannot lead to a phase change. Also, even though the uncertainties may be significant, they are mostly systematic, rather than random. Thus, the uncertainty would not be able to account for a phase-shift of π rad, either.

At 200 K, the fringe contrast of the back-side absorptance has almost vanished (Figure 7.2, middle panel), whereas that of the front-side absorptance (Figure 7.1, middle panel) is very high. The phase-shift of π rad found in both the transmittance (Figure 6.18, from top to bottom panel) and back-side reflectance spectra (Figure 6.22, from top to bottom panel) when the 100 K and 300 K curves are compared, can of course be observed in the back-side absorptance (Figure 7.2, from top to bottom panel), too. However, the front-side reflectance data (Figure 6.20) show no phase shift at a temperature about 200 K and have a much higher fringe contrast than the transmittance (Figure 6.18). Thus the transmittance phase shift is masked by the front-side reflectance which has a zero phase shift, and the result is that the front-side absorptance shows no phase shift.

7.2.1.3 Fringe-averaged absorptance of Sample NIST 255

At each temperature the fringe-averaged absorptance, with $YBa_2Cu_3O_{7-\delta}$ in the normal state, is virtually constant and is given in Table 7.1 for both the front-side and the back-side incidence. It can clearly be seen that the back-side absorptance is higher than the front-side one. Furthermore, a similar inequality can be expected for the superconducting state, as well: indeed, the fringe-averaged front-side reflectance (Figure 6.21, eye-ball fringe-averaging) is always greater than the back-side one (Figure 6.23, eye-ball fringe averaging). Therefore, back-side illumination leads to the higher absorptance needed for making more sensitive detectors.

Table 7.1: Fringe-averaged front-side absorptance $\mathcal{A}_f$ and back-side absorptance $\mathcal{A}_b$ with $YBa_2Cu_3O_{7-\delta}$ in the normal state.

T,K	100	200	300
$\mathcal{A}_f$	0.30	0.29	0.21
$\mathcal{A}_b$	0.55	0.48	0.40

7.2.1.4 Effect of the film thickness

We have studied the effect of the $YBa_2Cu_3O_{7-\delta}$-film thickness on the absorptance. All parameters, as obtained by fitting the transmittance and reflectance data at 100 K, have been used, except for the $YBa_2Cu_3O_{7-\delta}$-film thickness d_f, which has been set equal to a number of values within the range from 2 to 512 nm, in order to calculate the respective absorptance values.

Because the absorptance is calculated from the reflectance and transmittance data using equation 7.1, let us first consider how those contributing components are affected by the thickness of the YBCO film.

The calculated transmittance spectra for an imaginary sample with all parameters equal to those of Sample NIST 255 at 100 K, except for the thickness of the

$YBa_2Cu_3O_{7-\delta}$ film which is used as an adjustable parameter, are given in Figure 7.3. The transmittance maxima from the top panel are shifted by π rad with respect to the maxima of the bottom panel. The middle panel illustrates the process of this phase shift[3], which imposes the use of three separate panels in order to avoid an entangled mess of the numerous curves. The ordinate scale of the three panels is different!

The fringe-averaged transmittance falls monotonically as the YBCO film becomes thicker and more opaque. Initially the fringe contrast of the transmittance spectra decreases with increasing the YBCO-film thickness. The curve with $d_f = 20$ nm has a strongly reduced fringe contrast in the low wave number range. This is due to the antireflecttion effect discussed in the previous chapter. Therefore at some YBCO-film thickness in the vicinity of $d_f = 20$ nm the fringe contrast must vanish, passing through its minimum. With further increasing of the film thickness, the fringe contrast grows, passes through a maximum at some d_f value between 32 and 64 nm, and starts to decline as the film is becoming too thick. The curve with $d_f = 512$ nm already has a very low fringe contrast, but this time it is simply due to the fact that the relatively thick film is getting close to being opaque within the studied spectral range.

The calculated front-side reflectance spectra for an imaginary sample with all parameters equal to those of Sample NIST 255 at 100 K, except for the thickness of the $YBa_2Cu_3O_{7-\delta}$ film which is used as an adjustable parameter, are given in Figure 7.4. No phase shift is present here and the curves are not entangled or

---

[3] It must be noted that in the previous chapter the film thickness is fixed (naturally) for any particular sample and the phase change therein is associated with a certain phase-change temperature at which the phase change with varying the temperature is fastest and a corresponding temperature range within which the entire phase change is completed. Similarly, here the temperature is fixed (at 100 K) and therefore the phase change is associated with a certain phase-change thickness of the YBCO film at which the phase change with varying the film thickness is fastest and a corresponding film-thickness range in which the entire phase change is completed.

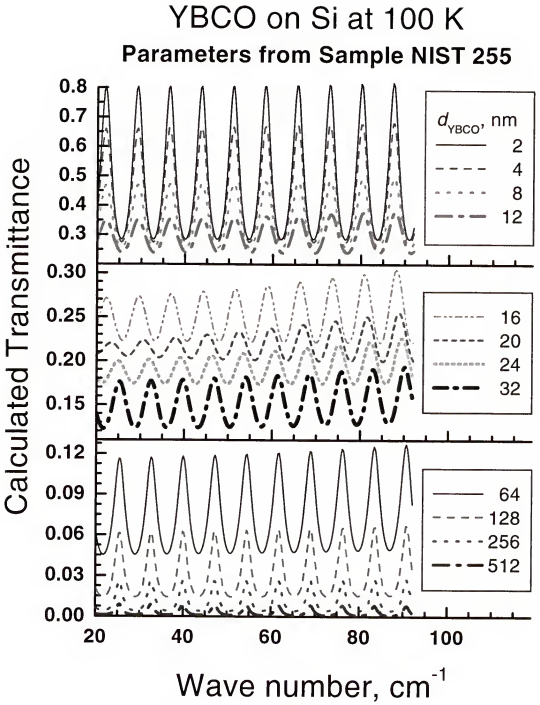

Figure 7.3: Calculated transmittance vs. wave number, with the thickness of $YBa_2Cu_3O_{7-\delta}$ film as an adjustable parameter, for a sample similar to Sample NIST 255 at 100 K.

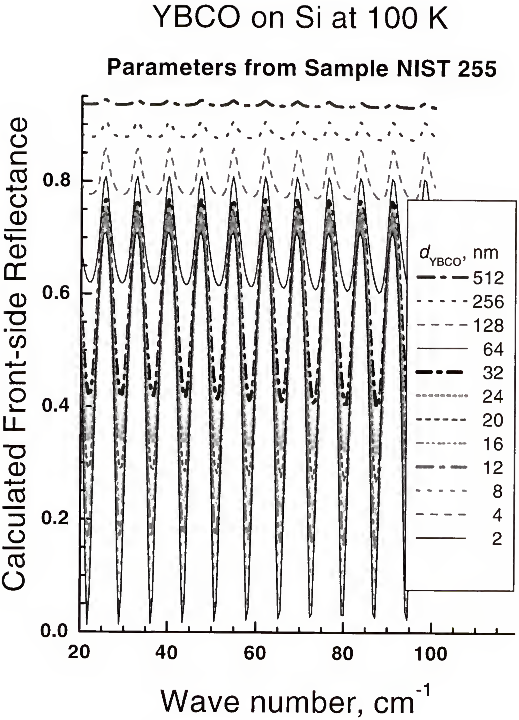

Figure 7.4: Calculated front-side reflectance vs. the wave number, with the $YBa_2Cu_3O_{7-\delta}$-film thickness used as an adjustable parameter, for a sample similar to Sample NIST 255 at 100 K.

overlapping in any complicated manner, which has allowed us to fan out all the curves on a single panel.

The fringe-averaged reflectance grows monotonically as the YBCO film becomes thicker, which is accompanied by a monotonic decrease of the fringe contrast as the increased front-side reflectance dominates over the fringes caused by the multiple-beam interference within the Si substrate. In other words, the fraction of infrared light that manages to traverse the film, get involved in the multiple-beam interference, and then part of it propagates back through the film to join the beam reflected from the front side of the sample, quickly decreases as the film grows thicker and less transparent.

The calculated back-side reflectance spectra for an imaginary sample with all parameters equal to those of Sample NIST 255 at 100 K, except for the thickness of the $YBa_2Cu_3O_{7-\delta}$ film which is used as an adjustable parameter, are given in Figure 7.5. Again, similarly to the case of the transmittance spectra, the back-side reflectance maxima from the top panel are shifted with respect to the maxima of the bottom panel. The middle panel illustrates the process of this phase shift. This phase shift and the partial overlap of the various curves impose once again the use of three separate panels in order to avoid an entangled mess of the numerous curves.

Initially both the fringe-averaged back-side reflectance and the fringe contrast of the back-side reflectance spectra decrease with increasing the YBCO-film thickness. As was the case with the transmittance, the curve with $d_f = 20$ nm has a strongly reduced fringe contrast in the low wave number range. This is due to the antireflecttion effect discussed in the previous chapter. Therefore at some YBCO-film thickness in the vicinity of $d_f = 20$ nm the fringe contrast must vanish, passing through its minimum. With further increasing of the film thickness, the fringe contrast grows, passes through a maximum at some d_f about 128 nm, and

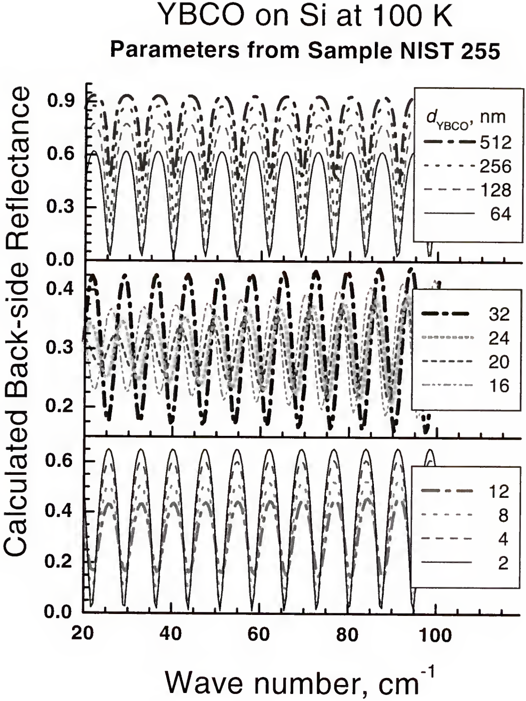

Figure 7.5: Calculated back-side reflectance vs. wave number, with the $YBa_2Cu_3O_{7-\delta}$-film thickness as an adjustable parameter, for a sample similar to Sample NIST 255 at 100 K.

starts to decline as the film is becoming thicker and getting closer to a perfect reflector. With increasing the film thickness above the point where the fringe contrast is vanishing at low wave numbers, the fringe-averaged back-side reflectance grows monotonically and is as high as 0.70-0.75 at $d_f = 512$ nm.

In theory, for a bare Si substrate, the transmittance and reflectance maxima are $\mathcal{T}_{max} = 1 = \mathcal{R}_{max}$, and their minima are $\mathcal{T}_{min} = 0 = \mathcal{R}_{min}$. The transmittance maxima and reflectance minima are centered at the wave numbers $\breve{\nu}_m^{(t)} = m\Delta\breve{\nu}$, where m is an integer, and $\Delta\breve{\nu} = (2\, n_{Si}\, d_{Si})^{-1}$ is the free spectral range for the wave number. At 100 K, with $n_{Si} = 3.390$, and $d_{Si} = 203.7\ \mu$m (for Sample NIST 255), we get $\Delta\breve{\nu} = 7.24$ cm^{-1}. Actually a much more accurate experimental value for the free spectral range, which takes into account all the intricacies of the multiple beam interference, can be found in Table 6.7. E.g., for the case of transmittance the free spectral range is $\Delta\breve{\nu} = 7.2065$ cm^{-1}.

Conversely, the center wave numbers for the reflectance maxima and transmittance minima are given by $\breve{\nu}_m^{(r)} = (m\ +\ 1/2)\ \Delta\breve{\nu}$.

As a further illustration for the significance of the YBCO film, the values of the third extrema of the calculated transmittance, front-side reflectance, and back-side reflectance versus the $YBa_2Cu_3O_{7-\delta}$-film thickness for an imaginary sample with all parameters equal to those of Sample NIST 255 at 100 K, except for the thickness of the $YBa_2Cu_3O_{7-\delta}$ film which is used as an independent variable, are plotted in Figure 7.6. The maximum values are given in the top panel and the minimum values in the bottom panel. Here one can clearly see the monotonic decrease of the transmittance and the monotonic increase of the front-side reflectance. All curves initially change faster and then the slope magnitude gradually decreases and at high thicknesses the curves asymptotically become horizontal. This holds true for both the minimum and maximum value. The back-side-reflectance maximum is growing steeply at very low thicknesses, passes through a maximum, then falls

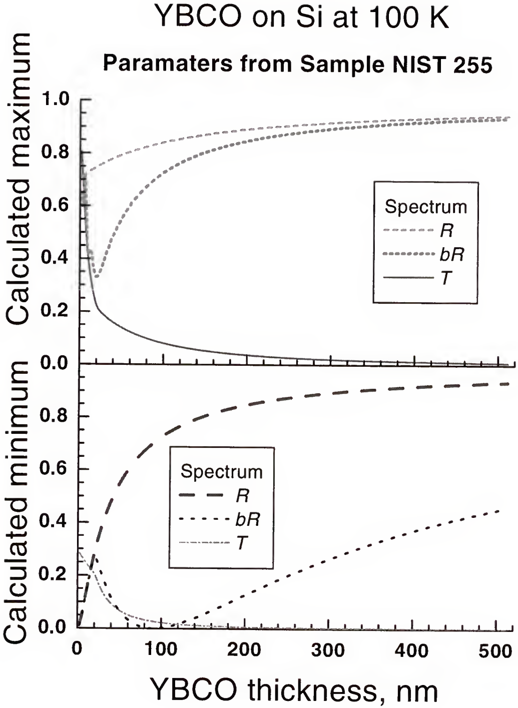

Figure 7.6: Calculated values of the third extremum for transmittance (T), front-side reflectance (R), and back-side reflectance (bR) vs. the thickness of the $YBa_2Cu_3O_{7-\delta}$ film for a sample similar to Sample NIST 255 at 100 K.

steeply and has a minimum around 20 nm, after which it grows initially fast and then its slope gradually decreases and the curve tends to become horizontal at very high thicknesses. The minimum in the vicinity of 20 nm occurs when the effective Fresnel coefficient for back-side reflectance from the total structure vanishes ($r_b = 0$), i.e., when $d_f \approx 20$ nm.

The back-side-reflectance minimum is zero if no film is present (naked silicon plate), then grows with the YBCO thickness, passes through a maximum around 20 nm, then falls and has a minimum around 90 nm, after which it grows moderately fast and its slope gradually decreases, but only slightly compared with the other curves.

Notably, at 21 nm the transmittance maximum (0.21554) and minimum (0.19685) are almost equal which means that the transmittance through a sample with a film of such a thickness has almost no fringes and is almost constant. Similarly, at 20 nm the back-side reflectance maximum (0.33140) and minimum (0.26526) are almost equal which means that the back-side reflectance from a sample with a film of such a thickness has almost no fringes and is almost constant, that is the back-side reflectance from a film with such a thickness is independent of the frequency, $\mathcal{R}_b \approx 0.28$, which is also equal to the front-side reflectance minimum $\mathcal{R}_f \approx 0.28$. Furthermore, most likely at some point within the film-thickness range 20-21 nm both the transmittance and back-side reflectance will become truly constant.

Inspection of the transmittance maximum and back-side-reflectance minimum curves with equation 7.1 in mind, makes it clear that one can expect the back-side absorptance to have a maximum at some thickness within the range 90-120 nm where both the transmittance maximum and minimum, as well as the back-side reflectance minimum, are low.

The calculated spectral positions of the third extrema for an imaginary sample with all parameters equal to those of Sample NIST 255 at 100 K, except for the thickness of the $YBa_2Cu_3O_{7-\delta}$ film which is used as an independent variable, are shown in Figure 7.7. The spectral position of the third maximum versus YBCO-film thickness can be found in the top panel and the spectral position of the third minimum is presented in the bottom panel, respectively. Note, that unlike the case in Figure 5 from our paper [125] (or Figure 6.4 in Kumar's dissertation [120]) where the calculation was done at two fixed wave number values (6.5 $\Delta\breve{\nu}$ and 7 $\Delta\breve{\nu}$, corresponding to $m = 6.5$, and 7) where the extrema should presumably be, here the extrema have been hunted in their exact position in order to account for the significant phase change that is present in the film-thickness range from 0 to 100 nm. The phase change is occurring faster between 15 and 25 nm. From 40 nm on, all transmittance and back-side-reflectance-extrema curves approach asymptotically their high-thickness constant value. Curiously, both the spectral positions of the back-side-reflectance maximum and minimum show a small, very narrow local minimum around film thickness of six nm. The reason for this is unclear. The position of the reflectance maximum is almost constant within the entire studied thickness range, but the reflectance minimum experiences a small variation distributed over the entire studied thickness range. This causes a slight asymmetric variation of the reflectance fringes with the thickness of the YBCO film.

Now we are ready to consider the effect of the YBCO-film thickness on the absorptance. The calculated front-side absorptance vs. the thickness of the $YBa_2Cu_3O_{7-\delta}$ film for an imaginary sample with all parameters equal to those of Sample NIST 255 at 100 K, except for the thickness of the $YBa_2Cu_3O_{7-\delta}$ film which is used as an adjustable parameter, is given in Figure 7.8. How these curves originate can be seen by taking into account equation 7.1 and juxtaposing

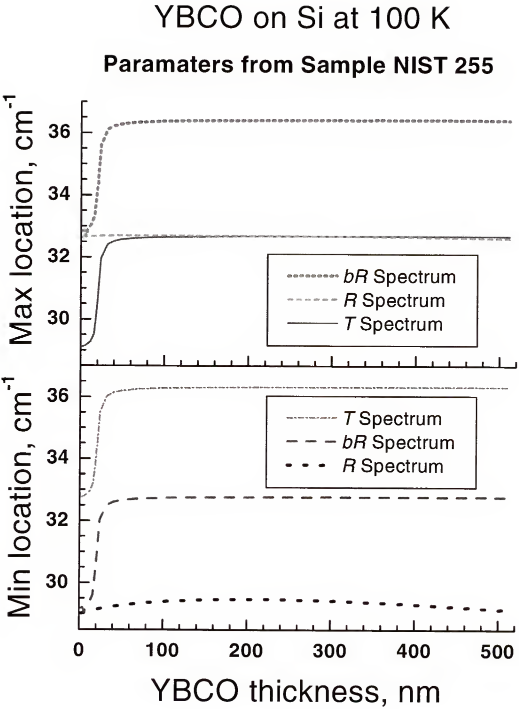

Figure 7.7: Calculated spectral positions of the third extremum for transmittance (T), front-side reflectance (R), and back-side reflectance (bR) vs. the thickness of the $YBa_2Cu_3O_{7-\delta}$ film for a sample similar to Sample NIST 255 at 100 K.

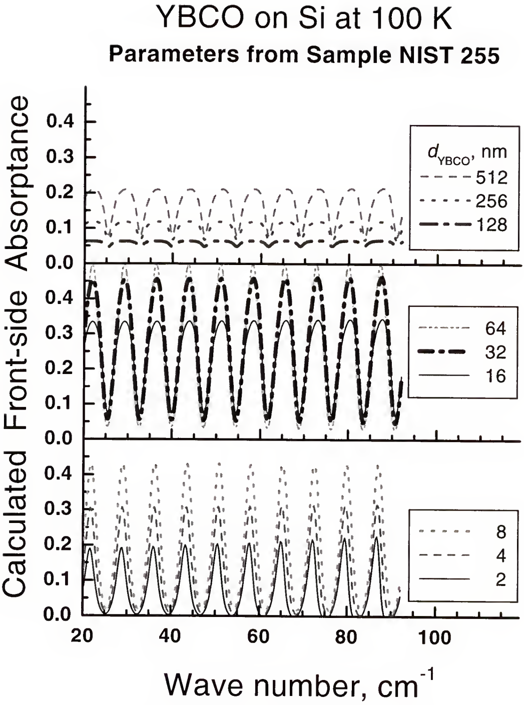

Figure 7.8: Calculated front-side absorptance vs. the thickness of the $YBa_2Cu_3O_{7-\delta}$ film for a sample similar to Sample NIST 255 at 100 K.

the transmittance (Figure 7.3) and front-side reflectance (Figure 7.4). Interestingly the phase shift seen in the transmittance curves, is completely masked by the higher fringe contrast of the front-side reflectance curve at low YBCO-film thickness where the transmittance is completely out of phase with the front-side reflectance. The dominating reflectance has no phase shift, and thus no phase shift can be seen in the front-side absorptance curves. The resultant effect is just a slight asymmetry of the fringes (the high-wave-number half of the maxima is wider than the low-wave-number half) at values of the YBCO thickness exceeding 16 nm.

The front-side absorptance maxima (Figure 7.8) are centered at ($\breve{\nu}_m^{(t)} = m\ \Delta\breve{\nu}$), whereas the front-side absorptance minima are centered at $\breve{\nu}_m^{(r)} = (m\ +\ 1/2)\ \Delta\breve{\nu}$, respectively, for the whole range of $YBa_2Cu_3O_{7-\delta}$ thicknesses that was covered in the calculations. Both the fringe-averaged absorptance and the fringe contrast of the absorptance grow as the $YBa_2Cu_3O_{7-\delta}$-film thickness is increased up to about 20 nm, pass through their maxima, and then diminish as d_f is increased further.

The calculated back-side absorptance vs. the thickness of the $YBa_2Cu_3O_{7-\delta}$ film for an imaginary sample with all parameters equal to those of Sample NIST 255 at 100 K, except for the thickness of the $YBa_2Cu_3O_{7-\delta}$ film which is used as an adjustable parameter, is given in Figure 7.9. How these curves originate can be seen by taking into account equation 7.1 and juxtaposing the transmittance (Figure 7.3) and back-side reflectance (Figure 7.5). Both the transmittance and back-side reflectance are characterized by a phase shift and are completely out of phase over the whole studied spectral range. But these two out-of-phase spectra do not cancel out when they are combined into the back-side absorptance: the latter is dominated by the back-side reflectance. Nevertheless, the spectral positions of the back-side-absorptance maxima correspond to the spectral positions of the transmittance maxima because of the negative sign in equation 7.1.

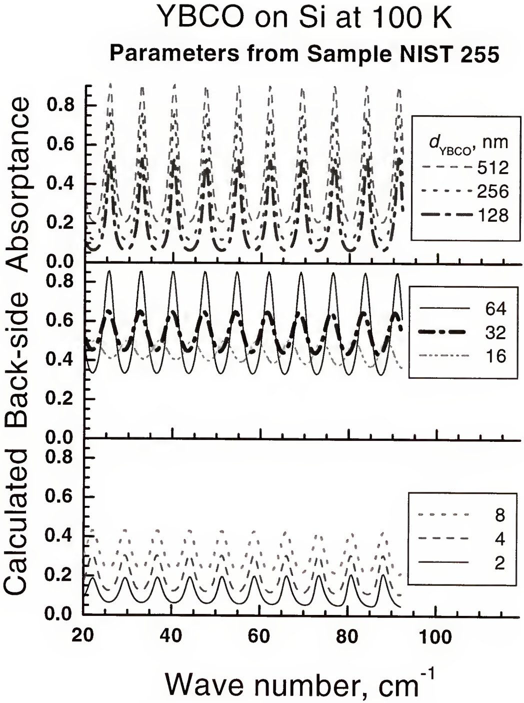

Figure 7.9: Calculated back-side absorptance vs. the thickness of the $YBa_2Cu_3O_{7-\delta}$ film for a sample similar to Sample NIST 255 at 100 K.

The back-side absorptance maxima (Figure 7.9) are centered at ($\breve{\nu}_m^{(t)} = m\ \Delta\breve{\nu}$), whereas the back-side absorptance minima are centered at [$\breve{\nu}_m^{(r)} = (m\ +\ 1/2)\ \Delta\breve{\nu}$], respectively, only when $d_f \lesssim 10$ nm. Within the $YBa_2Cu_3O_{7-\delta}$-thickness range from 10 to 40 nm approximately, a gradual phase shift occurs so that when $d_f \gtrsim$ 40 nm, the back-side absorptance maxima are centered at [$\omega_m^{(r)} = (m\ +\ 1/2)\ \Delta\omega$], and the back-side absorptance minima are centered at ($\omega_m^{(t)}\ =\ m\ \Delta\omega$), respectively. Thus, thin $YBa_2Cu_3O_{7-\delta}$ films are characterized by back-side absorptance with exactly the opposite phase to that of very thin films.

From Figures 7.8 and 7.9 it can be seen that the $YBa_2Cu_3O_{7-\delta}$-film thickness has a significant effect on the absorptance. The effect is especially strong for the back-side absorptance. Increasing the $YBa_2Cu_3O_{7-\delta}$-film thickness makes the film more opaque: the transmittance is decreasing whereas the reflectance is increasing. The competition between the latter two trends leads to the existence of an optimum $YBa_2Cu_3O_{7-\delta}$ thickness with which the absorptance would be maximum.

At 100 K, the $YBa_2Cu_3O_{7-\delta}$film thickness of about 20 nm corresponds to the back-side antireflection effect of the Si substrate which was described in the previous chapter. From the shown results of the calculations with twelve values of the $YBa_2Cu_3O_{7-\delta}$ thickness, it can be concluded that both the fringe-averaged and peak back-side absorptance pass through a maximum at some value of d_f in the range from 70 to 90 nm. This rough estimation is based on the fact that according to our calculations, at $d_f = 64$ nm the fringe-averaged absorptance is ≈ 0.60, and the peak absorptance is ≈ 0.87, whereas at 128 nm we found the second highest values ≈ 0.29 and ≈ 0.53, respectively. The maximum is local however. Indeed, after a minimum in the vicinity of $d_f = 128$ nm, both the average and peak absorptance resume their growth and at $d_f = 512$ nm already exceed the local maximum values. Therefore if one is interested in far-infrared detectors the choice is either back-side illumination of films with either $d_f =\gtrsim 64$ nm or $d_f > 500$ nm.

Upon comparing the bottom panels of Figures 7.1 and 7.2, it can be seen that at 100 K with $d_f = 35$ nm, the front-side-absorptance maxima are approximately equal to the back-side-absorptance minima, both sets of which are spectrally located at ($\breve{\nu}_m^{(t)} = m\ \Delta\breve{\nu}$). The relation $\mathcal{A}_b = \mathcal{A}_f$ also means that $\mathcal{R}_b = \mathcal{R}_f$, since the transmittance values for front-side and back-side incidence are identical. Another way to reach this relation is to assume that the "round-trip" phase change within the Si substrate is $\phi_{Si} = m\pi$, i.e., $\exp(\mathrm{i}\, 2\phi_{Si}) = 1$. As Kumar [120, p. 94] has suggested, the equality between the front-side and back-side absorptance, at particular frequencies for a given temperature and $YBa_2Cu_3O_{7-\delta}$-film thickness, can be used to check how accurate the measurements have been.

7.2.2 Absorptance in the Superconducting State

The absorptance spectra of Sample NIST 255, with $YBa_2Cu_3O_{7-\delta}$ in the superconducting state, have been calculated using the fits to the transmittance and reflectance data. Because in this state even the fringe-averaged absorptance is not constant within the whole studied spectral range, it is impossible to extend Table 7.1 simply by adding of a couple of new columns and we are limited to graphical representation only. The calculated front-side absorptance for the $YBa_2Cu_3O_{7-\delta}$ film of Sample NIST 255 at two temperatures, with the YBCO film in the superconducting state, is given in Figure 7.10 (at 50 K on the top panel and at 10 K on the bottom panel). The calculated back-side absorptance for the $YBa_2Cu_3O_{7-\delta}$ film of Sample NIST 255 at two temperatures, with the YBCO film in the superconducting state, is shown in Figure 7.11. In the superconducting state, both the fringe contrast of the absorptance and the fringe-averaged absorptance increase with frequency. The front-side absorptance minima are slightly shifted in frequency from those of the back-side absorptance. The shift is even stronger for the respective maxima. This shift in the extrema frequencies is due

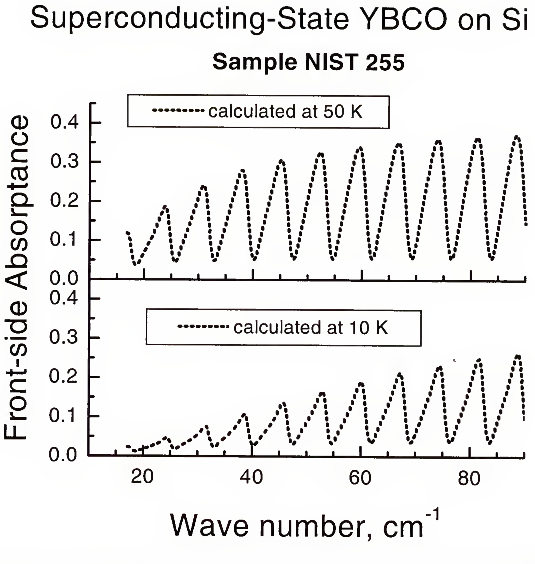

Figure 7.10: Front-side absorptance for the $YBa_2Cu_3O_{7-\delta}$ film of Sample NIST 255 at two temperatures in the superconducting state.

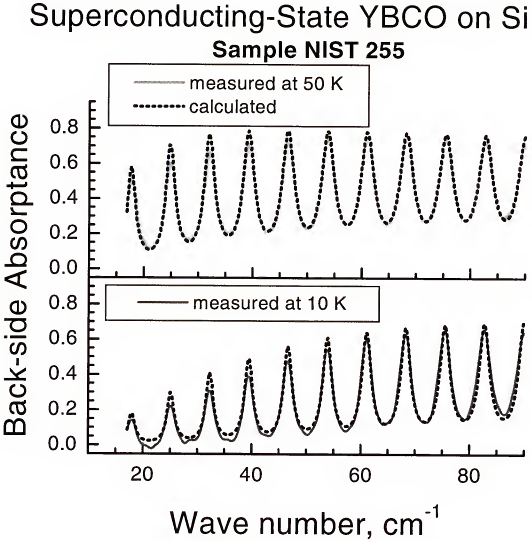

Figure 7.11: Back-side absorptance for the $YBa_2Cu_3O_{7-\delta}$ film of Sample NIST 255 at two temperatures in the superconducting state.

to the fact that the frequencies of the front-side-reflectance extrema are shifted in phase by π rad with respect to the transmittance extrema. Additionally, the amount of that shift depends on the $YBa_2Cu_3O_{7-\delta}$-film thickness, as discussed in the previous subsubsection (7.2.1.4). Therefore, the frequencies of the front-side absorptance extrema are determined by a competition between the contributions of the transmittance and front-side reflectance.

When the $YBa_2Cu_3O_{7-\delta}$ film is in the superconducting state, both the back-side and front-side absorptance are increasing functions of the temperature. As the temperature is lowered, the fraction of superconducting electrons f_s increases, which can be seen from the bottom two lines in Table 6.21. The absorptance in the superconducting state is proportional to the fraction of normal electrons $f_n = 1 - f_s$. Thus, the decrease of f_n as the temperature is lowered, leads to a respective decrease in the absorptance, which readily explains its observed temperature dependence.

Even within the spectral range from 40 to 100 cm^{-1} where the fringe-averaged front-side absorptance (Figure 7.10) and back-side absorptance (Figure 7.11) in the superconducting state are relatively high, they are nevertheless smaller than the corresponding quantities in the normal state (Figure 7.1 and Figure 7.2). Upon transition from the superconducting to the normal state, the fringe contrast of the front-side absorptance increases, whereas the fringe contrast of the back-side absorptance decreases, respectively. At higher frequencies from 80 to 100 cm^{-1} the back-side absorptance is as high as 0.8, but at low frequencies from 10 to 30 cm^{-1} it approaches or is even lower than that in the normal state. Therefore, as Kumar has suggested [120, p. 95], if the superconducting thin films are meant to be operated as far-infrared detectors at very low frequencies, a normal-metal coating of the $YBa_2Cu_3O_{7-\delta}$ film may be used in order to raise the detector absorptance.

7.3 Sample NIST 256

7.3.1 Absorptance in the Normal State

7.3.1.1 Front-side absorptance of Sample NIST 256

The calculated front-side absorptance for the $YBa_2Cu_3O_{7-\delta}$ film of Sample NIST 256 at three temperatures, with the YBCO film in the normal state, is given in Figure 7.12 (at 300 K on the top panel, at 200 K on the middle panel, and at 100 K on the bottom panel). These spectra are similar to the respective calculated spectra for Sample NIST 255.

7.3.1.2 Back-side absorptance of Sample NIST 256

The calculated back-side absorptance for the $YBa_2Cu_3O_{7-\delta}$ film of Sample NIST 256 at three temperatures, with the YBCO film in the normal state, is shown in Figure 7.13. As can be expected, the absorptance spectra of Sample NIST 256 are very similar to the absorptance spectra of Sample NIST 255. We know from Sample NIST 255 that in the vicinity of the phase-switch temperature the phase is unstable and hard to model, as it is very sensitive to even small uncertainties in a number of parameters. Though we are lacking the measured absorptance, the calculated back-side absorptance of Sample NIST 256 shows a significantly reduced fringe contrast (Figure 7.13, middle panel), whereas that of the front-side absorptance (Figure 7.12, middle panel) is very high, just like was observed for both the measured and calculated back-side absorptance of Sample NIST 255. Again, this is due to a phase-shift of π rad found in both the transmittance (Figure 6.25, from top to bottom panel) and back-side reflectance spectra (Figure 6.29, from top to bottom panel) when the 100 K and 300 K curves are compared. The only minor difference is that for Sample NIST 256 the exact temperature at which such a phase

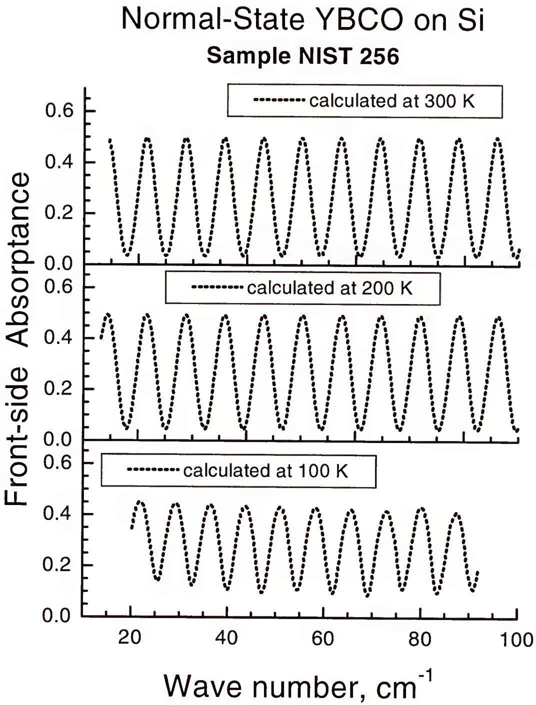

Figure 7.12: Front-side absorptance for the $YBa_2Cu_3O_{7-\delta}$ film of Sample NIST 256 at three temperatures in the normal state.

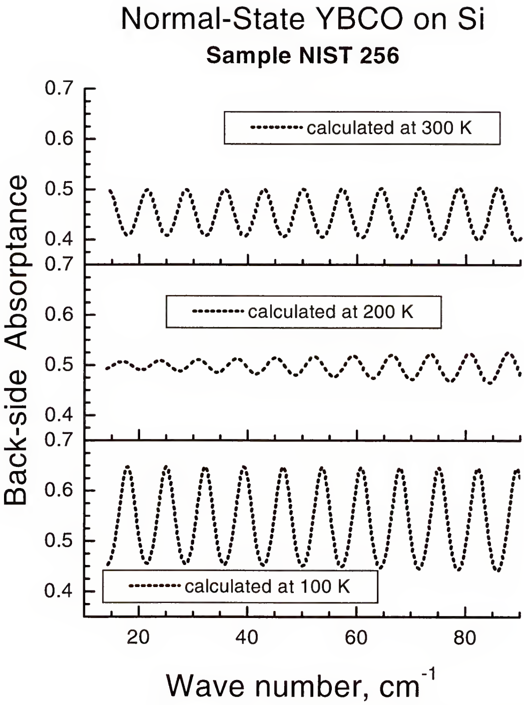

Figure 7.13: Back-side absorptance for the $YBa_2Cu_3O_{7-\delta}$ film of Sample NIST 256 at three temperatures in the normal state.

change occurs is not as close to 200 K as it is for Sample NIST 255. Nevertheless, the phase of the calculated spectrum at 200 K cannot be considered to be very reliable for the same reasons that were given for the respective spectrum of Sample NIST 255.

7.3.2 Absorptance in the Superconducting State

The calculated front-side absorptance for the $YBa_2Cu_3O_{7-\delta}$ film of Sample NIST 256 at two temperatures, with the YBCO film in the superconducting state, is given in Figure 7.14 (at 50 K on the top panel and at 10 K on the bottom panel). The calculated back-side absorptance for the $YBa_2Cu_3O_{7-\delta}$ film of Sample NIST 256 at two temperatures, with the YBCO film in the superconducting state, is shown in Figure 7.15. Once more, as was the case in the normal state, the calculated absorptance spectra for Sample NIST 256 in the superconducting state are very similar to the respective spectra for Sample NIST 255.

7.4 Sample NIST 73

Below 100 cm^{-1} the measured absorptance spectra of Samples NIST 73 and NIST 74 are very similar to the respective spectra of Samples NIST 255 and NIST 256. In the rest of the covered spectral range some features and peculiarities appear. Some of them are related to the known phonon oscillators characterizing the $YBa_2Cu_3O_{7-\delta}$ layer. The most prominent features from the YSZ layer and the wide phonon characterizing the SiO_2 layer are contributing to the total absorptance, too. Additionally, there are some unwanted parasitic effects, such as unnatural modulation of the absorptance fringes and even negative absorptance (which if it were true would imply that there was a source of free energy within the YBCO layer). The reasons for these artificial effects are the following: the

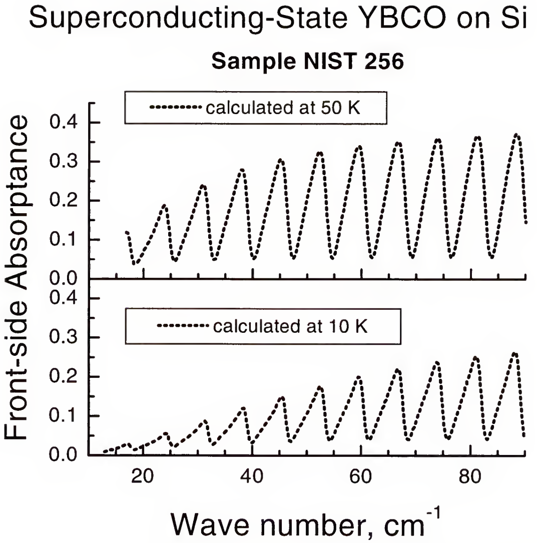

Figure 7.14: Front-side absorptance for the $YBa_2Cu_3O_{7-\delta}$ film of Sample NIST 256 at two temperatures in the superconducting state.

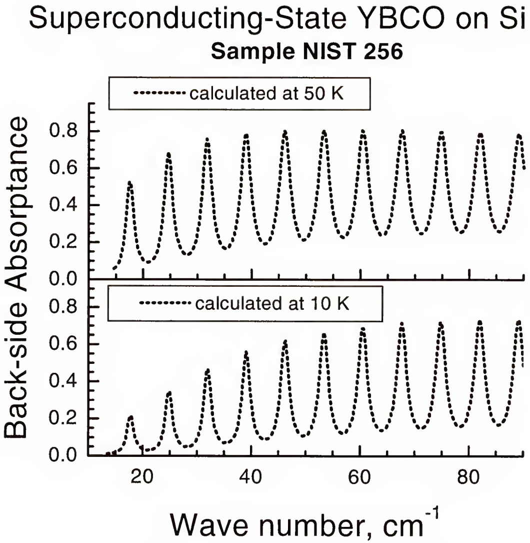

Figure 7.15: Back-side absorptance for the $YBa_2Cu_3O_{7-\delta}$ film of Sample NIST 256 at two temperatures in the superconducting state.

reflectance and transmittance have not been measured simultaneously during the same measurement, and the transmittance has been measured at normal incidence, whereas the reflectance has been measured at an incidence which is slightly oblique. Even though the difference in the apparent thickness of the Si substrate from one traversing of the sample is relatively small, because of the multiple-beam interference such a small difference is compounded and may result in a noticeably large effective difference. Furthermore, that effect is dependant on the single-bounce reflectivity from both interfaces and clearly the reflectivity of the film-side interface is strongly dependant on both the temperature and the wave number. As a result the dephasing of the reflectance fringes from the corresponding fringes of the transmittance increases non-linearly with the wave number. This parasitic effect can be avoided in various ways:

1. the best way is to measure both the transmittance and reflectance simultaneously and at normal incidence, but it would require non-trivial hardware changes to the interferometer;
2. maybe the second best way would be to rescale the apparent thickness of the silicon layer for the reflectance in such a way that the reflectance fringes are forced to correspond in their spectral position to the transmittance fringes;
3. another way to handle the situation with the available as-is data is to consider either the fringe-averaged absorptance, or the Fourier-transform filtered absorptance;
4. the easiest and fastest way is, after realizing what causes the strange peculiarities, to ignore them and resort to eye-ball fringe averaging.

As this dissertation is too thick already, the latter lazy approach beats them all.

Additionally, some fraction of the difference between the measured and calculated absorptance can be attributed to the effect of partial coherence, which was mentioned in the previous chapter, and which is especially strong for the case of reflectance.

7.4.1 Absorptance in the Normal State

7.4.1.1 Front-side absorptance of Sample NIST 73

The measured and calculated front-side absorptance for the $YBa_2Cu_3O_{7-\delta}$ film of Sample NIST 73 at three temperatures, with the YBCO film in the normal state, is given in Figure 7.16 (at 300 K on the top panel, at 200 K on the middle panel, and at 100 K on the bottom panel). The calculated front-side absorptance spectra are similar to the measured front-side absorptance, but is characterized by much higher fringe contrast because of the partial coherence of the slightly wedged samples.

7.4.1.2 Back-side absorptance of Sample NIST 73

The measured and calculated back-side absorptance for the $YBa_2Cu_3O_{7-\delta}$ film of Sample NIST 73 at three temperatures, with the YBCO film in the normal state, is shown in Figure 7.17. The match between the measured and calculated back-side absorptance spectra is impressive. These spectra hint that for Sample NIST 73 the antireflecttion and the related phase switch occur in the vicinity of 100 K. Indeed, the curve at 100 K shows a reduced fringe contrast below about 140 cm^{-1}, and in that same spectral range the phase of the measured absorptance gradually changes and at the lowest wave numbers is opposite to the phase of the calculated absorptance.

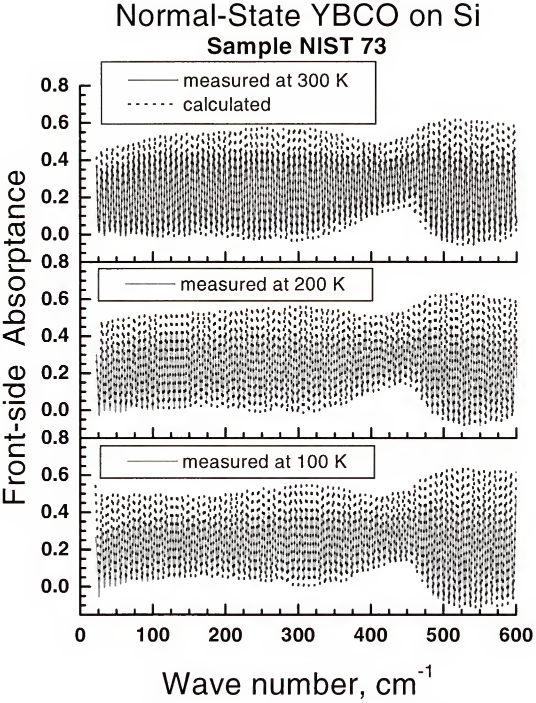

Figure 7.16: Front-side absorptance for the $YBa_2Cu_3O_{7-\delta}$ film of Sample NIST 73 at three temperatures in the normal state.

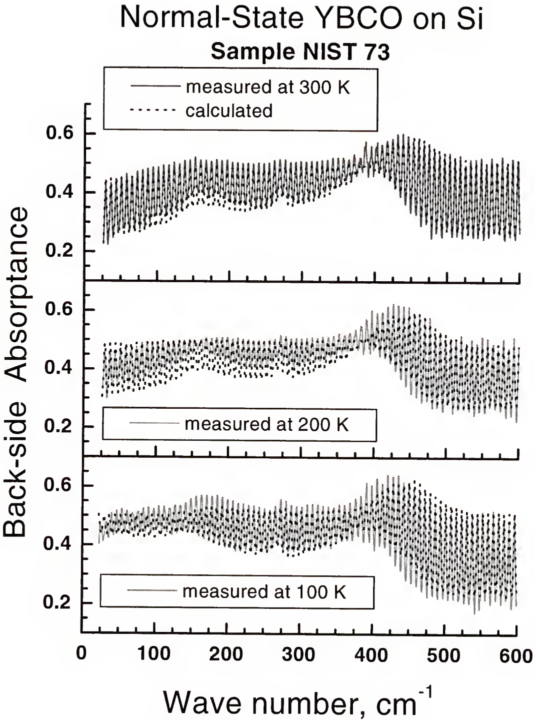

Figure 7.17: Back-side absorptance for the $YBa_2Cu_3O_{7-\delta}$ film of Sample NIST 73 at three temperatures in the normal state.

7.4.2 Absorptance in the Superconducting State

The measured and calculated front-side absorptance for the $YBa_2Cu_3O_{7-\delta}$ film of Sample NIST 73 at three temperatures, with the YBCO film in the superconducting state, is given in Figure 7.18 (at 50 K on the top panel, at 20 K on the middle panel, and at 10 K on the bottom panel). The correspondence between the measured and calculated spectra here is not good. At low wave numbers the discrepancy is due to the difference between the reflectance and its fit (Figure 6.34). A much better calculated absorptance could be obtained if the alternate reflectance fit (Figure 6.35) were used. Because of the different apparent thickness of the Si substrate obtained from the transmittance and front-side reflectance measurement (Table 6.13), as the wave number is increased the shift between the respective fringes of the transmittance and front-side reflectance increases. This leads to misleading negative values of the calculated front-side absorptance above 480 cm^{-1}. The fact that this effect is absent for the measured absorptance shows that the latter has somewhat reduced fringe contrast due to the partial coherence. On the other hand, the fact that the effect in question is absent in the normal state may be an indication that at low temperatures temperature gradients within the cold finger of the cryostat and the sample holder may be causing a slight displacement of the sample from its optimum position which can compromise the optical alignment.

The measured and calculated back-side absorptance for the $YBa_2Cu_3O_{7-\delta}$ film of sample NIST 73 at three temperatures, with the YBCO film in the superconducting state, is shown in Figure 7.19 (at 50 K on the top panel, at 20 K on the middle panel, and at 10 K on the bottom panel). Here the calculated absorptance curves follow the measured absorptance curves quite well.

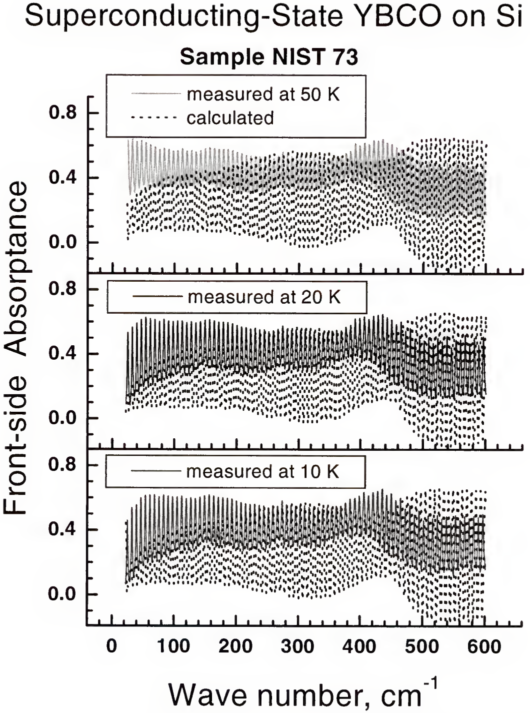

Figure 7.18: Front-side absorptance for the $YBa_2Cu_3O_{7-\delta}$ film of Sample NIST 73 at three temperatures in the superconducting state.

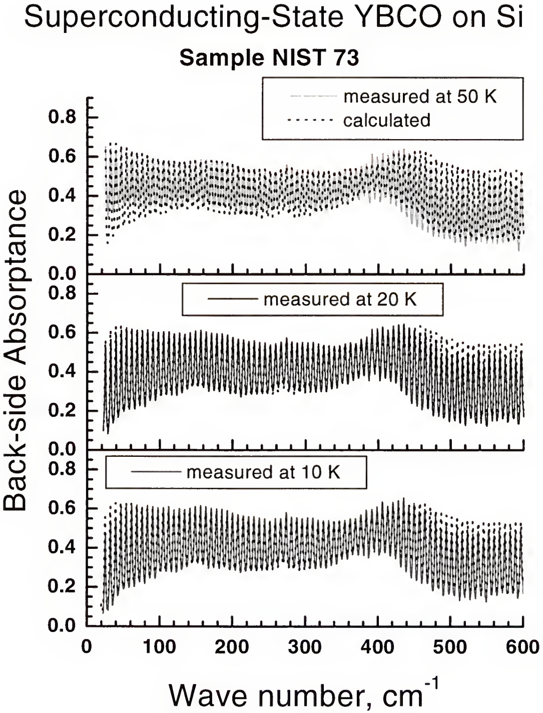

Figure 7.19: Back-side absorptance for the $YBa_2Cu_3O_{7-\delta}$ film of sample NIST 73 at three temperatures in the superconducting state.

7.5 Sample NIST 74

7.5.1 Absorptance in the Normal State

7.5.1.1 Front-side absorptance of Sample NIST 74

The measured and calculated front-side absorptance for the $YBa_2Cu_3O_{7-\delta}$ film of Sample NIST 74 at three temperatures, with the YBCO film in the normal state, is given in Figure 7.20 (at 300 K on the top panel, at 200 K on the middle panel, and at 100 K on the bottom panel). The top and bottom envelopes of the calculated absorptance generally follow the envelopes of the measured absorptance, but for a down shift which we cannot explain.

7.5.1.2 Back-side absorptance of Sample NIST 74

The measured and calculated back-side absorptance for the $YBa_2Cu_3O_{7-\delta}$ film of sample NIST 74 at three temperatures, with the YBCO film in the normal state, is shown in Figure 7.21. In the upper third of the studied spectral range the correspondence between the calculated and measured absorptance is reasonable. At lower wave numbers the general appearance of the two is similar, but the match is not that good. The calculated spectra imply that the non-reflection and the phase shift occur somewhere around 200 K, whereas the measured data suggest that this happens somewhere around 100 K.

7.5.2 Absorptance in the Superconducting State

The measured and calculated front-side absorptance for the $YBa_2Cu_3O_{7-\delta}$ film of Sample NIST 74 at three temperatures, with the YBCO film in the superconducting state, is given in Figure 7.22 (at 50 K on the top panel, at 20 K on the middle panel, and at 10 K on the bottom panel). At 10 K and 20 K the correspon-

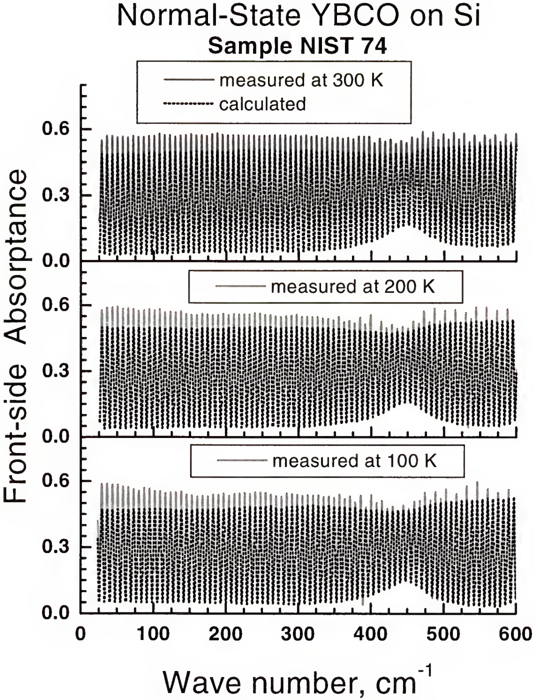

Figure 7.20: Front-side absorptance for the $YBa_2Cu_3O_{7-\delta}$ film of sample NIST 74 at three temperatures in the normal state.

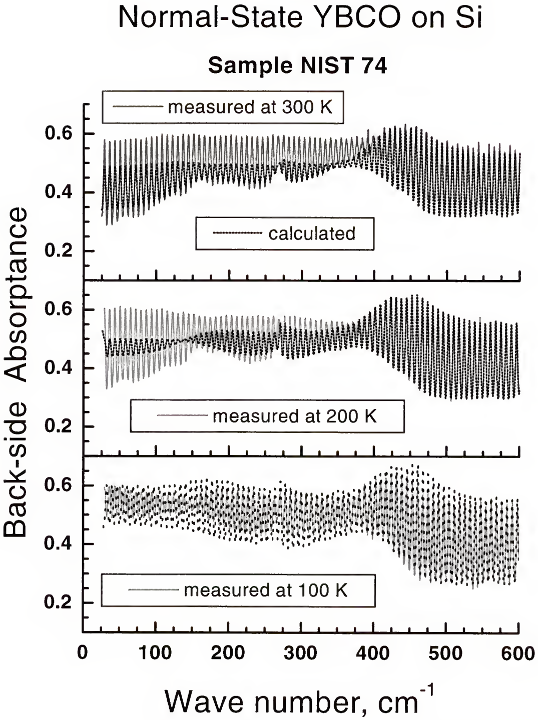

Figure 7.21: Back-side absorptance for the $YBa_2Cu_3O_{7-\delta}$ film of sample NIST 74 at three temperatures in the normal state.

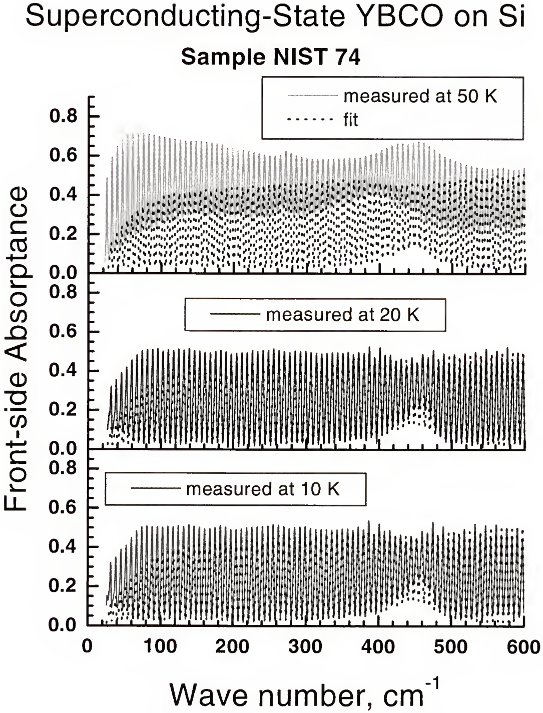

Figure 7.22: Front-side absorptance for the $YBa_2Cu_3O_{7-\delta}$ film of sample NIST 74 at three temperatures in the superconducting state.

dence between the measured and calculated front-side absorptance is reasonable, but the difference increases at lower wave numbers and becomes especially large at 300 K.

The measured and calculated back-side absorptance for the $YBa_2Cu_3O_{7-\delta}$ film of sample NIST 74 at three temperatures, with the YBCO film in the superconducting state, is shown in Figure 7.23 (at 50 K on the top panel, at 20 K on the middle panel, and at 10 K on the bottom panel). The match between calculated and measured absorptance is good except at the lowest wave numbers.

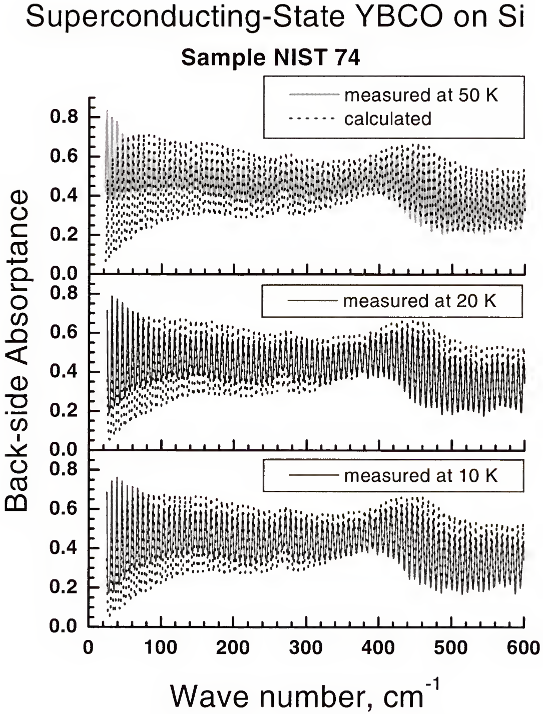

Figure 7.23: Back-side absorptance for the $YBa_2Cu_3O_{7-\delta}$ film of sample NIST 74 at three temperatures in the superconducting state.

CHAPTER 8
FABRY-PEROT RESONATORS

8.1 Introduction

This chapter presents our measurements of transmittance through Fabry-Perot resonators. It includes a review of previous studies, a description of the measurements, the measured and calculated transmittance, as well as analysis of the data, and discussion of the results. The latter covers the optimization of the resonance transmittance, as well as the effect of the thickness of the gap and the $YBa_2Cu_3O_{7-\delta}$-film thickness on the transmittance.

The theoretical background for the Fabry-Perot resonators was given in Section 3.5. The resonators which we have studied were made using $YBa_2Cu_3O_{7-\delta}$ films on Si substrates as reflectors. The two samples were mounted on a sample-holder, with the Si substrates to the outside, and the $YBa_2Cu_3O_{7-\delta}$ films to the inside, facing each other. They were kept apart by a suitable spacer, which determined the thickness of the vacuum gap separating the two $YBa_2Cu_3O_{7-\delta}$ films. The structure described above for the case of Fabry-Perot resonators 1 and 2 made with Samples NIST 255 and NIST 256 is illustrated in Figure 8.1. The nominal thickness for all layers is shown. The configuration is for transmittance measurement. In order to avoid unnecessary complication of the picture, only first-order reflections from each interface are shown on the figure. In reality as a result of the multiple beam interference within every layer, the beams transmitted through each interface are the result of the superposition of an infinite number of partial-beam components whose amplitude quickly decreases as their order increases. The samples that were used as reflectors for Fabry-Perot res-

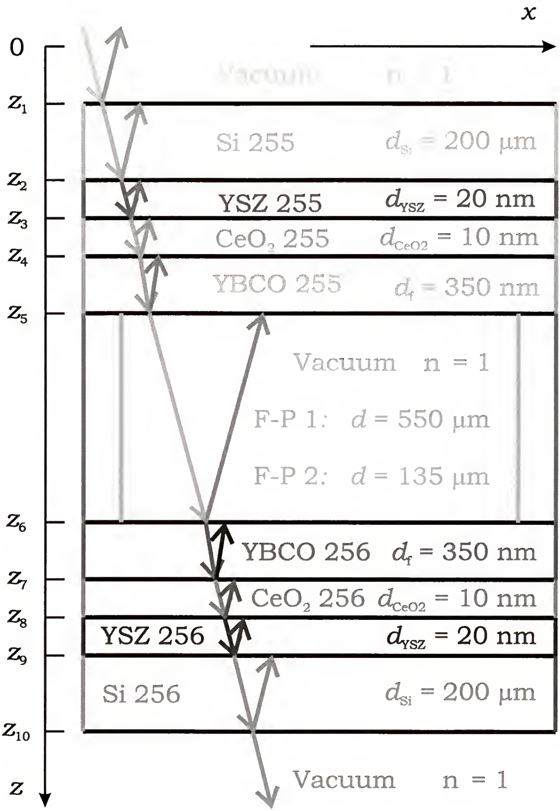

Figure 8.1: Structure of Fabry-Perot resonators 1 and 2 made of Samples NIST 255 and NIST 256 in a configuration for transmittance measurements.

onators 1 and 2 had been measured previously. Their transmittance, front-side reflectance, back-side reflectance, as well as front-side absorptance and back-side absorptance were covered in Chapter 6 and 7, respectively.

For our earlier measurements (see Kumar et al. [37]), we selected Samples NIST 255 and NIST 256, which had the closest characteristics from the batch of samples that we had measured at that time.[1] We measured two Fabry-Perot resonators made of Samples NIST 255 and NIST 256, with two different spacers. Our Fabry-Perot resonator 1 had a copper spacer 550 μm thick, whereas the polyimide spacer of Fabry-Perot resonator 2 was 132 μm thick.

In order to make the two samples as identical as possible, our more recent measurements were done on two pieces of Sample NIST 73. The latter were used as reflectors for our Fabry-Perot resonator 3.

The structure of Fabry-Perot resonator 3, made of two pieces from Sample NIST 73 is illustrated in Figure 8.2. The nominal thickness for all layers is shown. The configuration is for transmittance measurement. In order to avoid unnecessary complication of the picture, only first-order reflections from each interface are shown on the figure. In reality as a result of the multiple beam interference within every layer, the beams transmitted through each interface are the result of the superposition of an infinite number of partial-beam components whose amplitude quickly decreases as their order increases.

Additionally, a second-generation sample-holder was designed. It had provisions for coarse setting of the gap by means of a compression O-ring, and fine-tuning by a piezo-electric crystal tube. Unfortunately, we found that the O-ring, when frozen at low temperatures, changes its mechanical properties significantly. As a result the gap thickness changed with temperature.

---

[1] The performance of a Fabry-Perot resonator would be optimum provided its two reflectors are identical, and their reflectance is as high as possible.

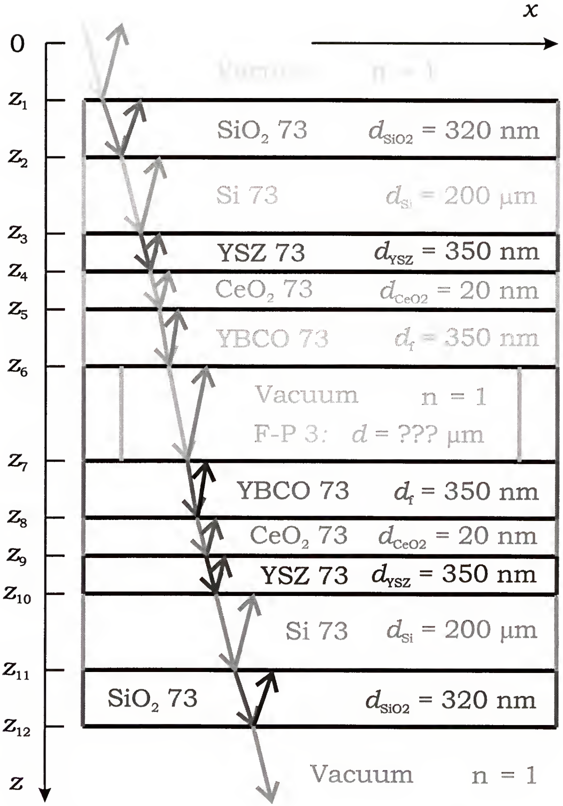

Figure 8.2: Structure of Fabry-Perot resonator 3 made of two halves of Sample NIST 73 and in a configuration for transmittance measurements.

To overcome this problem, and to improve the quality of the tuning, we designed a third-generation sample-holder which will be inherited by the next student/s who is/are to continue work on this project. It allows for coarse adjustment of the gap by three screws, and fine tuning by using three piezo-electric stacks offered commercially by Thorlabs, Inc.

The transmittance through Fabry-Perot resonators 1 and 2 was measured in the spectral range from 10 to 90 cm^{-1} at five fixed temperatures: three with the $\mathrm{YBa_2Cu_3O_{7-\delta}}$ in the normal state (300, 200 and 100 K) and two in the superconducting state (50 and 10 K).

The transmittance through Fabry-Perot resonator 3 was measured in the spectral range from 20 to 600 cm^{-1}at six fixed temperatures: three with the $\mathrm{YBa_2Cu_3O_{7-\delta}}$ in the normal state (300, 200 and 100 K) and three in the superconducting state (50, 20, and 10 K), but unfortunately our second-generation Fabry-Perot sample-holder failed at low temperatures and therefore only the results at 300 K can be deemed successful.

8.2 Theoretical Background of Superconducting Fabry-Perot Resonators

For our Fabry-Perot resonators we can readily apply the theory of a simple plane Fabry-Perot resonator, covered in Section 3.5. We only need to add some pertinent remarks here.

It can be shown that any multi-layered resonator structure can be reduced to an effective simple resonator with two interface surfaces. This can be done by first identifying the two main reflecting interfaces (i.e., the two inner-most interfaces characterized by significant single-interface reflectances), and then using the method of Rouard [30] twice: once, to reduce all interfaces, within the range bound by the radiation-exit side of the resonator structure and the middle plane between the two main reflecting interfaces of the resonator, to the second effective reflecting interface; and a second time, to reduce all interfaces, within the range bound by the middle plane between the two main reflecting interfaces of the resonator structure and its radiation-incidence side, to the first effective reflecting interface. The so-obtained two effective reflectors will be denoted with the Roman numbers II and I, respectively, used as subscripts. The unusual order, from high to low, was imposed by Rouard's method which starts from the radiation-exit layer, and ends with the radiation-entry layer.

When we are dealing with a multi-layered resonator structure, rather than a simple Fabry-Perot resonator, in addition to the primary or major fringes (those with the highest fringe contrast) there will be fringes of smaller fringe contrast, whose free spectral range is governed by the secondary, tertiary, etc. reflecting interfaces. If the resonator structure is symmetric with respect to the middle plane, we have a degenerate case, that is, the minor (secondary, tertiary, etc.) fringes due to side I would coincide with those due to side II. On the other hand, the asymmetric picture, where such a coincidence is not present in general for all minor fringes (but is still accidentally possible for some special ones), can be very complicated.

Initially, the presence of minor fringes cannot be readily seen from equation 3.202, because by means of oscillating single-effective-interface reflectance R and transmittance T (with subscripts I or II, respectively), they are hidden into F and $\mathcal{T}_{res}$, as defined by equations 3.200 and 3.201. We can also return back to equation 3.196 and note that the primary (major) fringes are due to the sine function, whereas the minor fringes are due to oscillations of R and T, as mentioned in the previous sentence.

Due to coupling of the primary set of fringes with the minor ones, and the assumptions that were made (neglected frequency dependence of the resonant transmittance and the phase changes upon reflection—see Section 3.5), the actual characteristics (such as finesse, bandwidth, resonant transmittance as well as frequencies of the maxima, half-maxima, and minima) of the resonator structure may differ slightly (and sometimes even significantly) from the simple results obtained in Section 3.5. Also, when the primary fringes have a very high fringe contrast, the minor fringes may be masked in a narrow spectral ranges centered about each major minimum.

As the order of the set of fringes increases, in most cases its fringe contrast approaches zero very fast. Additionally, very thin layers will produce fringes with a very high free spectral range—as a result the whole studied spectral range can lie entirely close about the wide minor maximum. Moreover, since the high-order (above secondary) interfaces normally have much lower reflectance, the respective minor fringe contrast will be very low. Thus, high-order fringes may be hard to find, especially when the single-interface reflectance of the primary and/or secondary interfaces is significantly higher than that of higher-order interfaces.

In our measurements we have observed only primary (due to a resonance within the vacuum gap), and tertiary (due to a resonance within the Si substrate) fringes. Because of the very small thickness of the $YBa_2Cu_3O_{7-\delta}$ layer, the secondary fringes, due to a resonance within that latter, have a very high free spectral range and cannot be observed within the studied spectral range. All other layers (buffer layers, and SiO_2) are either very thin, or with interfaces characterized by low reflectance, or both. Therefore, fringes of no higher order than tertiary have been (or can be) observed.

Let us denote the secondary optical thickness, i.e., the optical thickness of the medium between the primary and secondary reflecting interfaces, with $d_{sec} = \sum_j n_j d_j$ (the sum is over all layers between the primary and secondary interface). Then the vacuum-gap thickness d can be called primary optical thickness. Now, when $d_{sec} < d$ the primary free spectral range is smaller than the secondary one, or in other words the primary maxima are more (less) frequent than the secondary ones. Conversely, when $d_{sec} > d$ the primary free spectral range is bigger than the secondary one, or in other words the primary maxima are less frequent than the secondary ones. Since in our particular case the secondary fringes are not observable, the reasoning in this and next paragraph can still be valid if we replaced "secondary" ($_{sec}$) with "tertiary" ($_{ter}$). Note that when conducting layers are present, their refractive index, and hence their optical thickness, are complex quantities.

Through fine tuning of the vacuum-gap thickness d, the latter can be made commensurate to the secondary optical thickness d_{sec}. When that is done, either (if $d_{sec} > d$) each primary maximum will coincide with one of the secondary ones, or (if $d_{sec} < d$) each secondary maximum will coincide with one of the primary ones. A commensurately-tuned Fabry-Perot resonator would be able to operate at a number of narrow spectral ranges centered about its lower-order primary fringes and therefore it can act as a comb-filter. It must be noted here, that when $d \ll d_{sec}$ the resonator is commensurately self-tuned: the minor fringes are so frequent that inevitably one of them will be in the vicinity of some major fringe. Additionally, when $d \gg d_{sec}$, the resonator is also commensurately self-tuned: the major fringes are so frequent that inevitably one of them will be in the vicinity of some minor fringe.

Alternately, one can choose to count only the essential interfaces—those that cause observable fringes. If that choice were made, in the special case of our resonators, what I called above tertiary fringes would become secondary ones. Such renumbering could cause confusion, though.

Finally, if one is interested in selective tuning for a particular narrow spectral range, one can use incommensurate tuning which causes only one of the primary maxima to coincide with one of the minor maxima, suppressing all others to a certain extend. This effect was mentioned in our paper [37] and the dissertation of my collaborator A. R. Kumar [120], though we had not coined the term incommensurate tuning yet. Because of the commensurate self-tuning phenomenon mentioned earlier, incommensurate tuning is practical only when $d \sim d_{sec}$.

Fabry-Perot resonators, pre-tuned during manufacture can be produced by using Si substrates, covered with buffer layers and $YBa_2Cu_3O_{7-\delta}$ films on both sides. This will decrease the tertiary fringe contrast by a factor of two (as a single substrate is used instead of two), but the price to pay is that post-manufacture tuning will be impossible or at least hard to do—one has to find ways to control either the thickness or the refractive index of the substrate.

A number of methods, like Rouard's, Vašíček's, Crook's [30], and the transfer-matrix method [30,159,165,120], can be used for numerical calculation of the transmittance of the multi-layered resonator structure. However, equations 3.196–3.202 separate the contribution of major and minor resonances in a very "transparent" way, which make them convenient for discussion and analysis of our experimental data.

8.3 Review of Previous Studies

Soon after the discovery of high-temperature superconductors [166], thin films of such materials, deposited on transparent-in-the-far-infrared substrates, were considered as a potential substitute for the metal-mesh reflectors normally used in far-infrared resonators [157]. Metallic meshes are characterized by a high normal-type conductivity. Electrical currents, induced into the mesh wires by electromagnetic radiation, lead to Joule losses. Therefore metallic meshes absorb in the infrared spectral range [167], and such absorption lowers the finesse of the resonators.

Superconducting electrons, on the other hand, do not have Joule losses, i.e., they do not absorb, for frequencies up to that corresponding to the respective energy gap of the superconductor. For high-temperature superconductors, the gap frequency is within the far-infrared spectral range. Therefore, using such materials as reflectors of Fabry-Perot resonators is expected to lead to higher finesse values than those obtained with metal-mesh reflectors. But due to the fact that in thin superconducting film a certain fraction of the electrons remains in the normal state even at very low temperatures, some residual absorption is still present in superconducting Fabry-Perot resonators, too. However, as an additional bonus, by being more opaque at high frequencies than metallic meshes, high-temperature superconductors suppress the parasitic sensitivity to such high-frequency radiation [157].

Renk et al. [157] reported using high-temperature superconducting thin films as reflectors in Fabry-Perot resonators for the spectral range bound from above by 300 cm^{-1}. Their reflectors were $\mathrm{YBa_2Cu_3O_{7-\delta}}$ films of thickness 100 nm deposited on MgO substrates of thickness 1 mm, separated by a cavity of length[2] 44 μm. They obtained peak transmittance about 0.016 with a finesse F ca. 30 for the first-order resonance. The low value of the resonant transmittance is caused by using relatively thick $\mathrm{YBa_2Cu_3O_{7-\delta}}$ films.

Wiese et al. [168] used a resonator made of two different reflectors: a 50 nm-thick $\mathrm{YBa_2Cu_3O_{7-\delta}}$ film deposited on a 0.35 mm-thick MgO substrate, and a 70 nm-thick $\mathrm{YBa_2Cu_3O_{7-\delta}}$ film deposited on a 0.25 mm-thick MgO substrate. They reported peak transmittance about 0.16 and finesse F ca. 55 for the first-order resonance positioned ca. 80 cm^{-1}. This was a move in the right direction: the peak transmittance can be sufficiently high only when the $YBa_2Cu_3O_{7-\delta}$ films are thin enough, otherwise the above-mentioned residual absorption would waste a significant part of the incident infrared radiation. But using an asymmetric resonator is counter-productive as it lowers the transmittance.

---

[2] Herein, we prefer to use "thickness of the gap" rather than "cavity length".

Pechen et al. [169] used as reflectors 30 nm-thick $YBa_2Cu_3O_{7-\delta}$ films deposited on 0.5 mm-thick Si substrates. At 10 K, for the first-order resonance in the vicinity of 60 cm^{-1}, they measured peak transmittance about 0.6 and finesse F ca. 20. Their peak transmittance exceeded the accomplishments from the previous studies, but the resonance in the substrates lead to strong sidebands (in the preceding section I called them tertiary fringes) that overlap the main resonance peaks.

We used thinner Si substrates [120,37], which allowed us to separate the primary resonance from the minor fringes due to parasitic interference within the substrates.

8.4 Measured Fabry-Perot Transmittance

A cross-section of our early Fabry-Perot resonators is shown in Figure 8.1. For these earlier measurements of Fabry-Perot resonator we used as reflectors Samples NIST 255 and NIST 256. Their transmittance, front-side reflectance and back-side reflectance were presented in Chapter 6, and their front-side absorptance and back-side absorptance were covered in Chapter 7. The two films are held at a distance by means of a wafer-like spacer that determines the thickness of the vacuum cavity of the structure. Our Fabry-Perot resonator 1 had a copper-plate spacer of thickness 550 μm, whereas the Fabry-Perot resonator 2 had a polyimide-sheet spacer of thickness 132 μm. The thickness of the spacer was measured by a micrometer. The actual thickness of the cavity turned out to be slightly greater than that of the respective spacer. Our calculated spectra fit well to the measured ones if we assumed that the thickness of the cavity for Fabry-Perot resonator 1 was 555 μm, and the thickness of the cavity for Fabry-Perot resonator 2 was 139 μm (see next section).

For transmittance measurements we have used the sample-holder shown schematically in one of our papers [37, Fig. 2]. S-wise-curved beryllium copper strips were employed as springs that press the samples, with the spacer between them, to one of the two side plates of the sample-holder. Each of these copper springs was fastened with a tiny screw at a corner of the plate.

These earlier transmittance measurements were performed on our slow-scan Michelson interferometer within the spectral range from 10 to 90 cm^{-1}.

8.4.1 Fabry-Perot resonator 2

The measured transmittance through our Fabry-Perot resonator 2 (the one with polyimide spacer) is shown in Figure 8.3 (at three temperatures with YBCO in the normal state) and Figure 8.4 (at two temperatures with YBCO in the superconducting state).

The primary fringes of the transmittance i.e., the transmittance maxima due to the resonance within the vacuum cavity, are located at wave numbers $\breve{\nu}_m = m/(2d)$, where $m = 1, 2, \ldots$ is an integer counting the order of the fringes, and $d = 139$ μm is the vacuum-cavity thickness of the Fabry-Perot resonator 2.

From the latter equation we get that the first- and second-order primary transmittance resonances should be centered close to 36 cm^{-1} and 72 cm^{-1}, respectively. The actual resonance wave numbers may be slightly different due to a possible slight wave-number variation of the phase change ϕ_I (ϕ_{II}) upon reflection from reflector I (II), respectively, as was discussed in Section 3.5, but this wave-number shift should be negligible. By accident, for the case of our Fabry-Perot 2 resonator, the positions of the primary maxima (given above) happen to almost

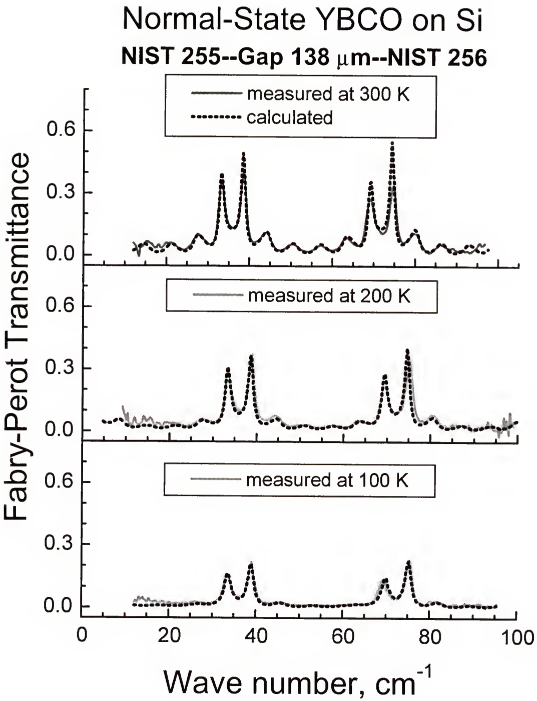

Figure 8.3: Transmittance through Fabry-Perot resonator 2, constructed from NIST 255 and NIST 256 separated by a polyimide spacer, at three temperatures with both $YBa_2Cu_3O_{7-\delta}$ layers in the normal state.

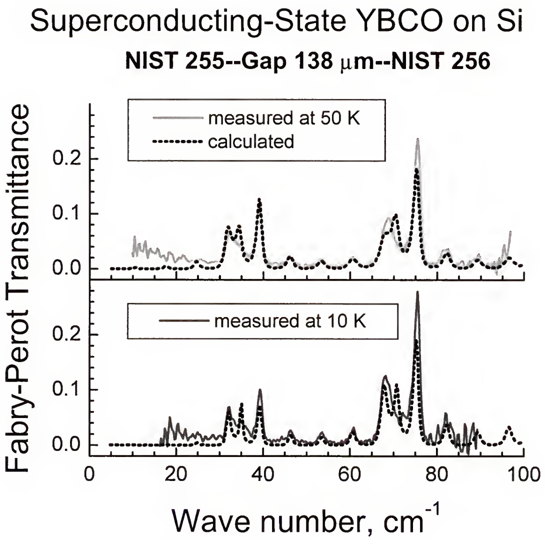

Figure 8.4: Transmittance through Fabry-Perot resonator 2, constructed from NIST 255 and NIST 256 separated by a polyimide spacer, at three temperatures with both $YBa_2Cu_3O_{7-\delta}$ layers in the superconducting state.

coincide with the positions of the minor minima. The fact, that at temperature 300 K and 200 K six minor fringes can be observed between the two major ones, is an indication that the minor fringes have approximately six times smaller free spectral range than the major ones. A similar relationship is also, very roughly speaking, true for the minor and major bandwidth. As a result the two major maxima that are observed in the studied spectral range are split into two almost equal halves (especially at room temperature) by the superimposed narrow, but deep, minor minima. In other words, the two major maxima are seen through the twin-peaked "template" of the two minor maxima that surround them almost symmetrically. Hence, the temperature behavior of the four highest maxima that were observed can be governed to some extent by a complex interplay between the major peaks and the minor valleys that overlay or surround those major peaks. This is due to the coupling between the major (cavity) resonance with the minor (substrate) one.

As the temperature is lowered, the frequencies of the primary transmittance peaks remain approximately constant—the thermal shrinking of the spacer is negligible within the covered temperature range. However, the minor free spectral range changes from ca. 6.0 cm^{-1} at 300 K and 200 K, to ca. 7.2 cm^{-1} at 100 K, 50 K, and 10 K. This can be seen easily if one notices that at the two higher temperatures there are six minor fringes between the two major ones, and at the three lower temperatures there are five minor fringes between the two major ones, respectively. At all temperatures, however two of the minor minima approximately coincide with the two major maxima within the covered spectral range. Namely, at the two higher temperatures the sixth and twelfth minor minima coincide with the major maxima at 36 and 72 cm^{-1}, whereas at the three lower temperatures the fifth and tenth minor minima coincide with the same major maxima at 36 and 72 cm^{-1}, respectively.

To a certain extent, the temperature dependence of the minor free spectral range can be explained by the temperature dependence of the optical thickness of Si (mainly due to its refractive index factor): it decreases slightly as temperature is lowered which causes the minor free spectral range to grow somewhat. The stepwise switch-over from six to five minor maxima is due to the interaction between the three components (two of which are almost degenerate due to the very similar thickness of the two Si substrates) of this compound resonator.[3]

Tiny temperature changes in the central frequency, bandwidth, and finesse of the minor fringes lead to the fact that as the temperature is lowered from 300 K to 200 K and 100 K, the minor minima split the major maxima in a less symmetrical way—the high-frequency "half" of a major peak becomes higher than its low-frequency "brother". This leads to small apparent shifts in the frequency of the major-maxima "halves".

To simplify our treatment, let us assume that the Fabry-Perot resonator is symmetric, i.e., that its two reflectors are identical. This allows us to drop the Roman subscripts I and II, and equations 3.200 and 3.201 are reduced, respectively, to

$$F = \pi R^{1/4} (1 - R)^{-1}, \tag{8.1}$$

$$\mathcal{T}_{res} = T^2 (1 - R)^{-2}. \tag{8.2}$$

Using the energy conservation relation

$$T + R + A = 1, \tag{8.3}$$

---

[3] This is in a way similar to the well-known effect of interaction between two atoms on their energy levels as from initial isolation (very far apart from each other) they are brought closer together.

where A is the absorptance of the $YBa_2Cu_3O_{7-\delta}$ film, equation 8.2 can be transformed into [170]

$$\mathcal{T}_{res} = (1 + A/T)^{-2}. \tag{8.4}$$

With the $YBa_2Cu_3O_{7-\delta}$ film in the normal state, the measured $\mathcal{T}_{res}$ decreases by a factor of two as the temperature is lowered from 300 to 100 K. At the same time, according to equation 8.4, the value of A/T increases. This is easy to understand: $YBa_2Cu_3O_{7-\delta}$ in its normal state behaves as a metal—lowering of the temperature leads to increasing of its electrical conductivity, and hence its reflectance will grow at the expense of its transmittance. The film-side absorptance remains roughly constant within the temperature range from 100 to 300 K (see Chapter 7: Figure 7.1 and Figure 7.12 in particular) [125]. Therefore, as the temperature is lowered, with the $YBa_2Cu_3O_{7-\delta}$ film still in the normal state, the resonant transmittance decreases and the finesse increases, i.e., the bandwidth decreases.

Increasing of the single-bounce reflectance from the $YBa_2Cu_3O_{7-\delta}$ film, with the single-bounce reflectance from the Si substrate remaining almost constant, leads to a decreasing effect of the minor resonance within the Si substrates. This results in a decreasing minor-fringe contrast upon lowering the temperature, with the $YBa_2Cu_3O_{7-\delta}$ film in the normal state.

When the $YBa_2Cu_3O_{7-\delta}$ film is in the superconducting state, its reflectance is even higher which leads to a further decrease in the minor fringe contrast. At lower frequencies, however, the transmittance of a single reflector is quite low (see Figures 6.19 and 6.26). Hence at these low frequencies and low temperatures, the first reflector does not feed enough of the incident radiation to the main (cavity) resonator. This explains why the first-order major maximum is lower than the second-order one.

Similarly, at high frequencies, the transmittance of a single reflector at 10 K is higher than that at 50 K (see Figures 6.19 and 6.26). Therefore, for these high frequencies, at 10 K the first reflector feeds more of the incident radiation to the main resonator than at 50 K. The latter explains why at the second-order major resonance (76 cm^{-1}) the resonant transmittance increases from 0.24 at 50 K to 0.28 at 10 K.

The normal-state and the superconducting-state optical properties of $YBa_2Cu_3O_{7-\delta}$ differ significantly. High-temperature superconducting materials, in their superconducting state are characterized by almost perfect reflection and very small absorption (due to the remaining normal electrons) for radiation at frequencies within their superconducting energy gap. Decreasing the temperature leads to an increase in the fraction of superconducting electrons, and, correspondingly, to a decrease in the far-infrared absorptance [25]. Therefore, the increase in the peak transmittance, as the temperature is lowered from 50 K to 10 K, can be explained by the lowering of the absorptance within the $YBa_2Cu_3O_{7-\delta}$ films.

Similarly to the normal state case, the reflectance increase as the temperature is lowered, leads correspondingly to a decrease of the bandwidth, and an increase of the finesse. The measured values for the finesse at 76 cm^{-1} are about 20 at 50 K and 23 at 10 K.

8.4.2 Fabry-Perot resonator 1

The measured transmittance through our Fabry-Perot resonator 1 (the one with the copper spacer) is shown in Figures 8.5 (at three temperatures with YBCO in the normal state) and 8.6 (at two temperatures with YBCO in the superconducting state).

The primary fringes of the transmittance i.e., the transmittance maxima due to the resonance within the vacuum cavity, are located at wave numbers $\breve{\nu}_m =$

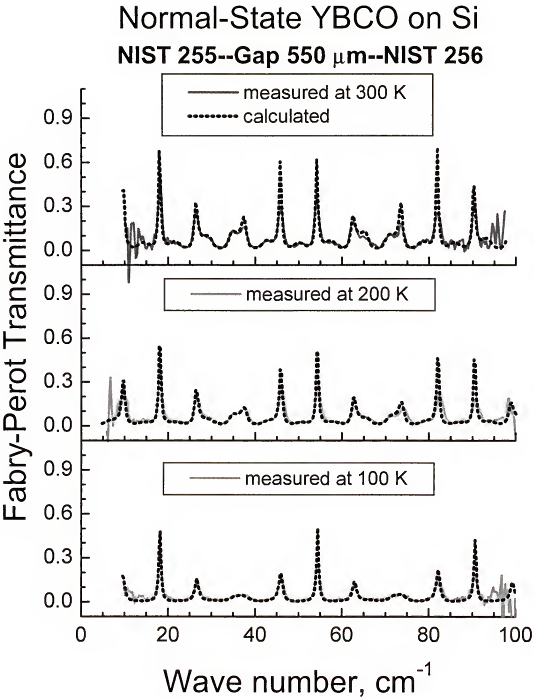

Figure 8.5: Transmittance through Fabry-Perot resonator 1, constructed from NIST 255 and NIST 256 separated by a copper spacer, at three temperatures with both $YBa_2Cu_3O_{7-\delta}$ layers in the normal state.

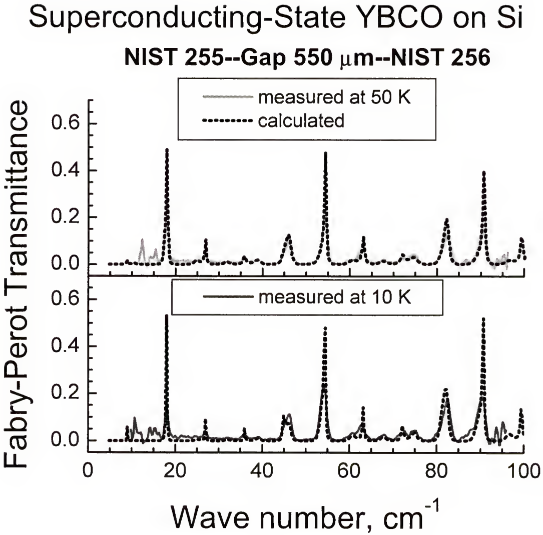

Figure 8.6: Transmittance through Fabry-Perot resonator 1, constructed from NIST 255 and NIST 256 separated by a polyimide spacer, at three temperatures with both $YBa_2Cu_3O_{7-\delta}$ layers in the superconducting state.

$m/(2d)$, where $m = 1, 2, \ldots$ is an integer counting the order of the fringes, and $d = 555$ μm is the vacuum-cavity thickness of the Fabry-Perot resonator 1. The major resonance peaks of the transmittance are centered at about 9 cm^{-1}, 18 cm^{-1}, 27 cm^{-1}, etc.

Some of the details about the transmittance of the Fabry-Perot resonator 2, described above, can be traced for the case of the Fabry-Perot resonator 1, too. However, Figures 8.5 and 8.6 are much more complicated and less illustrative than Figures 8.3 and 8.4, respectively, and the reason for that fact is the following: in the case of the Fabry-Perot resonator 1 the optical thickness of the Si substrates is comparable to the thickness of the cavity, which leads to comparable free spectral ranges: major (9 cm^{-1}) and minor (6 cm^{-1} at the two higher temperatures, or 5 cm^{-1} at the three lower temperatures). This leads to complicated Moiré patterns. One can imagine looking through two "combs"—one corresponding to the major fringes and another one for the minor fringes. The "combs" are characterized by similar constants and at least one of them is temperature dependent. Incidentally, the bandwidths of the major and minor fringes also happen to be comparable.

8.4.3 Fabry-Perot resonator 3

The transmittance through Fabry-Perot resonator 3 made with the two halves from Sample NIST 73 are shown herein. Since our second-generation sample holder failed, the transmittance is shown only for three temperatures in the normal state in Figure 8.7. As the temperature is lowered the free spectral range of the major maxima increases which is a clear tell-tale sign that the sample holder is not functioning as expected, but is rather slipping into the frozen O-ring.

8.5 Calculated Transmittance

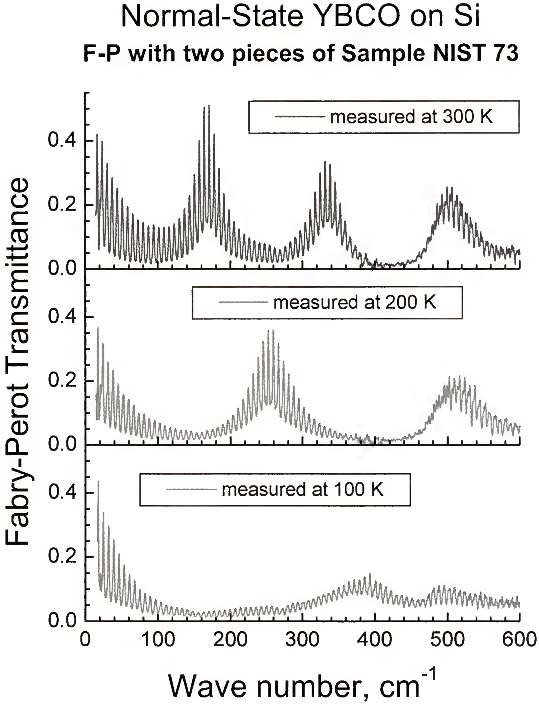

Figure 8.7: Transmittance through Fabry-Perot resonator 3 made from the two halves of Sample NIST 73 facing each other, at three temperatures in the normal state.

Compared to Experiment.

It was mentioned in Subsection 3.4.3 that there are several methods for calculating the optical properties of multi-layered structures. For our earlier measurements we assumed we are dealing with reflectors that have only two layers: a thin absorbing $YBa_2Cu_3O_{7-\delta}$ film deposited onto a thin (i.e., coherent), transparent Si substrate. To calculate the transmittance trough the Fabry-Perot resonator, we have used the same optical parameters of the $YBa_2Cu_3O_{7-\delta}$ film and Si substrate that were obtained from fitting the transmittance through, as well as the front-side and back-side reflectance from the single reflectors (see Table 6.21, or the more detailed Table 6.15 and Table 6.16). The only parameter that was varied this time was the thickness of the vacuum cavity d.

Kumar and Zhang [120,37] used the matrix method (Subsection 3.4.4, and in particular equation 3.195) to calculate, not only the transmittance and reflectance, but also the phase change ϕ_I upon reflection from reflector I. (The respective characteristics for reflector II are assumed to be similar, as all other properties for Samples NIST 255 and NIST 256 are). Their results for the transmittance and reflectance are practically indistinguishable from or very close to the fits that we have presented in Chapter 6, as can be expected, even though we have used a different approach. A plot of the phase change upon reflection from Sample NIST 255 can be found in our article [37, Figure 7] or in Kumar's dissertation [120, Figure 7.7]. Then Kumar substituted all calculated quantities into equations 3.197 and 3.196 (the latter equation can of course be substituted equivalently by equations 3.200–3.202). Finally, he varied the fitting parameter d which enters into the equations through the round-trip-within-the-substrate phase β.

Using the same (or very close) values of all parameters, I applied again our custom-software (program "flmfit") for fitting the optical properties of multi-layered structures. It is noteworthy, that Kumar and I, using two different methods of fitting the same experimental data, independently obtained very close results for the fit parameters and calculated spectra.

The fit parameters used for the two reflectors are slightly different even though Samples NIST 255 and NIST 256 are from the same batch. As explained in Chapter 6, this can be due to minor variations in the conditions within the deposition chamber, or post-deposition treatment of the samples. Such variations can affect the optical parameters of the samples, especially the fraction of superconducting electrons below the critical temperature T_c.

As mentioned in Chapter 6, we have assumed that the refractive index of Si depends only on the temperature. For the spectral range from 10 to 100 cm^{-1}, the refractive index of Si changes from 3.416 at 300 K to 3.387 at 10 K as obtained from fitting the interference fringes in the reflectance from a bare Si substrate (see Table 6.1). The Si substrate thickness is d_{Si} = 203.7 mm (205.3 mm) for Sample NIST 255 (NIST 256), respectively.

The temperature variation of the Si substrate thickness d_{Si} is within 0.024 % throughout the temperature range covered by us, and can therefore be neglected. The upper bound of the uncertainty for both the refractive index and the thickness of Si determined by us, is about 0.049 %. The surfaces are optically smooth—the root-mean-square roughness is only a few nanometers. Within the studied spectral range the wavelengths are longer than 100 μm for our earlier measurements, and longer than 16.(6) μm for our more recent measurements, respectively. Hence, the effect of surface roughness can also be neglected.

The transmittance of the Fabry-Perot resonator is very sensitive to the thickness of the cavity d. This allowed us to find that the actual thickness of the cavity differs slightly from the thickness of the spacer measured at room temperature by a micrometer. E.g., the thickness of the polyimide spacer from the micrometer was

132 μm, whereas by fitting of the transmittance through Fabry-Perot resonator 2 we determined that the cavity length is 139 μm at 300 K and 134 μm at 10 K. Most likely this small disagreement is due to inadequate pressure by the beryllium copper springs. This is tricky, as increasing the pressure might break easily the very thin samples we are using as reflectors. The temperature change of d can be attributed to thermal contraction of the polyimide film as the temperature is lowered.

Very important for Fabry-Perot resonators is to what a degree the two reflectors are parallel to each other. In our early measurements we relied only on a flat spacer and compression springs to ensure that the two reflectors are sufficiently parallel. At room temperature this produced good results. As the temperature is lowered, however, there is an increasing vertical temperature gradient along the sample holder. This may cause a slight deviation of the two reflectors from their optimum position and additionally it may compromise the mutually parallel alignment of the two films, which in turn leads to a significant reduction of the fringe contrast and the resonant transmittance.

Indeed, the laws that govern the interference within thin films are strictly applicable only to completely coherent cases. The effect of partial coherence on the optical properties of thin films have been studied by many researchers, e.g., Chen and Tien [171], and Anderson and Bayazitoglu [172]. Other reasons for reduced coherence can be the finite spectral resolution and beam divergence [150].

For the earlier measurements we did on our Michelson interferometer the frequency step between the data points was about 0.28 cm^{-1} and the spectral resolution was 0.56 cm^{-1}. The spatial incoherence, due to non-parallel reflectors and beam divergence, depends on frequency. Following Grossman and McDonald [173], we get for the frequency-dependent effective resolution in frequency ϵ_ω the following empirical relation

$$\epsilon_{\breve{\nu}} \;=\; \sqrt{0.56^2 \;+\; (0.02\breve{\nu})^2}. \tag{8.5}$$

The latter equation gives an effective resolution within the range from 0.6 to 2.1 cm^{-1} as the wave number $\breve{\nu}$ is varied within the spectral range from 10 to 100 cm^{-1}.

The calculated transmittance of the Fabry-Perot resonator agrees well with the measured one, except for the fact that the calculated transmittance always has a higher fringe contrast and peak transmittance (see Figure 8.3 and especially Figure 8.4, as well as Figure 8.5 and Figure 8.6). We attribute the discrepancy to spatial non-coherence which is discussed at the end of this section. Therefore, equation 8.5 can be used to improve the agreement between the measured and the calculated transmittance of the Fabry-Perot resonator. For this purpose, Kumar has averaged each point (at wave number $\breve{\nu}_P$) of the calculated transmittance within the spectral range from $(\breve{\nu}_P - \epsilon_{\breve{\nu}}/2)$ to $(\breve{\nu}_P + \epsilon_{\breve{\nu}}/2)$ cm^{-1} [120].

As an example, Figure 4 from our paper (Kumar et al. [37]) allows one to compare the calculated and measured transmittance after the effect of partial coherence has been taken into account, for the highest and lowest temperatures at which measurements were done on Fabry-Perot resonator 2. One can see that the agreement is very good with a couple of exceptions at 10 K, in the vicinity of the two major maxima (within the spectral ranges from 30 to 37 cm^{-1} and from 65 to 72 cm^{-1}).

The respective information about Fabry-Perot resonator 1 is presented in Figure 5 in our paper [37].

An easier way to account for the effect of partial coherence is to average several curves calculated with thickness of the cavity varied in a narrow range about its optimum value. The effect of partial coherence is illustrated in Figure 6 from our paper [37], where the calculated transmittance is shown for both the perfectly coherent (no averaging), and partially coherent (with averaging) cases. The effect of partial coherence is especially large for very sharp (small bandwidth, high resonant transmittance) peaks. The spectral weight is preserved: the peaks that are lower due to partial coherence are also wider.

A possibility to fine-tune the parallel alignment after the samples have settled at any desired temperature, just before starting the measurement, is highly desirable for the future experiments. In my opinion the spectral resolution we used is adequate.

8.6 Discussion

8.6.1 Coupling of Simple Resonators into a Compound One

As hinted earlier, our Fabry-Perot resonator is actually comprised of three coupled resonators: the cavity resonator is surrounded by the two Si-substrate resonators. The latter two are degenerate, provided the two substrates are identically similar to each other. Treating the two degenerate resonators as one, we can reduce the total number of different resonators to be considered to two. Each of them, taken separately, is a rather simple version of the original resonator of Fabry and Perot. However, they are coupled through the $YBa_2Cu_3O_{7-\delta}$ film, which complicates the picture significantly.

For simplicity, let us initially assume that the resonators are coupled directly, that is the compound resonator is formed by two bare Si plates (without the $YBa_2Cu_3O_{7-\delta}$ films) with a cavity between them. The transmittance through such a structure can easily be visualized as the Moiré pattern that would be produced by overlaying of two "combs", each with a "tooth" period that is inversely proportional to the thickness of the respective simple resonator. In this analogy the transmittance will be described by the product of the "tooth"-heights of the overlapping portions of the two "combs", i.e., the portions of the back "comb" which are hidden by the front "comb".

Now let us phase in the $YBa_2Cu_3O_{7-\delta}$ layers. The problem is that they are characterized by a complex refractive index. If the radiation resonated within one of the simple resonators everything would be almost as if the $YBa_2Cu_3O_{7-\delta}$ layers were still absent. Their only effect would be a change of the single-bounce reflectance for the two interfaces Si-$YBa_2Cu_3O_{7-\delta}$ which would lead to shortening the "teeth" of the "comb" corresponding to the respective substrate, due to the increased effect of the cavity resonance (both of its reflectors increased their single-bounce reflectance whereas only one side of the substrate resonator did so). However, since the $YBa_2Cu_3O_{7-\delta}$ films are so thin that they are not completely opaque, a certain fraction of the far-infrared radiation leaks through, thus coupling the cavity and substrate resonators. Every time this happens, the radiation that is leaking through picks up some complex phase change, which depends on both the frequency and the temperature. This coupling-by-leakage effect is responsible for the complicated pattern of the transmittance through the compound Fabry-Perot resonator, and its temperature dependence. The imaginary part of the phase is simply related to the attenuation due to absorption within the $YBa_2Cu_3O_{7-\delta}$ film. Because the films are very thin, and also because only a small percentage of the radiation leaks through to couple the simple resonators into a compound one, the attenuation is relatively small and as a first approximation can be neglected.

8.6.2 Partial Fabry-Perot Resonators

In this subsection the contribution of the various components of our compound[4] Fabry-Perot resonator 2 (Si 255–YBCO 255–Gap–YBCO 256–Si 256) will be studied by considering calculations for imaginable model multi-layered structures including only certain elements of the complete compound Fabry-Perot resonator. I have tentatively called such imaginable structures "partial Fabry-Perot resonators". Some of these structures can be realized in a straightforward manner, others, e.g., those that contain one or more free-standing $YBa_2Cu_3O_{7-\delta}$ layer/s, can only be imagined, or at least can be extremely hard to produce using the current state-of-the-art techniques for sample preparation.

At room temperature, the calculated transmittance through various imaginable structures is compared to the calculated—to avoid fluctuation due to experimental uncertainties—transmittance through our Fabry-Perot 2 resonator (the one with the polyimide spacer) in Figure 8.8 (two symmetric and one asymmetric three-layered structures) and Figure 8.9 (several other asymmetric four- or three-layered structures).

The transmittance through two free-standing $YBa_2Cu_3O_{7-\delta}$ films—equivalent to the $YBa_2Cu_3O_{7-\delta}$ films of Samples NIST 255 and NIST 256, respectively—separated by a gap is shown on the middle panel of Figure 8.8. The slight asymmetry due to the small difference between the two films is not essential in this case. That is, the three structures YBCO 255–Gap–YBCO 256, YBCO 255–Gap–YBCO 255, and YBCO 256–Gap–YBCO 256 would have virtually the same transmittance.

The transmittance spectrum through a plain silicon plate oscillates with the wave number between 0.29 and 1.00, whereas the reflectance spectrum oscillates

---

[4] Here Sample NIST 255 (NIST 256) is represented by its two most essential layers Si 255 (Si 256) and YBCO 255 (YBCO 256), respectively.

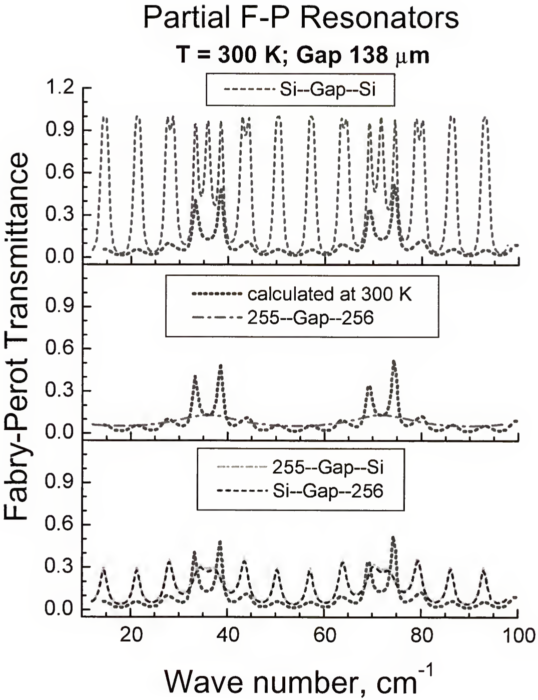

Figure 8.8: Calculated Transmittance through various three-layered partial Fabry-Perot resonators juxtaposed with the calculated transmittance through Fabry-Perot resonator 2 at room temperature.

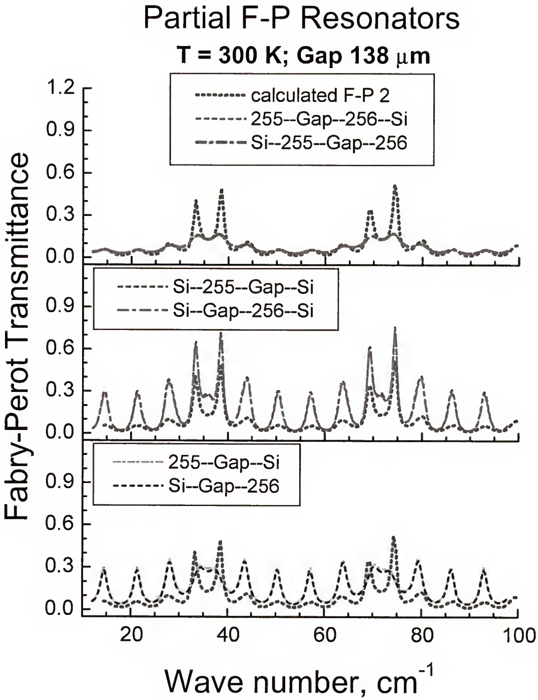

Figure 8.9: Calculated Transmittance through various four- and three-layered partial Fabry-Perot resonators juxtaposed with the calculated transmittance through Fabry-Perot resonator 2 at room temperature.

between 0.00 and 0.71. Combining these two ranges, one might expect that the transmittance through a Fabry-Perot resonator with two naked Si plates might oscillate between zero and one. However, the calculated transmittance through two plain silicon plates separated by a gap (Si 255–Gap–Si 256) is shown on the top panel of Figure 8.8. The minima are as if "riding" on top of the wavy line (the calculated transmittance for an imaginary Fabry-Perot resonator consisting only of two free standing film with a gap between them) shown in the middle panel of the same Figure. In principle the maxima should also ride on a similar wavy line shifted higher from the bottom envelope by 1.00. However, the transmittance cannot exceed one, and so the portions of peaks that would have to rise above one, actually get "folded" or "inverted" upside down. Furthermore, the two major maxima which should be highest, are not "folded" just once, but are doubly "folded".

The bottom panel of Figure 8.8 shows the transmittance through the asymmetric three-layered structures YBCO 255–Gap–Si 256 and Si 255–Gap–YBCO 256. The respective two curves are close to each other, but do not overlap completely. Most of the difference is due to the slight difference between the two films YBCO 255 and YBCO 256. Only a negligible fraction of that difference can be attributed to the slight difference of the thickness of the two Si plates. That is, the structures YBCO 255–Gap–Si 255 and Si 255–Gap–YBCO 256, or YBCO 255–Gap–Si 256 and Si 256–Gap–YBCO 256 would produce virtually the same graph as the bottom panel of Figure 8.8. Away from the major maxima one can clearly see the fringes due to the Si substrate, but because only one Si plate is present rather than two the amplitude should be halved compared to the top panel if it were not for the attenuation caused by the YBCO absorption. In the vicinity of the major maxima two of the silicon fringes almost coalesce due to the interaction between the gap resonance and the Si resonance. The bottom envelope is similar to the wavy line from the middle panel which is governed by the gap resonance.

The top panel of Figure 8.9 shows two resonators which differ from those on the bottom panel of Figure 8.8 by the YBCO layer deposited on the Si plate. From another perspective, starting from the complete Fabry-Perot resonator 2, only one Si plate has been eliminated. With two YBCO layers in each of those two resonators the amplitude of the Si resonances is reduced further. Because of the significantly decreased amplitude of the Si resonances, their interaction with the gap resonances is indiscernible. Both the top and bottom envelopes are similar to the wavy line from the middle panel of Figure 8.8 which is governed by the gap resonance.

The bottom panel of Figure 8.9 is just a repetition of the bottom panel Figure 8.8, and is filling the empty spot for easier comparison.

The middle panel of Figure 8.9 shows two resonators which differ from those on the bottom panel of either Figure 8.8, or Figure 8.9 by the Si plate added to support the previously free-standing YBCO. Or, starting from the complete Fabry-Perot resonator 2, only one YBCO film has been eliminated. With two Si plates in each of those two resonators and only one absorbing YBCO film, the amplitude of the Si resonances is second highest after the Si only resonator from the top panel of Figure 8.8. Because of the significantly increased amplitude of the Si resonances, their interaction with the gap resonances is significant and has resulted in the appearance of ghost maximum at the position of the gap maximum. This ghost maximum is actually the sum of the tails of the two adjacent Si maxima whose form has been modified by the interaction with the gap resonance. Unexpectedly, though only one YBCO reflector stands by the gap, the gap resonance is very pronounced, and is even stronger than that for the complete Fabry-Perot resonator 2. In the vicinity of the major minima the both the top and bottom envelopes are similar to the wavy line from the middle panel of Figure 8.8 which is governed by the gap resonance, but in the vicinity of the major maxima both envelopes are pushed up due to the much stronger gap resonance here.

We believe that a Fabry-Perot resonator formed by deposition of YBCO films onto both sides of a Si plate can be benefitial for applications where stable, pre-tuned resonators or comb filters are needed. We expect such a structure to have relatively suppressed Si fringes, and enhanced gap fringes in comparison with the complete Fabry-Perot resonator 2 that has additionally a second Si plate and a vacuum gap.

8.6.3 Optimization of the Resonant Transmittance

The transmittance of any Fabry-Perot resonator depends strongly on its reflectors, which can be seen directly from equation 3.201 or 8.2. Examination of these equations shows that the resonant transmittance of the compound resonator depends only on the reflectance and transmittance of the two reflectors, but not on the cavity thickness.

Kumar [37,120] has shown how to optimize the maximum transmittance for a particular maximum. This in fact accomplishes selective, that is, incommensurate tuning of a Fabry-Perot resonator. It can be beneficial for selective detectors whose design is optimized for a narrow spectral range.

8.6.4 The Effect of the Vacuum-Gap Thickness

By setting the thickness of the gap to such values that the optical thickness of the Si substrates and the gap are commensurate, one can obtain variously tuned comb filters as well. To illustrate this fact, the calculated transmittance through a number of commensurately tuned Fabry-Perot resonators at room temperature is presented in Figures 8.10–8.19. In the figure captions the respective ratio

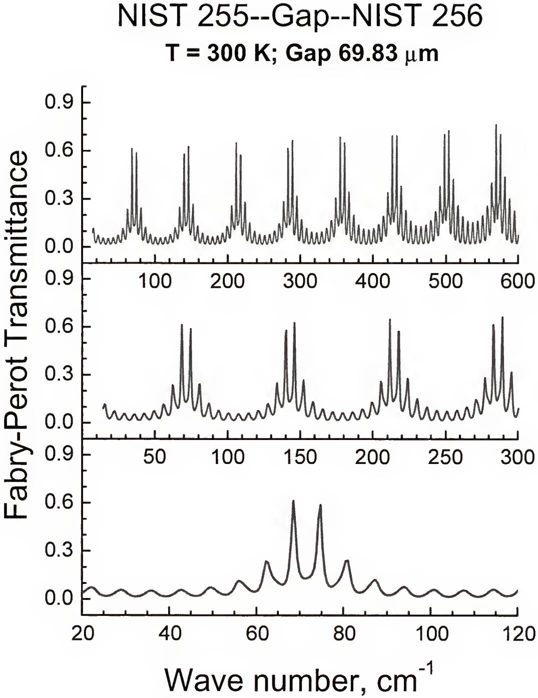

Figure 8.10: Calculated Transmittance through a Fabry-Perot resonator, constructed from NIST 255 and NIST 256 separated by a gap of thickness $d = 69.83\ \mu\text{m}$ (ratio 1:10).

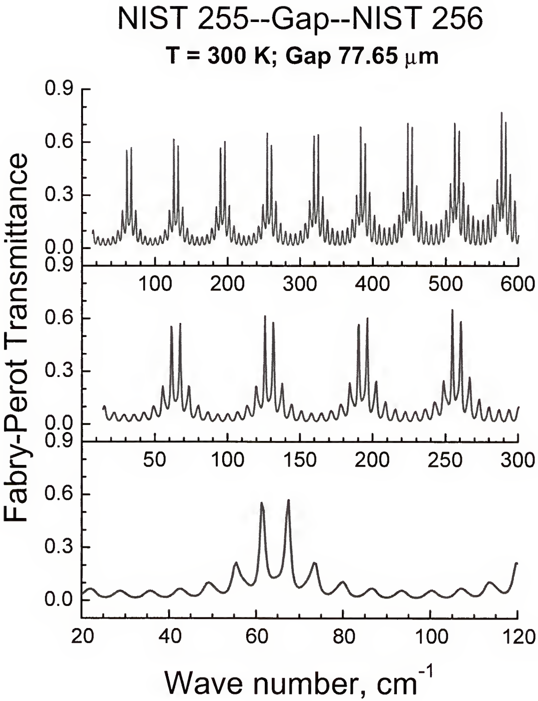

Figure 8.11: Calculated Transmittance through a Fabry-Perot resonator, constructed from NIST 255 and NIST 256 separated by a gap of thickness $d = 77.65\ \mu$m. (ratio 1:9)

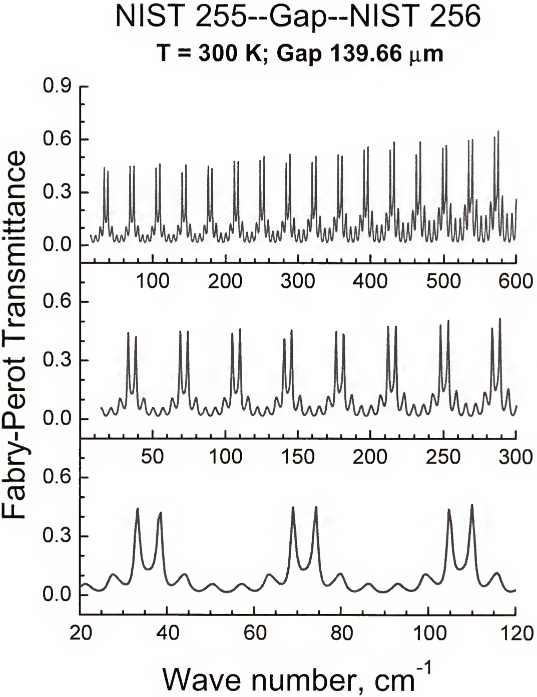

Figure 8.12: Calculated Transmittance through a Fabry-Perot resonator, constructed from NIST 255 and NIST 256 separated by a gap of thickness $d = 139.66\ \mu m$. (ratio 1:5)

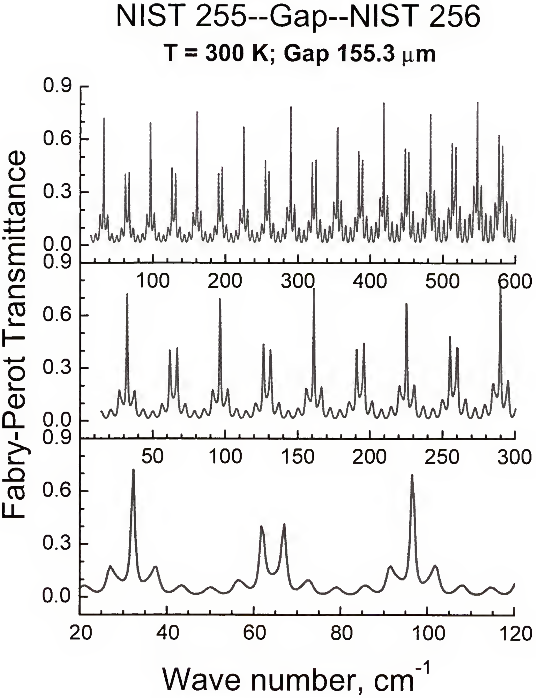

Figure 8.13: Calculated Transmittance through a Fabry-Perot resonator, constructed from NIST 255 and NIST 256 separated by a gap of thickness d = 155.30 μm. (ratio 2:9)

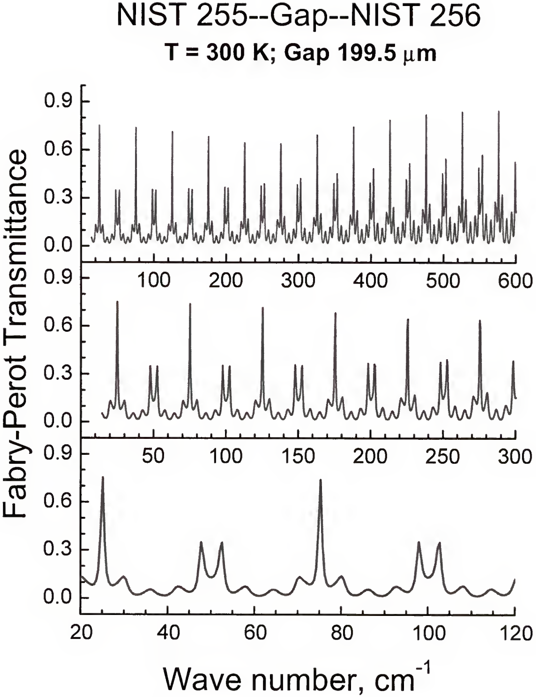

Figure 8.14: Calculated Transmittance through a Fabry-Perot resonator, constructed from NIST 255 and NIST 256 separated by a gap of thickness $d = 199.50\ \mu m$. (ratio 2:7)

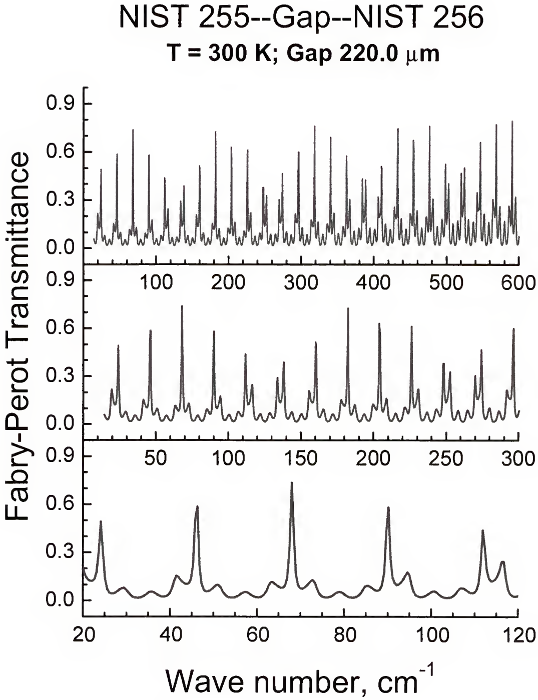

Figure 8.15: Calculated Transmittance through a Fabry-Perot resonator, constructed from NIST 255 and NIST 256 separated by a gap of thickness d = 220.00 μm. (ratio 6:19)

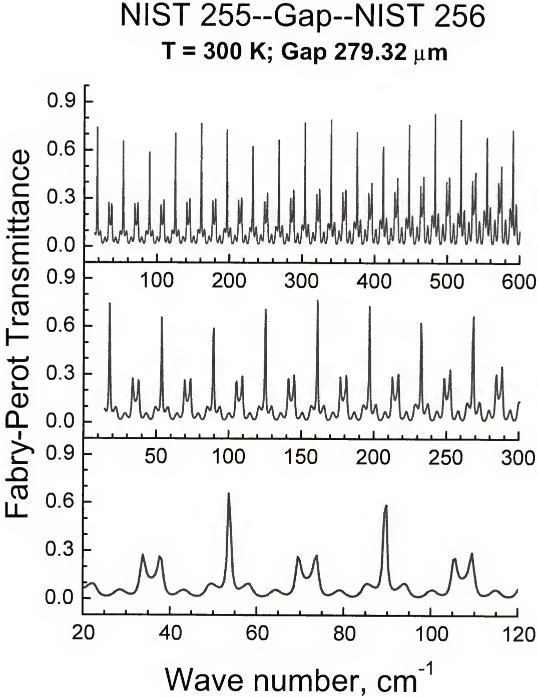

Figure 8.16: Calculated Transmittance through a Fabry-Perot resonator, constructed from NIST 255 and NIST 256 separated by a gap of thickness $d = 279.32\ \mu m$. (ratio 2:5)

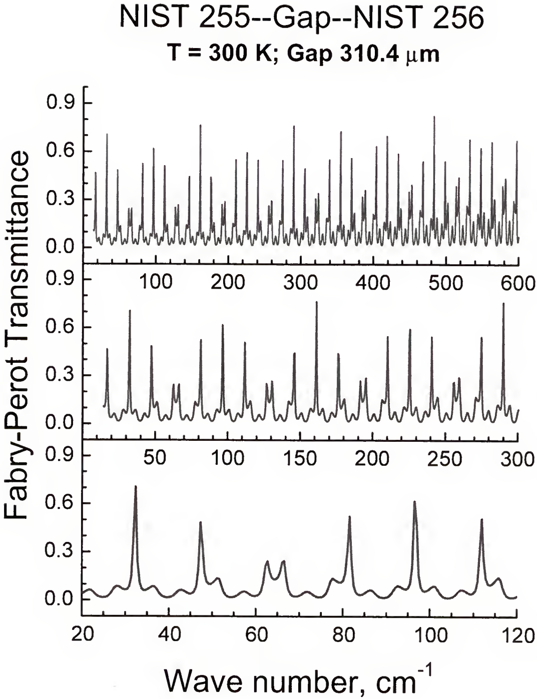

Figure 8.17: Calculated Transmittance through a Fabry-Perot resonator, constructed from NIST 255 and NIST 256 separated by a gap of thickness d = 310.40 μm. (ratio 4:9)

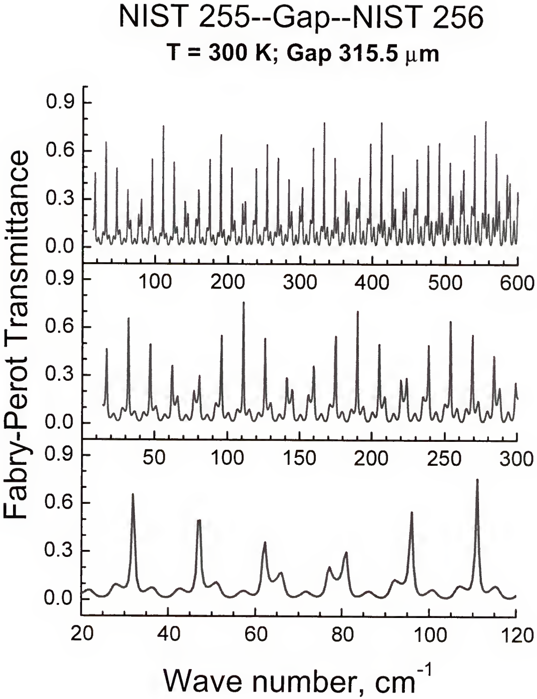

Figure 8.18: Calculated Transmittance through a Fabry-Perot resonator, constructed from NIST 255 and NIST 256 separated by a gap of thickness $d = 315.50\ \mu\text{m}$. (ratio 2:11)

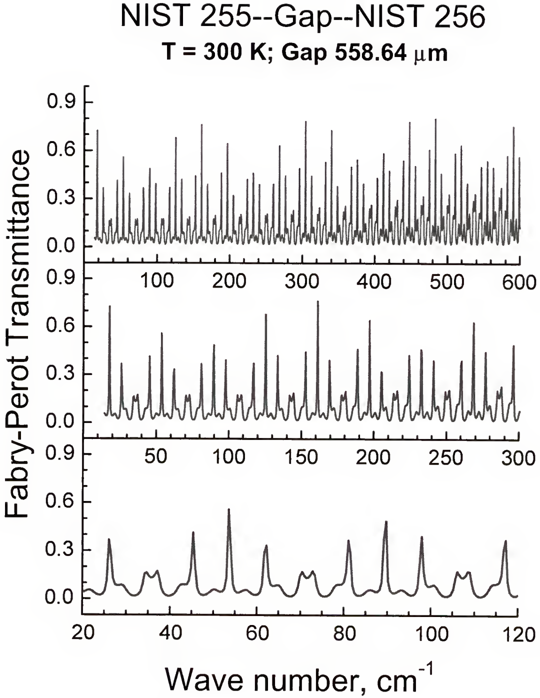

Figure 8.19: Calculated Transmittance through a Fabry-Perot resonator, constructed from NIST 255 and NIST 256 separated by a gap of thickness $d = 558.64\ \mu$m. (ratio 4:5)

of the optical thickness of the Si substrate to the vacuum-gap thickness is given. Starting with these ratios and the respective thicknesses of the gap, one has another way to determine the optical thickness of the Si substrate. Indeed from the last figure we have $d_{Si}(300\text{ K}) = 5\,d\,/\,(4\,n_{Si})(300\text{ K}) = 5 \times 558.64\ \mu\text{m}\,/\,(4 \times 3.4161) = 204.41 \pm 0.05\ \mu\text{m}$ which agrees very well with the average of the thickness of both Si substrates given in Table 6.21: $(203.7 + 205.3)\ \mu\text{m}\,/\,2 = 204.5 \pm 0.14\ \mu\text{m}$.

In order to facilitate the observation of large-, intermediate- and small-scale variation, the transmittance is depicted in three wave number scales at a ratio of 6:3:1. It must be noted that these curves are idealized, as they are extrapolated outside the 10-90-cm^{-1}-range in which Samples NIST 255 and NIST 256 were measured. Thus they do not take into account the mid-infrared and phonon bands of YBCO or the YSZ layer. It is interesting to note that in some cases a comb filter which on a large scale is clearly commensurately tuned, may seem selectively tuned on a small scale.

Comb filters with high-temperature-superconducting thin films may find interesting applications in the telecommunications industry or for aerospace and defense purposes.

In the next edition of this dissertation there will be transmittance spectra through more realistic comb filters based on the parameters determined for Samples NIST 73 and NIST 74.

8.6.5 The Effect of the $YBa_2Cu_3O_{7-\delta}$ Film Thickness

Naturally, the thickness of the YBCO film affects all characteristics of the reflector of the Fabry-Perot resonators, including the transmittance, front-side reflectanceand back-side reflectance, as well as the front-side absorptance and back-side absorptance. And in turn, all of these characteristics determine the properties of the entire composite Fabry-Perot resonator, and especially its modulated comb-like transmittance. As the YBCO film gets thicker, clearly the transmittance of the individual reflector and thereby of the entire resonator will decrease. As a result the resonant (peak) transmittance, given by equation 3.201 (or equation 8.2 for the symmetric case), will decrease, too.

On the other hand, as the YBCO film thickness grows the reflectance of the samples used as reflectors will increase, too, which will result in significant improvement of the finesse given by equation 3.198.

The above expectations were confirmed by calculations with the "flmfit" program in which the thickness of the YBCO film was varied either symmetrically (on both reflectors), or asymmetrically (on either one of the two reflectors). As seen from the first of the several considered fractional Fabry-Perot resonators, with zero thickness of the YBCO film the peak transmittance is so high that it gets "folded". The peak transmittance starts to decrease as soon as an YBCO is added and gradually decreases further as the film grows in thickness.

As the thickness increases, however, the Si resonance is gradually suppressed and looses its importance. Simultaneously, the bandwidth of the major (gap resonance) maxima decreases faster than the resonant transmittance, and as a result the finesse grows.

Therefore, one must be content with some trade-off and be ready to compromise on a case-by-case basis, depending on which is more important for a particular application of a Fabry-Perot resonator: higher resonant transmittance or better finesse and selectivity. Generally, in order to obtain a resonator with transmittance that is sufficiently high, the thickness of the YBCO film should be 50 nm or less. And in order to get a finesse that is sufficiently high, the thickness of the YBCO film must be 20 nm or more. We found that 35 nm is a reasonable compromise for our purposes.

Another factor that is important for the operational performance of the Fabry-Perot resonators is the quality of the superconducting film: improved quality of the film would lead to increased fraction of superconducting carriers at low temperatures which in turn will lead to a reduced residual absorption and therefore increased reflectance in the superconducting state at low wave numbers. As a result both the peak transmittance and the finesse will be improved.

CHAPTER 9
CONCLUSION

In this dissertation far-infrared spectra of $YBa_2Cu_3O_{7-\delta}$ films deposited on Si substrates have been measured at several temperatures between 10 K and 300 K and the results have been analyzed. Our earlier measurements were within the spectral range from 10 to 90 cm^{-1}, whereas the more recent studies covered a wider range: from 20 to 600 cm^{-1}. Transmittance, front-side and back-side reflectance were measured on a number of samples. The transmittance and the respective reflectance data were combined to obtain the front-side and back-side absorptance of the films. The analysis of the data allowed us to reach some conclusions important for potential applications.

The values for the back-side reflectance and absorptance of multi-layered structure with more than one layer, can be much different from the respective values when the incidence is on the front-side. The measured higher back-side reflectance and absorptance from the samples have demonstrated that such a configuration could be implemented in far-infrared intensity modulators and bolometers.

The transmittance and reflectance of the samples are characterized by fringes due to multiple-beam interference within the silicon substrate. As the temperature is lowered, the DC conductivity of the $YBa_2Cu_3O_{7-\delta}$ film increases, and the modulus of the low-frequency reflection coefficient at the film–substrate interface approaches unity. This is the major reason for the temperature variation of the interference pattern.

When the wave impedance of the $YBa_2Cu_3O_{7-\delta}$ film is appropriately matched with the wave impedance of the Si substrate the latter will act as an antireflective coating for the film. Under such conditions the substrate resonance is suppressed and therefore the fringe contrast of the measured reflectance and transmittance either vanishes or is strongly reduced. At the central frequency of the spectral range where antireflective effect is present, the reflection coefficient of the film-substrate interface changes its sign which results in a phase change by π rad. This effect can be seen clearly in the interference pattern.

Conversely, at low temperatures, for those spectral ranges where the antireflection condition is not met, the transmittance maxima are higher. Indeed, in the superconducting state the film acts as a reflective coating for the Si substrate, leading to an increased resonance due to multiple-beam interference within the substrate. The back-side reflectance is also strongly increased when the film undergoes the superconducting phase transition. These observations have demonstrated that cuprate thin films on transparent substrates can be applied in the design of far-infrared devices, e.g., resonators and modulators.

The transmittance and reflectance data can be fit by using the Drude–Lorentz model for the film in the normal state, and the two-fluid model for the film in the superconducting state. The Si substrate is modeled by a real refractive index with a slight temperature dependence. The negligible spectral dependence of the refractive index of Si has been ignored. For our more recent measurements, which covered a wider spectral range, and were done on samples with a much thicker YSZ buffer layer, we have included phonons of the thin SiO_2 layer on the back-side of the substrate, as well as in the YSZ layer. The calculated spectra match well the measured data. Using the fit parameters, we have calculated the spectral dependence of the complex refractive index, conductivity, and permittivity for the $YBa_2Cu_3O_{7-\delta}$ films at various temperatures. As the superconducting phase transition occurs, the refractive index (real part) becomes small with respect to unity, whereas the extinction (imaginary part) increases and is frequency dependent. Respective changes are manifested in the other characteristics which are equivalent, that is, contain the same amount of information, sometimes in a more convenient format. In the spectral range above 100 cm^{-1}some phonon oscillators and mid-infrared bands become important and leave their signature on the on the studied optical characteristics The knowledge about the optical characteristics such as the refractive index, conductivity, and permittivity of YBCO films obtained from this study can prove to be important for the design of promising devices using HTSC thin films.

The measured or calculated transmittance and front-side or back-side reflectance have been used to obtain the measured or calculated front-side or back-side reflectance and absorptance. The back-side absorptance exceeds the front-side absorptance. Our calculations have shown that the absorptance depends strongly on the thickness of the $YBa_2Cu_3O_{7-\delta}$ film. At an optimum film thickness the absorptance of the sample reaches its local maximum, which is exceeded above 500 nm. Films that are so thick are not very interesting whenever some transmittance is desirable, but can be applied for detectors. The optimum thickness of the film is different for front-side and back-side incidence. At the central frequencies of the fringes, the optimized back-side absorptance can exceed 0.9. We believe our data and analysis of the absorptance will be useful for designers of far-infrared detectors using $YBa_2Cu_3O_{7-\delta}$ films.

Cuprate thin films deposited on transparent substrates outperform metallic meshes as reflectors for resonators, especially in the far-infrared region. Due to Joule losses, metallic meshes absorb radiation which limits the finesse of the the resonators. Ideally, reflectors in the superconducting state should not have losses within the frequency range bound from above by the superconducting gap which is in the far-infrared spectral range. In reality such reflectors are characterized by some residual losses due to carriers that have not condensed into Cooper pairs. But these residual losses are much lower than the Joule losses of metallic meshes.

We made Fabry-Perot resonators from two samples facing each other and separated by a spacer. The measured transmittance spectra through these resonators have proven that similar high-temperature superconducting films deposited on Si substrate (that do not absorb in the far-infrared) could be used to design resonators characterized by high finesse and high resonant transmittance in the far-infrared spectral range.

The thin substrates of our samples have allowed us to make resonators characterized by a higher resonant transmittance than previous attempts and at the same time to keep the finesse sufficiently high. In the normal state the resonant transmittance increases with temperature, whereas in the superconducting state the resonant transmittance decreases with temperature, i.e., it is high at very low temperatures. The calculated transmittance of the Fabry-Perot resonators agrees well with the measured transmittance. The agreement is improved further if we take into account partial coherence.

Optimization procedures for the resonators have been described. The transmittance of the resonator can be affected strongly by any of the layers of the total resonator structure. The resonant transmittance can be maximized if the cavity resonance is tuned to coincide with one of the substrate resonances (incommensurate tuning suitable for selective detectors). If commensurate tuning (suitable for comb filters) is desired, one would get periodically coincident resonances. In the resonator design one must make a compromise: a thicker $YBa_2Cu_3O_{7-\delta}$ film would increase the finesse at the expense of a decreased resonant transmittance. Our studies have proven that $YBa_2Cu_3O_{7-\delta}$ thin films on relatively thin Si substrates can be implemented in the design of far-infrared Fabry-Perot resonators.

Naturally, we expect that as time goes by the film deposition techniques will evolve further to allow fabrication of uniform cuprate thin films of a higher quality and with reproducible characteristics. A higher-quality film would have a lower residual absorption in the superconducting state which would improve the performance of the resonator. If the relatively uniform spot of the sample has an area that is large enough, a most symmetrical Fabry-Perot resonator can be obtained by breaking the sample into two pieces which can be used as the two reflectors of the resonator.

In our measurements we have used two generations of resonator sample holders. In the first-generation the resonator gap was determined by a suitable spacer. The second generation was meant to allow alignment during measurements in vacuum at low temperature. Unfortunately this sample holder turned out to be unsuccessful. Based on the accumulated knowledge, we designed a third-generation resonator sample holder in which the negative sides of the previous generations have been eliminated. This sample-holder enables alignment during experiments which allows one to keep the two reflectors strictly parallel to each other at any temperature. Thus, we hope to overcome the negative effects of temperature gradients causing thermal stress and leading to misalignment of the two reflectors. This sample-holder will be used by the next student that will continue work on the project.

Furthermore, if no tuning during operation is desired, in principle it is possible to produce resonators by depositing buffer layers and films on both sides of the substrate. In this case the Si substrate acts as the resonator cavity. Naturally, once the thickness of the substrate has been chosen, the tuning of the resonator has been fixed to a periodical set of frequencies.

For any future work on a similar project, it is recommended to use a mechanism that will improve the alignment between the two reflectors and that will allow tuning of the cavity thickness during measurement. A high spectral resolution should also be used to discern sharp transmittance peaks.

For a better description of the superconducting state, I'd recommend to the next students working on similar projects: after quick measurements for selecting good samples, to do a detailed measurement at the lowest temperature (usually 10 K), and then at $T_c/2$, $3T_c/4$, $7T_c/8$, T_c, and 3 temperatures in the normal state (for $YBa_2Cu_3O_{7-\delta}$ these can be 100, 200, and 300 K).

REFERENCES

[1] C. P. Poole, Jr., H. A. Farach, and R. J. Creswick, *Superconductivity* (Academic Press, San Diego, CA, 1996).

[2] L. D. Landau and E. M. Lifshitz, *The Classical Theory of Fields*, Vol. 2 of *Course of Theoretical Physics* (Butterworth-Heinemann, Woburn, MA, 1997).

[3] J. A. Stratton, *Electromagnetic Theory* (McGraw-Hill, New York, NY, 1941).

[4] L. D. Landau and E. M. Lipshitz, *Electrodynamics of Continuous Media*, Vol. 8 of *Course of Theoretical Physics* (Butterworth-Heinemann, Woburn, MA, 1996).

[5] M. Born and E. Wolf, *Principles of Optics*, seventh ed. (Cambridge University Press, Cambridge, UK, 1999).

[6] J. D. Jackson, *Classical Electrodynamics*, 3rd ed. (John Wiley & Sons, New York, NY, 1998).

[7] D. J. Griffiths, *Introduction to Electrodynamics*, 3rd ed. (Prentice Hall, Englewood Cliffs, NJ, 1998).

[8] J. F. James, *A Student's Guide to Fourier Transforms* (Cambridge University Press, Cambridge, UK, 1995).

[9] M. K. Barnoski, *Introduction to Integrated Optics* (Plenum Press, New York, NY, 1974).

[10] A. N. Matveev, *Optics* (Mir Publishers, Moscow, Russia, 1988).

[11] G. Burns, *Solid State Physics* (Academic Press, San Diego, CA, 1990).

[12] P. Diament, *Wave Transmission and Fiber Optics* (Macmillan Publishing Company, New York, NY, 1990).

[13] N. W. Ashcroft and N. D. Mermin, *Solid State Physics* (Saunders College Publishing, Fort Worth, TX, 1976).

[14] *Academic Press Dictionary of Science and Technology*, edited by C. Morris (Academic Press, San Diego, CA, 1992).

[15] *Fizicheskiy Entsiklopedicheskiy Slovar' (Physics Encyclopaedic Dictionary)*, edited by A. M. Prohorov (Sovetskaya Encyclopedia, Moscow, Russia, 1983), (In Russian).

[16] H. C. Ohanian, *Physics*, 2nd ed. (W.W. Norton & Company, New York, NY, 1989).

[17] F. Wooten, *Optical Properties of Solids* (Academic Press, New York, NY, 1972).

[18] P. Yeh, *Optical Waves in Layered Media*, *Wiley Series in Pure and Applied Optics* (John Wiley & Sons, New York, NY, 1988).

[19] P. Drude, Ann. d. Physik **1**, 566 (1900).

[20] P. Drude, Ann. d. Physik **3**, 369 (1900).

[21] J. M. Ziman, *Principles of the Theory of Solids*, 2nd ed. (Cambridge University Press, New York, NY, 1979).

[22] H. Haug and S. W. Koch, *Quantum Theory of the Optical and Electronic Properties of Semiconductors*, 3rd ed. (World Scientific, Singapore, 1991).

[23] D. B. Tanner and T. Timusk, in *Physical Properties of High Temperature Superconductors I*, edited by D. M. Ginsberg (World Scientific, Singapore, 1989), Chap. 7, pp. 341–407.

[24] E. Hagen and H. Rubens, Ann. d. Physik **11**, 873 (1903).

[25] D. B. Tanner and T. Timusk, in *Physical Properties of High Temperature Superconductors III*, edited by D. M. Ginsberg (World Scientific, Singapore, 1992), Chap. 5, pp. 363–469.

[26] C. Kittel, *Introduction to Solid State Physics*, seventh ed. (John Wiley & Sons, New York, NY, 1996).

[27] G. B. Arfken and H. Weber, *Mathematical Methods for Physicists*, fifth ed. (Academic Press, Cambridge, UK, 2000).

[28] M. Tinkham, *Introduction To Superconductivity*, 2nd ed. (McGraw-Hill Companies, New York, NY, 1996).

[29] J. R. Waldram, *Superconductivity of Metals and Cuprates*, 2nd ed. (Cambridge University Press, New York, NY, 1979).

[30] O. S. Heavens, *Optical Properties of Thin Solid Films* (Dover Publications, Englewood Cliffs, NJ, 1991).

[31] Z. Knittl, *Optics of Thin Films (An Optical Multilayer Theory)*, *Wiley Series in Pure and Applied Optics* (John Wiley & Sons, New York, NY, 1976).

[32] A. W. Crook, J. Opt. Soc. Amer. **38**, 954 (1948).

[33] F. Abelès, Ann. d. Physique **3**, 504 (1948).

[34] P. Rouard, Ann. d. Physique **7**, 291 (1937).

[35] A. Vašíček, J. d. Phys. **11**, 342 (1950).

[36] J. M. Vaughan, *The Fabry-Perot Interferometer: History, Theory, Practice and Applications* (Adam Hilger, Bristol, UK, 1989).

[37] A. R. Kumar, V. A. Boychev, Z. M. Zhang, and D. B. Tanner, ASME J. Heat Transfer **122**, 785 (2000).

[38] G. Hernandez, *Fabry–Perot Interferometers*, Vol. 3 of *Cambridge Studies in Modern Optics* (Cambridge University Press, Cambridge, GB, 1986).

[39] M. V. Klein and T. E. Furtak, *Optics*, 2nd ed. (John Wiley & Sons, New York, NY, 1986).

[40] G. R. Fowles, *Introduction to Modern Optics*, 2nd ed. (Dover Publications, Englewood Cliffs, NJ, 1989).

[41] K. F. Renk, in *Studies of High Temperature Superconductors*, edited by A. V. Narlikar (Nova Science Publishers, Commack, NY, 1992), Vol. 10, pp. 25–62.

[42] A. V. Puchkov, D. N. Basov, and T. Timusk, J. Phys. Cond. Mat. **8**, 10049 (1996).

[43] T. Timusk and B. Statt, Rep. on Prog. in Phys. **62**, 61 (1999).

[44] D. N. Bassov and T. Timusk, in *Handbook on the Physics and Chemistry of Rare Earths*, edited by K. A. Gschneidner, Jr., L. Eyring, and M. B. Maple (Elsevier Science, North-Holland, Singapore, 2001), Vol. 31, Chap. 202, pp. 437–507.

[45] S. Tajima, S. Uchida, S. Tanaka, S. Kanbe, K. Kitazawa, and K. Fueki, Jap. J. Appl. Phys. **26**, L432 (1987).

[46] J. Orenstein, G. A. Thomas, D. H. Rapkine, C. B. Bethea, B. F. Levine, R. J. Cava, E. A. Reitman, and J. D. W. Johnson, Phys. Rev. B **36**, 729 (1987).

[47] S. L. Herr, K. Kamarás, C. D. Porter, M. G. Doss, D. B. Tanner, D. A. Bonn, J. E. Greedan, C. V. Stager, and T. Timusk, Phys. Rev. B **36**, 733 (1987).

[48] D. A. Bonn, J. E. Greedan, C. V. Stager, T. Timusk, M. G. Doss, S. L. Herr, K. Kamarás, and D. B. Tanner, Phys. Rev. Lett. **58**, 2249 (1987).

[49] K. Kamarás, C. D. Porter, M. G. Doss, S. L. Herr, D. B. Tanner, D. A. Bonn, J. E. Greedan, A. H. O'Reilly, C. V. Stager, and T. Timusk, Phys. Rev. Lett. **59**, 919 (1987).

[50] C. M. Varma, S. Schmitt-Rink, and E. Abrahams, Solid State Comm. **62**, 681 (1987).

[51] J. Orenstein and D. H. Rapkine, Phys. Rev. Lett. **60**, 968 (1988).

[52] Z. Schlesinger, R. T. Collins, and M. W. Schafer, Phys. Rev. B **36**, 5275 (1987).

[53] G. A. Thomas, A. J. Millis, R. N. Bhatt, R. J. Cava, and E. A. Reitman, Phys. Rev. B **36**, 736 (1987).

[54] S. Etemad, D. E. Aspnes, M. K. Kelly, R. Thomson, J.-M. Tarascon, and G. W. Hull, Phys. Rev. B **37**, 3396 (1988).

[55] S. Etemad, D. E. Aspnes, P. Barboux, G. W. Hull, M. K. Kelly, J.-M. Tarascon, R. Thomson, S. L. Herr, K. Kamarás, C. D. Porter, and D. B. Tanner, Mat. Res. Soc. Symp. Proc. **99**, 135 (1988).

[56] K. Kamarás, M. G. Doss, S. L. Herr, J. S. Kim, C. D. Porter, G. R. Stewart, D. B. Tanner, D. A. Bonn, J. E. Greedan, A. H. O'Reilly, C. V. Stager, T. Timusk, B. Keszei, S. Pekker, G. Hutiray, and L. Mihály, Mat. Res. Soc. Symp. Proc. **99**, 777 (1988).

[57] J. Orenstein, G. A. Thomas, D. H. Rapkine, C. B. Bethea, B. F. Levine, B. Batlogg, R. J. Cava, J. D. W. Johnson, and E. A. Reitman, Phys. Rev. B **36**, 8892 (1987).

[58] J. M. Tarascon, L. H. Greene, W. R. McKinnon, G. W. Hull, and T. H. Geballe, Science **235**, 1379 (1987).

[59] D. A. Bonn, A. H. O'Reilly, J. E. Greedan, C. V. Stager, T. Timusk, K. Kamarás, and D. B. Tanner, Phys. Rev. B **37**, 1547 (1988).

[60] D. A. Bonn, A. H. O'Reilly, J. E. Greedan, C. V. Stager, T. Timusk, K. Kamarás, and D. B. Tanner, Mat. Res. Soc. Symp. Proc. **99**, 227 (1988).

[61] T. Timusk, D. A. Bonn, J. E. Greedan, C. V. Stager, J. D. Garrett, A. H. O'Reilly, M. Reedyk, K. Kamarás, C. D. Porter, S. L. Herr, and D. B. Tanner, Physica C **153-155**, 1744 (1988).

[62] T. Timusk, S. L. Herr, K. Kamarás, C. D. Porter, D. B. Tanner, D. A. Bonn, J. D. Garrett, C. V. Stager, J. E. Greedan, and M. Reedyk, Phys. Rev. B **38**, 6683 (1988).

[63] J. M. Tarascon, W. R. McKinnon, L. H. Greene, G. W. Hull, and E. M. Vogel, Phys. Rev. B **36**, 226 (1987).

[64] M. Gurvitch and A. T. Fiory, Phys. Rev. Lett. **59**, 1337 (1987).

[65] J. Orenstein, G. A. Thomas, D. H. Rapkine, A. J. Millis, L. F. Schneermeyer, and J. V. Waszczak, Physica C **153-155**, 1740 (1988).

[66] G. A. Thomas, J. Orenstein, D. H. Rapkine, M. Capizzi, A. J. Millis, R. N. Bhatt, L. F. Schneermeyer, and J. V. Waszczak, Phys. Rev. Lett. **61**, 1313 (1988).

[67] D. van der Marel, J. van Elp, G. A. Sawatzky, and D. Heitmann, Phys. Rev. B **37**, 5136 (1988).

[68] J. Tanaka, K. Kamiya, M. Shimizu, M. Simada, C. Tanaka, H. Ozeki, K. Adachi, K. Iwahadhi, F. Sato, A. Sawada, S. Iwata, H. Sakuma, and S. Uchiyama, Physica C **153-155**, 1752 (1988).

[69] J. Tanaka, K. Kamiya, and S. Tsurumi, Physica C **153-155**, 653 (1988).

[70] S. Tajima, S. Uchida, H. Ishii, H. Takagi, S. Tanaka, U. Kawabe, H. Hasegawa, T. Aita, and T. Ishiba, Mod. Phys. Lett. B **1**, 353 (1988).

[71] R. T. Collins, Z. Schlesinger, G. V. Chandrasekhar, and M. W. Shafer, Phys. Rev. B **39**, 2251 (1989).

[72] T. Koide, H. Fukutani, A. Fujimori, R. Suzuki, T. Shidara, T. Takahashi, S. Hosoya, and M. Sato, Jap. J. Appl. Phys. **26-3**, 915 (1987).

[73] D. A. Bonn, J. E. Greedan, C. V. Stager, T. Timusk, K. Kamarás, C. D. Porter, M. G. Doss, S. L. Herr, and D. B. Tanner, Solid State Sci. **1**, 349 (1987).

[74] M. K. Kelly, P. Barboux, J.-M. Tarascon, D. E. Aspnes, W. A. Bonner, and P. A. Morris, Phys. Rev. B **38**, 870 (1988).

[75] H. P. Geserich, B. Koch, G. Scheiber, J. Geerk, H. C. Li, G. Linker, W. Weber, and W. Assmus, Physica C **153-155**, 661 (1988).

[76] D. C. Mattis and J. Bardeen, Phys. Rev. **111**, 412 (1958).

[77] S. Uchida, T. Ido, H. Takagi, T. Arima, Y. Tokura, and S. Tajima, Phys. Rev. B **43**, 7942 (1991).

[78] S. Uchida, H. Takagi, and Y. Tokura, Physica C **162-164**, 1677 (1989).

[79] S. Tajima, T. Ido, S. Ishibashi, T. Itoh, H. Eisaki, T. Arima, H. Takagi, and S. Uchida, Phys. Rev. B **43**, 10496 (1991).

[80] S. L. Cooper, G. A. Thomas, J. Orenstein, D. H. Rapkine, A. J. Millis, S.-W. Cheong, A. S. Cooper, and Z. Fisk, Phys. Rev. B **41**, 11605 (1990).

[81] M. S. Hybertsen and L. F. Mattheiss, Phys. Rev. B **60**, 1661 (1988).

[82] H. Krakauer and W. E. Pickett, Phys. Rev. Lett. **60**, 1665 (1988).

[83] F. Herman, R. V. Kasowski, and W. Y. Hsu, Phys. Rev. B **38**, 204 (1988).

[84] M. Tanaka, T. Takahashi, H. Katayama-Yoshida, S. Yamazaki, M. Fujinami, Y. Okabe, W. Mizutani, M. Ono, and K. Kajimura, Nature **339**, 691 (1989).

[85] Y.-Y. Wang and A. L. Ritter, Phys. Rev. B **36**, 736 (1987).

[86] B. O. Wells, Z.-X. Shen, D. S. Dessau, W. E. Spicer, C. G. Olson, D. B. Mitzi, A. Kapitulnik, R. S. List, and A. Arko, Phys. Rev. Lett. **65**, 3056 (1990).

[87] A. Maeda, M. Hase, I. Tsukada, K. Noda, S. Takebayashi, and K. Uchinokura, Phys. Rev. B **41**, 6418 (1990).

[88] M. Reedyk, D. A. Bonn, J. D. Garrett, J. E. Greedan, C. V. Stager, T. Timusk, K. Kamarás, and D. B. Tanner, Phys. Rev. B **38**, 11981 (1988).

[89] Y.-Y. Wang, G. Feng, and A. L. Ritter, Phys. Rev. B **42**, 420 (1990).

[90] O. V. Kosogov, M. V. Belousov, V. A. Vasil'ev, V. Y. Davydov, K. G. Dyo, A. A. Kopylov, V. D. Petrikov, and V. V. Tret'yakov, JETP Lett. **48**, 530 (1989).

[91] J. Humlicek, E. Schmidt, L. Bocanek, M. Carriga, and M. Cardona, Solid State Comm. **73**, 127 (1990).

[92] A. M. Rao, P. C. Eklund, G. W. Lehman, D. W. Face, G. L. Doll, G. Dresselhaus, and M. S. Dresselhaus, Phys. Rev. B **42**, 193 (1990).

[93] P. Calvani, M. Capizzi, S. Lupi, P. Maselli, D. Peschiaroli, and H. Katayama-Yoshida, Solid State Comm. **74**, 1333 (1990).

[94] L. Forro, G. L. Carr, G. P. Williams, D. Mandrus, and L. Mihály, Phys. Rev. Lett. **65**, 1941 (1990).

[95] D. B. Romero, G. L. Carr, D. B. Tanner, L. Forro, D. Mandrus, L. Mihály, and G. P. Williams, Phys. Rev. B **44**, 2818 (1991).

[96] R. E. Glover and M. Tinkham, Phys. Rev. B **107**, 844 (1956).

[97] R. E. Glover and M. Tinkham, Phys. Rev. B **108**, 243 (1957).

[98] D. B. Romero, C. D. Porter, D. B. Tanner, L. Forro, D. Mandrus, L. Mihály, G. L. Carr, and G. P. Williams, Solid State Comm. **82**, 183 (1992).

[99] D. B. Tanner, D. B. Romero, K. Kamarás, G. L. Carr, L. Forro, D. Mandrus, L. Mihály, and G. P. Williams, in *Electronic Structure and Mechanisms for High-Temperature Superconductivity*, edited by G. C. V. et al. (Plenum Press, New York, 1991).

[100] S. Martin, A. T. Fiory, R. M. Fleming, L. F. Schneermeyer, and J. V. Waszczak, Phys. Rev. B **41**, 846 (1990).

[101] J. Schützmann, W. Ose, J. K. K. F. Renk, B. Roas, L. Schultz, and G. Semann-Ischenko, Europhys. Lett. **8**, 679 (1989).

[102] .

[103] J. Orenstein, G. A. Thomas, A. J. Millis, S. L. Cooper, D. H. Rapkine, T. Timusk, L. F. Schneermeyer, and J. V. Waszczak, Phys. Rev. B **42**, 6342 (1990).

[104] K. Kamarás, S. L. Herr, C. D. Porter, N. Tache, D. B. Tanner, S. Etemad, T. Venkatesan, E. Chase, A. Inam, X. D. Wu, M. S. Hedge, and B. Dutta, Phys. Rev. Lett. **64**, 84 (1990).

[105] R. J. Bell, *Introductory Fourier Transform Spectroscopy* (Academic Press, New York, NY, 1972).

[106] B. C. Smith, *Fundamentals of Fourier Transform Infrared Spectroscopy* (CRC Press, Boca Raton, FL, 1996).

[107] W. Herres and J. Gronholtz, Comp. App. Lab. **2**, 216 (1984).

[108] Z. M. Zhang, A. R. Kumar, V. A. Boychev, and D. B. Tanner, Appl. Phys. Lett. **73**, 1907 (1998).

[109] B. Schrader, in *Infrared and Raman Spectroscopy, Methods and Applications*, edited by B. Schrader (VCH, Weinheim, Germany, 1995), Chap. 3, pp. 63–78, 97–108, 120–135.

[110] L. Genzel, in *Millimeter and Submillimeter Wave Spectroscopy of Solids*, edited by G. Grüner (Springer, Berlin, Germany, 1998), Vol. 74, Chap. 5, pp. 169–220.

[111] P. R. Griffiths and J. A. de Haseth, *Fourier Transform Infrared Spectroscopy* (John Wiley & Sons, New York, NY, 1986).

[112] J. Gronholtz and W. Herres, Instruments & Computers **3**, 10 (1985).

[113] J. Gronholtz and W. Herres, Instruments & Computers **3**, 45 (1985).

[114] J. Chamberlain, *The Principles of Interferometric Spectroscopy* (John Wiley & Sons, Chichester, UK, 1979).

[115] K. D. Möller and W. G. Rothschild, *Far-Infrared Spectroscopy* (WILEY-INTERSCIENCE, John Wiley & Sons, New York, NY, 1971).

[116] F. Gao, *Temperature Dependence of Infrared and Optical Properties of High-temperature Superconductors*, PhD dissertation, University of Florida, Gainesville, FL, 1992.

[117] M. A. Quijada, *Anisotropy in the Infrared, Optical and Transport Properties of High-temperature Superconductors*, PhD dissertation, University of Florida, Gainesville, FL, 1994.

[118] Y.-D. Yoon, *Optical Properties of Cuprates and Related Materials*, PhD dissertation, University of Florida, Gainesville, FL, 1995.

[119] N. Tache, *Infrared and Optical Studies of Rare Earth Substitutions in High-temperature Superconductors*, PhD dissertation, University of Florida, Gainesville, FL, 1997.

[120] A. R. Kumar, *Far-Infrared Radiative Properties of Superconducting YBCO Films Deposited on Silicon Substrates*, PhD dissertation, University of Florida, Gainesville, FL, 1999.

[121] D. John, *Optical Properties of Cerium Activated Calcium Thiogallate and Strontium Sulphide Phosphors*, PhD dissertation, University of Florida, Gainesville, FL, 1997.

[122] J. D. LaVeigne, *Time-resolved Infrared Spectroscopy at the NSLS U12IR Beamline*, PhD dissertation, University of Florida, Gainesville, FL, 2001.

[123] J. Hwang, *Electrochemical Spectroscopy of Conjugated Polymers*, PhD dissertation, University of Florida, Gainesville, FL, 2001.

[124] A. R. Kumar, Z. M. Zhang, V. A. Boychev, D. B. Tanner, L. R. Vale, and D. A. Rudman, ASME J. Heat Transfer **121**, 844 (1999).

[125] A. R. Kumar, Z. M. Zhang, V. A. Boychev, and D. B. Tanner, Microscale Thermophysical Engineering **3**, 5 (1999).

[126] E. V. Loewenstein, D. R. Smith, and R. L. Morgan, Appl. Opt. **12**, 398 (1973).

[127] V. V. Sobolev, S. A. Alekseev, and V. I. Donetskih, *Raschety Opticheskih Funktsii Poluprovodnikov po Sootnosheniqm Kramersa-Kroniga; Calculations of Optical Functions of Semiconductors using Kramers–Kronig Relations* (Shtiintsa, Kishinev, USSR, 1976), p. 124, In Russian.

[128] V. I. Gavrilenko, A. M. Grehov, D. V. Korbutqk, and V. G. Litovchenko, *Opticheskie svoystva poluprovodnikov, Spravochnik; Optical Properties of Semiconductors, Handbook* (Naukovaq dumka, Kiev, USSR, 1987), p. 180–184, In Russian.

[129] Y. S. Touloukian, R. K. Kirby, R. E. Taylor, and T. Y. Lee, *Thermophysical Properties of Matter The TPRC Data Series* (IFI/Plenum, New York, NY, 1977), Vol. 13, pp. 154–162.

[130] *American Institute of Physics Handbook*, 3rd ed., edited by D. E. Gray (McGraw–Hill, New York, NY, 1972), pp. 4.128 – 4.129.

[131] *Handbook of Physical Quantities*, edited by I. S. Grigoriev, E. Z. Meilikhov, and A. A.Radzig (CRC Press, Boca Raton, FL, 1977), p. 289.

[132] E. E. Russell and E. E. Bell, J. Opt. Soc. Am. **57**, 341 (1967).

[133] W. G. Spitzer and D. A. Kleinman, Phys. Rev. **121**, 1324 (1961).

[134] *Handbook of Optical constants of Solids*, edited by E. D. Palik and G. Ghosh (Academic Press, Boston, MA, 1997).

[135] *Inorganics and Related Compounds* (Sadtler Research Laboratories, Inc., Philadelphia, PA, 1965).

[136] R. A. Nyquist and R. O. Kagel, *Infrared Spectra of Inorganic Compounds* (Academic Press, New York, NY, 1965).

[137] R. F. Belt and R. Uhrin, in *Science and Technology of Thin Film Superconductors*, edited by R. D. McConnell and S. A. Wolf (Plenum, New York, 1989), Vol. 2, p. 353.

[138] J. M. Phillips, J. Appl. Phys. **79**, 1829 (1996).

[139] D. Grischkowsky and S. Keiding, Appl. Phys. Lett. **57**, 1055 (1990).

[140] A. Hadni, X. Gerbaux, H. M. Cudraz, M. Tazawa, J. C. Mage, B. Marcilhac, Mercandalli, and D. Mansart, Physica C **245**, 219 (1995).

[141] K. Kamarás, S. L. Herr, C. D. Porter, N. Tache, D. B. Tanner, S. Etemad, T. Venkatesan, E. Chase, A. Inam, X. D. Wu, M. S. Hedge, and B. Dutta, Phys. Rev. Lett. **64**, 1692 (1990).

[142] L. Genzel, M. Bauer, M. Cardona, E. Schönherr, and A. Simon, Phys. Rev. B **40**, 2170 (1989).

[143] E. Liarokapis, E. I. Kamitsos, T. Leventouri, and F. D. Medina, Physica C **157**, 551 (1989).

[144] M. K. Crawford, G. Burns, and F. Holtzberg, Solid State Comm. **70**, 557 (1989).

[145] R. T. Collins, Z. Schlesinger, F. Holtzberg, and C. Feild, Phys. Rev. Lett. **63**, 422 (1989).

[146] S. Onari, S. Hidaka, T. Arai, and T. Mori, Solid State Comm. **71**, 195 (1989).

[147] R. Feile, Physica C **159**, 1 (1989).

[148] Z. M. Zhang, T. A. Le, M. I. Flik, and E. G. Cravahlo, ASME J. Heat Transfer **116**, 253 (1994).

[149] M. I. Flik, Z. M. Zhang, K. E. Goodson, M. P. Siegal, and J. M. Philips, Phys. Rev. B **46**, 5606 (1992).

[150] Z. M. Zhang, in *Proc. Tenth Intl. Heat Transfer Conf.*, edited by G. F. Hewitt (Brighton, UK, 1994), Vol. 2, pp. 177–182.

[151] D. A. Bonn, P. Dosanjh, R. Liang, and W. N. Hardy, Phys. Rev. Lett. **68**, 2390 (1992).

[152] L. Mechin, J. C. Villegier, G. Rolland, and F. Laugier, Physica C **269**, 124 (1996).

[153] S. W. McKnight, K. P. Stewart, H. D. Drew, and K. Moorjani, Infrared Physics **27**, 327 (1987).

[154] C. M. Varma, P. B. Littlewood, S. Schmitt-Rink, E. Abrahams, and A. E. Ruckenstein, Phys. Rev. Lett. **63**, 1996 (1989).

[155] A. Virosztek and J. Ruvalds, Phys. Rev. B **42**, 4064 (1990).

[156] S. M. Quinlan, P. J. Hirschfeld, and D. J. Scalapino, Phys. Rev. B **53**, 8575 (1996).

[157] K. F. Renk, J. Betz, J. Schützmann, A. Prückl, B. Brunner, and H. Lengfellner, Appl. Phys. Lett. **57**, 2148 (1990).

[158] L. Genzel, M. Bauer, R. Yoder, and H.-U. Habermeier, Solid State Comm. **81**, 589 (1992).

[159] C. G. Malone, Z. M. Zhang, M. I. Flik, and E. G. Cravahlo, IEEE Trans. Appl. Supercond. **3**, 2852 (1993).

[160] F. Gao, G. L. Carr, C. D. Porter, D. B. Tanner, S. Etemad, T. Venkatesan, A. Inam, B. Dutta, X. D. Wu, G. P. Williams, and C. J. Hirschmugl, Phys. Rev. B **43**, 10383 (1991).

[161] S. Cunsolo, P. Dore, S. Lupi, R. Trippetti, C. P. Varsamis, and A. Sherman, Physica C **211**, 22 (1993).

[162] P. E. Phelan, G. Chen, and C. L. Tien, J. Heat Transfer **114**, 227 (1992).

[163] G. L. Carr, M. Quijada, D. B. Tanner, C. J. Hirschmugl, G. P. Williams, S. Etemad, B. Dutta, F. DeRosa, A. Inam, T. Venkatesan, and X. Xi, Appl. Phys. Lett. **57**, 2725 (1990).

[164] Z. M. Zhang and A. Frenkel, J. Supercond. **7**, 871 (1994).

[165] A. R. Kumar and Z. M. Zhang, in *Recent Research Developments in Applied Spectroscopy*, edited by S. Pandalai (Research Signpost, India, 1999), Vol. 2, pp. 99–112.

[166] J. G. Bednorz and K. A. Müller, Z. Phys. B **64**, 189 (1986).

[167] P. Belland and J. C. Lecullier, Appl. Opt. **19**, 1946 (1980).

[168] P. Wiese, S. Riederer, J. Schutzmann, B. Gorshunov, J. Betz, and K. F. Renk, Intl. J. Infrared and Millimeter Waves **13**, 65 (1992).

[169] E. V. Pechen, S. Vent, B. Brunner, A. Prückl, S. Lipp, G. Linder, O. Alexandrov, J. Schützmann, and K. F. Renk, App. Phys. Lett. **61**, 1980 (1992).

[170] K. F. Renk and L. Genzel, Appl. Opt. **1**, 643 (1962).

[171] G. Chen and C. L. Tien, ASME J. Heat Transfer **114**, 636 (1992).

[172] A. R. Anderson and Bayazitoglu, J. Thermophys. Heat Transfer **10**, 26 (1996).

[173] E. N. Grossman and D. G. McDonald, Optical Engineering **34**, 1289 (1995).

BIOGRAPHICAL SKETCH

I was born on December 6, 1954, in Sofia, Bulgaria. I am married and have two teenage daughters. In 1980 I graduated from Sofia University, Sofia, Bulgaria, with an MS degree in Semiconductor Physics. My MS thesis *"Temperature Dependence of Co_3O_4 Transport Properties"* was supervised by Prof. Milko N. Iliev. We found a new behavior of conductivity with temperature.

My past employment record:

- Institute of Non-Ferrous Metallurgy, Sofia, Bulgaria, Physicist, 1980–82;
- Bulgarian Academy of Sciences, Solar Energy Lab, Sofia, Bulgaria, Physicist, 1982–88; studied photoresisting properties of II-VI compounds and amorphous silicon;
- University of Mining and Geology, Sofia, Bulgaria, Full-time Teaching Assistant, 1988–93; Taught about 1500 undergraduate students (labs, discussions, written and oral exams). Proofread their new lab manual when I joined;
- University of Florida, Gainesville, FL, Summer Internship, 1994; Assembled electronic circuits for custom-built He-level meters under the supervision of Dr. Gary Ihas and Larry Frederick;
- University of Florida, Gainesville, FL, Graduate Assistant, 1993–2001; Doctoral research presented herein, and teaching lab sections to about 400 students. Participated in moving and settling of Dr. Tanner's infrared lab into the New Physics Building. Spent a lot of time for restoring a large, custom-made Michelson interferometer.

I joined Dr. Tanner's group in 1994, but started working more actively in 1996, after completing the major course requirements.

By this moment I have coauthored seven research papers in refereed journals and have reported at several meetings and workshops.

Currently I am a Member of the American Physical Society and the Optical Society of America. I am a former member of the Bulgarian Physical Society.

By the time of commencement I hope to have found a research and development position as a scientist, physicist, or optical engineer in the high-tech industry, possibly optical telecommunications. But if the hi-tech stocks do not recover fast from their spring melt-down and current recession, I may end up doing time as a post-doctoral associate, instead.

I certify that I have read this study and that in my opinion it conforms to acceptable standards of scholarly presentation and is fully adequate, in scope and quality, as a dissertation for the degree of Doctor of Philosophy.

David B. Tanner, Chairman
Professor of Physics

I certify that I have read this study and that in my opinion it conforms to acceptable standards of scholarly presentation and is fully adequate, in scope and quality, as a dissertation for the degree of Doctor of Philosophy.

Arthur F. Hebard
Professor of Physics

I certify that I have read this study and that in my opinion it conforms to acceptable standards of scholarly presentation and is fully adequate, in scope and quality, as a dissertation for the degree of Doctor of Philosophy.

Charles F. Hooper, Jr.
Professor of Physics

I certify that I have read this study and that in my opinion it conforms to acceptable standards of scholarly presentation and is fully adequate, in scope and quality, as a dissertation for the degree of Doctor of Philosophy.

Selman P. Hershfield
Associate Professor of Physics

I certify that I have read this study and that in my opinion it conforms to acceptable standards of scholarly presentation and is fully adequate, in scope and quality, as a dissertation for the degree of Doctor of Philosophy.

Zhuomin M. Zhang
Professor of Mechanical Engineering

This dissertation was submitted to the Graduate Faculty of the Department of Physics in the College of Liberal Arts and Sciences and to the Graduate School and was accepted as partial fulfillment of the requirements for the degree of Doctor of Philosophy.

December 2001

Dean, Graduate School